Université de Liège – Académie Wallonie-Europe
Faculté des Sciences

MORPHOLOGY AND DYNAMICS OF THE IO UV FOOTPRINT

Dissertation présentée par
Bertrand BONFOND
en vue de l'obtention du grade
de
Docteur en Sciences

A Marie,

Acknowledgments

Je tiens remercier en particulier le professeur Jean-Claude Gérard pour m'avoir permis de travailler sur ce sujet fascinant au sein du LPAP en m'accordant à la fois sa confiance et les moyens de mener à bien cette étude. Pour un passionné de tout ce qui concerne l'Espace comme moi, l'opportunité de travailler sur de véritables images provenant du Télescope Spatial Hubble fut un honneur et un plaisir au quotidien. Je le remercie, ainsi que le docteur Denis Grodent, pour leur encadrement et leur disponibilité exceptionnels. Tout ce que je sais aujourd'hui sur les magnétosphères des planètes géantes et sur l'analyse des images HST, je le dois à leur patience et à leur compétence scientifique. En outre, je voudrais remercier ma collègue de bureau, le docteur Aikaterini Radioti, pour sa bonne humeur et ses avis éclairés.

Je remercie également Angela Della Vecchia, Anne Mouchet, Caroline Blockx, Cédric Cox, Lauriane Soret, Mahdia Belounis, Marie Dury et Valérie Coumans sans qui l'ambiance du labo ne serait pas ce qu'elle est. Merci enfin à tous les membres du LPAP et de l'UMCCB pour leur accueil et les conseils que chacun m'aura donné durant ces dernières années.

Je voudrais exprimer toute ma reconnaissance envers mes parents, Marie-Lise et Ronan, pour avoir supporté mes états d'âmes et mes angoisses pendant de très longues années, ainsi qu'à ma compagne, Marie, pour avoir pris la relève. Son soutien et sa compréhension furent vraiment précieux, en particulier ces derniers temps.

Enfin, mes remerciements vont à ma famille qui m'a toujours soutenu ainsi qu'à mes potes avec qui j'ai partagé pas mal de bons moments durant cette thèse.

"There is a theory which states that if ever anyone discovers exactly what the Universe is for and why it is here, it will instantly disappear and be replaced by something even more bizarre and inexplicable.

There is another theory which states that this has already happened."

Douglas Adams

Abstract

The Io UV footprint (IFP) is one of the most spectacular signatures of the Io-Jupiter interaction. It consists of several auroral spots and an extended tail which are located close to the feet of the magnetic field lines passing through Io in each hemisphere. The purpose of the present study is to demonstrate that a careful analysis of the Io UV footprint based on observations acquired with the STIS and ACS high resolution and high sensitivity FUV cameras on board the Hubble Space Telescope can provide us with essential information on the ongoing physical processes. The thesis is organized around basic questions: "What is the Io footprint?", "Where is the Io footprint?", "How high is the Io footprint?", "How big is the Io footprint?" and finally: "How bright is the Io footprint?" The answers to these questions have profound implications for the understanding of the phenomenon.

Among the most important results of this work is the unexpected finding of a faint auroral spot appearing upstream of the main Io spot in one hemisphere while only downstream spots are seen in the opposite hemisphere. The detailed study of the evolution of the inter-spot distances puts previous models describing the footprint morphology under question. We propose a new interpretation which involves that some spots are caused by electrons accelerated away from the planet along the field lines in one hemisphere, crossing the equatorial plane in the form of electron beams and precipitating in the opposite hemisphere, creating the so-called Trans-hemispheric Electron Beam (TEB) spots.

The information provided by the position of the satellite footprints is not restricted to the interaction between the moon and the Jovian magnetosphere. The analysis of the footpaths of Io, Europa and Ganymede helped us to further constrain the magnetic field models, notably through the identification of a large magnetic anomaly in the northern hemisphere. Additionally, the study of the speed of the Io footprint along its reference contour suggests that a second anomaly regions may also exist in the North.

In this work, we present a new and direct method to measure the altitude of the different footprint features. The main spot and the tail emissions have a peak altitude of 900 km while the peak altitude of the Trans-hemispheric Electron Beam spot is 700 km. These results suggest that the main spot and tail emissions are caused by the precipitation of electrons with a mean energy around 1 keV, far lower than the 55 keV value previously derived from spectral measurements. The vertical extent of these emissions is surprisingly broad (scale height $\sim$400 km) and is best fitted with an incoming kappa electron energy distribution (spectral index $\sim$2.3). This suggests that the electron acceleration is supplied by processes related to inertial Alfvén waves rather than by quasi-static potentials as proposed by some theoretical models.

The size of the main footprint spot is carefully estimated on a much larger image sample than before: its length along the footpath is $\sim$900 km while its width perpendicular to the footpath is $<$200 km. Larger lengths are sometimes observed but in that case, they are attributed to the mix of individual spots. The spot length is larger than the projected diameter of Io around the magnetic field lines but is consistent with recent simulations.

As far as the Io footprint brightness is concerned, variations on two timescales have been studied. On timescales of minutes, systematic brightness fluctuation on the order of 30% (and going up to 50%) are observed. Additionally, cases of simultaneous variations of the main and the TEB spots are reported, which suggests that the process that triggers these fast variations is located close to the planet. Variations of the main spot brightness with the System III longitude of Io are also analyzed. Our new measurement method fully considering the multi-spot structure of the IFP and the real geometry of the observations provides more accurate estimates for the precipitating energy flux (between 100 and 500 mW/m^2 for the main spot). The main spot brightness peaks at 110° and 290° longitude, which could be attributed either to an enhanced interaction strength when Io is near the dense torus center or to spots merging which is also observed to occur in these sector. Nevertheless, strong North-South asymmetries are also observed, which suggests that the surface magnetic field strength also influences the spots brightness.

Résumé

L'empreinte aurorale d'Io est l'une des signatures les plus impressionnantes de l'interaction Io-Jupiter. Présente dans chaque hémisphère, elle se situe à proximité des pieds des lignes de champ magnétique qui interceptent Io et se compose de plusieurs taches suivies d'une longue trainée. Cette étude vise à démontrer qu'une analyse minutieuse de l'empreinte UV d'Io basée sur les observations des instruments STIS et ACS du Télescope Spatial Hubble peut apporter des informations cruciales sur les processus physiques qui sont en jeu. Cette thèse est organisée autour de questions relativement basiques: "Qu'est-ce que l'empreinte d'Io?", "Où se trouve-t-elle?", "A quelle altitude se trouve-t-elle?", "Quelle est sa taille?" et enfin "Quelle est sa brillance?". Les réponses à ces questions ont de profondes implications pour la compréhension du phénomène.

Parmi les résultats principaux de ce travail, il y a la découverte inattendue d'une faible tache aurorale apparaissant en amont de la tache principale dans un hémisphère alors que les seules taches observées dans l'hémisphère opposé sont situées en aval. L'étude détaillée de la distance inter-taches remet en question les précédents modèles décrivant la morphologie de l'empreinte. Nous proposons ici une nouvelle interprétation de certaines de ces taches: elles seraient causées par des électrons initialement accélérés le long des lignes de champ dans la direction opposée à Jupiter, qui ensuite traverseraient le plan équatorial sous la forme de faisceaux d'électrons et qui précipiteraient finalement dans l'hémisphère opposé en générant la tache du Faisceau d'Electrons Trans-hemisphérique (FET).

Les informations fournies par la position des empreintes de satellites ne se limitent pas à l'interaction entre Io et la magnétosphère de Jupiter. L'analyse des contours parcourus par les empreintes d'Io, d'Europe et de Ganymède permet de mieux contraindre les modèles de champ magnétique joviens, entre autre à travers l'identification d'une importante anomalie magnétique dans l'hémisphère nord. De plus, l'étude de la vitesse de l'empreinte d'Io le long du contour de référence suggère qu'elle pourrait être accompagnée d'une deuxième anomalie dans cet hémisphère.

Dans cette étude, nous présentons une méthode directe pour mesurer l'altitude des différentes sous-structures qui forment l'empreinte. Le pic d'émissions de la

tache principale et de la trainée est situé à 900 km d'altitude alors que celui de la tache FET est à 700 km. Ces résultats suggèrent que la tache principale et la trainée sont la conséquence de la précipitation d'électrons ayant une énergie moyenne d'approximativement 1 keV, une valeur largement inférieure aux 55 keV déduits à partir de précédentes mesures spectrales. L'extension verticale de ces émissions est étonnamment large (hauteur d'échelle: $\sim$400 km) et la distribution d'énergie des électrons incidents qui reproduit au mieux les observations est une distribution kappa d'indice spectral 2.3. Cela suggère que l'accélération des électrons est liée à des ondes d'Alfvén inertielles plutôt qu'aux potentiels quasi-statiques proposés par certains modèles théoriques.

La taille de la tache principale a été mesurée sur un ensemble d'images beaucoup plus étendu qu'auparavant: sa longueur le long du contour est de $\sim$900 km alors que sa largeur telle que mesurée perpendiculairement à celui-ci est de $<$200 km. Des longueurs plus importants sont parfois observées mais elles résultent de la superposition partielle de plusieurs taches individuelles. La longueur des taches est plus grande que la projection du diamètre d'Io le long des lignes de champ, ce qui était prévu par des simulations récentes.

En ce qui concerne la brillance des taches, deux échelles de temps ont été étudiées en particulier. A l'échelle de la minute, nous avons mis en évidence des fluctuations de l'ordre de 30% de la brillance moyenne et pouvant atteindre jusqu'à 50 % de celle-ci. Dans certains cas, on observe des variations corrélées de la tache principale et de la tache FET, ce qui suggère que le processus qui induit ces variations rapides se situe près de la surface de Jupiter. Les variations de la brillance de la tache principale en fonction de la longitude Système III d'Io ont également été analysées. Notre nouvelle méthode de mesure prend pleinement en compte la géométrie de l'observation ainsi que le fait que l'empreinte est composée de différentes taches, ce qui permet une estimation plus précise du flux d'énergie incident (entre 100 et 500 mW/m^2 pour la tache principale). La brillance de la tache principale possède deux maxima, un à 110° et un autre à 290° de longitude. Ces augmentations de brillance peuvent avoir deux origines: soit elles sont dues à l'augmentation de l'intensité de l'interaction entre Io et le plasma quand Io est proche du centre du tore, soit elles sont liées à la superposition des taches principales et FET qui se produit également dans ces secteurs. Néanmoins, de fortes asymétries Nord-Sud sont aussi observées, ce qui semble indiquer que l'intensité du champ magnétique de surface joue aussi un rôle en ce qui concerne la brillance des spots.

Contents

Chapter 1

Introduction

1.1 Why study the Io footprint?

Solar system planets are usually seen as huge balls of rock or gas limited to their planetary radius. However, their influence on the surrounding environment extends much beyond the upper limit of their atmosphere.

Their gravitational influence enables a variety of smaller astronomical objects to orbit around them. Jupiter, for instance, is surrounded by a multitude of satellites (63 have been observed so far). Four particularly big moons, Io, Europa, Ganymede and Callisto stand among these satellites. These moons are called Galilean satellites, after their discovery by Galileo Galilei in 1610. The present study focuses on Io, which is both the closest and the most turbulent of these four. Its surface is spotted with erupting volcanoes that project plumes of material up to 300 km in altitude.

Planets also have an electromagnetic sphere of influence, a region where phenomena are dominated or organized by the planetary magnetic field. These regions may be pictured as cavities dug into the solar wind and are called magnetospheres. Aurorae are radiative emissions resulting from the precipitation of high energy particles into the planetary atmosphere. They are often considered as the imprint of the different phenomena occurring inside the magnetosphere. This view is particularly relevant for the subject of this work: the Io footprint. The goal of this study is to understand the auroral feedback which arises when the most volcanic body of the solar system meets the most strongly-magnetized planet.

The Io ultraviolet (UV) auroral footprint is one of the most spectacular consequences of the strong interaction between Io and the magnetosphere of Jupiter. It consists of bright spots visible in both hemispheres of Jupiter's atmosphere. Their

latitude is a few degrees equatorward from the main polar aurorae and their longitude is linked to the orbital position of Io with respect to Jupiter. Recent studies showed that these spots can be multiple and are followed by a faint trailing tail of UV emissions (*Clarke et al.*, 2002; *Gérard et al.*, 2006). These studies also demonstrated that the brightness of the Io spots is evolving with typical timescales of hours. The objective of the present work is to characterize as precisely as possible the morphology and the dynamics of these footprint spots in order to unveil the mechanisms that cause them.

The observable signature of the Io-Jupiter interaction is not a unique exotic phenomenon. The finding of similar interactions with Europa and Ganymede has led to the conclusion that the Io case could be the paradigm of a possibly widespread phenomenon in the universe. It is most likely that similar interactions could occur between an exoplanet and its satellites, and the same kind of mechanism has also been proposed for the interaction between a planet orbiting a white dwarf or between a magnetic and a non-magnetic white dwarf (*Bhardwaj and Michael* (2002)). However, the most dramatic examples of similar interactions have been recently found to take place between an exoplanet an its parent star. In the last decade, several cases of periodic enhancements of the chromospheric emissions of stars correlated with the orbital period of giant planets in a close orbit have been found (*Shkolnik et al.*, 2003; *Shkolnik et al.*, 2005). Additionally, photometric satellite observations performed by MOST (*Walker et al.*, 2008) and CoRoT (*Pagano et al.*, 2009) also found evidences for stellar spots caused by a magnetic interaction between exoplanets and their parent stars.

The first clues for the Io-Jupiter interaction come from the radio domain and the first evidence for light emissions on Jupiter related to Io were found in the infrared (IR) wavelengths. However, thanks to the successive improvements of the Hubble Space Telescope (HST) instruments, the richest database concerning the Io footprint currently lies in the far ultraviolet (FUV) domain. Several early studies have been carried out based on HST data, which unraveled some essential characteristics of the Io footprint. However, many grey areas still remained concerning the ongoing mechanisms related to the Io-Jupiter interaction and some early results appear to be contradictory.

1.2 Outline of the thesis

This thesis is divided into two parts, spreading over nine chapters. A large part of my contribution to the study of the Io footprint consisted of resolving technical image processing issues that were not specifically related to the footprint. Among these tasks were the construction of a standardized database containing all the existing high-resolution FUV observations of the Jovian aurorae and the compilation of a complete catalog of all these images and spectra. Another task was the development of automatic methods to find the planetary center and orientation on the images. Therefore, I have deliberately isolated most of the technical discussions related to the dataset and images processing in Chapter 2. The idea is to separate the common technical issues from the detailed analysis and interpretation of the different Io footprint characteristics. Moreover, these methods have also been developed so that they can be applied to other studies using HST images, both for Jupiter and Saturn. Some readers might be only interested in this technical part and not in Io footprint related issues. In addition to these generic image processing procedures, I have been given the opportunity to apply a method that I specifically developed for characterizing the Io footprint tail (see Chapter 5) to the main auroral emissions at Saturn. Consequently, I decided to report the outcome of this latter study in Appendix 1.

The second part of my thesis, which actually constitutes the core of the present work, is formed by this introduction and chapters 3 through 8. The goal of this part of my thesis is to demonstrate that a careful analysis of the Io footprint characteristics on the HST FUV images from the STIS and ACS instruments can provide us with crucial information to understand the Io-Jupiter electromagnetic interaction. The present manuscript is articulated around five basic questions:

- What is the Io footprint? (Chapter 3)
- Where is the Io footprint? (Chapter 4)
- How high is the Io footprint? (Chapter 5)
- How big is the Io footprint? (Chapter 6)
- How bright is the Io footprint? (Chapter 7)

We will see that the answer to each of these questions has very profound implications for the Io-Jupiter electromagnetic interaction and its underlying physics. However,

my approach is not inductivistic. Various theoretical models have made predictions for these different quantities. In each case, these predictions were tested against the observations. As a result, some models were validated while others were discarded. However, the most interesting cases arise when the observational results do not match any previous model expectations. It is then necessary to propose alternative interpretations and test them against other types of measurements.

Before diving into the detailed exploration of the Io UV footprint, I will present briefly the two actors of the celestial play we are concerned with: Jupiter and its magnetosphere on one side and Io on the other. A section is also dedicated to the different models that have been developed in order to describe the interaction. Then, the observations related to Io-Jupiter interaction are examined. These observations are the starting point of our investigations. Finally, the last section of the introductory chapter consists of a short description of the two instruments that have been considered in the present work.

1.3 Coordinate systems

Since Jupiter is a gaseous planet, no coordinate system can be related to the crustal rotation as is the case for rocky or icy bodies. Consequently, several coordinate systems have been defined relative to the motion of the cloud bands or to the rotation of the magnetic field.

As far as the polar aurorae are concerned, the most relevant coordinate system is the so-called System III, since the main auroral features are approximately fixed in this reference frame. This coordinate system is bound to the Jovian magnetic field. More precisely, it is defined by the rotational period of decametric radio sources in Jupiter's ionosphere. This coordinate system is left-handed, i.e. the longitudes increase from dusk to dawn through noon. The System III longitude of the intersection point of the Earth-Jupiter line with the Jovian surface (i.e. the sub-Earth longitude) is called the Central Meridian Longitude (CML).

Another coordinate system is widely used, notably for describing the position of the moons relative to the observer on the Earth. The reference meridian is fixed relative to the Earth-Jupiter line, 0° being in the anti-Earth direction. This coordinate system is right-handed, i.e. the longitudes increase from dawn to dusk through noon.

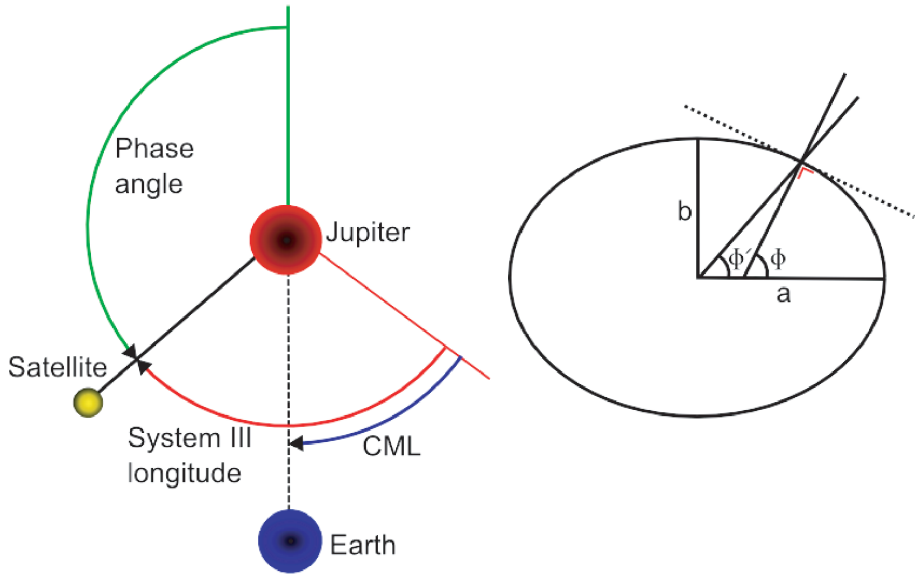

Figure 1.1: (Left) Illustration of the System III coordinate system and the phase angle. The green arc represents the phase angle of the satellite. The red arc represents its System III longitude. The blue arc represents the central meridian longitude (CML). (Right) Illustration of the planetocentric (Φ') and planetographic (Φ) latitudes.

Since Jupiter's shape is an ellipsoid[1], two latitude systems also co-exist: the planetocentric (or jovicentric in this case) and the planetographic (or jovigraphic) latitudes. The first one (Φ') refers to the angle between the line joining the planet center to the considered point and the equatorial plane, while the second one (Φ) refers to the angle between the normal to the surface at the considered point and the equatorial plane. These two angles are related by the following formula:

$\tan(\Phi') = \frac{b^2}{a^2}\tan(\Phi)$

where a is the semi-major axis of the ellipsoid and b the semi-minor axis.

1.4 The Jovian magnetosphere

Eight spacecrafts have carried out in-situ observations of Jupiter's magnetosphere, most of them during single fly-bys of the giant planet. The first were Pioneer 10 and Pioneer 11, respectively in 1973 and 1974. Then followed Voyager 1 and Voyager 2 in 1979 and 1982 respectively, and the solar wind explorer Ulysses in 1992. The latter

[1]The equatorial radius is 71492 ± 4 km and the polar radius is 66854 ± 10 km (*Weiss*, 2004).

is the only one which did not probe the Jovian magnetosphere within the equatorial plane but crossed it from North to South. The Galileo spacecraft is the first and the only Jovian orbiter so far. Its orbit insertion occurred in 1995 and it operated for eight years before being navigated into Jupiter's atmosphere at the end of the mission lifetime. During the Galileo era, the Cassini spacecraft encountered Jupiter in late 2000 before reaching Saturn, its final destination, in 2004. The spacecraft which flew by Jupiter most recently was New Horizons in February 2007, on its way to Pluto and beyond. This last opportunity of in-situ measurements inspired the Hubble Space Telescope large observation campaign discussed below (see Chapter 2) and which constitutes the core of our image database.

The Jovian magnetosphere is the largest magnetosphere of the solar system. The distance from the planet center to the dayside magnetopause can reach ∼100 Jovian radii (R_J), while the limit is only ∼10 Earth radii for our planet. If Jupiter's magnetosphere were visible to the naked eye, it would appear bigger than our moon in the sky. Jupiter's internal magnetic dipole axis is tilted by 9.6° from the rotation axis of the planet and its rotation period is 9h55m. As stated in Section 1.3, the System III longitudes as well as the global shape of the aurorae are fixed relative to the magnetic field. The Jovian magnetosphere differs from the Earth's in two main aspects: the plasma source and the energy source. The Earth magnetosphere is a solar wind-driven magnetosphere in which both the plasma and the energy mainly originate from the solar wind. Jupiter's magnetosphere is an internally-driven magnetosphere and the available energy is mainly provided by the rapid rotation of the planet's strong magnetic field. Additionally, the magnetospheric plasma essentially originates from an internal source: Io's volcanism. Io and its surrounding environment provide approximately 1 ton/s of plasma into the Jovian magnetosphere[2] while the solar wind and the atmospheric escape from Jupiter only provide <100 kg/s and ∼ 20 kg/s respectively (*Khurana et al.*, 2004).

The Jovian magnetosphere is usually divided into 3 regions: the inner magnetosphere, the middle magnetosphere and the outer magnetosphere. The inner magnetosphere is mainly controlled by the Jovian internal magnetic field. The main features are the inner radiation belts and the Io plasma torus which stands from 5 to 10 R_J. The latter is a doughnut shaped reservoir of charged particles origi-

[2]This value of 1 ton/s is in fact the quantity of neutrals provided by Io, however about half of them experience charge exchange processes and escape from the Jovian system as energetic neutral atoms (ENAs) (*Dols et al.*, 2008).

nating from Io's intense volcanism (see next section). In the inner magnetosphere, the rapidly rotating internal magnetic field enforces the plasma to corotate with the planet. Two processes drive auroral emissions in this region: the Io-magnetosphere interaction and the plasma injections. The first mechanism is the core of the present work and will be described in detail in the next sections. The second feature involves injections of hot plasma which suddenly move inwards and then drift with respect to the bulk rotational flow of plasma in an energy-dispersed way (i.e. low energy electrons drift faster than the high energy ones). Their auroral signatures are System III-fixed patchy emissions as seen on Figure 1.2.

The middle magnetosphere spans from 10 to 40 R_J. In this region, the internal field influence weakens and the azimuthal currents radially distort the field lines and confine the plasma into a thin current sheet (see Figure 1.3). Additionally to their azimuthal motion, the field lines loaded by the iogenic plasma slowly migrate outward while emptied flux tubes move inward. When the ionosphere-magnetosphere interaction becomes insufficient to provide enough angular momentum to the plasma, the initially rigid corotation of the equatorial plasma disk progressively breaks down with increasing distance. This process involves radial currents which close through field aligned currents and ionospheric Pedersen current, forming a current loop. It is the large field aligned potentials generated by the equatorward branch of the current loop which are thought to be responsible for the main aurora (see review in *Clarke et al.*, 2004).

The outer magnetosphere ranges from 40 R_J to the magnetopause. It is the region where the internally driven Vasyliunas reconnection cycle takes place (*Vasyliunas*, 1983). On Earth, tail reconnections are triggered by the solar wind activity, forming the so-called Dungey cycle. On Jupiter, the tail reconnections observed every 2-3 days are caused by the continuous mass loading of the magnetotail field lines. At some point, the magnetic tension is no longer able to compensate for the centrifugal force, so that reconnections occur and plasmoids are released with a typical period of 2 to 3 days (Figure 1.4). The faint and transient spots observed directly poleward from the main auroral oval are related to this phenomenon (*Grodent et al.*, 2004; *Radioti et al.*, 2008b). The highly variable polar auroral emissions are also related to the processes taking place in the outer magnetosphere. Some authors have suggested that some of these emissions could be related to an Earth-like solar wind driven Dungey reconnection cycle (*Cowley et al.*, 2003; *Grodent et al.*, 2003b). However, *McComas and Bagenal* (2007) argued that the rotational and

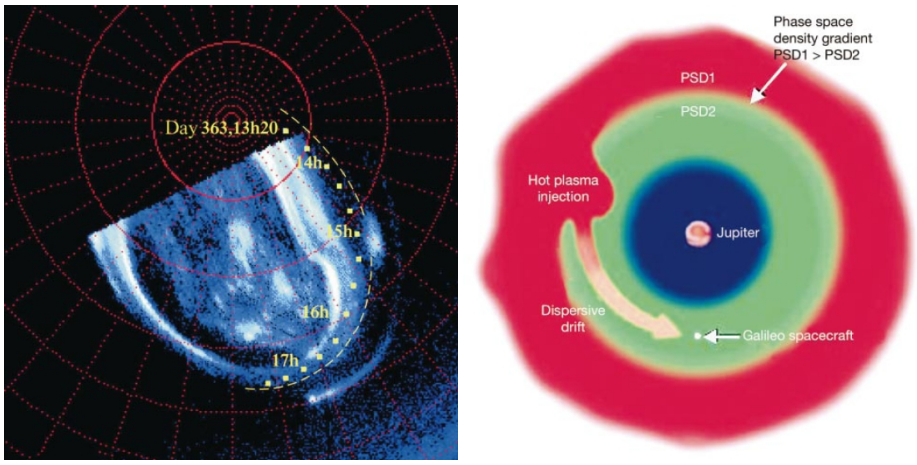

Figure 1.2: (left) Polar projection of the northern aurora simultaneous to Galileo plasma injection observations. The luminous patch related to these injections is the large spot close to the "15h" indication. (right) Illustration of the process explaining both Galileo and HST observations. Hot plasma is rapidly injected into the inner magnetosphere and then experiences a dispersive drift (from *Mauk et al.*, 2002).

convection timescales on Jupiter and on Earth are so different that Jovian reconnections should preferentially take place on the magnetopause flanks instead of in the central magnetotail.

The location of the Jovian magnetopause strongly depends on the solar wind dynamic pressure, so that the dayside magnetopause distance typically fluctuates from ∼45 to 100 R_J. On the nightside, the magnetotail extends as far as the orbit of Saturn.

1.5 The Io-Jupiter interaction

1.5.1 Orbits and tides

In the remainder of this work, I will assimilate the Io-Jupiter interaction to the electromagnetic interaction. However, this is not the only interaction coupling Jupiter's and Io's fates. The gravitational interaction is the root cause for Io's volcanism through tidal heating. An important feature of Io, Europa and Ganymede is that their orbit periods are integer multiples of each other. Io rotates twice as fast as Europa, which in turn rotates twice as fast as Ganymede. This resonance (called a Laplace resonance) enhances the orbits' eccentricities, since the moons are sys-

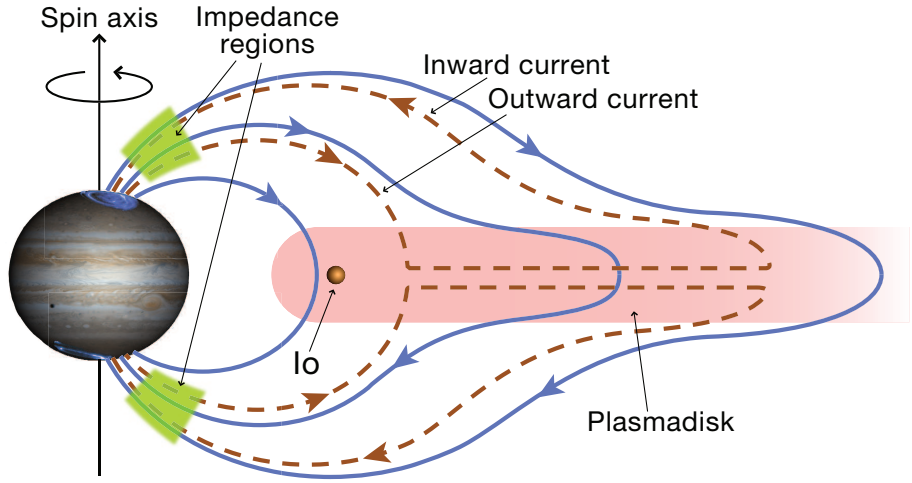

Figure 1.3: Illustration of the inner and middle magnetosphere. Io, located at 6 R_J is the main source of the magnetospheric plasma. The ionized particles are first located in a dense plasma torus along the Io orbit and corotate with the magnetic field. This plasma is also slowly migrating outward, feeding the rest of the magnetosphere. This diffusing plasma is essentially confined in the current sheet. The azimuthal current in the current sheet distends radially the magnetic field lines (blue solid lines). The current loop formed by the radial component of the current sheet, the field aligned currents and the Pedersen current in the ionosphere transfer angular momentum from the ionosphere to the plasma and is represented by the red dashed line (from *http://lasp.colorado.edu/~bagenal/JPO/diagrams.html*).

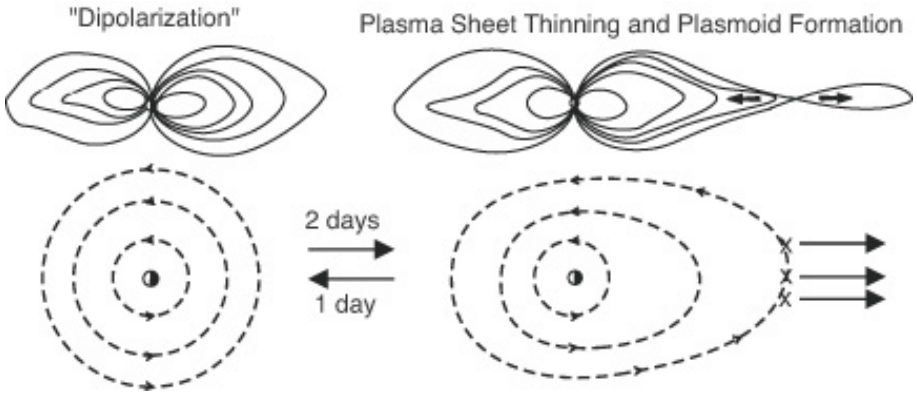

Figure 1.4: Illustration of the internally driven reconnection cycle. Starting from a relatively dipolar configuration, the newly injected plasma from Io progressively loads the flux tubes, leading to the thinning of the plasma sheet. When the magnetic tension becomes unable to counterbalance the centrifugal forces, reconnections occur, plasmoids are released and the magnetosphere comes back to the initial dipolar configuration (from *Krupp et al.*, 2004).

tematically pulled in the same direction at the same location on their orbit. The proximity of the giant planet creates a bulge on Io and forces Io's spin period to be equal to its orbit period. If Io's orbit were perfectly circular, the bulge would always face Jupiter. However, Io's orbit is an ellipse and the moon is orbiting faster than it is spinning at perijove, while it is spinning faster than it is orbiting at the apojove. Additionally, since the gravitational forces are stronger at the perijove, the bulge is also larger. All these processes conspire to mix Io's lower mantle material, and this tidal heating provides a considerable amount of energy (on the order of 5×10^{13} W).

The gravitational interaction not only has an impact on Io's tides, but it also triggers tides on Jupiter. Both Io's and Jupiter's tides affect Io's orbital dynamics. Jupiter's fast spinning pulls the bulge created by Io towards the leading direction (see Figure 1.5). The consequences are a deceleration of Jupiter's rotation and an increase of Io's orbital velocity, which sends Io further away from Jupiter. Focusing now on Io at the perijove, Io's bulge is lagging compared to the orbital motion, which tends to accelerate Io's rotation but slows down Io along its orbit. The effects of Io's bulge are opposite at the apojove, but since Io is further out, the consequences are not as important. Thus, in total, Io's tidal effect tends to bring it closer to Jupiter.

We can notice that Jupiter's tides tend to move Io inwards while the Io tides tend to move Io in the opposite direction. A recent study (*Lainey et al.* (2009)) demonstrated that since 1891, Io has moved 55 km inward while Europa and Ganymede

have moved outward by 125 km and 365 km, respectively. Consequently, the authors concluded that the three moons' orbital periods are slowly evolving away from the Laplace resonance. The long term consequence will be that Io's orbit will become more circular and that the strong volcanism will most probably vanish. The following sections reveal that this prediction will have important consequences for the Jovian auroral activity.

1.5.2 Io and the plasma torus

Even though the situation could plausibly change in the long term, Io is currently the most volcanic body of the solar system. More than 100 active volcanoes have been detected on its surface. This volcanism is the source of Io's tenuous atmosphere, mainly made of SO_2. This atmosphere loses mass to the Jovian magnetosphere and beyond at a rate on the order of 1 ton per second. Consequently, Io is the main source of the Jovian magnetospheric plasma. This Iogenic plasma is mostly made of ions originating from the SO_2 molecule, i.e.mainly S^+, S^{++}, S^{+++}, O^+ and O^{++}. A fraction of this plasma is directly picked-up from Io's exosphere. Another population of the atmospheric particles escapes from Io's gravitational influence as neutrals and forms an extended (more than $\sim$10 R_{Io}) neutral cloud around the satellite. These neutrals can then be ionized through electron impact and charge exchange. This neutral cloud is expected to be the main mass and energy source for the plasma torus (*Dols et al.*, 2008). Presumably, newly created plasma first remains at rest in the wake of Io. These particles are then accelerated up to corotation with the Jovian magnetic field through electromagnetic coupling with Jupiter (see Section 1.5.4.6). The strong magnetic field of Jupiter confines this dense plasma along Io's orbit and forms the plasma torus. Io rotates around Jupiter at 17 km/s while the plasma torus rotates at 74 km/s. The plasma stream velocity relative to Io is thus 57 km/s. The plasma torus is latitudinally confined around its centrifugal equator, which is different from both the rotational and magnetic equators of Jupiter. This equatorial plane is tilted relatively to the Io orbital plane because of the tilt of the Jovian magnetic field (see Figure 1.6a). As a consequence, Io's centrifugal latitude evolves with the Jovian rotation, moving from the northern border of the torus to its southern border and *vice-versa*, as a function of the System III longitude of Io (see Figure 1.6b). In addition to the tilt of the centrifugal plane, the torus is shifted to the dawn side because of the East-West electric field in the Jovian magnetosphere

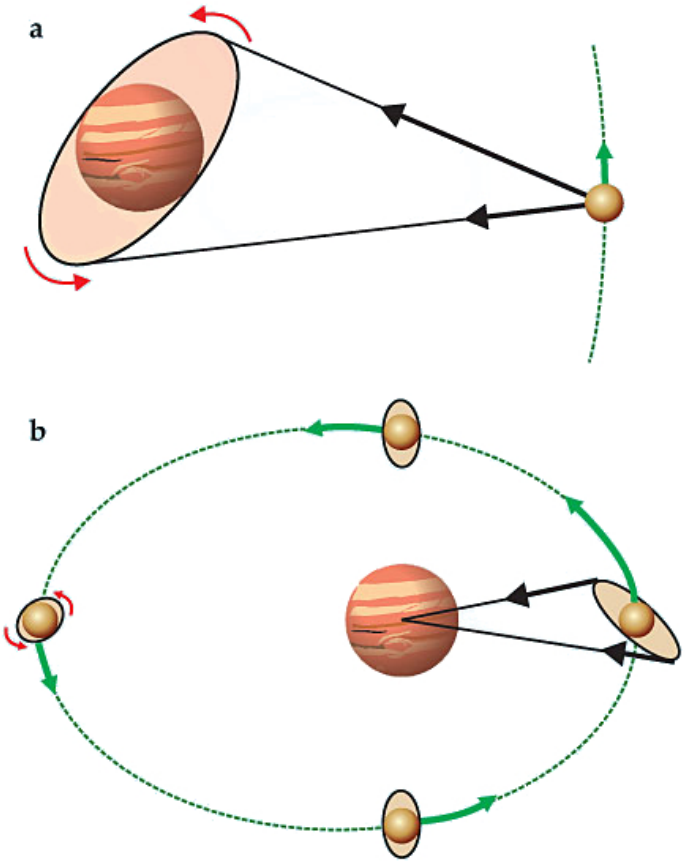

Figure 1.5: Tides in Jupiter and its innermost large moon, Io, have opposite effects on Io's orbit. (a) Io's gravity creates a tidal bulge in Jupiter, which is pushed by Jupiter's rotation (red arrows) ahead of the Io–Jupiter line. Gravitational interaction (black arrows) between Io and the bulge slows Jupiter's rotation and increases Io's orbital energy. (b) Jupiter also creates a tidal bulge in Io. Because Io has an elliptical orbit, its instantaneous orbital speed varies (green arrows). At its most distant point from Jupiter, Io rotates (red arrows) faster than it orbits, so the bulge lies slightly ahead of the Io–Jupiter line in the direction of Io's rotation. At its nearest point to Jupiter, the opposite is true. As a result, Jupiter exerts a force on Io that diminishes Io's orbital energy. The tidal bulges and orbit eccentricity are exaggerated for clarity. (adapted from *Miller* (2009))

(*Smyth and Marconi*, 1998).

1.5.3 The local electromagnetic interaction

In their review of the magnetic interactions of satellites with the giant planets' magnetospheres, *Jia et al.* (2009a) distinguish four categories of satellites:

- inert satellites (such as Tethys, Rhea),
- satellites with an intrinsic magnetic field (Ganymede),
- satellites with an internally induced magnetic field (Europa, Callisto) and
- satellites with significant neutral sources and strong plasma interactions (Io, Enceladus, Titan).

Galileo observations demonstrated that Io has no significant internal magnetic field, whether induced or intrinsic. However, Io has a neutral atmosphere that significantly affects the plasma stream. The origins of this patchy SO_2 atmosphere are the volcanoes and the subsequent sublimation of frost ejecta. Ionization caused by the impact of the neutrals with electrons from the plasma torus as well as photo-ionization (to a lesser extent) generate an ionosphere around Io. Additional ionization caused by field aligned electron beams (see Section 1.6.6) is thought to contribute to the dense wake of stagnant plasma observed downstream of Io (*Frank and Paterson*, 1999; *Hinson et al.*, 1998; *Saur et al.*, 2002; *Dols et al.*, 2008).

Focusing on the electromagnetic interaction, the relative motion of Io with respect to Jupiter's magnetic field causes a motional electric-field across Io. Electric currents can consequently flow from the Jovian side of Io to the anti-Jovian side, owing to the conductivity of Io's ionosphere. These currents force the incoming plasma to strongly slow down upstream of the moon. Only a small part of the torus particles can penetrate into the ionosphere while the remainder is directed around Io and accelerates around the flanks. The addition of newly created plasma into the flux tubes generates mass loading and slows the bulk flow, since these particles were initially at rest compared to Io. At the same time, the charge separation that immediately follows the ionization causes pick-up currents, since the electron gyro-center is shifted towards Jupiter while the ion gyro-center is shifted away from the planet. However, calculations from *Saur et al.* (2003) show the main contributor to the strong Io-plasma torus interaction is the elastic collisions between ions and atmospheric neutrals rather than the mass loading.

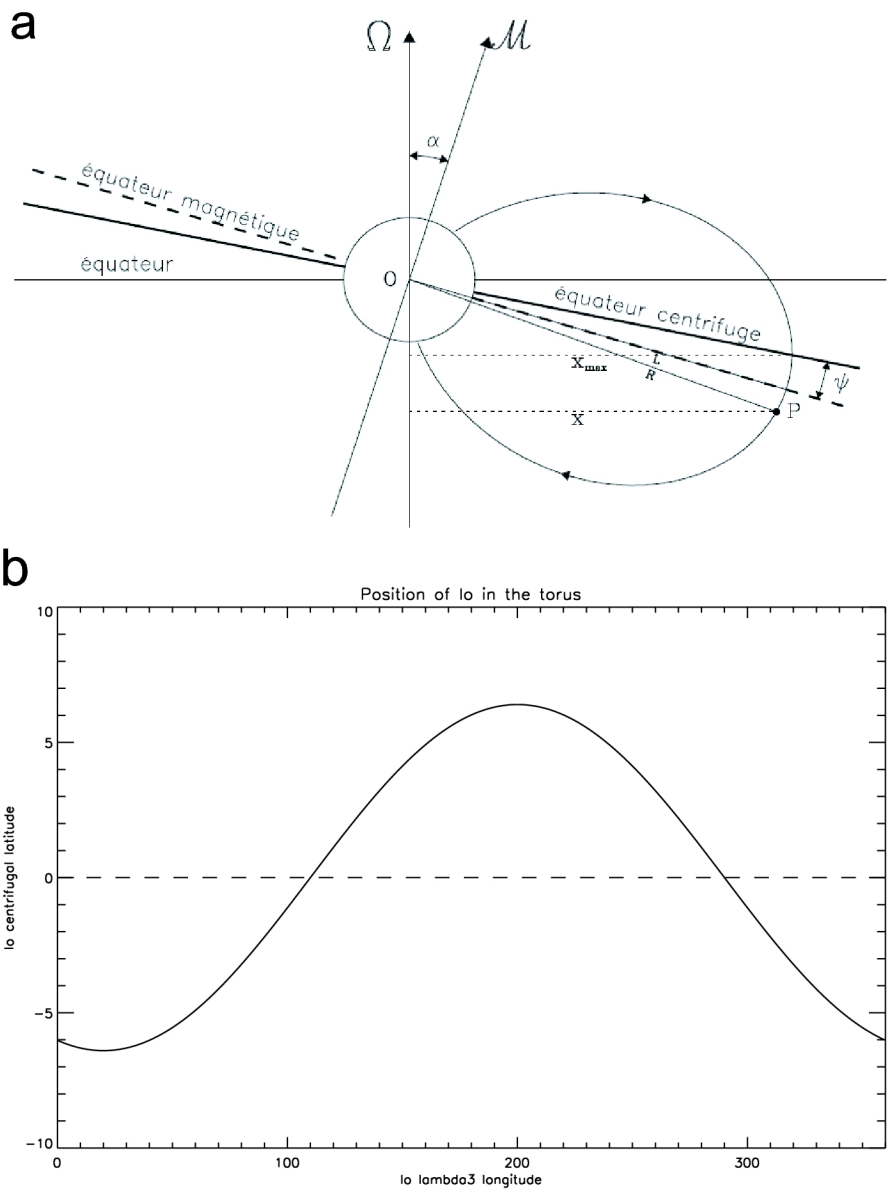

Figure 1.6: (a) Illustration of the torus centrifugal equator (thick solid line) compared to Io's orbital plane (thin solid line) and to the Jovian dipolar equator (dashed line). Ω represents the Jovian rotation axis and M represents the magnetic field dipolar axis. (From *Moncuquet* (1997)) (b) Plot of the centrifugal latitude of Io in the plasma torus as a function of its System III longitude.

1.5.4 The far-field electromagnetic interaction

1.5.4.1 The Alfvén waves

In ideal magneto-hydrodynamics (MHD) applied to compressible fluids, three wave propagation modes can be found. Two of them are compressional modes and thus imply density variation in the plasma. These waves are called the fast and the slow magneto-sonic waves. The last mode has an intermediate phase speed, is a transverse mode only and is called an Alfvén wave. Out of the three modes, only the Alfvén waves are able to carry an electric current. Nevertheless, the electric field does not vary along the magnetic field lines (i.e. in the parallel direction). Consequently, these waves are normally not able to accelerate electrons along the field lines. However, when the ideal MHD conditions are no longer fulfilled, dispersive effects arise, i.e. kinetic and inertial effects. When dispersive corrections are accounted for, a parallel component arises for the electric field and thus electron acceleration becomes possible. The corrections related to the electron inertia are expected to become important close to Jupiter, where the electron thermal speed is small compared to the Alfvén speed. On the other hand, the kinetic effects are expected to arise when the plasma becomes denser and the magnetic field weaker, which is the case closer to Io. However, *Jones and Su* (2008) argued that both effects compete within the plasma torus, leading to a weak electron acceleration at low centrifugal latitudes. Outside the torus, the inertial term clearly dominates and the related parallel electric field is maximum approximately $1R_j$ above the planetary surface. Finally, the authors suggest that this parallel electric field is directed planet-ward during a half phase and anti-planet-ward during the other half phase, leading to electron acceleration in both directions.

1.5.4.2 The unipolar inductor

The early models of the interaction between Io and Jupiter have been proposed by *Piddington and Drake* (1968) and *Goldreich and Lynden-Bell* (1969) to explain the Io-related radio emissions (see Section 1.6.5). The principle of the unipolar inductor is relatively simple. The motion of a conductive body embedded into a magnetic field induces an electric field perpendicular to the magnetic field and to the motion direction. In our case, since the magnetic field is oriented from North to South and since Io is rotating counter-clock wise (as viewed from the North), this motional electric field direction is anti-Jovian. The electric circuit is

closed through supposedly perfectly conducting magnetic field lines and through the Pedersen current in the Jovian ionosphere (see Figure 1.7). According to this model, the Io-Jupiter interaction is modeled as a direct current flow between the moon and its planet. The current flows from Io along one-half the surface of the Io flux tube (i.e. the field lines passing through Io) and flows in the other direction in the other half. Initially, the current was supposed to circulate through Io's interior, but this assumption was later replaced by Pedersen and Hall currents in Io's ionosphere. In this model, the conductivity of the satellite and of the field lines are assumed infinite, so that the intensity of the current is only limited by the Pedersen conductivity in Jupiter's ionosphere. *Goldreich and Lynden-Bell* (1969) computed that such current would reach $1.1 \times 10^6 A$. In this theoretical framework, the magnetic force on the current which flows through Io gives rise to a torque which transfers angular momentum from Jupiter's spin into Io's orbital motion[3]. The perturbed field lines are then bended in the downstream direction with respect to Io. These authors computed a lead angle[4] of 12°. In this model, the auroral footprint would thus lie at the foot of the perturbed flux tube.

It is noteworthy to state that the direct current model has always been considered by their authors as a simplifying hypothesis. The interaction was assumed to propagate in the form of Alfvén waves and the assumption was only valid if the perturbation reflected at the Jovian ionosphere was able to reach Io before the satellite moved away. However, this hypothesis seemed reasonable since the magnetosphere of Jupiter was considered as a very tenuous medium and the Alfvén speed was assumed close to the speed of light (see next section).

1.5.4.3 Alfvén wing model

After the Voyager encounters, the ability of the Alfvénic perturbation to come back to Io before the satellite moved significantly due to orbital motion was questioned

[3]This statement has been made assuming that Io's interior was the conducting body. Later evolutions postulated that momentum was instead transferred to the newly created Iogenic plasma.

[4]In this context, the lead angle is the longitudinal difference between the foot of an imaginary unperturbed field line passing through Io and the foot of the perturbed field line. We will see later that the lead angle is now often used to refer to the longitudinal difference between the foot of the unperturbed flux tube and the observed Io footprint. The discrepancy is that it is no longer assumed that the observable footprint lies at the foot of the perturbed flux tube.

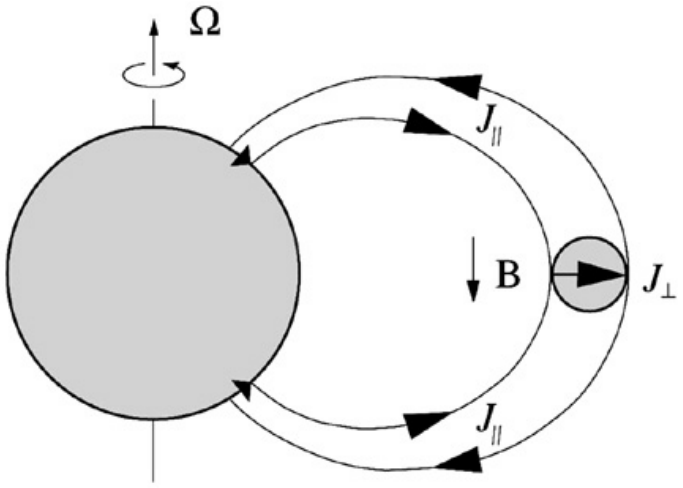

Figure 1.7: Schematic illustration of the unipolar inductor mechanism. The motion of Io in Jupiter's magnetosphere induces an electric field across the moon. Since the Iogenic ionosphere is conducting, a current can flow from the Jovian to the anti-Jovian side of Io and close through the magnetic field lines and Pedersen currents in Jupiter's ionosphere. (From *Thomas et al.*, 2004)

because the speed of the Alfvén waves strongly depends on the plasma density[5] and the spacecraft fly-bys had just unveiled the existence of the dense plasma torus. Other models were thus proposed to describe the propagation of the Alfvén waves without the direct current circuit hypothesis. In these models, the current does not flow along the magnetic field lines but is aligned with the characteristics of the Alfvén waves, called the Alfvén wings (*Neubauer*, 1980) (See Figure 1.8). In a simplified picture, the Alfvén waves propagate along the field lines and the field lines are drifting away from Io. Since the Alfvén speed is limited, especially in the dense torus, the perturbation propagates obliquely relatively from Io and the locus of perturbed points forms the Alfvén wings. The round trip Alfvén propagation time is estimated around ∼1200 seconds when Io is in the center of the torus (*Crary and Bagenal*, 1997). The maximum lead angle computed from Voyager derived torus density profiles is $\sim 8^\circ$ (*Prangé et al.*, 1996).

As discussed by *Neubauer* (1980) and confirmed both numerically and analytically by *Wright* (1987) and *Wright and Schwartz* (1989), the Alfvén waves experience

[5]
$$\mathbf{V}_{Alfven} = \frac{\mathbf{B}}{(\mu_0 \rho)^{1/2}}$$
where $\mathbf{V}_{Alfven}$ is the Alfvén speed, $\mathbf{B}$ is the magnetic field vector and ρ is the mass density.

reflections owing to density and magnetic field gradients both at the Jovian ionosphere and at the torus border. These reflections can lead to different interference patterns and thus generate multiple spots in the footprints or multiple radio arcs.

1.5.4.4 Electron acceleration mechanisms

The above model describes how the current flows between Io and Jupiter but does not really explain how this current accelerates the particles from a few eV in the torus to keV when precipitating into Jupiter's ionosphere. A first explanation could be that, when a field aligned current reaches a low density region at high latitude, the number of charge carriers decreases and the particles of this region are accelerated in accordance with the conservation of the current. On the other hand, another model suggests that the magnetic shear at high latitude could enhance parallel electric fields through resistive instabilities (*Kopp et al.*, 1998). A third model also proposed that the strong current flowing between Io and Jupiter could generate ion-cyclotron waves that could then excite kinetic Alfvén waves. These low frequency kinetic Alfvén waves could in their turn accelerate particles along the magnetic field lines (*Das and Ip*, 2000). Finally, *Crary* (1997) argued that Alfvén waves are totally reflected by the density gradients at the torus border so that no energy could reach Jupiter in this form. However, by considering the finite electron inertia, this author proposed that the electric field associated with the kinetic Alfvén waves could accelerate electrons inside the torus trough repeated Fermi acceleration. However, as described above, the most likely candidates to accelerate the precipitating electrons are the electric fields created at high latitudes when inertial effects in the Alfvén wave propagation become significant (*Jones and Su*, 2008).

1.5.4.5 Further evolutions of the models

Galileo in situ measurements showed that the field lines are strongly slowed down after contacting Io, leaving more time for the Alfvén waves to come back close to their emission points. As a consequence, models similar to the unipolar inductor were again seen as a possible solution. For example,*Crary and Bagenal* (1997) proposed a hybrid model in which the interaction begins as an Alfvénic disturbance and evolves downstream to a direct current loop. *Pontius* (2002) proposed a formulation of the wing current that combines properties of the unipolar inductor model with others from the Alfvén wing model. *Saur et al.* (2004) describe the unipolar induc-

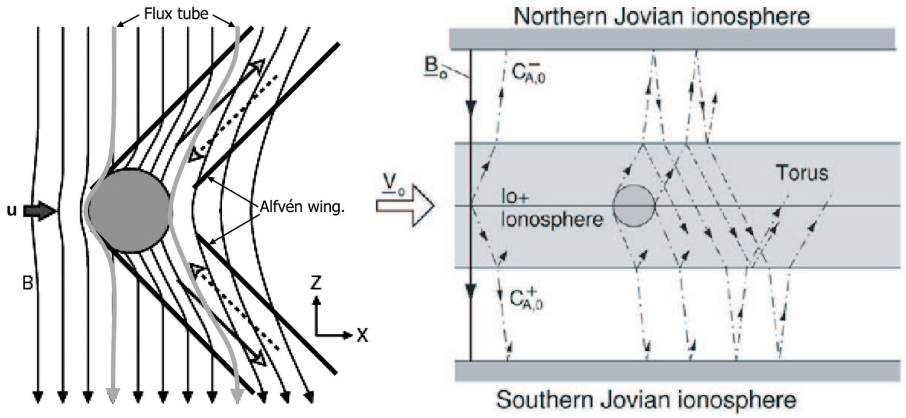

Figure 1.8: (Left) Side view illustration of the Alfvén wings model. The thin dark vertical lines represent the magnetic field lines while the Alfvén wings are represented with bold oblique lines. The Io flux tube is shown in grey. (From *Kivelson et al.*, 2004) (Right) Scheme of the possible reflections of the Alfvén wings. Reflections can occur at the inner boundary of the torus, in the Jovian ionosphere or at the outer boundary of the torus, leading to different reflection patterns. (From *Saur et al.*, 2004)

tor model and the ideal Alfvén wing model as two extreme cases of a more general description of the Alfvén waves propagation. The intermediate situation is called the mixed Alfvén wave disturbance system and it involves only partial feedback between Io and the reflecting boundary[6]. Recently, *Jacobsen et al.* (2007) used a 3D non-linear MHD simulation to study the propagation and the reflection of the Alfvén waves when the Io-plasma interaction is nearly saturated (i.e. when the plasma is nearly stopped relative to Io, in accordance with the observations). According to their simulations, the strength of the interaction strongly influences the propagation pattern. They notably found that, in case of strong interaction, the reflected waves can be nearly anti-parallel to the incident direction. They also showed that constructive and negative interferences take place, modifying the current pattern and thus influencing the auroral footprint morphology.

The plasma wave instrument on board Galileo also recorded intense electromagnetic waves at frequencies up to several times the proton gyro-frequency when crossing the Alfvén wings. *Chust et al.* (2005) interpreted these "high frequency/small scale" electromagnetic waves as the signature of the filamentation of the Alfvén

[6]In the ideal Alfvén wing model, no feedback does exist and the Alfvénic conductivity controls the electric current while in the unipolar inductor case, the feedback is strong and the Jovian ionospheric Pedersen conductivity controls the current.

waves. According to these authors, filamentation can transfer energy from large scale Alfvén waves into smaller scale waves which could transfer energy through the torus boundaries more efficiently.

1.5.4.6 The trailing trail

The discovery of an extended wake of plasma downstream of Io as well as the observations of a more than 100° long trailing tail emission downstream of the brightest spot gave rise to new models describing this feature of the footprint (*Hill and Vasyliūnas*, 2002; *Delamere et al.*, 2003; *Ergun et al.*, 2009). *Delamere et al.* (2003) divide the Io-plasma interaction into 3 phases. Phase I consists of the interaction between the corotating flux tube and Io, as described in the above sections. Phase II describes the acceleration of the wake plasma by an electrodynamic coupling with the surrounding torus plasma[7] before the Alfvén waves have reached the torus boundary. This coupling does not accelerate completely the wake plasma and the full corotation can only be achieved when coupling with Jupiter's ionosphere is attained. Phase III is the quasi-steady state weak coupling to Jupiter. During this last phase, these authors assume that high latitude field aligned electric fields are generated when the sub-corotating flux tubes decouple from Jupiter. These electric fields are thought to accelerate the electrons that cause the trailing tail auroral emissions. The other two models only focus on Phase III but they do not postulate such a decoupling between the flux tubes and the ionosphere. The model from *Hill and Vasyliūnas* (2002) is more similar to the unipolar inductor model. It is based on the assumption that the finite ionospheric Pedersen conductivity limits the current flowing between the wake plasma and Jupiter and thus prevents the charged particles to immediately reach full corotation. The *Ergun et al.* (2009) model is based on the same formulation, but they added a new current-voltage relationship which models a quasi-static potential drop to accelerate the tail electrons.

1.6 Observations

The Io-plasma torus interaction can be probed with a variety of observational tools. Each one provides a different contribution to the understanding of the physics of the phenomenon. Some have been acquired from ground based observatories, some

[7] I.e. the unperturbed corotating plasma.

required a space telescope and the last type consists of in-situ measurements or close images from interplanetary probes.

1.6.1 The Infrared footprint

The first detection of the auroral footprint of the Io-torus interaction was achieved at the $3.4\mu m$ infrared (IR) wavelength (*Connerney et al.*, 1993). These images were obtained with the 3-m telescope of the Infrared Telescope Facility (IRTF) at Mauna Kea, Hawaii. The observed IR emissions are dominated by the H_3^+ molecular ion. Ionization of the H_2 molecule by electron impact creates an H_2^+ molecular ion. This ion then quickly interacts with another H_2 molecule to form an H_3^+ molecular ion plus a hydrogen atom. Since H_3^+ is formed at the base of the thermosphere, its emissions are not affected by the absorbing layer located below the methane homopause. On the other hand, all emissions from lower altitudes, such as thermal emissions from Jupiter or reflected sunlight, are strongly weakened, so that the contrast between auroral emissions and background emissions is very pronounced.

Connerney et al. (1993) measured the longitudinal spacing between the location of the Io footprint and the foot of the unperturbed field lines passing through Io according to the O6 magnetic field model. This angle ranged from 15° to 20° and was systematically a lead angle, i.e. the location of the footprint is located downstream of the orbital position of the moon. They argued that these values are considerably larger than the angle expected from the Alfvén wings theory. Additionally, they found no correlation between the lead angle and the System III location of the footprint. Finally, they suggested that the non-detection of the northern footprint in the area where the magnetic field was the strongest could be an indication that the ionosphere Pedersen conductivity was playing a role in the footprint brightness. Consequently, the authors concluded that these elements were in favor of a strong unipolar inductor interaction controlled by the Pedersen conductivity of the ionosphere of Jupiter.

Connerney et al. (1998) used the location of the Io footprint on IRTF infrared and HST FUV images in order to constrain magnetic field models. Indeed, the location of the footprint provides information on the polar surface magnetic field that is not accessible with probes remaining in the equatorial plane. Consequently, the authors derived a 4th order spherical harmonic model constrained by in-situ measurements provided by the magnetometers onboard Voyager 1 and Pioneer 11

and by the mapping of the Io footprint positions into the equatorial plane. This model is called VIP4 for Voyager Io footprint Pioneer 4th order model.

IR images also suggested that some emission was sometimes present 10° downstream from the beginning of the spot. Additionally, *Connerney and Satoh* (2000) reported the presence of multiple spots separated by 5° downstream from Io. They noted that spot multiplicity is more in agreement with the Alfvén waves theory. A possible explanation for the presence of these previously unidentified features could be the improvements of the IRTF instrument and the image processing techniques and/or the increase of the torus density in the 1998-1999 era. However, the image shown in Figure 6 of *Connerney and Satoh* (2000) is peppered by speckles usually related to deconvolution algorithms, which sheds some doubts on the existence of this chain of spots.

In conclusion, the ideas concerning the Io footprint theoretical explanations evolved in response to the increase of the observational database and to the improvements of the instruments and data processing. The lead angle measurements were first in favor of the unipolar inductor but the discovery of secondary spots was then considered as a strong argument strengthening the Alfvén wings theory. We will see in the next section that the conclusions based on the analysis of the UV footprint followed a similar evolution.

1.6.2 The ultraviolet footprint

We have seen in the previous section that observation through near infrared windows is possible from ground observatories. Unfortunately, the far ultraviolet wavelength range is not accessible from Earth because of the strong absorption by the atmosphere. Accordingly, observations of the Jovian UV aurorae are only achieved from space telescopes. The most powerful one at this time is the 2.4 m wide Hubble Space Telescope (HST). All the studies of the Io UV footprint have been done with its successive cameras. Figure 1.9 illustrates the evolution of the Jovian aurorae FUV imaging performances with these different instruments. Unlike IR emissions, which are believed to be thermalized, either by precipitation induced collisional heating or by Joule heating, the FUV emissions result directly from collisional excitation of H_2 and H atmospheric particles with electrons. Jovian FUV auroral images include H_2 Lyman band emissions as well as the Werner band series, plus the H Lyman-α line. In this study, we both considered images including or rejecting H Lyman-α

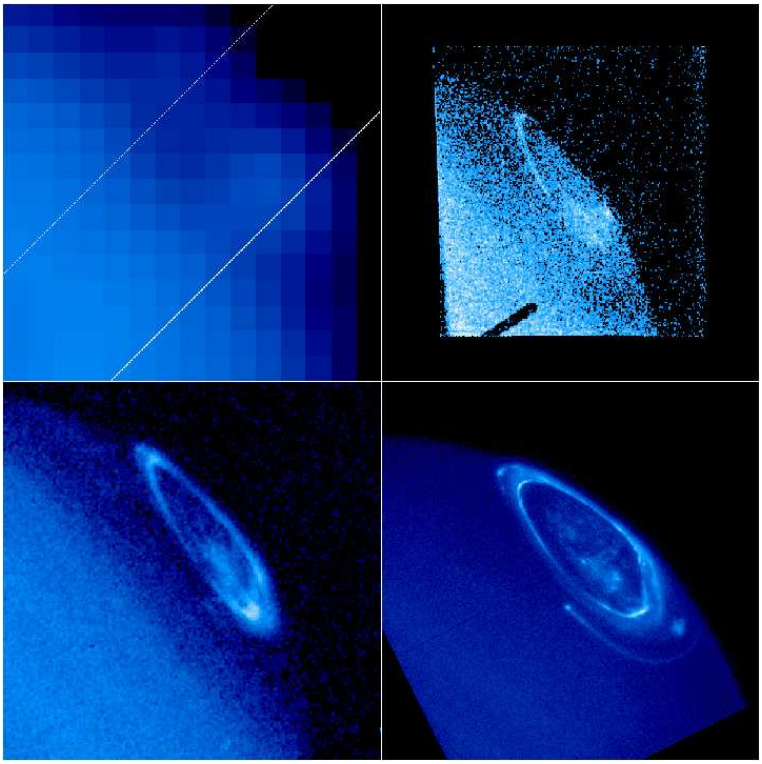

Figure 1.9: Comparison of UV images of Jupiter's aurora from IUE (simulated, upper left), HST post-COSTAR FOC (upper right, 716 sec), HST WFPC 2 (lower left, 500 sec), and HST STIS (lower right, 120 sec). Each of these images is of the northern aurora near 180° CML, and they are presented with the "pipeline" processing and background subtraction for an equal comparison. For the IUE panel, the WFPC 2 image has been convolved with a 6 arcsec FWHM function to simulate the IUE angular resolution within the large aperture (marked with white lines). (From *Clarke et al.*, 2004)

emission.

A controversy exists on the first discovery of the Io UV footprint. *Prangé et al.* (1996) claimed that they demonstrated the existence of the UV footprint on one image acquired with the Faint Object Camera (FOC) onboard the Hubble Space Telescope. On the other hand, *Clarke et al.* (1996) estimated that this single observation did not identify the Io footprint by itself and they brought stronger evidences of the presence of the Io UV footprint on Wide Field Planetary Camera 2 (WFPC2[8]) images. However *Prangé et al.* (1998) presented a new set of FOC images showing

[8]The WFPC2 camera is another imaging camera onboard HST that provides a better signal to noise ratio than FOC but a reduced angular resolution (0.0455 arcsec per pixel).

	Emitted power	Input power	Brightness
Prangé et al., 1996	5×10^{10}W	$2 - 3 \times 10^{11}$W	700 kR
Clarke et al., 1996		10^{11}W	60-120 kR
Prangé et al., 1998		$0.8 - 5 \times 10^{11}$W	
Clarke et al., 1998			35-250 kR
Gérard et al., 2006		$0.4 - 8 \times 10^{10}$W	25-220 kR
Sério and Clarke, 2008			40-480 kR

Table 1.1: List of the published emitted and electron precipitated power for the FUV Io footprint. For the *Gérard et al.* (2006) paper, the printed value is 0.4-8 GW but, after verification, it appears that this 10 times smaller value came from a typo in a conversion coefficient. We thus considered here the corrected value.

the Io footprint as well as its trailing tail.

Similarly to the Infrared wavelength observations, the measurements of the lead angles[9] were thought to be the best way to discriminate the unipolar inductor model from the Alfvén wings model. Lead angles between 0 and 15° were also found in UV but none of these results led to firm conclusions because of the expected inaccuracy of the magnetic field models. Moreover, lag angles (i.e. negative lead angles) have been reported (*Prangé et al.* (1998); *Clarke et al.* (1998); *Gérard et al.* (2006)), even though they do not make sense according to all current theories.

As far as the involved input power and emitted brightness are concerned, the published values range respectively from 4 to 300 GW and from 25 to 700 kilo-rayleighs[10] (kR). These numbers are compiled in Table 1.1.

The next generation UV camera was the Space Telescope Imaging Spectrograph (STIS). This instrument combines the resolving power of the FOC camera[11] with an unprecedented sensitivity. Several major breakthroughs have been made with this camera such as the discovery of secondary spots downstream of the main one (*Clarke et al.*, 2002). The proximity of these multiple spots first suggested that they all belong to the interaction region close to Io. Nevertheless, a more detailed study by *Gérard et al.* (2006) demonstrated a link between the inter-spot distance and

[9]The lead angle is defined here as longitudinal difference between the foot of undisturbed field lines passing through Io and the actual footprint location.

[10]1kR=10^9 photons cm^{-2} s^{-1} into 4π steradians

[11]The FOC angular resolution is 0.014 arcsec per pixel, but, practically, these images have to be re-binned to 0.028 arcsec per pixel in order to be usable. The situation is nearly identical with STIS since a high resolution (0.012 arcsec per pixel) mode does exist, but is generally not used because it does not bring any quality improvements. The STIS resolution is then fixed to 0.024 arcsec per pixel.

the location of Io in the torus (see Figure 1.10). When Io is close to the northern border of the torus, the northern footprint is faint and the inter-spot between the two first spots is maximum. The situation is the same for the southern footprint when Io is south. Alternatively, when Io is located in the center of the torus, its brightness is maximum and only a unique spot is visible in each hemisphere. The authors thus concluded that Alfvén waves reflections on the inner border of the plasma torus would qualitatively explain the evolution of the inter-spot distance. They also showed a similar correlation between the main spot brightness and Io's latitude in the torus (see Figure 1.11). This correlation had already been searched in WFPC2 data, but unsuccessfully because of the lack of data (*Clarke et al.*, 1998). The authors suggested that the plasma density controls the brightness since the IFP brightens when it approaches the dense torus center and vanishes when it approaches the borders. Based on a larger set of STIS data, *Serio and Clarke* (2008) confirmed the link between the brightness and Io's centrifugal latitude. They attributed this behavior to the increase of the collision rate and mass loading when Io approaches the dense torus center.

STIS observations from *Clarke et al.* (2002) also clearly confirmed the FOC observations (*Prangé et al.*, 1996) of the long trailing tail up to 100° behind the footprint. The authors argued that this tail could not be due to some afterglow but is linked to high energy particle precipitation.

Another controversial topic is the spatial extent of the Io footprint. FOC images seemed to indicate that the size of the footprint was comparable to the projected size of Io in the ionosphere (*Prangé et al.*, 1996; *Prangé et al.*, 1998). Consequently, these observations suggested that the interaction region in the equatorial plane was confined within a few Io radii. Nevertheless, the estimated size was based on the measurement of the footprint latitudinal width and not on the longitudinal length. As far as the length is concerned, the elongation measured up to 4.5° and was attributed to the blurring owing to long exposure times (from 535 to 1421 seconds) combined with the distortion of the magnetic field lines. On the other hand, WFPC2 observations lead to footprint as long as 1000-2000 km even after correction of the rotational blurring(*Clarke et al.*, 1996) while STIS observations gave lengths between 500 and 3000 km (*Clarke et al.*, 2002). These measurements thus suggested that the interaction region was more than 10 times larger than Io. Nevertheless, in the *Clarke et al.* (2002) paper describing the STIS results, the authors assimilated both primary and secondary spots to the interaction region. In their interpretation of the footprint

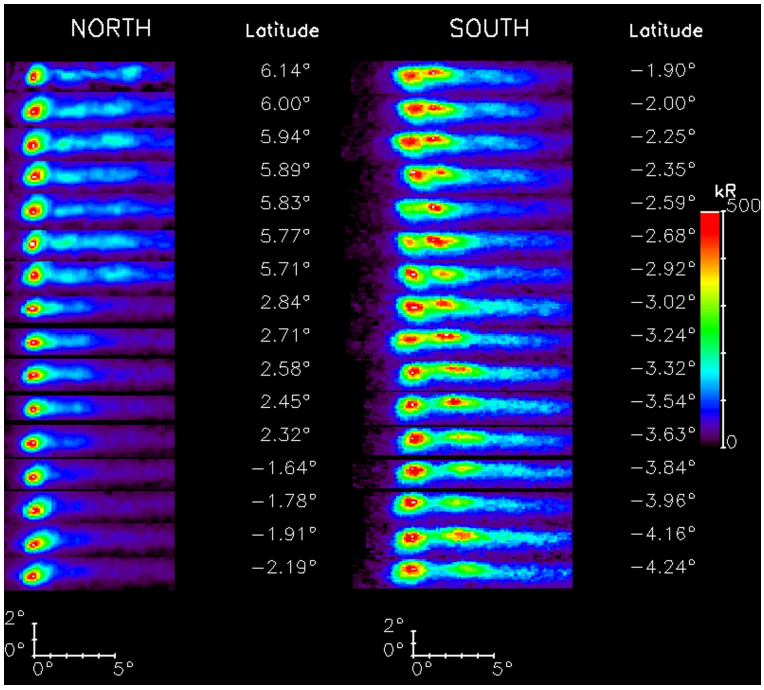

Figure 1.10: Samples of rectified traces of the Io footprint as a function of the centrifugal latitude of Io. It is noticeable that multiple spots are observed in the northern hemisphere when Io is close to the northern torus boundary (and vice-versa for the southern footprint). On the other hand, only one spot can be identified when Io is close to the torus center. (From *Gérard et al.*, 2006)

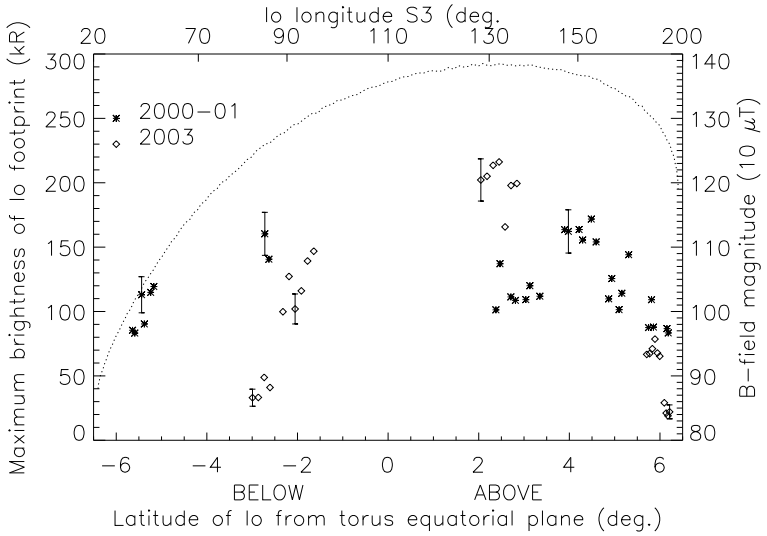

Figure 1.11: Plot of the maximum brightness of the northern main spot as a function of the centrifugal latitude of Io in the torus. The dotted line represent the surface magnetic field magnitude of the foot of the Io flux tube. We can see that the main spot is brighter when is is close to the dense torus center while its brightness decreases when Io is close to the torus border. (From *Gérard et al.*, 2006)

morphology, *Gérard et al.* (2006) separated the different spots. By measuring the size of the first spot only, they came to the conclusion that the size of the spot ($\sim 0.9°$) approximately corresponds to the size of Io when mapped back into the equatorial plane along the field lines. Finally, *Serio and Clarke* (2008) reported estimates of the IFP diameter as measured perpendicularly to the downstream direction. Their values range from $\sim$ 500 km to $\sim$ 2000 km.

Early estimates of the IFP color ratio led to the conclusion that the energy of the precipitating electrons was similar to the energies related to the main oval (*Clarke et al.*, 1996). Later and more detailed studies with the GHRS and the STIS spectrographs led to the conclusion that the IFP electrons have a mean energy definitively less than electrons precipitated into the main auroral oval, typically on the order of 55 keV[12] (*Dols et al.*, 2000; *Gérard et al.*, 2002). They also showed that the brightness drop in the tail was mainly caused by a drop of the electron flux rather than to a decrease of their mean energy.

[12]In comparison, the main oval precipitating electrons have an energy between 30 and 200 keV(*Gustin et al.*, 2004b).

1.6.3 The visible footprint

Additionally to the infrared and ultraviolet emissions, the Jovian aurorae also consist of visible emissions. The visible aurora is too weak to be detected against the bright reflected sunlight. However, the Galileo orbiter provided the first images of the aurorae at visible wavelength while orienting its camera on the night side. These unique observations provided by the Solid State Imager (SSI) instrument have been reported by *Ingersoll et al.* (1998) and by *Vasavada et al.* (1999).

The Io footprint is detected on 10 out of 24 images of the northern aurora acquired by Galileo from November 1996 to November 1997. The SSI clear filter (effective wavelength: 385-935 nm) is used for all these images and the exposure times are between 1.06 and 12.8 seconds. The System III Io longitudes range from 80° to 235° and the images come from 3 different Galileo orbits (C3, C10 and E11). Additionally to their unique wavelength, these observations provide an unprecedented spatial resolution between 26 and 134 km.

Vasavada et al. (1999) described the footprint as a circular patch with a FWHM diameter around 450 ± 100 km when Io has a System III longitude between 82° and 110°. On the other hand, *Ingersoll et al.* (1998) reported a more elongated spot with a FWHM size of 300×500 km and a full width (FW) of 500×1200 km. In a few images, the footprint appears as a pair of spots separated by 0.5° in longitude. In order to complete this morphological description, the SSI camera also detected a faint trailing tail similar to those observed in the UV and IR wavelength.

The observed lead angles range from 0° to 2° and the authors indicate that these numbers are more consistent with the Alfvén wings models than with the lead angle expected from the unipolar inductor. Finally, the maximum brightness is between 0.2 and 1 MR and the total power is estimated between 0.2 and 0.7 GW.

More recently, the LOng-Range Reconnaissance Imager (LORRI) visible panchromatic camera on board the New Horizons spacecraft also acquired visible images of the Io footprint (*Gladstone et al.*, 2007). On these images, the main spot width is around 400 km and its vertical extent is as large as 1000 km. Additionally, other spots are seen both upstream and downstream of the main ones (Figure 3.7).

1.6.4 Aurorae at Io

Usually, aurorae are found close to the poles, but on Io, auroral emissions are mainly located at the Jovian and anti-Jovian equatorial sides (Figure 1.12). According to

the model proposed by *Saur et al.* (1999), the divergence of the flow around Io caused by the electrodynamic interaction forces the electron flux tubes to reach preferentially the flanks of the satellite (*Saur et al.*, 2000). These auroral emissions are produced by impact excitation of neutral oxygen and sulfur atoms by hot electrons. Io's aurorae have been observed with HST, Galileo's Solid State Imager (SSI) and with ground-based observations (see review in *Saur et al.*, 2004). The spots rock up and down relative to Io so that they are located at the magnetic field tangent points (*Roesler et al.*, 1999). In FUV observations, the anti-Jupiter side is brighter, probably owing to Hall effect that rotates the electron flow and causes the hot torus electrons to enter Io's atmosphere preferentially by the anti-Jovian side (*Saur et al.*, 2000). However, on SSI images, the Jovian side frequently appears brighter. This opposite behavior has tentatively been attributed to a local concentration of molecular SO_2 from venting volcanoes (*Geissler et al.*, 2001). *Retherford et al.* (2007), based on FUV ACS images of Io during eclipses, confirmed that the location of the emissions is partly influenced by the location of the volcanic plumes. These authors also studied the relative influence of volcanoes and frost sublimation as sources of Io's atmosphere. They concluded, combining Io auroral images from ACS and from the Alice UV spectrometer on board New-Horizons, that volcanoes only provide 1 to 3% of the dayside atmosphere. FUV STIS observations showed that the equatorial spots brightness increases when Io is closer to the denser torus center (*Retherford et al.*, 2000). Similar results have been shown from ground-based [O I] 6300 Åmeasurements (*Oliversen et al.*, 2001). Short timescales (∼15-20 minutes[13]) and strong (typically ∼20-50 %) brightness fluctuations have also been observed and ascribed to fluctuations of the electron energy flux.

Additionally to the equatorial spots, faint polar glows have been observed both on visible (*Geissler et al.*, 2001) and FUV images (*Retherford et al.*, 2003) and appeared brighter on the pole closest to the centrifugal equator. These results suggested that this glow was generated by the interaction between Io's atmosphere and plasma torus electrons. Finally, enhanced emissions in Io's wake have been observed on STIS spectra by *Wolven et al.* (2001).

1.6.5 Io related radio emissions

Bigg (1964) has been the first to link some decametric radio emissions originating

[13]The detection of the exact timescale is limited by the sampling rate and thus could be smaller.

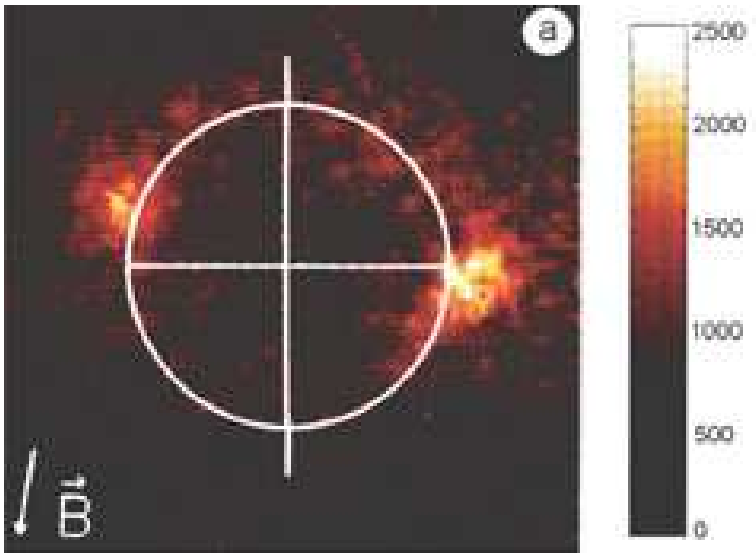

Figure 1.12: Image of OI 1356 Å Io's aurora. We can notice that the the spots are located at the tangent points relatively to the magnetic field lines. Additionally, the anti-Jovian spot is brighter (From *Roesler et al.*, 1999).

from Jupiter to the orbital position of Io. These Io related emissions are called Io-DAM (*Queinnec and Zarka*, 1998; *Saur et al.*, 2004). They occur when Io's phase angle is either close to 90° or close to 230°. Their frequencies range from ∼1 to 40 MHz and presumably correspond to the local electron gyro-frequency. According to the current magnetic field models, the lower frequency limit corresponds to an altitude of 1-2 R_J while the upper limit corresponds to the surface of Jupiter. The Io-DAM are elliptically polarized, but those which are dominantly right-handed originate from the northern hemisphere while the left-handed emissions are related to the southern one. These emissions appear as arcs in the frequency-time plane (i.e. in dynamic spectra) on timescales of minutes to hours. Four types of arcs are observed, noted A, B, C and D. A and B arcs are mostly right-handed while C and D are mostly left-handed. B and D arcs appear when Io is near dawn while A and D arcs occur when Io is near dusk. Each type has a specific shape in dynamic spectra. Figure 1.13 illustrates their different morphologies as they appear in dynamic spectra. The most widespread explanation for these arcs is that the radio waves are emitted along a conical sheet less than 2° thick and with a 70 ± 5° aperture half angle with respect to the magnetic field orientation. According to the magnetic field models, these arcs probably originate from field lines leading the unperturbed IFT by ∼10 to 30°. The orbital position of Io is not the only condition for Io-DAM occurrence. The arcs

are only observed when Io is in some specific locations in the magnetic field, with System III longitudes ranging from ∼170° to ∼310°, depending on the type of arc. These constraints appear as occurrence regions once translated into the CML-Io phase plane. Intense sporadic bursts on timescales of milliseconds, called S-bursts, are also observed a few percent of the time. They mainly consist in negatively drifting[14] features (see Figure 1.13d) and are consequently assumed to be associated with reflected electrons travelling from Jupiter to Io. Analysis of these S-bursts suggest electric potential jumps of ∼1keV accelerating electrons toward Jupiter and mostly localized at an altitude of 0.1 R_J, while the mean energy of the emitting electrons lies around 4 keV (*Hess et al.*, 2007). Moreover, *Hess et al.* (2009) showed that these acceleration structures can last for ∼10 minutes and move away from the planet. Additionally, new structures seem to appear every ∼200 seconds.

The Io-DAM generation mechanism is most probably the cyclotron-maser instability (CMI) and is related to unstable populations of electrons with energies from 1 to 10 keV. A necessary condition to the wave growth is that the gradient of the electron distribution function along the perpendicular velocity[15] axis is positive (see details in *Wu*, 1985). For example, this condition is encountered with loss cone distributions, in which a part of the electron population is lost into the atmosphere. This is the reason why the radio arcs are supposed to be directly related to the precipitating electrons leading to the footprint. Unfortunately, attempts to link radio and optical morphologies have been unsuccessful so far.

1.6.6 Electron beams at Io

The Galileo probe flew-by Io on six occasions and the Energetic Particles Detector (EPD) operated during 5 of these encounters (*Williams et al.*, 1996; *Williams et al.*, 1999; *Mauk et al.*, 2001; *Williams and Thorne*, 2003). Two of them occurred above the polar caps, one occurred in the wake region, one on the anti-Jupiter flank and one obliquely in front of the satellite (see Figure 1.14). Bi-directional electron beams have been identified on three (and possibly four) occasions out of these five cases. The half width of the beams is around 7°. The source altitude was estimated from these observations to be located around 0.6-0.7 Jovian radii (R_j) above the surface of Jupiter (*Williams et al.*, 1999). The PLasma Spectrometer (PLS) onboard Galileo

[14]By negatively drifting, it is meant that the frequency decreases with time.

[15]The velocity of a particle embedded into a magnetic field is usually decomposed into two components, one parallel to the field lines and one perpendicular to the field lines.

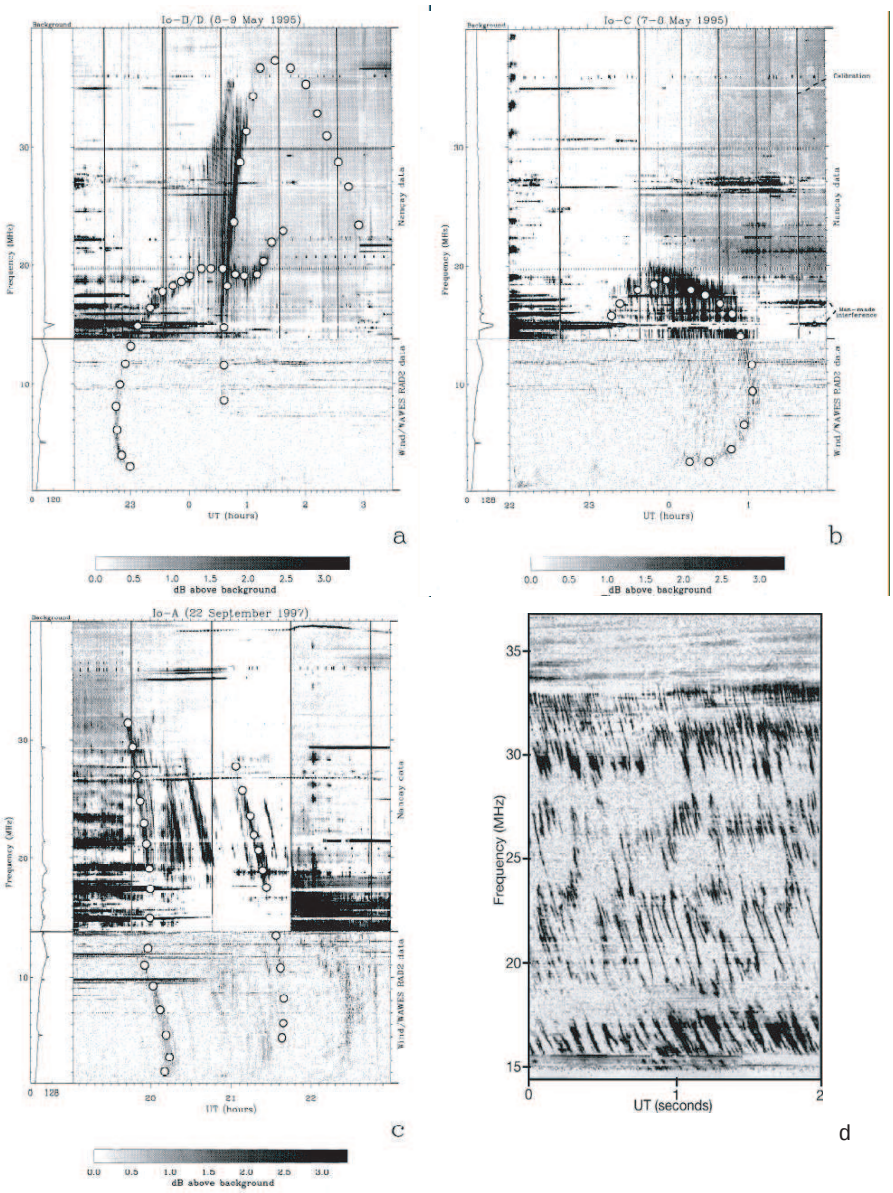

Figure 1.13: Examples of dynamic spectra of radio arcs. (a) B and D arcs. (b) C arc. (c) A arc. (d) Example of S-bursts. ((a), (b) and (c) from *Queinnec and Zarka*, 1998 and (d) from *Saur et al.*, 2004)

showed that the energy of these electrons extended towards lower energies (100 eV-1 keV) (*Frank and Paterson*, 1999; *Frank and Paterson*, 2000b; *Frank and Paterson*, 2002). After the first fly-by in the wake, these electron beams have been tentatively related to the UV footprints. *Frank and Paterson* (1999), for example, suggested that the beams could lead to a 3×10^{10} W total precipitated energy flux if the interaction cross section in the equatorial plane was 5400 km wide. Later fly-bys upstream and along Io's flank showed that the electron beams cross section was not extended in front and beside the moon. Since the electron beams cross section is much more restricted than previously proposed, the precipitated power deduced from UV footprint measurements appears hard to reach. Consequently, *Mauk et al.* (2001) proposed, by analogy with Earth processes, that these beams could originate from the planet-ward side of the current created by the Io interaction. Indeed on Earth, equatorward currents are associated with the electrostatic acceleration of electrons down into the atmosphere. On the other hand, FAST spacecraft in situ measurements also showed that the Earth-ward currents accelerate electrons towards the magnetosphere and thus create electron beams. The last encounters were polar fly-bys and revealed uni-directional Io-ward beams when flying over the Io polar caps, confirming the Jovian origin of source region (*Williams and Thorne*, 2003).

1.6.7 Galileo radio-occultation, magnetometer and plasma measurements

The finding of the electron beams were not the only valuable information obtained during these Io flybys. They also provided us with evidence of strong magnetic field perturbations taking place in Io's vicinity. Diversion and acceleration of the plasma flow have been observed around Io's flanks while stagnant plasma accompanied with a significant field depression were found in the wake region. Two scenarii were initially compatible with these measurements: the perturbations could have been attributed either to an internal magnetic field or to currents associated with the interaction between the plasma flow and Io's ionosphere or mass loading region. However, magnetic field measurements acquired during the two polar flybys finally led to the conclusion that Io has no appreciable internal field and that the observations can be fully explained with an Alfvénic model (see reviews by *Saur et al.*, 2004 and by *Jia et al.*, 2009a). Finally, radio occultation measurements reported by *Hinson et al.* (1998) indicate that the wake plasma is relatively quickly re-accelerated

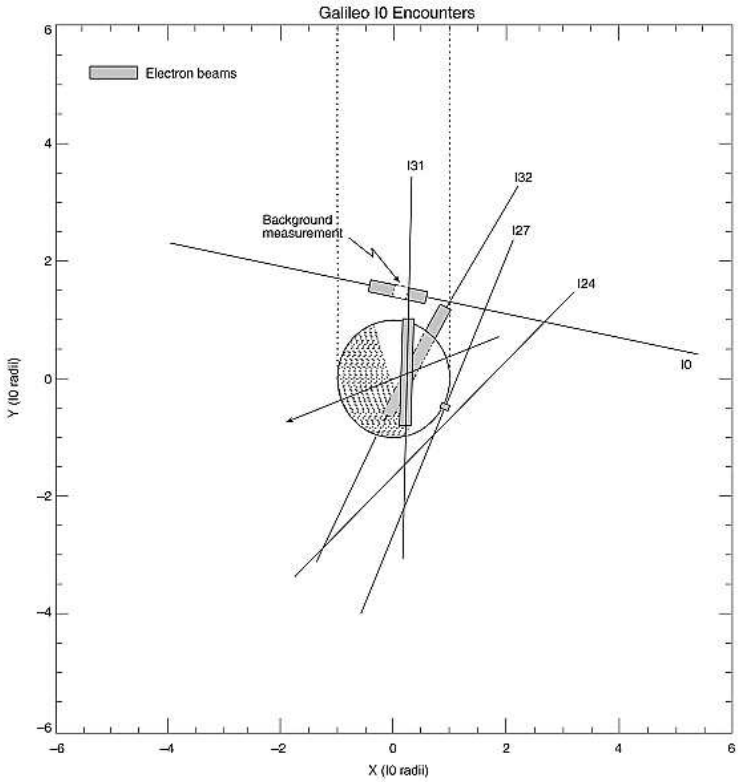

Figure 1.14: Location of the electrons beams as observed by Galileo EPD instrument. (From *Williams and Thorne*, 2003)

since it already reaches full corotation after 7 Io radii.

1.7 Description of the instruments

The present study is based on observations acquired with two UV cameras onboard the Hubble Space Telescope: the Space Telescope Imaging Spectrograph (STIS) and the Advanced Camera for Surveys (ACS). The UV channels of both instruments are based on the same technology: the Multi-Anode Microchannel Array (MAMA). Indeed, the detector of the ACS instrument is a flight spare model of the STIS detector. Figure 1.15 illustrates the design of these two detectors. The most important part of the device is the curved microchannel plate (MCP). Its upper face is covered by an opaque CsI photocathode. The MAMA is a photon counting detector. When a UV photon hits this layer, it produces a primary photoelectron that enters the microchannel. The electron cascade that follows produces a pulse of 4×10^5 secondary electrons at the exit of the MCP. The anode array then records the pulse and the signal is processed by the instrument electronics. The planar MgF_2 window above the device cuts off the wavelength shorter than 1150 Å. The field electrode between the MgF_2 window and the MCP is used to repel electrons that would be emitted away from the MCP back into the channel. The following sections describe these instruments with more details.

1.7.1 The Space Telescope Imaging Spectrograph

STIS is an imaging spectrograph that operates from near infrared to far ultraviolet (FUV) wavelength. The Space Shuttle crew installed it in February 1997 during the second servicing mission, together with the Near Infrared Camera and Multi-Object Spectrometer (NICMOS). The power system failed in August 2004, but the instrument was repaired during the last Space Shuttle servicing mission in May 2009. The prime capabilities of STIS are the spatially resolved spectroscopy from the UV to the near-IR (1150-10300 Å) and the echelle spectroscopy in UV. This versatile instrument also provides objective-prism spectroscopy and coronographic imaging. However, in this work, we are only interested in its imaging capabilities. STIS contains 3 different detectors:

- a CCD covering a 52×52 arcsec^2 field of view (FOV) and operating from 2000 to 10300 Å,

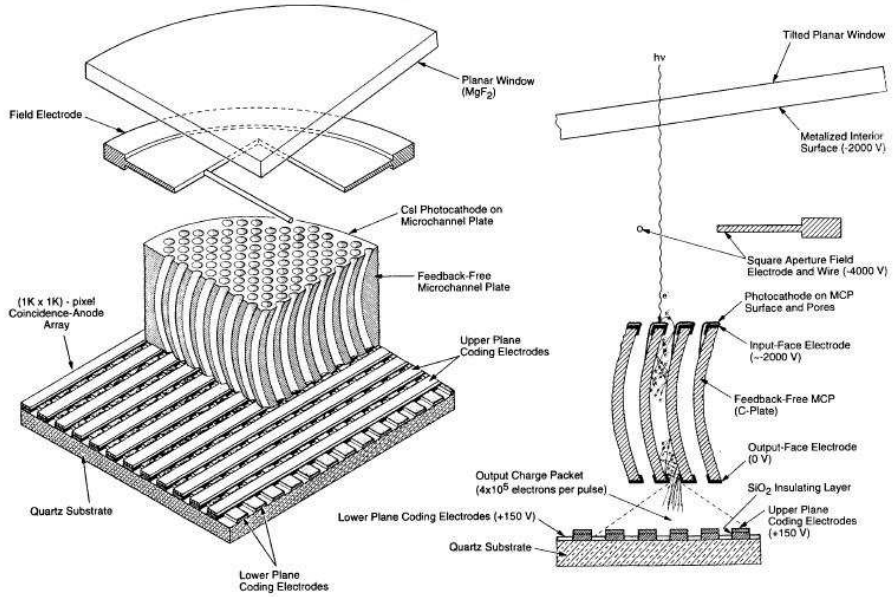

Figure 1.15: Design of the CsI MAMA detectors. This design is identical for STIS FUV-MAMA and the ACS SBC detectors. See the text for a more complete description. (From *Quijano et al.*, 2007))

- a Cs_2Te MAMA (NUV-MAMA) with a 25×25 arcsec^2 FOV and operating from 1600 to 3100 Å,
- a CsI MAMA (FUV-MAMA) covering a 25×25 arcsec^2 FOV and operating from 1150 to 1700 Å.

Since we are interested in the far UV H_2 Lyman and Werner as well as H Ly-α auroral emissions, only FUV-MAMA images have been used in this study. The two MAMAs have the unique capability of very high time-resolution (125 μs) imaging and spectroscopy. Two observation modes thus exist for STIS FUV-MAMA observations: the standard ACCUM mode, which produces images where the number of counts is accumulated for each pixel, and the TIME-TAG mode, which produces a list of detection events by recording the location and the arrival time of each count. Two filters have been mainly used: the CLEAR filter which includes the 1216 Å Ly-α band and the F25SRF2 filter (also known as the Strontium Fluoride filter) which mostly rejects this band. Figure 1.16 provides the throughputs of these filters as well as ACS's ones. Figure 1.17 compares the point spread functions of the STIS and ACS instruments for the four filters under consideration in this work. The full

widths at half maximum (FWHM) of these PSFs all lie between one and two pixels.

1.7.2 The Advanced Camera for Surveys

ACS has been installed in March 2001 in replacement of the Faint Object Camera (FOC) during servicing mission 3B. As its name suggests, this instrument is mainly designed for deep wide-field survey imaging of the sky (*Pavlovsky et al.*, 2006). Its main detector is a $2 \times 2048 \times 4096$ pixels CCD covering a 202×202 arcsec^2 field of view and operating in the visible and near-UV wavelength. Along with this Wide Field Channel (WFC) ACS has also two other high resolution channels. The High Resolution Channel detector is a CCD covering a 29×26 arcsec^2 field of view operating from 1700 Å to 11000 Å. The third channel, the one we are interested in, is the Solar Blind Channel (SBC). Its field of view is 35×31 arcsec^2 wide and its MAMA detector operates in the 1150-1700 Å range. The detector spatial resolution is 0.034×0.030 arcsec per pixel. The ACCUM mode is the only observation mode available. The HRC and the SBC share the same optical channel with the same corrective optics to compensate for the spherical aberration of the HST primary mirror. Prism spectroscopy is also available for the SBC channel but only its imaging capabilities have been used for this study. Like the STIS FUV-MAMA, the SBC MAMA has both local ($\geq$ 50 count/second/pixel) and global ($>$ 200000 count/second) maximum illumination rates. Because of its higher throughput, the total count rate is more limiting than for STIS and it constrains the observations to only the small portion of the planet including the polar regions while a larger part of the disk could fit into the field of view. Like for STIS images, two filters have been mainly used: the F115LP filter which includes H Ly-α band and the F125LP filter which rejects it.

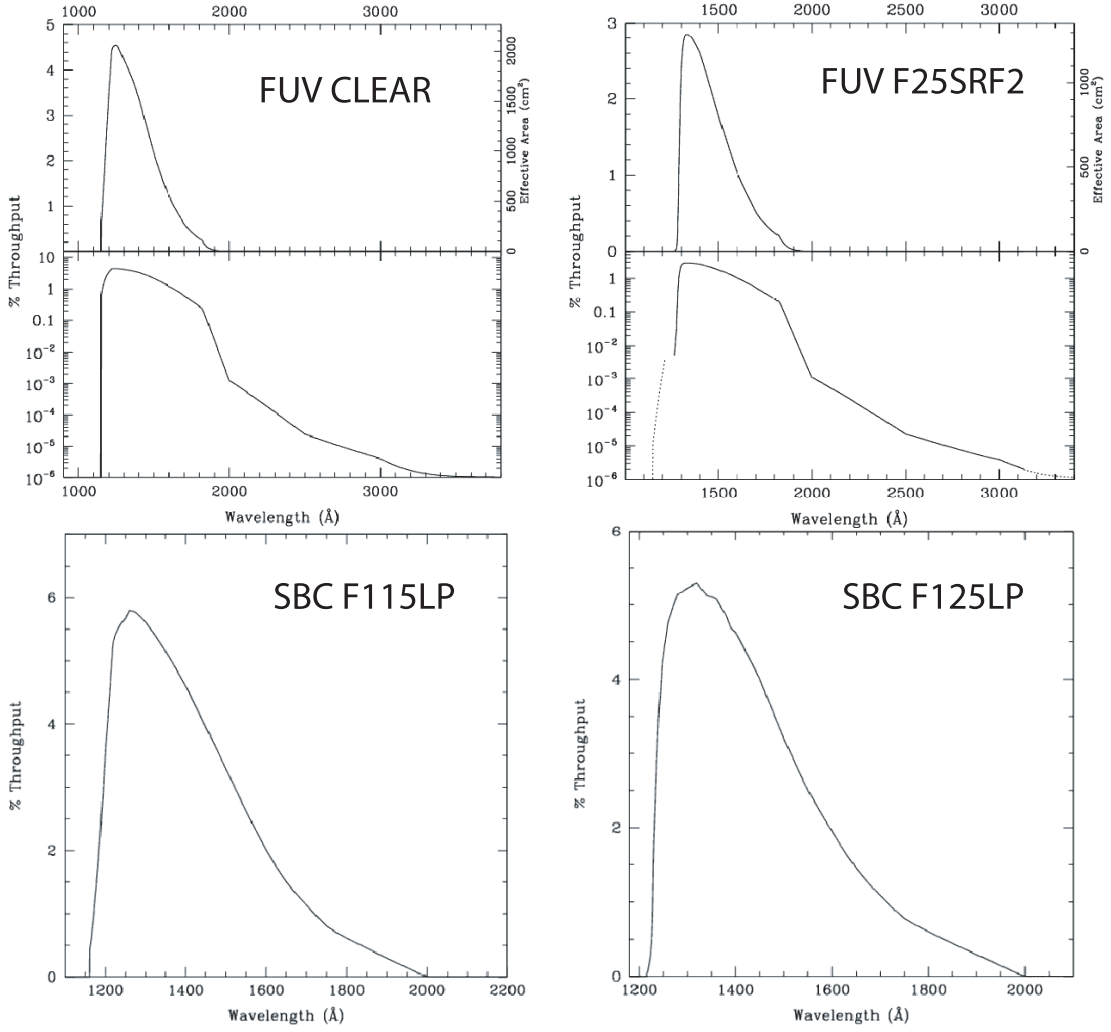

Figure 1.16: The two upper plots show the throughputs of the STIS CLEAR and F25SRF2 filters. The two lower plots show the throughputs of the ACS F115LP and F125LP filters. The CLEAR and F115LP filters have more or less the same characteristics but the ACS F125LP filter has a maximum throughput larger than 5% while the maximum throughput of the equivalent STIS F25SRF2 filter is less than 3%. (from *Pavlovsky et al.*, 2006)

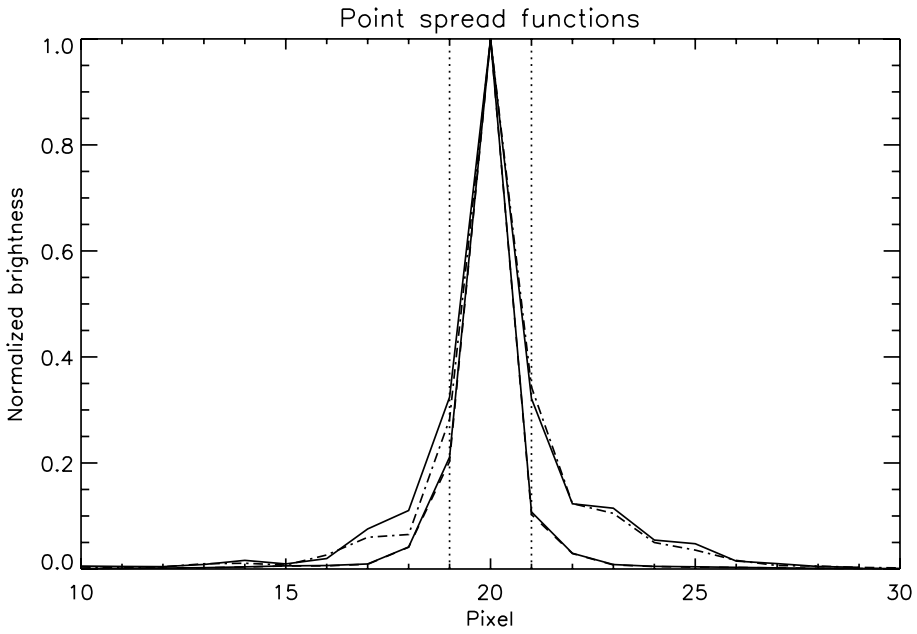

Figure 1.17: Comparison of the point spread functions for the four filters considered in this work. The solid line is for the F115LP ACS filter, the dashed line is for the F125LP ACS filter, the dash-dotted line is for the Strontium Fluoride STIS filter and the dash-dot-dotted line is for the STIS Clear filter. These PSF are computed with the TinyTim software (*http://www.stsci.edu/software/tinytim/tinytim.html*).

Chapter 2

Catalog and data processing

2.1 Foreword

As discussed in the introductory chapter, the Io-Jupiter electro-magnetic interaction gives rise to an auroral footprint on the giant planet. The goal of my thesis is to demonstrate that a methodical analysis of UV images of Jupiter's aurorae can significantly contribute to the understanding of this phenomenon. In order to achieve this goal, some rather technical steps have to be taken before moving into the more interpretative part of the work. For example, prior to any detailed investigation, we need to make an inventory of these images and to compile it into a catalogue together with relevant parameters related to each particular observation.

The basic pieces of information we can extract from these images are 1) the position of a particular structure and 2) its brightness. In the context of planetary astronomy, locating a feature usually consists in determining its longitude and latitude on the planet. As a result, we first need to determine the location of the planetary center and the orientation of the planetary rotation axis on the images. Unfortunately, the Hubble Space Telescope pointing parameters are not known with sufficient accuracy for our purpose. The precision of the guide star catalog is on the order of 1 arcseccond while we require and accuracy around 1 pixel, i.e. 0.025-0.03 arcsecond. Since we cannot use the telemetry information contained in the image headers, I developed techniques to retrieve these parameters with the appropriate accuracy from the images themselves.

As far as the brightness is concerned, it is crucial to isolate the intrinsic auroral emissions from background emissions. These background emissions originate from two sources: the geocoronal emissions from the Earth's upper atmosphere that gen-

STIS Clear	STIS SRF2	ACS F115LP	ACS F125LP
0.0236	0.0006	0.0287	0.0015

Table 2.1: Mean number of counts per second and per pixel caused by geocoronal emissions for the different filters considered in this work. The filters excluding H Lyman-α emissions are far less affected by these emissions than those including this line.

erate a uniform noise on the image and Jupiter's planetary disk emissions. These disk emissions are mainly caused by dayglow emissions and by solar light reflections on the Jovian atmosphere. The geocoronal emissions rarely exceed a few counts per pixel for typical HST exposures and can be easily deduced from the brightness measured on an area located away from the planet.

These tools were developed in such a manner as to be easily used by many. This approach allowed me to be involved in many other studies based on Hubble Space Telescope images. Some of these studies will be simply listed at the end of this chapter while others, more closely related to the satellite footprints, are discussed more thoroughly in the relevant chapter.

2.2 HST Observation Programs

More than two thousand UV images and spectra of Jupiter have been taken with the high resolution cameras (STIS and ACS) on board HST since 1997. Each set of images from the different programs has been processed at the time it was acquired. However, several critical corrections and improvements have been added to the processing pipeline with time. In order to perform efficient statistical or detailed analysis of the Jovian aurora in general and of the Io footprint in particular, we needed a well organized data base taking into account the more recent image processing methods. It has been thus decided to re-download all the images and spectra and to process them with the best available reference files[1]. We also processed them with our own routines in a standardized way in order to produce files readily usable with the IDL software. For example, these routines extract and store independently individual exposures when several of them are recorded into the same source file. Other routines generate series of 10-second exposure time images out of

[1]The reference files are the files describing the different corrections that have to be applied to the raw image. It includes the files related to the dark, the flat field and the geometric correction.

the time-tag event lists.

The database consists of the observations acquired during programs 7308 (Clarke)[2] , 7309 (Gérard), 7769 (Prangé), 8108 (Emrich), 8171 (Clarke), 8657 (Clarke) , 9685 (Elsner) 10140 (Grodent), 10507 (Grodent) and 10862 (Clarke). Table 2.2 provides a list of characteristics of these programs together with a one line summary of their scientific objectives. Apart from proposals 8171, 10140 and 10862 which included some observations specifically dedicated to the Io footprint, the presence of the Io footprint on the images was usually not considered as a primary objective. This is an additional justification for building a complete catalog and database in order to select subsets of images where Io is in an appropriate configuration. It also made it possible for us to determine the previously unexplored configurations of Io relative to the plasma torus, which turned out to be particularly useful when the 10862 observation program was put together.

The Hubble Space Telescope orbits around the Earth in approximately 96 minutes at a mean altitude of ∼600 km. Since Jupiter lies close to the ecliptic plane, HST can point at it only during half an orbit, i.e. for ∼45 minutes. During the remainder of the orbital period, Jupiter is occulted by the Earth. In the present work the term "HST orbit" designates the continuous time period during which Jupiter can be seen from Hubble.

The 10862 program is the largest program ever established to observe Jupiter and Saturn. Within a few months of Spring 2007, HST acquired between twice and three times more images of Jupiter than during the previous 10 years. The Jovian side of the campaign[3] was divided into 3 parts. The first part consisted in acquiring images during one orbit for 20 consecutive days and took place from February 20 to March 11 2007, simultaneously to the New-Horizons probe Jupiter fly-by. The second part also consisted in acquiring images during at least one orbit per day from February 20 to March 11. This second time period was chosen close to opposition, from May 11 to June 11, so that MHD simulations can be used to propagate solar wind conditions measured at Earth up to Jupiter. Moreover, on 6 occasions, Jupiter was observed during two to five orbits on the same day. The third part consisted in 10 orbits spread from March 2 to April 24 and exclusively dedicated to the Io and Ganymede footprints.

[2]The name in the parenthesis is the name of the Principal Investigator (or PI) of the programs.

[3]The 10862 campaign was essentially dedicated to the study of the response of the Jovian and Kronian magnetospheres to the solar wind. Therefore, 879 images of Saturn's aurora have also been acquired.

Proposal ID	PI Name	Number of images	Number of time-tags	Number of spectra
7308	J.T.Clarke	40	6	21
Abstract: WFPC2 and STIS auroral observations concurrent to magnetospheric Galileo observations.				
7309	J.-C. Gérard	2	1	6
Abstract: Search for the signature of the H_2 dayglow in the equatorial regions.				
7769	R. Prangé	34	2	16
Abstract: Spectral and imaging observations of the polar regions giving access to auroral atmospheric parameters.				
8108	C. Emrich	0	0	22
Abstract: High resolution STIS spectral observations.				
8171	J.T.Clarke	19	13	36
Abstract: Spectroscopic and imaging study of the satellite footprints during the Galileo mission.				
8657	J.T.Clarke	190	18	37
Abstract: Study of the solar wind impact on the Jovian magnetosphere concurrent to in situ solar wind measurements during the Cassini fly-by.				
9685	R. Elsner	45	6	0
Abstract: Coordinated HST and Chandra observations of Jupiter in order to determine the origin of the X-ray aurorae.				
10140	D. Grodent	100	0	0
Abstract: Study the possible northern Jovian magnetic field anomaly.				
10507	D. Grodent	71	0	0
Abstract: Study of the diffuse auroral emissions poleward and equatorward of the main oval.				
10862	J.T.Clarke	1619	0	0
Abstract: Study of the influence of the solar wind on Jovian magnetosphere and aurorae during the New Horizon probe fly-by.				

Table 2.2: Description of the executed HST programs considered in this study. Only the UV observations were accounted for. The number of time-tags refers only to imaging time-tags. The spectral time-tags are counted in the spectra column.

Moreover, such a large amount of data also required a catalog gathering at the same time information concerning the observation itself (instrument, filter, etc.) and planetary ephemeris (sub-solar latitude, Io System III longitude, etc.). The next sections describe how the catalog has been built, what are the stored parameters and where they come from. The catalog consists of a structure variable saved in an IDL file. In addition to the IDL file, a descriptive ascii file has been generated for each observation, compiling the parameters considered in our catalog.

2.3 Information sources

All the HST data stored on our file system comes from the Space Telescope European Coordinating Facility (ST-ECF) and from the Space Telescope Science Institute (STScI). The first step consists in building a list of all the relevant observations. Knowing the names of the HST programs, the observation list has been computed with the ST-ECF web site [4]. The main information source about the data itself comes from the *.fits* files headers. These headers collect technical information about the data and the telescope telemetry. When a parameter is both available from the websites and from the *.fits* header, the header was always preferentially used. For example, there was a systematic 1 second difference in the start dates between the *.fits* files and on the websites concerning the WFPC2 observations. As far as the ephemeris are concerned, the information is computed with a FORTRAN code based on libraries from the Navigation and Ancillary Information Facility (NAIF) SPICE system [5]. This program was written by Denis Grodent and has been slightly modified in order to provide the sign of the pitch angle[6]. All the temporal data are calculated for the initial moment of the exposure.

Several catalog fields are links to some relevant files, such as the reduced image file or preview images or movies. Other parameters required additional computing like the estimated position of the satellite footprints. Their location on the planet

[4] http://archive.eso.org/wdb/wdb/hst/science/form

[5] http://naif.jpl.nasa.gov/naif/

[6] In this context, the pitch angle is the apparent angle between Jupiter's projected rotation axis and the celestial north direction. It should not be mixed up with the pitch angle describing the angle of a particle velocity relatively to the magnetic field. This angle in measured counter-clockwise. In order to compute the sign of the pitch, the modified program first computes the vector formed by the cross product of North direction vector with the Earth-Jupiter vector. The sign of the pitch angle is equal to the sign of the dot product of this vector with the Jovian rotation axis.

comes from the longitude of the satellites mapped into the ionosphere with the VIP4 magnetic field model. For Io, the VIT4 model[7] has been used and an approximation of the lead angle has also been taken into account. This estimate comes from a 3rd order Fourier fitting of Infrared lead angle measurements provided by J. E. P. Connerney (personal communication). Given the inaccuracies of the magnetic field models and the existence of poorly constrained lead angles, these parameters do not provide reliable positioning of the satellite footprints but just an indication of their likely locations. The accuracy is on the order of 5° in every direction for Europa and Ganymede. For Io, the error can reach up to 15° in the poorly constrained regions.

The last type of parameter is related to our "in-house" data processing. Since the center of the planet on the image as well as its exact orientation are poorly known from telemetry, limb and band fitting methods have been built in the framework of this study. These parameters are also included in the catalog. Similarly, some parameters issued from eye detection of particular footprint features are also included. Note also that some fields are left empty for later use.

[7]The VIT4 model is an unpublished improved version of the VIP4 model and is used by the courtesy of J. E. P. Connerney. This model is essentially constrained by the IFP latitudes, since the probe field measurements are only used to compute the magnetic field intensity. The northern Io contour provided by this model is closer to the observations than the previous one .

2.4 Field description

Name	Type	Origin	Description
target_name	string	header	target name
target_ra	float	header	sighting right ascension
target_dec	float	header	sighting declination
target_descr	string	web	target description
instr	string	header	instrument
data_set	string	header	data set name
hemisphere	string	calculated	hemisphere ("N" for North, "S" for South)
release_date	string	web	release date
date	string	header	date at the begining of the exposure
expt	float	header	exposure time in seconds
filter	string	header	filter
pi_name	string	header	PI name
prop_id	string	header	proposal ID
sp_vers	string	web	spacecraft version
grating	string	header	grating
asn_id	string	header	not used
asn_type	string	header	not used
number	float	header	number of observations in the dataset
camera	string	header	camera
obs_mode	string	header	observation mode
min_wl	float	header	minimum wavelength
max_wl	float	header	maximum wavelength
dispersion	float	header	Not used
bandwidth	float	header	Not used
cent_wl	float	header	central wavelength
pitch	float	SPICE	pitch angle counted counter-clockwise in degrees
jup_ra	float	SPICE	Jupiter right ascension
jup_dec	float	SPICE	Jupiter declination
incl	float	SPICE	angular position of the north pole
latst	float	SPICE	sub-earth latitude in degrees

Name	Type	Origin	Description
cml	float	SPICE	central meridian longitude in degrees System III
latss	float	SPICE	sub-solar latitude in degrees
lonss	float	SPICE	sub-solar longitude in degrees System III
d	float	SPICE	Earth-Jupiter distance in km
light_time	float	SPICE	Earth-Jupiter light-time in seconds
eq_rad	float	SPICE	Jovian equator radius in arcsec
pol_rad	float	SPICE	Jovian polar radius in arcsec
aurora_param	20 floats		Aurora parameters
aurora_comment	string		comments on the aurora
phase_io	float	SPICE	Io phase angle in degrees
lbd3_io	float	SPICE	System III Io longitude in degrees
io_param	20 floats array		Io footprint parameters
io_param(0)	float	computed	Io centrifugal latitude in degrees
io_param(1)	float	vis. insp.	visibility of the Io footprint (0 for no, 1 for yes and 2 for undetermined and -1 if not filled)
io_param(2)	float	vis. insp.	visibility of the precursor (0 for no, 1 for yes and 2 for undetermined and -1 if not filled)
io_param(3)	float	computed	Io footprint System III longitude
io_param(4)	float	computed	Io footprint phase angle
io_param(5)	float	computed	Io footprint latitude
Io_comment	string		comments on the Io footprint
phase_euro	float	SPICE	Europe phase angle in degrees
lbd3_euro	float	SPICE	Syst. III Europe longitude in degrees
euro_param	12 floats array		Europe footprint parameters
euro_param(3)	float	computed	Europa footprint System III longitude
euro_param(4)	float	computed	Europa footprint phase angle
euro_param(5)	float	computed	Europa footprint latitude
euro_comment	string		comments on the Europe footprint

Name	Type	Origin	Description
phase_gany	float	SPICE	Ganymede phase angle in degrees
lbd3_gany	float	SPICE	Syst. III Ganymede longitude in degrees
gany_param	12 floats array		Ganymede footprint parameters
gany_param(3)	float	computed	Ganymede footprint System III longitude
gany_param(4)	float	computed	Ganymede footprint phase angle
gany_param(5)	float	computed	Ganymede footprint latitude
gany_comment	string		comments on the Ganymede footprint
phase_calli	float	SPICE	Callisto phase angle in degrees
lbd3_calli	float	SPICE	Syst. III Callisto longitude in degrees
calli_param	12 floats array		Callisto footprint parameters
calli_comment	string		comments on the Callisto footprint
rootname	string	header	rootname (unique for each image)
extension	string		extension (ex: _rzd)
preview_link	string		link to the preview
video_link	string		link to the video preview
i_s	string	header	image or spectrum The first letter is "I" for images and "S" for spectra. The next two letters are "UV" for UV and "VI" for visible.
tele_data	10 floats array		telescope data
tele_data(0)	float	header	OM1LVPST detector temperature (for the Landsman 98 blotch correction)
tele_data(1)	float	header	detector orientation (i.e. angle between the north axis and the image y axis) measured counter-clockwise in degrees
tele_data(2)	float	defined	angle per pixel (arcsec/pixel)
tele_data(3)	float	header	x dimension of the reduced image (pixel)
tele_data(4)	float	header	y dimension of the reduced image (pixel)
tele_data(5)	float	defined	x position of the Jovian center on the reduced image (pixel)

Name	Type	Origin	Description
tele_data(6)	float	defined	y position of the Jovian center on the reduced image (pixel)
tele_data(7)	float	computed	x position of the Jovian center on the reduced image (pixel)
tele_data(8)	float	computed	y position of the Jovian center on the reduced image (pixel)
tele_data(9)	float	computed	quality flag for the center computation
tele_data(10)	float	computed	corrected pitch angle (degrees)
tt_start	5 floats array		initial moments of the Good Time Interval
tt_stop	5 floats array		final moments of the Good Time Interval
link	string		link to the reduced image
orb	string	calculated	rootname of the first image of the orbit
comments	string	inspection	comments : It contains the "MISSING FILES"statement if the data are not available.

Table 2.3: List of the parameters available in the catalog.

2.5 Data reduction

The WFPC2 data have not been re-reduced yet, neither have the STIS spectra since none of them have been considered in this study. As far as the STIS images and time-tag sequences are concerned, the original data are coming from the *_x2d.fits* files. The ACS images were reduced with the *Multidrizzle* software. The next paragraphs discuss the relevance of corrections applied additionally to the standard pipeline. For STIS data, homemade procedures have been built according to Space Telescope Science Institute (STScI) reports. Since we were looking for a "state of the art" standardized database, we reviewed all the routines as well as their relevance.

2.5.1 STIS data

The dark current[8] on STIS FUV-MAMA has a mean value $\sim 7\times10^{-6}$ count/s/pixel, which is very low. It can be decomposed into two components. The first one is a uniform and temperature-independent flux of 1.6×10^{-6} count/s/pixel while the second can reach 2×10^{-4} count/s/pixel, is temperature dependent and is localized on the upper left part of the image array. *Landsman* (1998) established that the best monitored detector temperature for estimating the temperature dependence was the OM1LVPST low voltage supply temperature. This temperature is available in the *_spr.fits* engineering file that comes with every observation and is included in the catalog. Nevertheless, since this correction is not accurate and remains below 1 count per pixel for every imaging observation (exposure times $< 150s$), we chose not to correct for this dark current component.

As far as the geometric distortion corrections are concerned, *Walsh et al.* (2001) released an Instrument Science Report (ISR) in 2001 describing the correction method for both the NUV and the FUV MAMA. It is based on a third order polynomial description of the geometric distortion field for each detector. The first STIS pipelines did not complete the geometric correction so that homemade procedures relying on the reported method and set of coefficients have been built and used. In 2004, *Maiz-Apellaniz and Ubeda* (2004) released another ISR establishing that the previous geometric correction was not correct for the NUV-MAMA. According to this report, the way the 2001 polynomial parameters have been derived was erroneous. Consequently the FUV-MAMA set of polynomial coefficients is probably incorrect too. Even if the complete set of geometric coefficients have not been computed yet for the FUV detector, STScI provided a new set of coefficients for correcting the fact that the pixels' surface are not exactly squared but rectangular (the y-scale of the pixels is approximately 1% larger than the x-scale). In order to compare the old but full 2001 correction and the new "rectangle-to-square-only" correction, we processed the same Saturn image with both methods and we tried to determine which method best fits the rings. As the old 2001 parameters gave significantly worse results, we chose to correct only the rectangular aspect of the pixels, as performed in the new STIS pipeline for the *_x2d* images. However, the best geometric correction will only be achievable when the STScI releases an updated set of correction parameters.

[8]The dark current is the signal current that flows in a photodetector when it is placed in total darkness

2.5.2 ACS images

The ACS data are directly coming from the *Multidrizzle* image processing pipeline from the STScI[9]. The subtlety arises from the fact that the total number of counts per second on the geometrically corrected images is erroneously 1.63 time larger than on the non-corrected image. Following the purely geometric correction (i.e. relocating the pixels at their correct place), *Multidrizzle* applies an additional photometrical correction for the pixel area. The pixel area map in use for SBC is the same as for the HRC detector, since they share the same deforming[10] optical path. The problem is that this pixel area map (PAM) is normalized to 0.025 arcsec square while the SBC pixels are 0.03377×0.0301 wide. Consequently, the number of counts is artificially multiplied by the pixel surface ratio. We took this effect into account and corrected the count rates accordingly.

2.6 Determination of the planetary center location and rotation axis orientation

The limited accuracy of the HST guide star catalog and the uncertainty in the start time of the tracking motion prevent us from precisely locating the center of Jupiter on the images just from pointing information. However, the determination of the planetary center is a mandatory step before locating any structure in the images. Additionally, the accurate positioning of the center is crucial for building polar projections of the auroral emissions. Several techniques have been used through the years, from manual positioning of a grid to semi-automatic limb fitting methods. The manual positioning remains the more precise technique because all the useful elements, such as the altitude of auroral arcs above the limb or the relative motion of an auroral feature from one image to another, can be taken into account by the operator. Nevertheless, this technique suffers from two major drawbacks: the subjectivity of the operator and the time these manual manipulations consume. Since the data base tremendously inflated with the 10862 observation campaign, this

[9] *http : //stsdas.stsci.edu/pydrizzle/multidrizzle/*

[10] By deforming it is meant that we cannot use the raw image without straightening the geometry. It does not imply that the optics of the instrument is ill designed. Actually, the optical path is designed to compensate the deformation caused by the spherical aberration of the main mirror. The distortion of the raw image stems from the fact that the focal surface is not perpendicular to the chief ray.

method was seen as impracticable for providing first results in a reasonable amount of time. Another major advantage of an automatic procedure is that the complete dataset can be quasi-immediately reprocessed if needed, which is impossible for manual methods. The limb-fitting method[11] designed by Adem Saglam was first developed for Saturn (*Saglam*, 2004), where the illuminated limb is sharp, and then adapted to Jupiter. The method is based on modeling the edge of the planet with a parametric step function. The operator has to select a rectangle containing a section of the limb free from auroral emissions. Each line (or row) is then fitted with the step function. The limb is computed by fitting the contour ellipse of the planet computed from the ephemeris to all the detected step points. Unfortunately, this technique also depends on the operator subjectivity through the rectangle selection and can sometimes be inaccurate, especially for the non-illuminated limb which can hardly be modeled with a step function. Therefore, we developed an automatic procedure based on the detection of the planetary limb inflection point to compute the planetary center.

A multi-step strategy has often been used in the method described below. This approach has been requested by the huge number of particular or problematic cases on one hand and by the demanded final precision on the other hand. The strategy thus consists in a robust but rather imprecise first step and on a refined and more precise second step. Figure 2.5 summarizes the successive tasks of the limb fitting method.

Should the filter perfectly isolate the H_2 and H UV emissions below 1650 Å, the limb altitude would be related to the UV dayglow emission. However, the planetary disk seen on ACS (and STIS in a lesser extent) FUV images mainly results from the reflected solar continuum in longer wavelengths that is leaking into the detector[12] (*Boffi et al.*, 2008). Consequently, a reasonable assumption is that the limb altitude as detected on the images indeed corresponds to the reflected sunlight limb with an inflection point located at the 1 bar level, corresponding to the 0 km altitude assuming an ellipsoid with an equatorial radius of 71492 km and a polar radius of 66854 km. In order to test this hypothesis, we used ACS images of Saturn acquired with the same filters. Saturn being located approximately twice further from the Sun than Jupiter (9.5 AU instead of 5.2 AU), the entire planetary disk as well as

[11] This method is no longer used for Saturn and has been replaced by a ring fitting method also developed by Adem Saglam.

[12] This effect is called red leak.

	Mean (km)	Std. dev. (km)
Equator	157	215
45°S	11	169
65°N	-74	101

Table 2.4: Mean altitude of the radial light curve inflection points on Saturn measured from the 1-bar level. Since one pixel subtends 180 km, we note that the mean altitude as well as the standard deviation of this altitude are on the same order or lower than the pixel size.

a large portion of the ring system appears on STIS and ACS FUV images. As a consequence, on these images, the planetary center can be computed with an independent method, i.e. by fitting the A, B and C rings in lieu of relying on the planetary limb. Elliptic bands, whose dimensions are deduced from ephemeris and from the detector plate scale, are adjusted to the observed rings. The center of these ellipses provides an excellent estimate of the planetary center, with a mean accuracy of $\sim$1 pixel. We then perform radial scans of the day-side limb and compute the altitude of the inflection point given the center location from the ring fitting (Figure 2.1). The mean altitude of the inflection point is measured at 0°, 45°S and 65°N latitudes on the sunlit side of the planet. In the three cases, the mean altitude is almost within a pixel from the 1 bar level (see Table 2.1). Since the atmospheric composition of both giant planets is similar, it is reasonable to assume that the conclusions drawn about the altitude of the inflection point at Saturn are applicable to Jupiter as well.

2.6.1 Co-adding the exposures

Our purpose is to build a fully automatic procedure to locate as accurately as possible the planetary center on all type of STIS and ACS images. The concept is close to the method developed by Adem Saglam, but brings some useful improvements. The first idea is to increase the signal to noise ratio at the maximum when selecting a limb profile. Since the HST pointing is very stable during an observation orbit[13], we summed all the images from the same orbit and acquired with the same pointing target. This is particularly convenient for the ACS observations, when up to 32

[13]The typical pointing stability drift when two guide stars are used is on the order of 0.01 arcsec per orbit, which is less than the size of 1 pixel (0.024 arcsec for STIS or 0.03 arcsec for ACS).

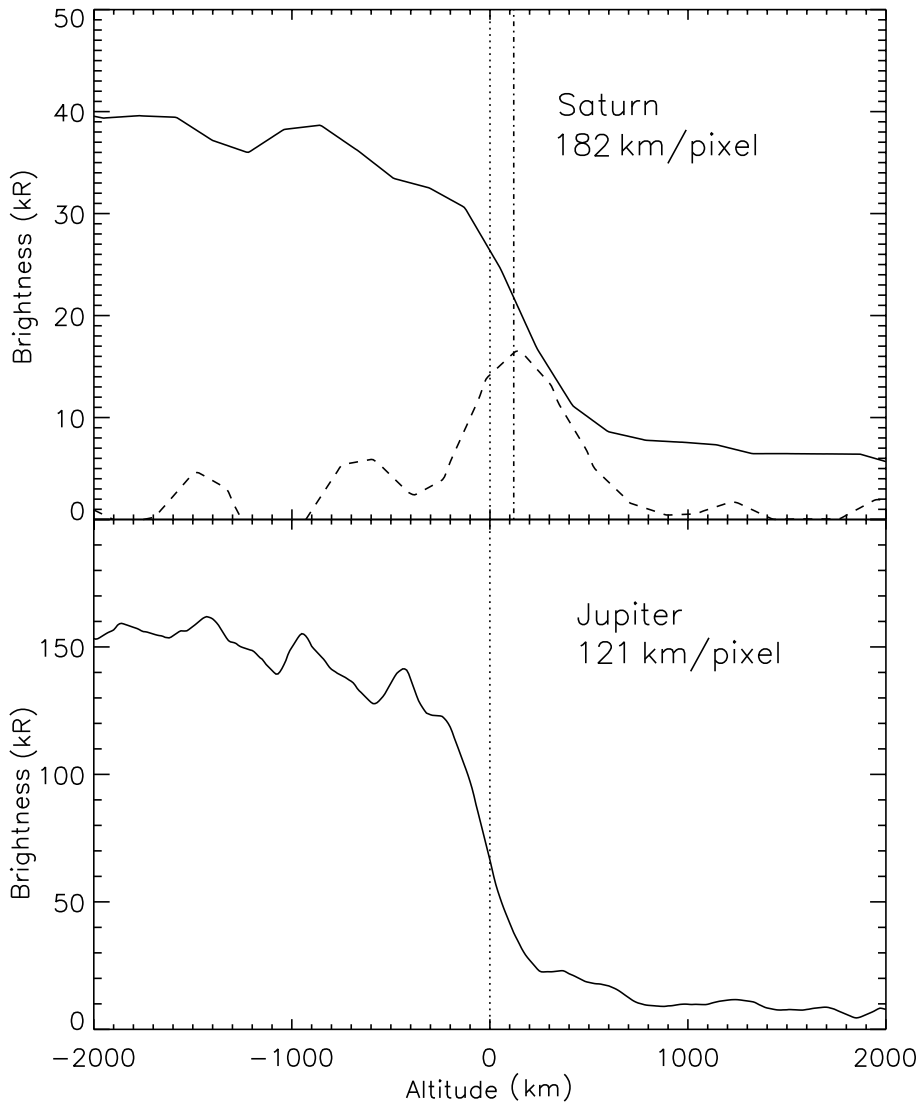

Figure 2.1: Example of an equatorial limb profile at Saturn (a) and at Jupiter (b). The dashed line represents the first derivative of the altitude of the brightness profile. The dotted line represents the 1 bar level, corresponding to 0 km. On Saturn, the altitude of the inflection point (highlighted by the dash-dotted line) is smaller than the pixel size. (from *Bonfond et al.*, 2009)

consecutive images have been acquired within a single orbit. As discussed below, this technique is more complex to apply to images from the 9685 STIS program.

2.6.1.1 Compensation of the inter-image shift for the program 9685

Since the STIS field of view is 25×25 arcsec^2 wide and since Jupiter's apparent diameter is about $\sim$50 arcsec wide, the planet cannot fit entirely into the instrument field of view. Approximately one quarter of the Jovian disk can be seen at a time. As a consequence, the telescope has to be pointed slightly northward from the Jovian center to observe the northern aurora and vice versa for the South. In the other HST/STIS programs, this shift had been calculated by the PI and the pointing position was given in celestial coordinates. However, for the 9685 program, it was requested to track a particular point on Jupiter's surface. The coordinates of this point are 170° in System III longitude and 67.8° in planetographic latitudes[14]. Since this particular point is rotating during an observation sequence, the planetary disk shifts from one image to the other. Consequently, it is necessary to compensate for this additional motion in order to re-align the limbs. Accordingly, a routine was developed in order to calculate the shift of each sub-image from a sequence relative to the first one. It simulates the motion of the point in planetary coordinates and computes the location difference in pixels from one frame to another. This function works for time-tag sequences as well as for sub-images from a same dataset. In Figure 2.2 the left panel represents the superposition of two images from the same dataset without the shift and on the right panel we applied the shift. In the second case, the two planetary disks are perfectly aligned.

2.6.2 Orienting all images consistently

In the following, the word "image" will be used to designate the sum of the exposures. The goal of the automatic limb fitting procedure is to process every image the same way, whatever the orientation of the planetary disk on the detector and whatever the observed hemisphere. Three cases can occur: the disk fills one, two or three corners of the image. In order to detect which configuration should be considered, we need to distinguish the population of points related to the background from the population of points related the planetary disk. This discrimination is performed by using the histogram of the image. In filtered images, there is a clear gap between the

[14]This corresponds to 65° in planetocentric coordinates.

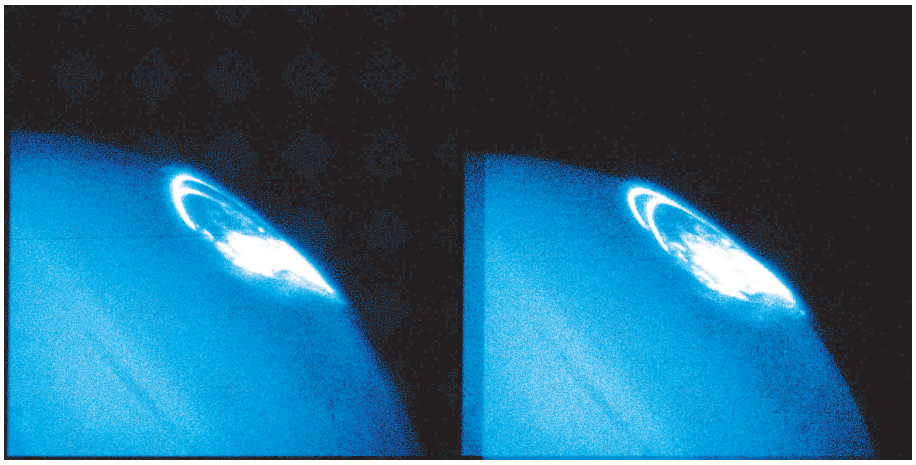

Figure 2.2: (left) Superposition of two exposures acquired during the same orbit 20 minutes apart. The two planetary disks are not aligned. (right) Superposition of the same two exposures, but shifted according to the routine results. The limbs are now perfectly aligned.

background population and the disk population so that the brightness threshold can be set to the value corresponding to the first minimum of the histogram. On unfiltered images, the situation can be more complex, especially for STIS Clear images. On the geometrically corrected images, the first population of points corresponds to the border points that do not belong to the raw image (see Figure 2.3). Their brightness has simply been set to zero in the pipeline. The second population belongs to the background points affected by $Ly-\alpha$ geocoronal emissions. The mean brightness of this population can be significantly different from zero so that a first minimum can appear on the histogram. The third population of points corresponds to the disk and auroral emissions. In this case, the second minimum threshold is considered instead of the first. At the end of this step, the threshold value is used by the procedure to discriminate roughly the points belonging to the disk from the others. The procedure then checks which corners are inside the disk and which are outside.

2.6.3 First guess of the planetary center

Given the position of the disk relative to the corners, the image is rotated in order to place the center of the disk in the lower left corner. If the disk fills two corners, the image is rotated so that the center is located on the left side. Knowing the

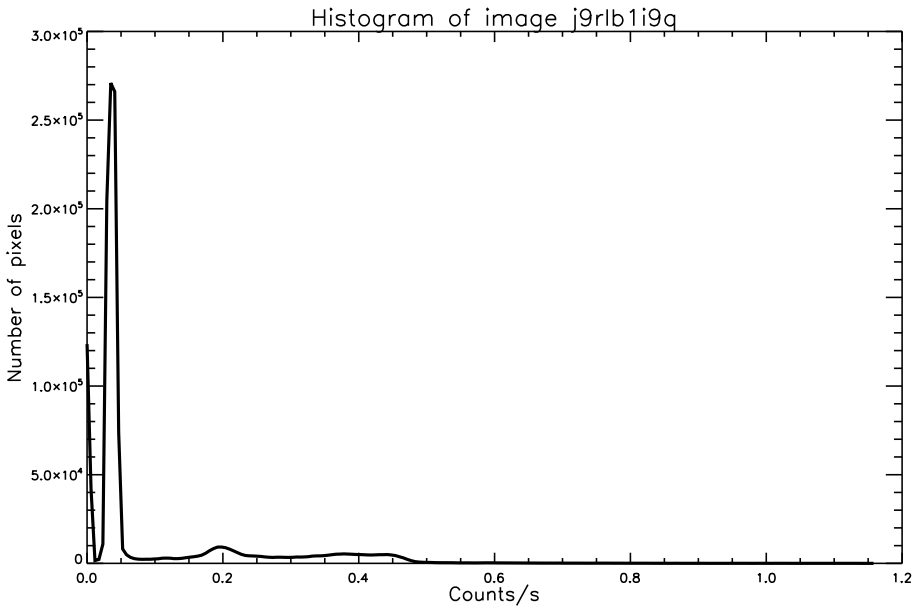

Figure 2.3: Histogram of the pixel values for a F115LP ACS image. The first peak at 0 count/s corresponds to the border points. the second maximum corresponds to the background points. The rest of the points originates from the planetary disk and the brighter points are from the aurora. In this case, the threshold is defined as the second minimum.

number of corners included into the disk, another routine locates two points at the edge of the disk taking the illumination of the limb into account. A different criterion is used for the sunlit or the dark side of the planet. At this point of the procedure, we know the quadrant in which the planet is located on the image and the approximate position of two points on the limb. A contour ellipse fitting routine based on ephemeris provides then a good first guess for the planetary center.

2.6.4 Masking the aurora

This rather accurate positioning of the center enables us to localize realistically and effectively the polar area on the images. Points in this area should be discarded from the limb scan because they are affected by high altitude auroral emissions. If a too optimistic criterion is considered, then the auroral emissions will dramatically damage the limb determination. On the other hand, if a too careful criterion is applied, then, the portion of the limb taken into account will be so restricted that no accurate limb fitting can be achieved. This is the reason why the first guess step is so important. Since the most equatorward emissions come from the Io footprint and tail, the auroral zone limit is defined 4° equatorward from the Io reference contour from *Grodent et al.* (2003a). This area enables us to build a mask of points to be discarded for the limb detection.

2.6.5 Scanning the limb

With the possibly misleading points due to auroral emissions eliminated, we can refine the determination of the limb position. The next step consists in scanning the disk boundary as approximated by the first guess ellipse in order to accurately find the location of the limb. The limb point is defined as the inflection point of the radial profile (*Vincent et al.*, 2000). Every degree starting from the bottom of the rotated images, a corresponding point from the first guess ellipse is localized and the tangent to the ellipse at this point is computed. The image is then rotated around this point in order to align the tangent line to the Y axis. The procedure selects a 240×70 pixels rectangle centered on the rotation center. The rectangle is then re-binned into a 240 points profile (see Figure 2.4). Applying the two step strategy, a two part function is first fitted to the profile for a rough determination of the brightness decrease. The first part consists in a 2nd degree polynomial which

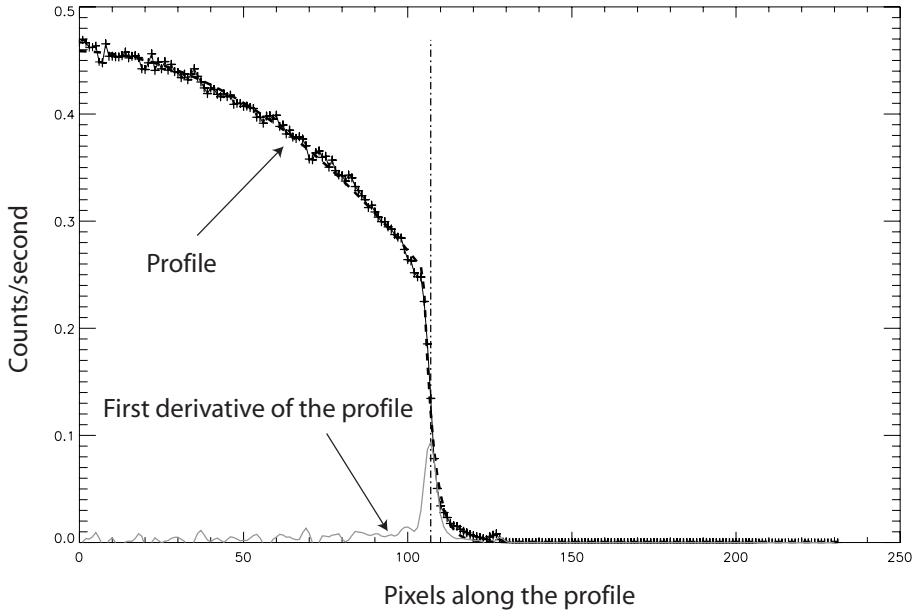

Figure 2.4: Typical limb profile for ACS data. The "+" symbols represent the actual profile. The dashed line is the polynomial-exponential fitting curve. The grey plain line represents the first derivative of the actual profile. The two step procedure, i.e. first fitting a curve and the then searching the inflection point in a restricted area, is particularly helpful for low signal to noise STIS data. The vertical dot-dashed line marks the position of the limb point.

models the behavior of the inside of the disk along a normal scan[15]. The second side of the curve is a decreasing exponential that models the transition from the disk to the background brightness. The second step consists in locating the inflection point of the profile in a restricted set of points in the part corresponding to the decreasing exponential. Finally, the locus of the inflection points is fitted with an ellipse in order to compute the coordinates of the center.

2.6.6 Deducing the orientation from the Jovian atmospheric band structure

The processing of Saturn ACS observations aquired in 2007 highlighted a systematic 0.7° error of the orientation angle when fitting synthetic rings to the image rings. Unfortunately, no ring system is visible on Jupiter HST FUV images. Neverthe-

[15]Since the orientation of the profile is perpendicular to the tangent to the ellipse, the scan is not exactly radial but normal to the limb. This is more accurate since the Jovian disk is an ellipsoid.

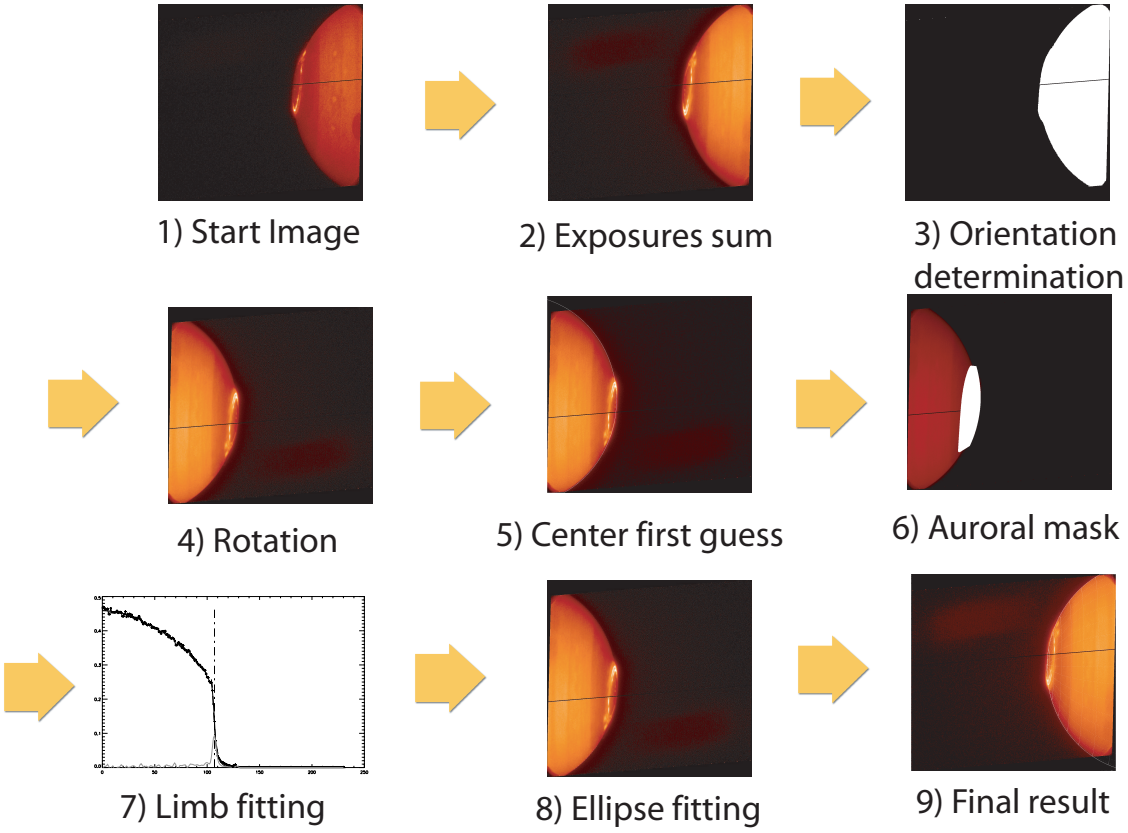

Figure 2.5: Summary of the limb fitting method.

less, the band structure of Jupiter also appears on the UV images[16] (*Vincent et al.*, 2000), even if the contrast between bands is fainter in the UV[17] than in the visible wavelengths. A band fitting procedure has been built in order to detect and measure a potential correction angle for the planetary orientation. In the southern hemisphere, the relatively sharp transition between the polar dark region and the first bright band has been used as a reference. Starting from the angle provided by ephemeris and telescope data, the algorithm projects the region of interest into the longitude-latitude space. The procedure then scans longitudinally the region and detects the maximum of the light curve slope along the meridian lines. These points are fitted linearly and the edges of the best fit line are projected into the image space. These points are then used in order to compute the correction angle directly into the original image. In order to assess and improve the accuracy of the method, a series of test angles are added to the unknown correction angle. If the procedure is efficient, it should be able to detect and measure these additional forced angles. Test angles from +1° to -1° with 0.2° steps have been used. Consequently, the value of the measured correction angle minus the test angle provides another estimation of the actual correction angle. Since the method is not perfect, some fluctuations of the measured correction angle as a function of the test angles remain (see Figure 2.6). Accordingly, the RMS departure of these fluctuations is an estimate of the intrinsic sensitivity of the method on each image and is on the order of 0.1°. The routine selects the mean value of the measured angles minus the test angles.

This procedure has only been tested on images from the 10862 program. In this image set, the mean correction angle is approximately 0.8° clockwise with an RMS deviation around 0.3° (Figure 2.7). The difference with the previous numbers is that here we evaluate the distribution of the measured values over the complete sample instead of the sensitivity on a unique image. These values are quasi-identical for both filters. No evolution has been found between the correction angle and the Day Of the Year (DOY). The deviation or the mean correction angle does not appear to be related to the CML. The root cause of the observed tilt can hardly be attributed to the guide stars inaccuracy because the angle would then be randomly distributed (the guide stars are not identical for each orbit). Inspections of set of images coming

[16]UV WFPC2 observations showed that the bright band correspond to subsidence areas while dark zones correspond to upwellings, contrary to the visible bands.

[17]The contrast between the bands , i. e. $I_d/I_b - 1$ where I_b and I_d are the brightest and the darkest portions of the bands, measured with the F160W filter on WFPC2 lies between 10 and 15% (*Vincent et al.*, 2000).

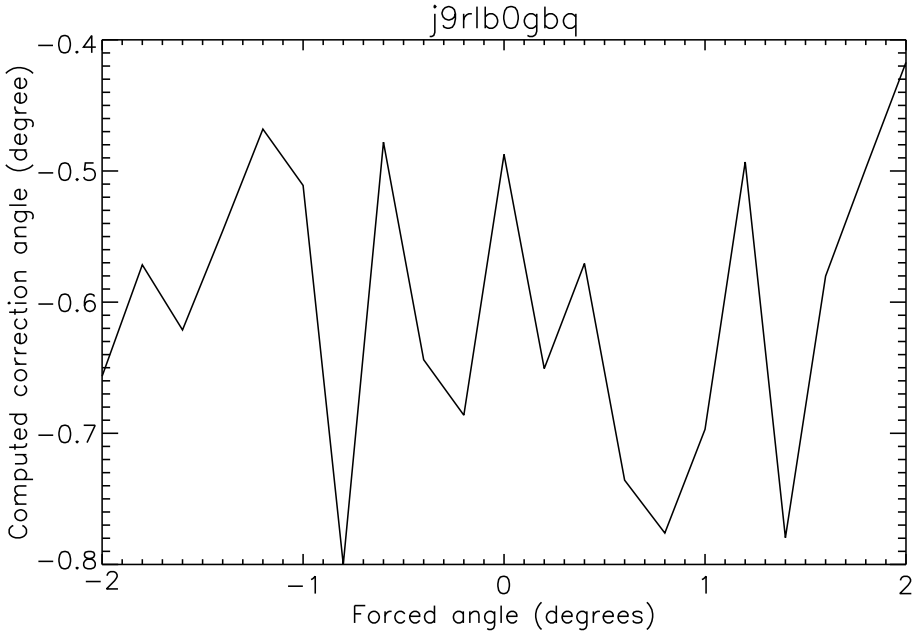

Figure 2.6: Measurement of the correction angle when different arbitrary test angles are introduced and then subtracted from the measurement. The test angles on this plot range from -2° to 2° but this range is reduced from -1° to 1° in the actual routine for computation time reasons. The RMS departure is on the order of 0.1°.

from successive orbits tend to indicate that a part of the departure from the norm could be attributed to intrinsic irregularities of the transition region between two bands. These irregularities are not surprising on these red-leak affected UV images since they are clearly noticeable on visible images (Figure 2.8).

As far as the northern hemisphere is concerned, the limit between the dark polar region and the first bright band is too blurred and cannot be used to detect the orientation angle. Several attempts to fit the maximum of the first bright band have been made, as well as attempts to fit the minimum of the first dark band. The latter provides slightly better results, but only when this band is well visible, that is when the bands are more or less parallel to a border of the image and when this dark band is not too close to the left border because of flat-fielding problems in this area (Figure 2.9). It is nevertheless obvious that none of these methods does provide a reliable estimate of the correction angle. The reason is that the contrast between the bands, their sharpness and their width vary with time and with longitude. This is also not surprising since these variations of the band structures are also obvious on visible images.

In conclusion and in agreement with Saturn observations acquired in 2007, a systematic correction of $0.7°$ to the orientation angle has been applied to every image, either North or South. New geometric correction coefficients have since been released so that the Saturn images acquired and processed since 2008 do no longer suffer from this orientation problem. Comparing the orientation angles indicated in the headers of the raw and rectified images, we see that the angular difference is $\sim 0.6°$. This number is so close from the one deduced from our previous measurements that the complete re-processing of the complete database was found unnecessary.

2.7 The Saturn observation catalog

We have seen above that Saturn images are often used as references when assessing image processing techniques for Jupiter. Indeed, Saturn is another usual planetary target for HST UV instruments. 1563 images have been acquired since 1997 with the WFPC2, STIS and ACS cameras. These observations used exactly the same instruments and the same set of filters as Jupiter images, so that they are processed in the same way. Consequently, we constructed a similar catalog for Saturn observations. This catalog includes observation campaigns 6854 (Trauger), 8158 (Prangé), 8117 (Trauger), 10083 (Clarke), 10862 (Clarke), 11566 (Nichols) and 11984 (Nichols).

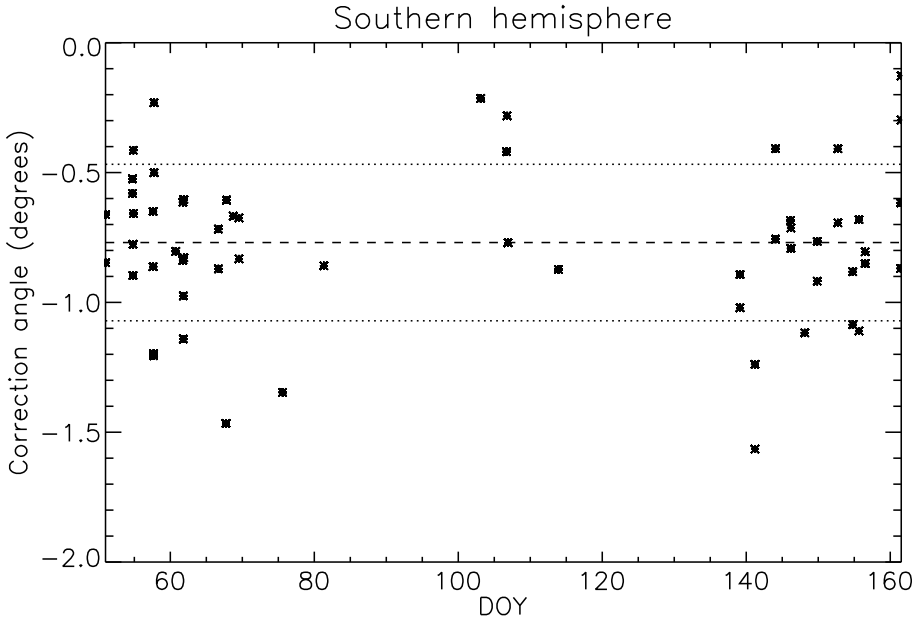

Figure 2.7: Correction angles determined from the orientation of the sharp transition region between the dark polar region and the first bright band for the southern hemisphere. The mean value of this correction is -0.77° (counter-clock wise) and is represented by the dashed line. The root mean square (RMS) deviation from this mean value is 0.3° and is represented by the dotted lines. From this plot we can see no obvious relationship between the correction angle and the Day Of the Year (DOY).

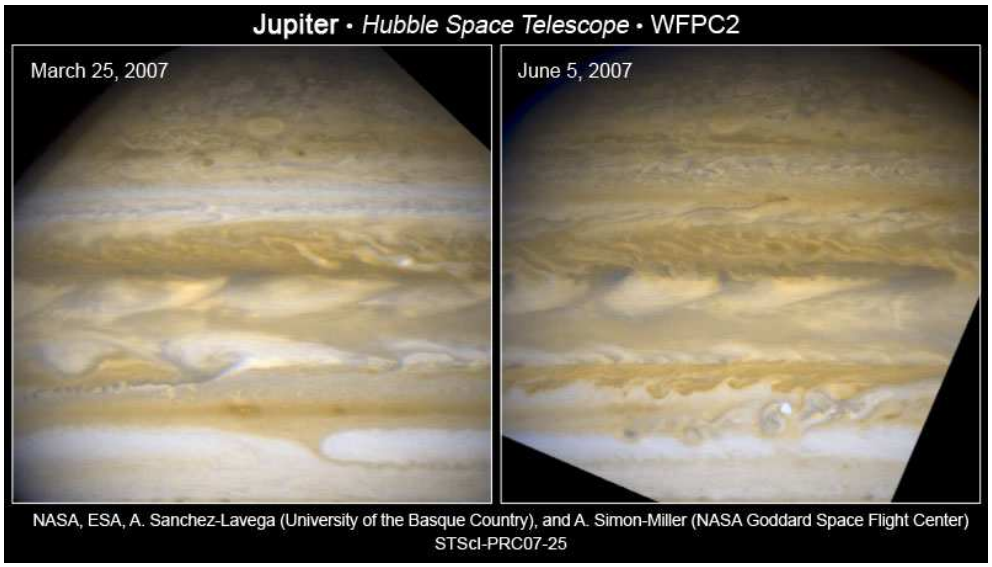

Figure 2.8: Recent WFPC2 images of the Jovian bands in the visible wavelength. It is clearly noticeable that the band contrast is changing with time and that they have sometimes irregular shapes.

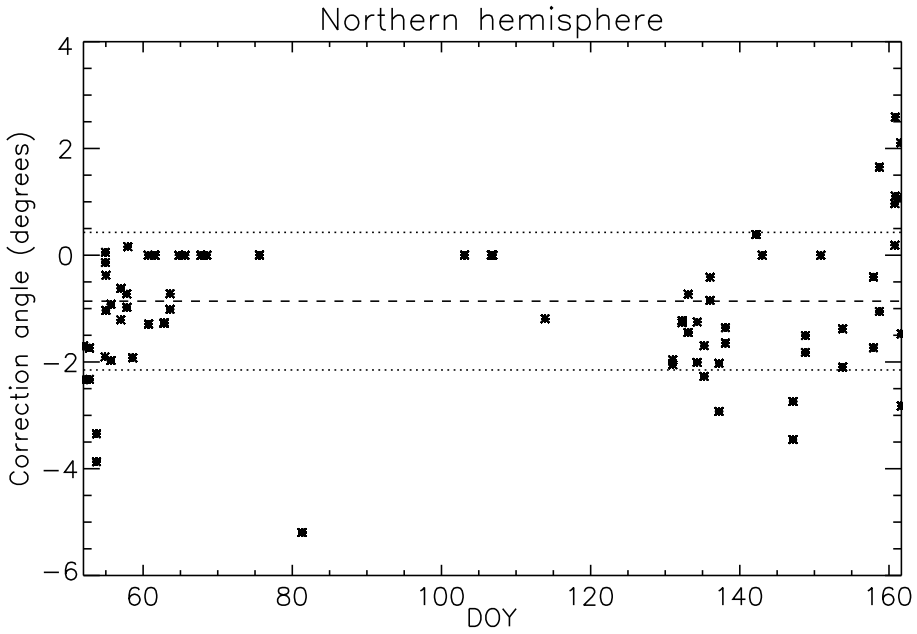

Figure 2.9: Correction angles determined from the orientation of the maximum of the first bright band for the northern hemisphere. The mean value of this correction is -0.86° and is represented by the dashed line. The root mean square deviation from this mean value is 1.3°. According to the scatter of the points on this plot, the results from this method cannot be considered as reliable.

The only differences are the center determination method and the satellite parameters. As mentioned above, Saturn's planetary centers are computed with a ring fitting method developed by Adem Saglam. Catalog fields related to Io, Europa, Ganymede and Callisto have been replaced by equivalent ephemeris parameters for Titan, Enceladus, Dione and Rhea.

2.8 Removing the planetary disk contribution

The planetary disks on STIS ans ACS images mainly originate from reflected sunlight on the planet. A classical method to model these emissions consist in modeling its variations with a generalized Minnaert function (e.g. *Vincent et al.*, 2000):

$$\ln(I\mu) = A + B\ln(\mu\mu_0) + C\ln(\mu\mu_0)^2 + D\ln(\mu\mu_0)^3$$

where I is the observed intensity, μ is the cosine of the observation zenith angle[18] and μ_0 is cosine of the solar zenith angle. This formula is an empirical function initially designed for modeling solar light scattering on the moon and has no particular physical meaning in our case. A careful analysis of the relationship between $\ln(\mu\mu_0)$ and $\ln(I\mu)$ on actual images for a given 1° wide latitude band on Jupiter shows that points on the sunlit side and points on the terminator side of the planet form two different populations (Figure 2.10). Hence, when we consider each population individually, the data points can be fitted with a linear law without the need of higher order terms. The fact that the fitting coefficients differs from the lit side to the terminator side is relatively problematic because it means that the set of coefficients should be re-considered when the angle between the Earth and the Sun as seen from Jupiter changes. For example, the Sun-Earth angle was close to 10° during the first part of the 10862 campaign while is was much closer to 0° degrees during the second one. Figure 2.11 shows an example of the A and B coefficients computed from two images acquired with the F165LP filter for each part of the campaign. When the Sun-Earth angle is close to 0° (dashed line), the behaviors on the lit and the terminator sides are similar, as expected. Similarly, they significantly differ when the absolute value of the angle increases.

The background planetary disks are built by fitting Minnaert coefficients to im-

[18]The observation zenith angle is the angle between the normal to the surface and the observer direction.

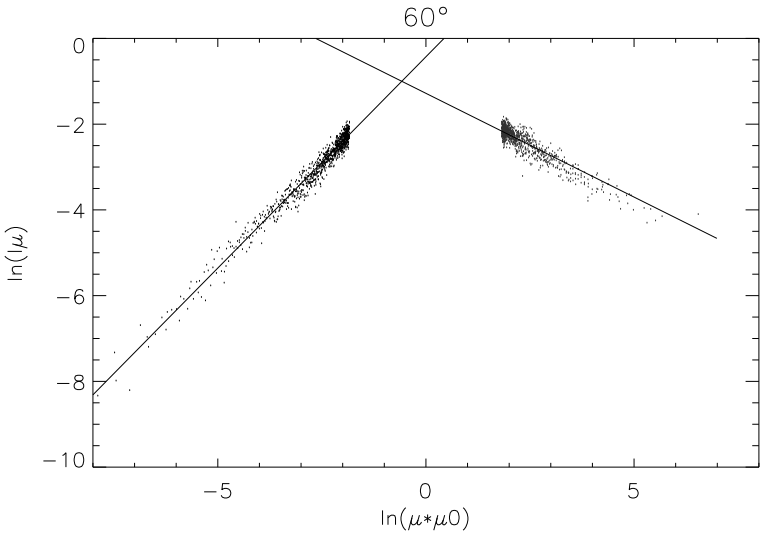

Figure 2.10: Example of the evolution of $\ln(I\mu)$ as a function of $\ln(\mu\mu_0)$. The data points with negative abscissae correspond to the lit side of the planet while points with positive abscissas correspond to the dark side (the sign of their abscissae are artificially inverted). The two sets of points have distinct behaviors which can be separately fitted with a linear law.

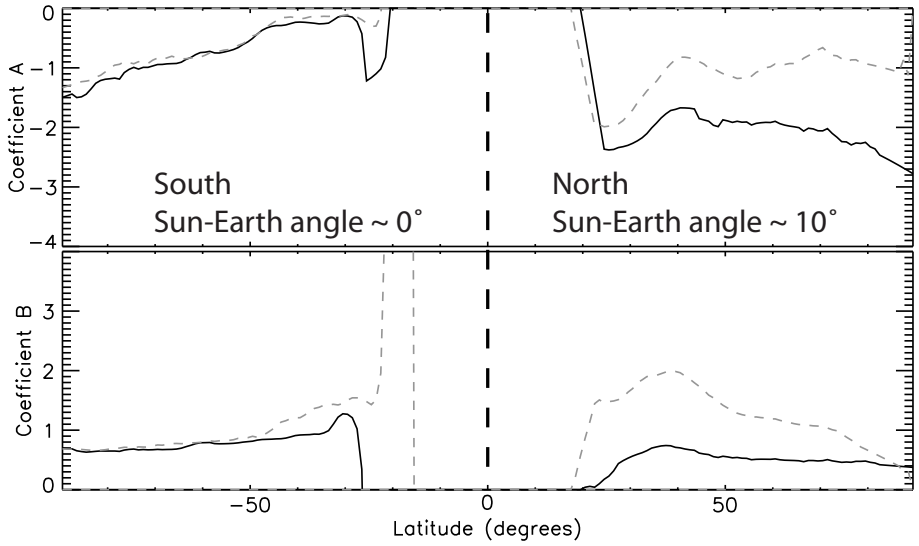

Figure 2.11: Evolution of the A and B parameters as a function of the band latitude for a F165LP filter image. This filter samples longer wavelength than the ones we usually use and is therefore less sensitive to the auroral emissions. The curves on the left part of the image correspond to a configuration where the Sun-Jupiter angle was close to 0° and no large differences are seen between the sunlit (solid line) and the terminator side (dashed line). The curves on the left part of the plot correspond to a configuration where the Sun-Jupiter angle was close to 10°. In this case, the A and B parameters are different for the sunlit and the terminator side.

ages void of any auroral emissions. These "disk only" images are constructed from a combination of real images. The idea is to assemble images where the aurora is located in a different sectors of the planet, through the use of masks hiding the auroral emissions. For example, we can use an image where the auroral emission is concentrated on the dusk side and another where the aurora is concentrated on the dawn side. For each of them, we manually define a mask hiding the auroral emissions. Then we re-size and rotate the second image so that the planetary centers and the orientations coincide (Figure 2.12). Afterwards, we can assemble the "disk only" image: when the brightness is available on both images, we consider the mean intensity, when only one brightness is available because its counterpart is hidden by the auroral mask, we consider this intensity and we discard points where no information is available. This assembled image can then be used to fit the Minnaert coefficients. Since the band intensity varies with latitude, we compute 4 coefficients per 1° wide band: two for the lit side and two for the terminator side. Very high latitude coefficients are usually missing because of the lack of data points. Low latitudes are also usually undersampled or affected by an unreliable flat field correction on the image borders. However, the typical IFP latitudes are always well covered and thus the disk can be removed accurately in these regions.

Based on the particular orientation of each image, a synthetic background planetary disk is generated for each image of the catalog. This disk can then be simply removed from the original image in order to isolate the auroral emissions.

2.9 Epilogue: contributions to the study of Jupiter's and Saturn's aurorae

The catalogs and the data processing techniques discussed above were necessary to study the satellite footprints and Io's auroral signature in particular. However, these techniques have also been used for studies of the giant planet aurorae unrelated to the Io footprint. A detailed description of these results is out of the scope of present thesis, but they nevertheless deserve to be quickly mentioned here.

The availability of a common and standardized catalog for all Jovian UV images, whatever the instrument or whatever the observation campaign, makes comparisons from one dataset to another easier. For example, *Grodent et al.* (2008b) showed that the location of the main auroral emissions as well as the location of the footpath of

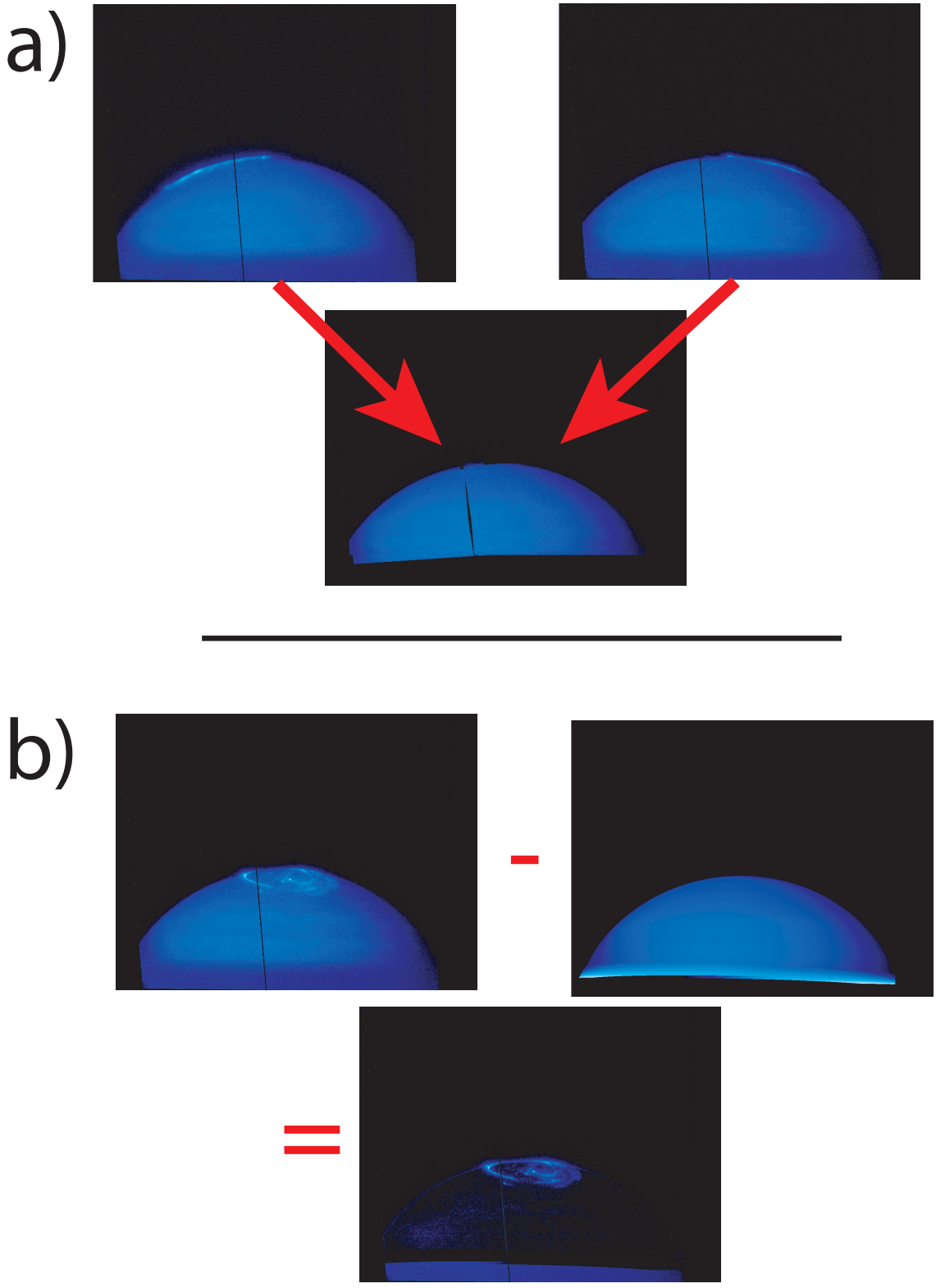

Figure 2.12: In order to determine the Minnaert coefficients, for given epoch and a given filter, we combine two or more images into an assembled image void of auroral emissions (a). These coefficients are then used to generate a synthetic background disk for each image (b).

Ganymede were varying by superimposing polar projection of the auroral emissions from different epoch (Figure 2.13). They showed that variations of the ring current characteristics could explain these changes.

Moreover, the accurate and systematic determination of the planetary center on Jupiter considerably facilitated the localization of the different features on Jupiter and the variation of these positions. Once the planetary centers and orientations are known, polar projections of the auroral features can be automatically computed. The limb fitting procedure presented here made the early production of the complete set of polar projections related to the 10862 campaign possible only a few weeks after the end of the observation campaign, significantly accelerating the production of scientific results. *Radioti et al.* (2008a) used these polar maps to produce statistics of the position of the discontinuity in the brightness of the main oval. This discontinuity has been associated to a reversal of the field aligned currents related to the breakdown of corotation of the magnetospheric plasma. In addition, the same early polar projections enabled the statistical analysis of the polar dawn spots (*Radioti et al.*, 2008b). The polar dawn spots are localized features present in the polar region (i.e. poleward of main auroral oval). Their re-occurrence period of 2 to 3 days strongly suggests that they are associated with internally driven magnetic reconnection in the Jovian magnetotail.

Other interesting auroral features on Jupiter are the faint diffuse emissions observed equatorward of the main oval. A comparison between simultaneous measurements made by HST and the Galileo spacecraft suggests that these diffuse emissions could be linked to the pitch angle distribution boundary(*Radioti et al.*, 2009b). This boundary corresponds to a transition region located in the middle magnetosphere between 10 and 17 R_j and where the distribution of the electron pitch angle changes from pancake to bi-directional.

Finally, the image processing routines and the Saturn catalog have been used to study transient features in the Kronian aurorae (*Radioti et al.*, 2009a). These time-varying emissions are though to be linked to energetic particle injections, similar to the injections thought to trigger the "plasma blob" emissions on Jupiter.

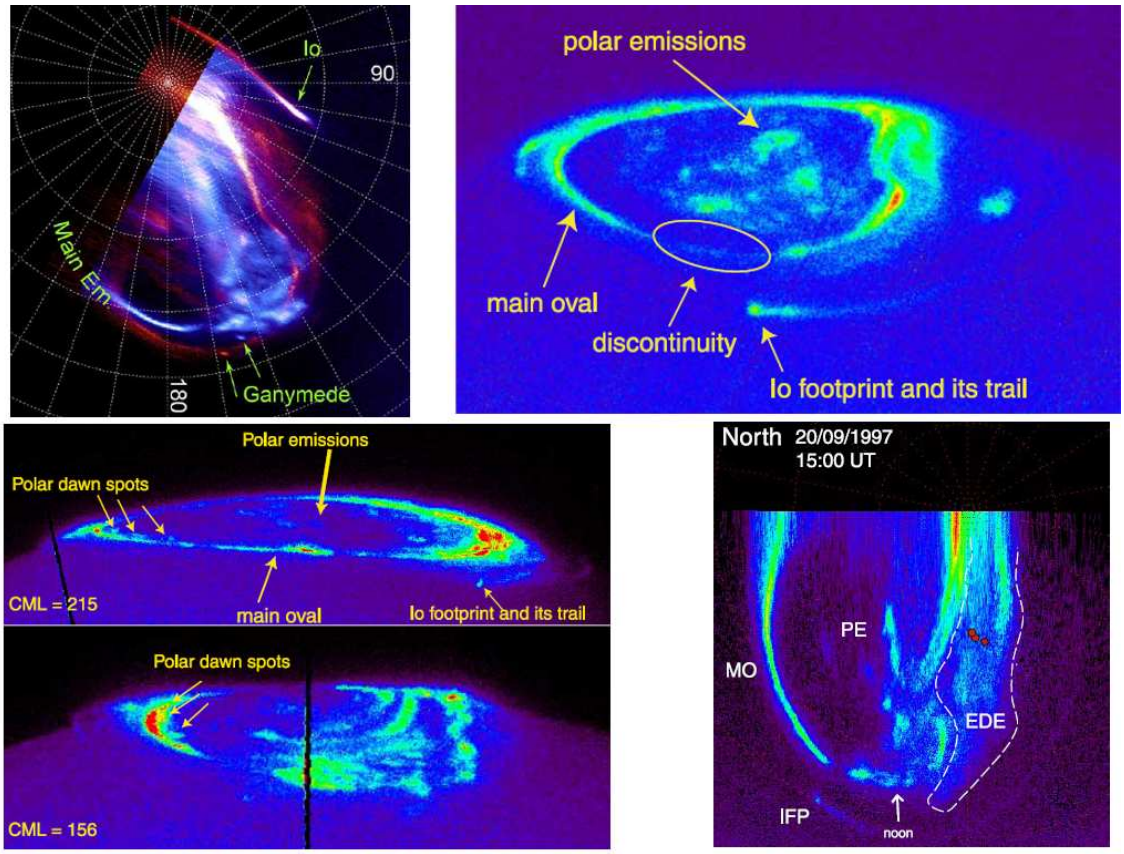

Figure 2.13: (top left) Superposition of two polar projections of the Jovian northern aurora. The red one was acquired in December 2000 with the STIS instrument while the blue one was acquired in April 2005 with the ACS camera. (from *Grodent et al.* 2008b) (top right) Image of the northern aurora highlighting the discontinuity of the main oval. (from *Radioti et al.* 2008a) (bottom left) Examples of polar dawn spots. These spots are though to be related to internally driven reconnections in the Jovian magnetosphere. (from *Radioti et al.* 2008b) (bottom right) Polar projection of a STIS northern aurora image acquired the same day at the time Galileo crossed of the pitch angle distribution (PAD) boundary. The dashed lines isolate the equatorward diffuse emissions (EDE). The red circles represent the projected locations where Galileo detected PDA boundaries and the red diamond represent the expected Ganymede footprint position when Ganymede's System III longitude is 40°. (from *Radioti et al.* 2009b)

Chapter 3

Spots multiplicity

3.1 Introduction to the Io footprint morphology

The first step in our endeavor to understand the Io footprint is the description of its morphology. What does it look like? What is its shape? Is it monolithic or composed of different structures?

The early detections of the IFP described it as a localized spot. When *Connerney et al.* (1993) first identified the Io footprint with the infrared IRTF telescope, they only observed a brighter area equatorward of the main auroral emissions. In the UV domain, *Prangé et al.* (1996) observed a bright spot associated with the Io footprint on one post-COSTAR FOC image. The authors also identified emission forming a faint arc starting from the brightest Io related emission and extending $\sim$20° downstream in the direction of Io's motion. These features, i.e. the bright Io spot and its tail, have later been identified on other images from the same instrument (*Prangé et al.*, 1998). The second generation WFPC2 camera showed a higher sensitivity, allowing an easier identification of the IFP on the images (*Clarke et al.*, 1996). While the FOC images rather showed the IFP as a small spot (with a transverse size of 400 (-200,+100) km) barely larger than the projection of Io along magnetic field lines (*Prangé et al.*, 1996; *Prangé et al.*, 1998), the WFP2 data showed the footprint as a much larger spot (1000 to 2000 km), suggesting that the interaction region in the equatorial plane was not restricted to Io but encompassed a broader region around the satellite. *Clarke et al.* (2002) explained the discrepancy between the two datasets by the lower sensitivity of the FOC instrument that only allowed the detection of the brightest part of the emission.

After identification in the IR and in the UV domains, the Io footprint has also

been detected in the visible domain with the Solid State Imaging camera on board the Galileo probe (*Ingersoll et al.*, 1998; *Vasavada et al.*, 1999). In the day-side of the planet, the strong solar light reflection prevents any observation of visible auroral emissions. Consequently, the visible aurora can only be observed in the night-side of Jupiter, i.e. from an in-situ observatory, contrary to IR and UV images. Nevertheless, the main strength of these observations is their angular resolution, since the one SSI pixel covers from 26 to 134 km on the planet. *Ingersoll et al.* (1998), based on images from the third Galileo orbit, described the IFP as an ellipsoidal spot (300×500 km FWHM) followed by a fainter downstream tail. On the other hand, *Vasavada et al.* (1999), analysed images from the third and the tenth orbits and described the spot more like a circular patch with a diameter of 450 ±100 km. On images acquired during the eleventh orbit, these authors note that the IFP appears as a pair of patches ∼0.5° apart. The estimate of the inter-spots distances as well as the size of the different IFP features on UV images will be described in Chapters 4 and 6 respectively. These visible images provide a crucial indication: the appearance of two spots instead of a single one. Although these observations in the visible provide very interesting information thanks to the original point of view and of the unequaled angular resolution, the available data are scarce and lack sensitivity. Indeed, the next steps forward were brought by the third generation UV camera on board the Hubble Space Telescope.

During the second HST Servicing Mission in February 1997, astronauts installed the Space Telescope Imaging Spectrograph (STIS) instrument. *Clarke et al.* (2002) used this camera to demonstrate that the Io spot was systematically followed, up to 100° downstream, by a faint but extended tail. Additionally, they showed that the bright part of the emission could show two types of morphology: a single spot, sometimes being as large as 15° FWHM in longitude or a pair of spots. Given that the two spots were 12° apart at maximum and that this size corresponds to the extension of the wake of stagnating plasma behind Io, the authors interpreted the IFP morphology, whether the spot is single or dual, as the footprint of the extended interaction region at Io, comprising the wake. Based on the same image dataset, *Gérard et al.* (2006) noticed that the number of spots, as well as the inter-spot distances, evolves with the location of Io in the plasma torus. They showed that the number of spots was larger when Io was away from the torus center. Additionally, they noted that the angular separation between the first and the second spots was decreasing in the northern hemisphere as Io is moving from the northern centrifugal

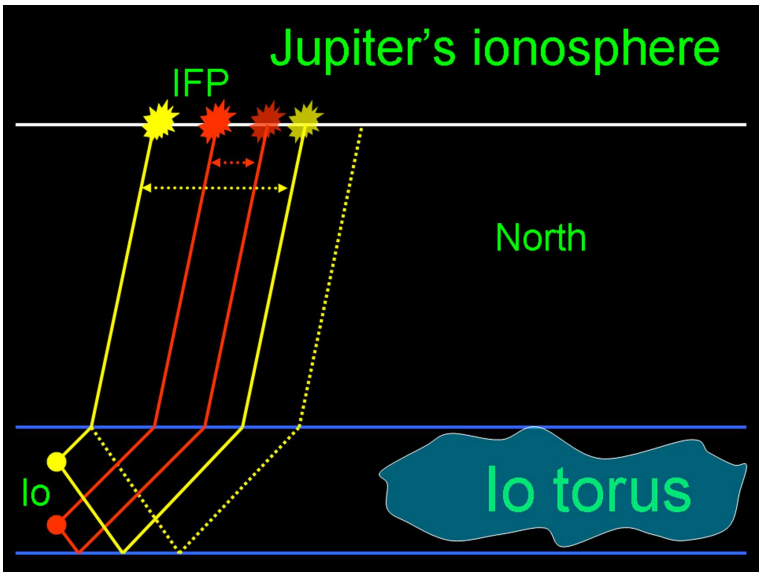

Figure 3.1: Illustration of the evolution of the spots separation in the Alfvén wings reflections scenario. For the northern spots, the inter-spot distance decreases as Io moves southward. (from *Gérard et al.* (2006))

latitudes towards the torus center. Alternatively, the inter-spot distance in the South increases as Io moves from the torus center to the southern most centrifugal latitudes. They attributed this evolution of the angular separation of the spots to reflections of the Alfvén wings on the torus borders. Considering the northern footprint, when Io is in the northern most part of the torus, the direct Alfvén wing immediately escapes from the torus while the reflected Alfvén waves have to cross the torus twice. The resulting propagation delay between the direct and the reflected path leads to a maximum separation angle. As Io moves toward the torus center, the direct wing cross a longer part of the torus while the reflected path length decreases, leading to smaller inter-spot distances (see Figure 3.1). We nevertheless note that the study of the northern footprint was mainly restricted to configurations in which Io has positive centrifugal latitude and vice-versa for the South.

In 2005, a HST observation program[1] of the northern Jovian aurora was executed in order to study a possible magnetic field anomaly in the 100° System III longitude sector. By chance, the Io footprint is clearly visible on some of these images. An intriguing faint emission was observed to prolong the main spot upstream. This faint emission was presented under the name "precursor" by *Grodent et al.* (2005b)

[1] Observation program "10140".

at the MOP meeting at Leicester. We shall see in the next section that these faint emissions, sometimes observed as a detached spot, occur systematically in one hemisphere when Io is in a particular position in the plasma torus. Strictly speaking, a precursor is a message announcing something that will appear later in time. The faint spot we are discussing here does not appear previously to anything, but is just located upstream of the main spot, thus leading the brightest emissions. This is the reason why I consider the expression "precursor" as inappropriate and have replaced it by the term "leading spot".

When the Spring 2007 "10862" observation campaign was designed, *Gérard et al.* (2006) had just highlighted the fact that the Io footprint morphology was varying with the centrifugal latitude of Io. But it was also evident that only half of the possible Io configurations in the Io torus had been observed and that consequently, half of the story was missing. In the northern hemisphere, IFP observations were only available when Io was in the northern part of the torus and vice-versa for the South. One of the only few exceptions were the 2005 images mentioned above.

Even if the core of the "10862" proposal was the measurement of the solar wind influence on the Jovian and Kronian aurorae, the LPAP team strongly insisted to dedicate 10 out the 128 Jupiter orbits to the study of the Io and Ganymede footprints. Therfore these 10 orbits were specially requested to observe the Io and Ganymede footprints in configurations known to be unfavorable for the viewing of the remaining of the aurora. Out of these 10 orbits, 8 were devoted to the Io footprint and 2 to the Ganymede footprint. Given the promising results acquired with the time-resolved time-tag sequences (see *Bonfond et al.*, 2007), but acknowledging that the STIS instrument was out of order since 2004, we chose to reduce the integration time to 30 seconds (instead of 100 for the 118 remaining orbits) in order to enable the study of the short timescale IFP brightness dynamics (see Chapter 7). The next section describes the outcome of this observation campaign and discusses their consequences in terms of interpretation of the footprint morphology and multiplicity.

3.2 Publication: *The UV Io footprint leading spot: A key feature for understanding the UV Io footprint multiplicity?*

B. Bonfond, D. Grodent, J.-C. Gérard, A. Radioti

Laboratoire de Physique Atmosphérique et Planétaire, Université de Liège, Liège, Belgium

J. Saur, S. Jacobsen

Institut für Geophysik und Meteorologie, Universität zu Köln, Cologne, Germany

This article was originally published in the March 2008 issue of Geophysical Research Letters.

3.2.1 Abstract

The electromagnetic interaction between Io and the Jovian magnetosphere generates a UV auroral footprint in both Jovian hemispheres. Multiple spots were observed in the northern Jovian hemisphere when Io was in the northern part of the plasma torus and vice-versa for the South. Based on recent Hubble Space Telescope (HST) measurements, we report here the discovery of a UV leading spot, i.e. a faint emission located ahead of the main spot. The leading spot emerges at System III longitudes between 0° and 100° in the northern hemisphere and between 130° and 300° in the southern hemisphere, i.e. in one hemisphere when multiple spots are observed in the other hemisphere. We propose as one potential mechanism that electron beams observed near Io are related to the generation of the leading spot and the secondary spot in the opposite hemisphere.

3.2.2 Introduction

The first indications of the strong interaction between the volcanic moon Io and the Jovian magnetosphere were discovered in the radio decametric domain (*Bigg*, 1964). The auroral footprints associated with this interaction were first observed in the infrared wavelength (*Connerney et al.*, 1993) and then in the UV wavelength (*Clarke et al.*, 1996).

The perturbation induced by the motion of Io in the plasma torus is thought to propagate along the magnetic field lines mainly in the form of Alfvén waves and being the root cause for the auroral Io footprint (IFP). Whether the Jovian ionosphere exerts a strong feedback (the unipolar inductor), a partial feedback (a mixed Alfvén wings system) or no feedback (the ideal Alfvén wings) on the current system is still an open question (see review by *Saur et al.* 2004). Alfvén waves are slower in the dense plasma torus confined around the centrifugal equator than outside the torus. Consequently, the Alfvén wings and their associate current system are tilted with respect to the background magnetic field. The longitudinal angle between the foot of unperturbed field lines passing through Io and the actual location of the footprint is called the lead angle. Moreover, substantial reflections of the waves are expected to occur where sharp density gradients exist, i.e. at the Jovian ionosphere and at the torus boundaries (e.g. *Wright and Schwartz*, 1989).

Gérard et al. (2006) showed that the footprint brightness depends on the centrifugal latitude of Io. They also demonstrated that the spot multiplicity and the inter-spot distances were directly linked to the position of Io in the plasma torus. The maximum multiplicity and the largest interval between the spots are observed in the northern hemisphere when Io is close to the northern torus boundary (and vice-versa for the South). However, the maximum distance between the first and the secondary spots is $\sim 4^\circ$ while linear Alfvén wing propagation models predict angles around 12° (*Dols*, 2001). Recently, *Bonfond et al.* (2007) reported that fast brightness fluctuations were also observed with timescales of 1-2 minutes in addition to the long timescale variations of the footprint brightness.

Recent observations of the IFP in configurations that had never been observed before reveal a new feature of the UV IFP morphology: a leading spot. Here we describe for the first time a complete set of the Io footprint morphologies and we discuss their interpretation.

3.2.3 Data Processing

This study is based on a comprehensive data base of 2120 high-resolution HST UV images acquired with the Space Telescope Imaging Spectrograph (STIS) and the Advanced Camera for Surveys (ACS) from 1997 to 2007. A total of 1619 images were taken during the HST large campaign in Spring 2007. The STIS camera provided the best angular resolution (0.024468 arcsec/pixels compared to 0.0301 arcsec/pixel

for ACS) while ACS has the best sensitivity. We considered images acquired with the Strontium Fluoride (F25SRF2) and the Clear filters for STIS, and with the F125LP and the F115LP filters for ACS. The F25SRF2 as well as the F125LP filters reject most of the Ly-α emissions, which are largely contaminated by the geocoronal emissions. We applied dark count subtraction, flat-fielding as well as geometrical corrections to every image considered in this work.

3.2.4 Observations

One of the multiple objectives of the recent HST campaign carried out with the ACS camera was to complete the System III (S3) coverage of the footprints. In particular, observations of the northern footprint when Io is close to the southern edge of the torus as well as observations of the southern footprint when Io is close to the northern edge of the torus were missing. We find that images of the IFP in these configurations systematically show a faint emission ahead of the main spot, which we call the leading spot. Figure 3.2 presents an example of leading spot in each hemisphere. Figure 3.3 illustrates the occurrence distribution of the leading emission as a function of S3 position of Io for the northern and the southern footprints. It is seen that the leading spot is present at S3 longitude ranging from 0° to 100° in the North. In this range, Io is located close to the southern edge of the torus. The cases around 10° are more complex to interpret because the viewing geometry is such that the footprint appears near the limb and its emission overlaps the main auroral emissions. In these cases, a careful look of the animation sequences from these image sets reveals a bright spot constantly ahead of the main Io spot. The longitude of the occurrences of the southern leading spot ranges from 130° to 300°. This corresponds to configurations where Io is located northward of the torus. The UV H_2 emitted power of the leading spot ranges from 0.6 GW to 1.9 GW.

The recent ACS observations complete the partial scheme of the UV footprint morphologies shown in Figure 5 of *Gérard et al.* (2006). We extracted 21 pixels wide stripes from the background subtracted images and stretched them in order to display the footprint shape as a function of the longitude mapped to Io's orbital plane. For this mapping, we used the VIP4 magnetic field model (*Connerney et al.*, 1998). The result is shown in Figure 3.4.

The Io footprint multiplicity follows a systematic scheme; when Io is close to the northern edge of the plasma torus, at S3 longitudes around 200°, three spots

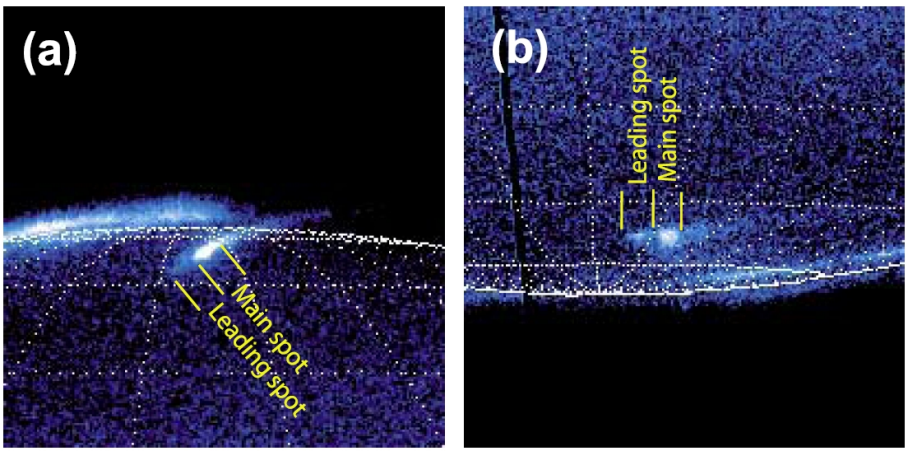

Figure 3.2: Example of leading spot (a) in the northern hemisphere (S3 longitude: ∼50°) and (b) in the southern hemisphere. (S3 longitude: ∼170°)

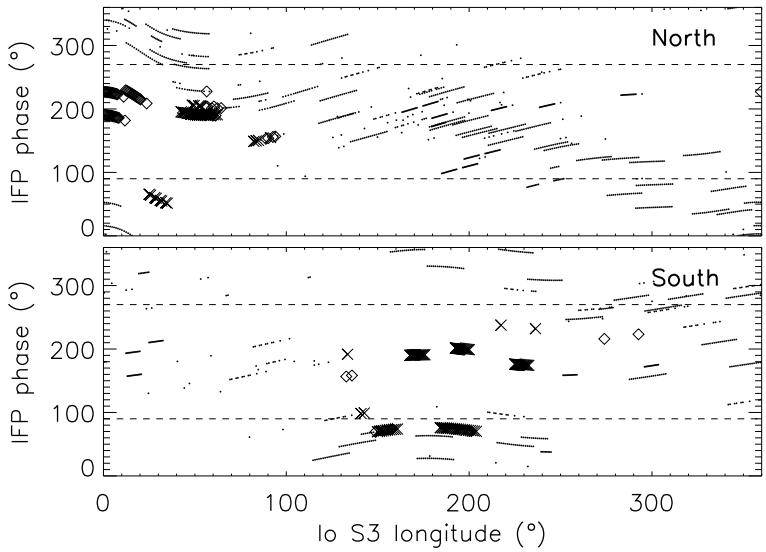

Figure 3.3: Occurrence of the leading spot in the northern hemisphere (Top panel) and in the southern hemisphere (Bottom panel). The dots represent the available observations, the crosses represent the cases where the leading spot is observed and the diamonds represent the uncertain cases.

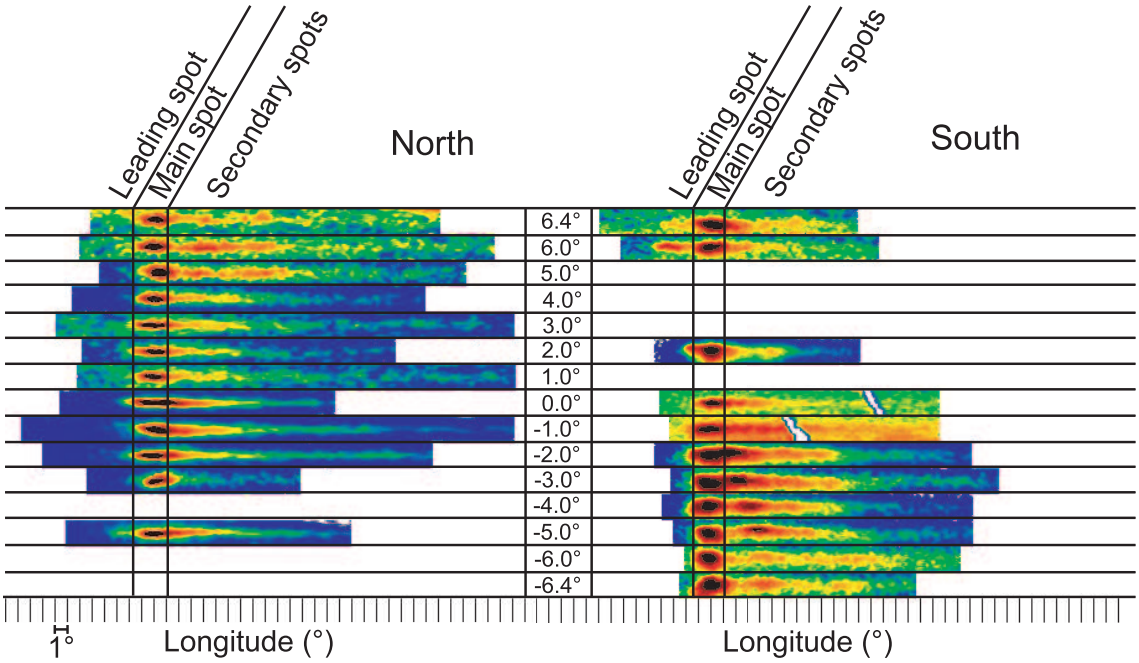

Figure 3.4: Scheme of the Io morphology as a function of the centrifugal latitude of Io in the torus. This Figure completes the scheme of the Io footprint morphologies as a function of the Io centrifugal latitude. The color table of each stripe is scaled individually for a clearer illustration of the morphology. The longitudes are not measured on the planet, but mapped to the equatorial plane along the magnetic field lines according to the VIP4 model for an easier comparison of both hemispheres.

can be seen in the northern hemisphere while a faint leading spot appears ahead of the southern main spot. Similarly, when Io is close to the southern edge of the plasma torus, at S3 longitudes around 20°, three spots clearly stand out from the tail emission in the southern hemisphere. In the North, a faint leading spot appears ahead of the main spot. The second spot in the South is generally brighter than in the North. On the other hand, when Io is located in the center of the torus, i.e. at longitudes around 110° or around 290°, only one bright spot sometimes followed by a fainter one can be seen in both hemispheres and no leading spot is observed.

At a given time, the distance between the leading spot and the main spot in one hemisphere is almost identical to the distance between the first and the secondary spots in the opposite hemisphere. For example, on 5 March 2007, a southern footprint image was acquired at 09:02 UT and then a northern spot image was acquired at 09:10 UT. In the South, the angular separation between the main spot and the leading spot on the planet is about 3.1° when mapped back in the equatorial plane. In the northern hemisphere, the separation between the main spot and the first secondary spot is about 3.4°.

In Figure 3.4 some northern spots appear to be elongated downstream. This effect is caused by limb brightening because of the viewing geometry of these cases. Consequently, these elongations should not be considered as intrinsic. Similarly, some stripes are slightly contaminated by the background auroral emissions (e.g. the top stripe in the North). Nevertheless, this scheme has the advantage of extracting the footprint morphology from the context of the global image for easier morphological comparisons.

3.2.5 Interpretation and discussion

The parallel evolution of the inter-spot distance in both hemispheres suggests that the leading spot and the first secondary spot are related. In this section, we present a possible interpretation of the footprint morphology taking the new observational features described before into account. This interpretation attempts to provide an explanation for three issues that were not solved with the previous interpretation of the footprint multiplicity: 1) the existence of the leading spot and its evolution with the centrifugal latitude of Io, 2) the small maximum inter-spot distance, 3) the bright southern secondary spot.

The main idea driving this interpretation rests on the assumption that the leading

and the secondary spot stem from a common mechanism. The electron precipitation related to the main spot is thought to be associated with upward current carried by the Alfvén wing. It is suggested that the downward segment of the current loop accelerates electrons towards the other hemisphere (see Figure 3.5). These accelerated electrons can then reach the other hemisphere within a few tens of seconds and precipitate into the ionosphere. When Io is close to the northern edge of the torus, the lead angle of the northern IFP is small while the lead angle of the southern IFP is large. Accordingly, the electron beam generated on the northern hemisphere would essentially follow the field lines whereas the Alfvén wing is tilted relative to the background field. Consequently, the beam would reach the southern hemisphere upstream from the southern main spot, creating the leading emission. On the other hand, the northward electron beam would reach the northern hemisphere downstream of the main spot, leading to the first secondary spot.

This scenario is supported by the Galileo spacecraft in-situ measurements of electron beams in the energy range from 100 eV to 150 keV (*Williams et al.*, 1999;*Frank and Paterson*, 1999). The origin of the beams has been attributed to electron acceleration related to the Jupiter-ward part of the current loop, by analogy to similar electron beams observed at Earth (*Mauk et al.*, 2001). These observations first suggested that there exists a direct relationship between these beams and the auroral emissions. However, this hypothesis was later questioned because the electron beams were found unable to carry enough power to generate the observed IFP, given the assumed extent of the beams close to Io (*Mauk et al.*, 2001). In this work we, however, need to compare the electron beam energy with the energy of the faint leading spot. Based on the spectra in *Mauk et al.* (2001), we find that the energy flux contained in the electron beams can deliver $\sim$30 mW/m^2 into Jupiter's ionosphere.The leading spot size on the images is approximately 350×150 km^2, so that the total power reaches $\sim$1.6 GW. Assuming a $\sim$15% efficiency (*Grodent et al.*, 2001), the injected power leads to $\sim$0.24 GW emitted power, on the same order but somewhat smaller than typical values of 0.7 GW for the leading spot. Since the beams have been observed in the center of Io's wake and during polar flybys, the current system might be more complex than illustrated in Figure 3.5. Alternatively, we can consider the energy radiated towards Jupiter by the Poynting-flux, which is distributed over the whole interaction region. This energy is converted, in parts, into electron heating and acceleration. Note, this does not affect the principles of our interpretation since electron beams and Alfvén wings follow different directions (except in the center of

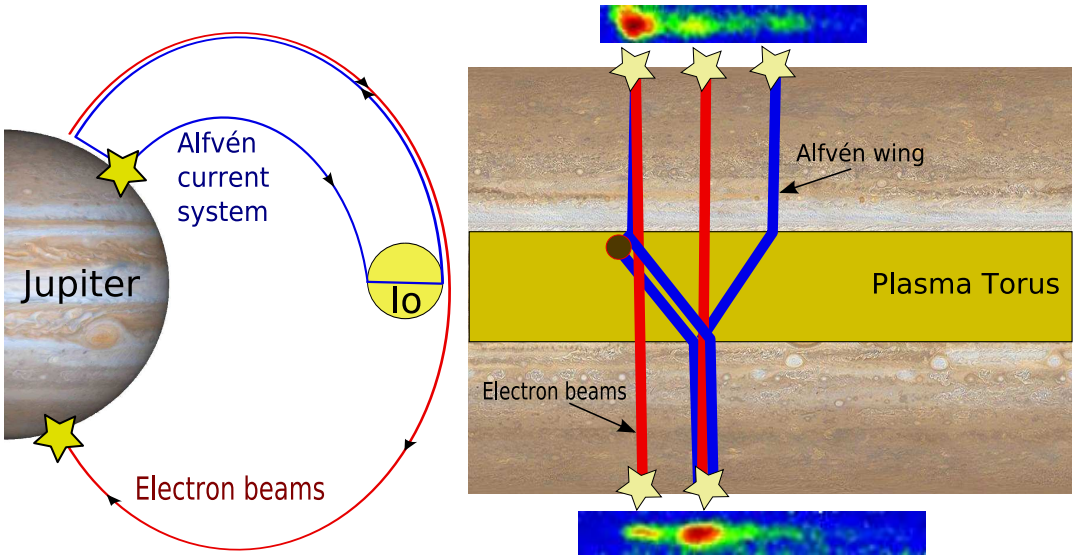

Figure 3.5: Illustration of the suggested mechanism that could explain the presence of the leading spot. The blue line shows the current flowing trough Io, then along the Alfvén wings and finally in the Jovian ionosphere. The electron beams are shown in red and the IFP spots are represented by stars. The left panel is a simplified side view of the conventional Alfvén current system. Some of the beam's electrons can precipitate if their mirror point is low enough, creating the leading spot. The right panel illustrates the geometry of the Alfvén wings propagation and their reflection against the inner boundary of the torus. In contrast to the Alfvén waves, the electron beams are not affected by the high torus density, which enables them to propagate rapidly from one hemisphere to the other, generating the leading and the first secondary spots.

a fully saturated Alfvén wing).

Another argument in favor of this interpretation is the brightness of the second spot in the southern hemisphere, which can sometimes be brighter than the first one. The S3 longitude range where the southern secondary spot is very bright corresponds to the region of weaker surface magnetic field. As a consequence, the secondary spot appears more affected by the surface field strength than the first one. If the pitch angle distribution of the electron beams is larger than the loss cone, as suggested by the Galileo observations, then the decrease of the surface field strength could significantly increase the number of precipitated electrons.

The third spot which is observed in both hemispheres at maximum 12° downstream of the main spot could be the spot related to the Alfvén wing reflection on the plasma torus boundary. Accordingly, the observed angular separation between the first and the third spot would agree with the results of linear simulations based on realistic torus density profiles (e.g. *Dols*, 2001).

Other mechanisms could also explain the structures described above. For example, a possible interpretation could be that the leading spot is actually a faint primary spot. As a result, the feature that we consider as the main spot may be seen as a very bright secondary spot. The intense emission of the second spot compared to first one could stem from constructive interferences of the Alfvén waves predicted by the models describing strong interaction between Io and the torus and modeling the non-linear effects (*Jacobsen et al.*, 2007).

The hypothesis of electron precipitation occurring upstream of the foot of the Alfvén wing has already been proposed by *Queinnec and Zarka* (1998) to explain the weak trailing arc of radio B arcs. These authors suggested that electron leakage on the Alfvén wing could be produced by parallel electric fields associated with the magnetic perturbation. However, it is difficult to link this process with the leading spot because the trailing arc originates from the northern hemisphere while the leading emissions are observed in the South for the same longitude range.

3.2.6 Conclusions

Recent observations of the Io UV footprint in previously unexplored configurations reveal a new feature of the Io footprint. The feature, that we name the leading spot, consists of a faint emission upstream of the main spot and appears in one hemisphere when Io is close the opposite border of the plasma torus. It is suggested that

this leading spot is produced by the same mechanism as the previously described secondary spot. These two spots would not be related to reflection of Alfvén waves on the torus border but would be caused by electron beams generated by downstream currents in the opposite hemisphere. These beams, probably linked to those observed by Galileo, could precipitate in the opposite Jovian hemisphere, creating a spot ahead or behind the main spot depending on Io's location in the torus. This conclusion is supported by the observation that the secondary spot appears brighter in the South when the southern surface magnetic field is weaker.

3.3 Complementary results on the Io footprint morphology

3.3.1 Particular cases

We have seen that the interpretation of the footprint in *Clarke et al.* (2002) as the signature of an extended interaction region or as a combination of different spots like in *Gérard et al.* (2006) or in *Bonfond et al.* (2008) are radically different. *Clarke et al.* (2002) probably based their conclusions on the finding of extremely large single spots. We confirm that such morphologies are indeed observed in some particular cases in the southern hemisphere when Io lies around 120°-140° S3 longitude (Figure 3.6a). However, images of the IFP acquired in the same region but at a different time show a slightly different picture, with a smaller main spot preceded by a tongue of fainter emission and followed by an extended zone of fainter emissions (Figure 3.6b). The longitude range under consideration corresponds to a sector where Io moves northward from the torus center and where we expect the leading spot to slowly emerge from the main one. One possible explanation is that the relative intensity of the different spots can vary from a period to another and we suggest that the extended footprint morphologies are in fact the result of the combination of bright spots close to each other, but unresolved in the STIS images.

3.3.2 The leading spots as seen by New Horizons

A confirmation of the systematic appearance of the leading spot when Io is close to the torus boundary has been presented by *Gladstone et al.* (2007). We have seen that Spring 2007 HST observing campaign was motivated by the simultaneous fly-by

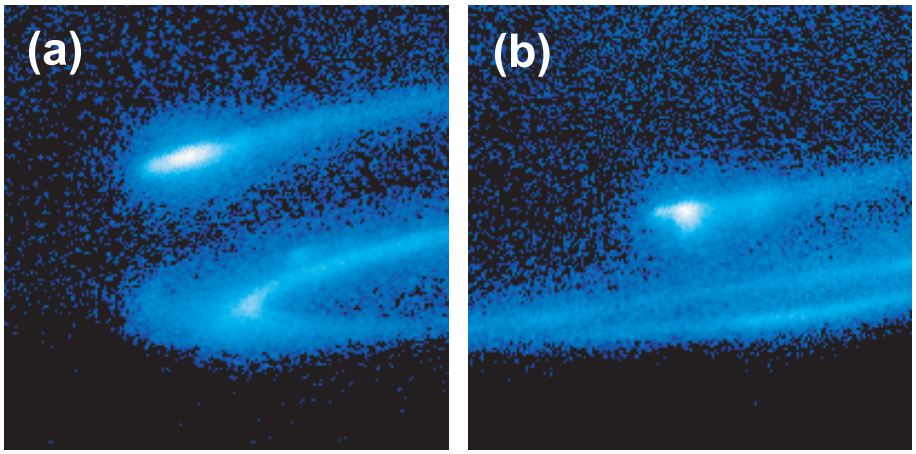

Figure 3.6: Comparison of two observations of the southern footprint in similar configuration. The System III longitude of Io is equal to 132.8° in the first case (a) and to 133.5° in the second case (b). In the first case, the spot appears as a very long but unique spot while in the second case, the main spot is reduced but preceded and followed by fainter emissions.

of Jupiter by the New Horizons probes en route to Pluto. During this fly-by, the LORRI panchromatic camera acquired images of the night side Jovian aurora in the visible wavelength (350 nm to 850 nm). Among these images, one shows a vertically elongated bright spot preceded upstream and followed downstream by two fainter spots. The upstream spot is called "precursor", following the terminology from *Grodent et al.* (2005b). In their study, the authors claim that no UV counterpart of this "precursor" spot can be seen in the HST images. Indeed, HST images have been acquired at the same time but only the Io tail can be seen on them, since the expected Io main spot phase angle is 52° (see table 4.1), that is out of the view of HST. However, HST/ACS images of the southern hemisphere taken when Io was in the same S3 sector clearly show the leading spot in this region. Thus the spots configuration on this LORRI image, including the secondary spot appearing downstream of the main emission, is totally consistent with the the general Io footprint morphology scheme we drew in this chapter.

3.3.3 Epilogue

The data acquired during the large "10862" observation campaign, considerably increased our Io footprint images database and provided us with images of the footprint in previously unexplored configurations. Dedicated observation orbits in

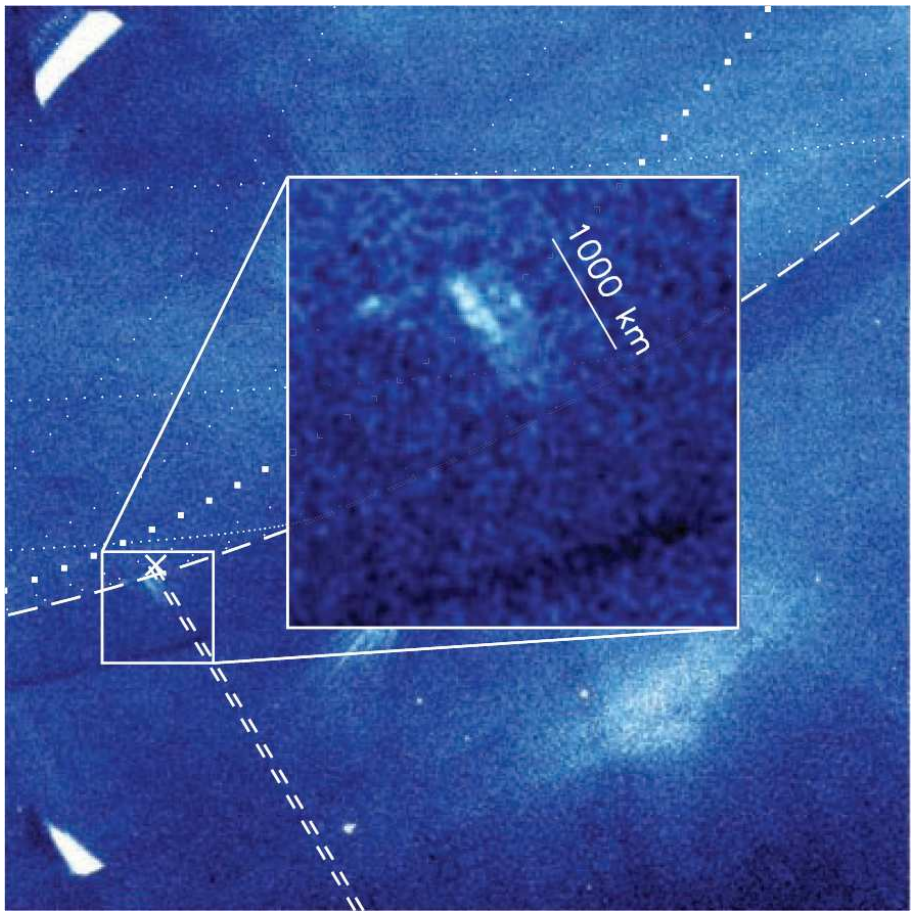

Figure 3.7: Zoom on the Io footprint as imaged by the LORRI pan-chromatic camera onboard the New-Horizons probe. (from *Gladstone et al.* (2007))

the 0° sector in the North and in the 150° sector in the South helped us to confirm and analyze the occurrence of a faint spot appearing upstream of the main Io spot. The coverage of the footprint evolution as a function of the position of Io in the Jovian magnetic field is now almost complete. It has become obvious that the footprint is composed of several spots (at least three), which move with respect to each other, plus a long fainter trail. I shall dedicate a complete Chapter to this later feature (Chapter 5).

It is possibly desirable to clarify here the terminology used in this thesis because there is considerable confusion in the literature. The term footprint is here used to designate the complete signature of the Io-Jupiter interaction in the Jovian aurorae. Depending on the context, Io footprint is used to designate both northern and southern features. For example, when I discuss electron acceleration mechanisms generating the Io footprint, I refer to the footprint phenomenon in general, whatever the hemisphere. However, I also use the term Io footprint to designate the Io-related auroral features in one specific hemisphere, particularly when I describe specific images (see Figure 3.7 for example). Thus, in each hemisphere, the footprint is composed of several spots and an extended downstream tail. The brightest spot is generally called the main spot. The downstream spots in the direction of the planetary rotation are called secondary spots. When a spot appears upstream of the main spot, as justified before, it is called the leading spot. The only exception concerns cases in the southern hemisphere for which one secondary spot progressively and momentarily becomes as bright or brighter than the main one (see Figure 1.8 in the South at -2.68° for example). However, since we can track the variations of the footprint brightness and since it is obvious that the brightness of the second spot is increasing with time, it would not make sense and it would be confusing to shift the appellations from one image to another in these very peculiar cases. These terms are phenomenological names for the different spots, free from any interpretation. It turned out that these names were confusing in the framework of the trans-hemisphere electron beams theory, because secondary spots can have different origins while leading and secondary spots could be caused by the same mechanism. Consequently, we proposed another terminology directly linked to this particular interpretation framework. The spot associated with the direct Alfvén wing is called the Main Alfvén Wing spot (MAW spot), the spot linked to the electron beam is logically designated as the Trans-hemisphere Electron Beam spot (TEB spot) and the spot related to Alfvén wave reflections on the torus boundaries is called the Reflected

Alfvén Wing spot (RAW spot).

Regularly during the short story of the Io UV footprint, new data substantially modified our understanding of the Io-Jupiter interaction. A signature of an extended interaction region or reflections of Alfvén waves cannot (at least not completely) explain the observed evolution of the IFP morphology as a function of the Io location. Consequently, we proposed a new interpretation of the IFP morphology, implying the precipitation of trans-hemispheric electron beams. These electron beams were already known to play a major role in the chemistry of the plasma ionization at Io (*Saur et al.*, 2002; *Dols et al.*, 2008). Our observations suggest that these beams also play a key role in the auroral footprint morphology. We have seen that a strong argument in favor of our new interpretation of the Io footprint morphology is the evolution of the inter-spot distances. The quantitative study of these distances will be the subject of a particular section of the next chapter.

Chapter 4

Spots position

4.1 Foreword

In the previous chapter we addressed the problem of the footprint morphology or, in other words, the problem of its general shape. We saw that the answer to the question "What does the Io footprint look like?" is already telling us a lot about the ongoing processes that connect Io to its parent planet. The footprint is composed of at least three spots (sometimes merged) followed by a long trailing tail. The multiplicity of the spots excludes the simplest unipolar inductor model, but the evolution of the spots position cannot be solely explained by reflections of Alfvén waves. We have proposed a new interpretation to explain the evolution of the IFP morphology and to reconcile the occurrence of the different IFP spots with the observation of electron beams at Io. We now continue our endeavor by answering another basic question: "What is the Io footprint location?". Of course, this question will immediately be followed by a recurrent questioning in this thesis: "What is it telling us about the Io-Jupiter interaction?".

We have seen in the introductory chapter that the Io footprint is a consequence of the interaction between Io and the Jovian magnetosphere and that the perturbation generated at Io propagates along the magnetic field lines convecting along Io. The position of the IFP thus contains two pieces of information. First, whatever the far field interaction model we consider, the IFP is connected to field lines crossing Io's orbit. If we extend this observation to the whole IFP footpath, i.e. the locus of the IFP, and to the other satellites footpaths as well, then we can conclude that any accurate Jovian magnetic field model should link the field lines crossing any satellite orbit to the corresponding footpath. Consequently, the position of the

satellite footprints on Jupiter is of particular importance because they can be used to constrain magnetic field models.

However, all the models describing the Io-Jupiter interaction predict that the footprint is not exactly located at the foot of the unperturbed field lines passing through Io but should lie a few degrees downstream. More interestingly, the different models do not agree on how far downstream the auroral emission should appear, allowing us, in theory, to validate some solutions and discard others. Another precious tool to validate the interpretation of one of the IFP spot as a result of the precipitation of trans-hemispheric electrons is the qualitative estimate of the different inter-spot distances. I will thus extend quantitatively and detail the conclusions that we reached in the previous chapter.

4.2 Satellites footpaths as constraints for improving Jovian magnetic field models

4.2.1 Models of the internal magnetic field

The idea of using the Io footprint location to constrain the magnetic field models appeared very early in the short story of the Io footprint. Indeed, the concept was proposed as soon as 1993 by *Connerney et al.* when they reported the first observations of the infrared auroral signature of the Io-Jupiter interaction. We must admit that the case of the Io footprint is exceptional in the studies of the aurorae. Whatever the planet under consideration, it has always been a considerable challenge to precisely relate phenomena taking place in the equatorial plane of the magnetosphere and their high latitude auroral counterparts. The problem is that we usually do not know the exact topology of the magnetic field, either because of the lack of observational constraints or because it strongly varies with time (or both, of course). In the case of the satellite footprints, if we neglect the lead angles, the connection between a given position in the magnetosphere and its projection on the planets along magnetic field lines is direct. Io, Europa and Ganymede can then be used as landmarks to estimate the mapping of auroral features on Jupiter. For example, *Radioti et al.* (2009b) made use of tabulated Ganymede footprint locations to discuss the mapping of in situ Galileo observations into the Jovian polar regions (Figure 2.13). The argument also works the other way round: *Radioti et al.* (2008a) used the position of Ganymede's footprint to demonstrate that the discontinuity in

the main emission maps to a region farther than 15 Jovian radii.

We should nevertheless distinguish Io from the other moons because they are not exactly located in the same region of the magnetosphere. Io is only $6R_j$ away from Jupiter and lies in the inner magnetosphere. In this region, the internal magnetic field from Jupiter is by far the dominant contributor to the magnetic field topology. Europa and, to a larger extent Ganymede, being respectively 10 R_j and 15 R_j away from Jupiter, lie in the middle magnetosphere. In this region, the magnetodisk becomes a major contributor to the field. The main effect of this disk of rotating plasma is to stretch the field lines away from Jupiter (see Figure 1.3). The magnetic field models are usually constructed as an "onion" to take these various effects into account. The core of the models represents the inner magnetic field and is usually described as a series expension using magnetic multipoles. Then layers are added, modeling the effect of the different currents flowing in the magnetosphere, like the ring current, the magnetopause currents or the cross tail currents (e.g. *Connerney*, 1981; *Khurana*, 1997;*Alexeev and Belenkaya*, 2005). On one hand, the different contributing currents and their related field contributions vary with time, notably owing to variations of the solar wind conditions. On the other hand, the inner magnetic field is supposed to remain relatively stable[1]. Fortunately, since Io is located in the inner magnetosphere, the influence of these external components is weak. The direct consequence of the above considerations is that the Io footprint can be used directly to constrain the inner magnetic field while we would need to take the ring current and its variations into account if we wanted to use the other footprints. For example, *Grodent et al.* (2008b) found significant latitudinal shifts of the northern main emissions and Ganymede footprint emissions when they compared Jupiter auroral UV images spanning nine years of observation[2]. They showed that variations of the current sheet width and density could explain the latitudinal migration of the emissions.

Anyway, the Ganymede and the Europa footprints had not been discovered when *Connerney et al.* released the VIP4 model in 1998. Previous models were based on least squares fits of in situ magnetic field measurements with spherical harmonics

[1]Comparing magnetic field measurements from Pioneer 11 (that flew by Jupiter in 1974), from Voyager 1 (fly-by: 1979) and from Ulysses (fly-by:1982), *Connerney et al.* (1996) did not notice any significant secular variation of the Jovian internal magnetic field parameters. On the contrary, *Russell et al.* (2001) reported a possible change of the magnitude of the dipole moment on the order of 1.5% from 1975 to 2000 based on Galileo measurements.

[2]The latitudinal variations were respectively on the order of 3° for the main emissions and 2° for the Ganymede footprint.

models. This time, the authors gathered enough IFP position datapoints both from IR and UV observations to reasonably cover the Io footpaths from both hemispheres. In order to find the best model to fit the observations, *Connerney et al.* (1998) computed the radius r_e at which a field line starting at an observed footprint location intercepts the jovigraphic equator for each iteration step. They then used a generalized inverse technique to determine the best 4th degree and order multipole model that simultaneously minimizes the quantity $r_e - r_{Io}$ ($r_{Io} = 5.9R_j$ being the Io's orbit radius) and fits in-situ measurements of the magnetic field from the Pioneer 11 and Voyager 1 spacecraft. Note that the only constraint is that the relevant model field lines reach Io's orbit, but the projected IFP positions are not constrained in longitude. High order terms in the multipole development of the magnetic field essentially affect the surface magnetic field but their influence weakens as the radial distance increases. Consequently only third order and degree terms where constrained by in-situ measurements from Pioneer 10 and 11, Voyager 1 and 2 or even Ulysses probes (e.g. *Connerney et al.*, 1996). Since the IFP projections along modeled field lines provide some information on the surface field, the VIP4 model resolves all but three of the fourth order terms. Of course, a natural consequence of these improvements is that the projection of the Io orbit back to the northern and southern ionospheres is in much better agreement with the IFP data points (Figure 4.1). We should note that the model described in the *Connerney et al.* (1998) paper is composed of two parts: the fourth order and fourth degree spherical harmonic model representing the internal Jovian magnetic field and the magnetodisk magnetic field model described in *Connerney* (1981). The authors applied this two part model to derive expected footpaths for Amalthea as well as for Europa and Ganymede.

Europa and Ganymede footprints have been formally identified in STIS images by *Clarke et al.* (2002) and the large Spring 2007 HST observation campaign considerably increased the available database. *Grodent et al.* (2008a) systematically measured the Io, Europa and Ganymede footprints position and built partial reference contours for these satellites. While the VIP4 predicts contours which are essentially parallel to each other, it is obvious that the observed footpaths diverge from each other in the longitude range from 80° to 150° (Figure 4.2 left). Additionally, images show a hinge in the northern Io tail around 110° longitude that is not reproduced by the VIP4 model. The authors noted that neither the divergence of the footpaths nor the presence of the hinge can be reproduced through a modification of spherical harmonics parameters of order ≤ 4. Additionally, the

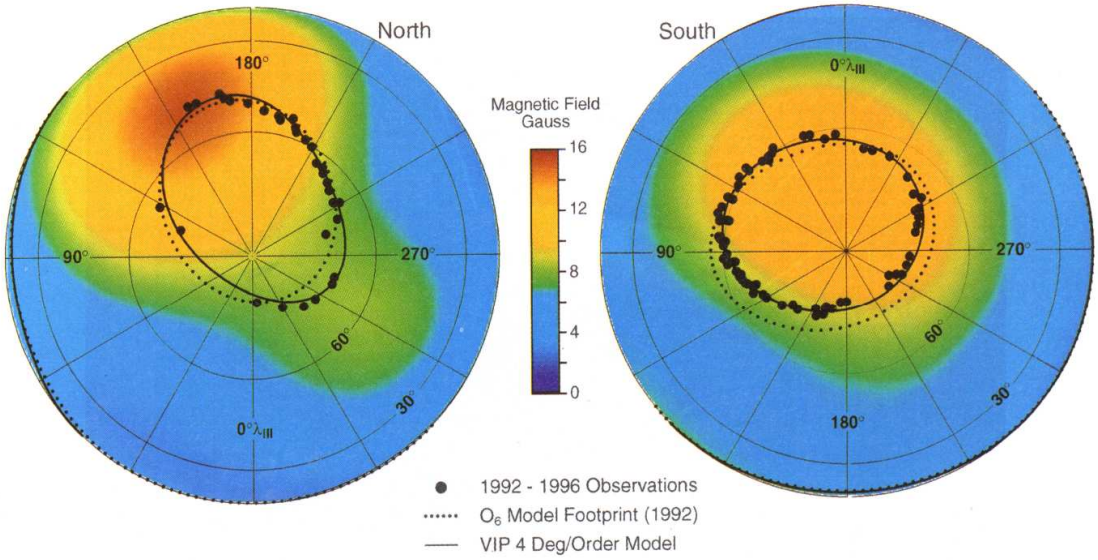

Figure 4.1: Orthographic polar projections of the surface field strength in the northern and southern hemisphere according to the VIP4 model. The polar projection of the Io orbit along the field lines as well as the footprint locations used to build the model are also represented. The projection of the Io orbit along the field lines according to the older O6 magnetic field model is also shown as dashed lines. We can see that the use of Io footprint as a constraint considerably improves the accuracy of the mapping (from *Connerney et al.*, 1998).

potential changes on these parameters should not affect the southern footpaths too much since such a divergence is not observed there. They proposed a novel solution to reproduce the northern footpaths: in addition to modified 3rd and 4th order parameters, their model also encompasses an off-centered dipole situated below the hinge region. Solutions of this kind are not unique and the authors indeed propose two different positions for the dipole that would equally be in accordance with the data. It should also be noted that these two perturbed models are only constrained by northern hemisphere data and do not fit the southern hemisphere footpath. One final comment on these models: the new surface magnetic field maps considerably differ from the VIP4 results (Figure 4.2 right). This observation calls for caution when correlating auroral or low altitude magnetospheric quantities to the magnetic field strength, whatever the model in use.

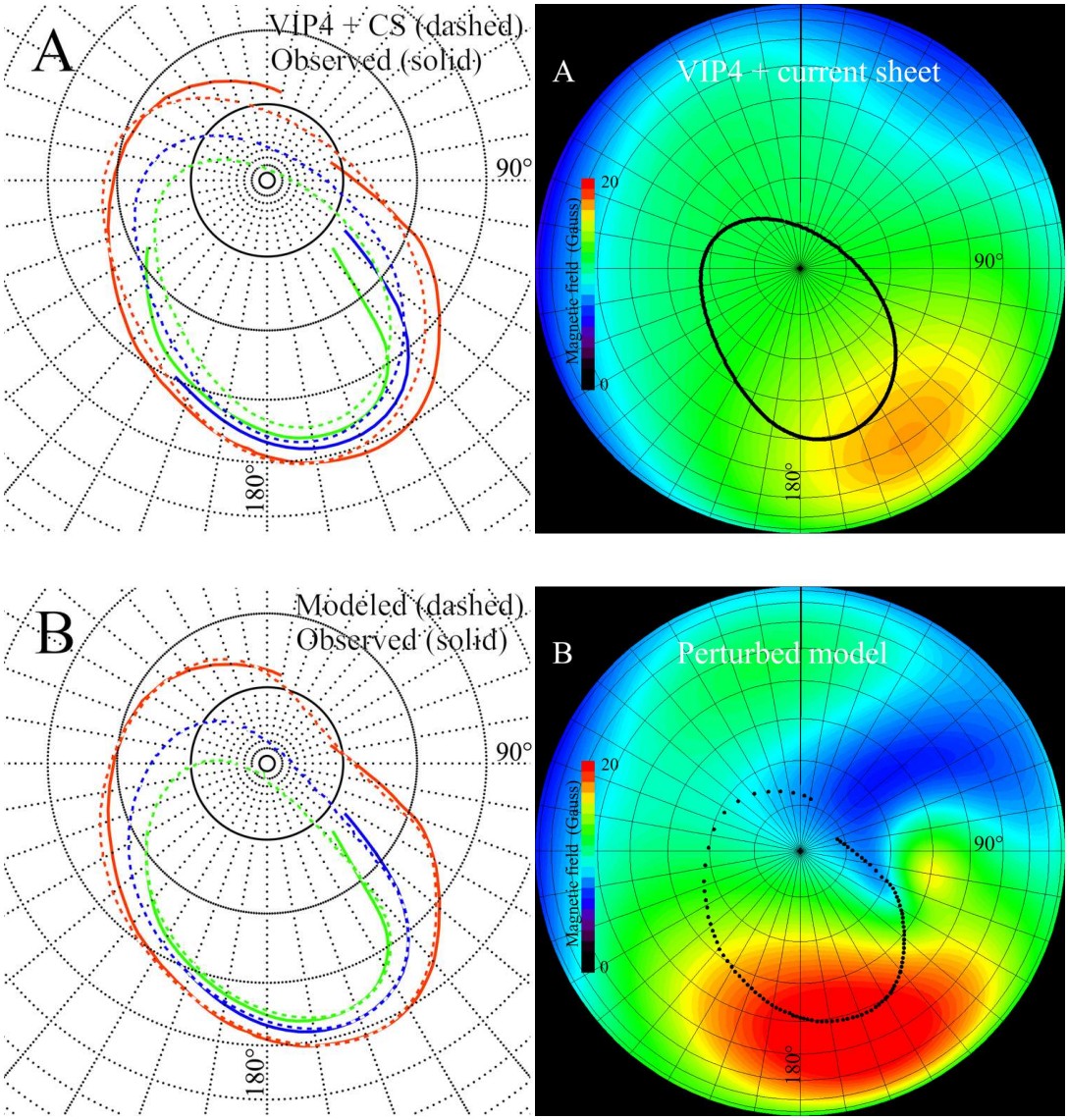

Figure 4.2: (left) The solid lines correspond to the observed contours for the Io (red), Europa (blue) and Ganymede (green) footprints in the northern hemisphere. The colored dashed lines are the projection of the satellites' orbits along the field lines from the VIP4 model (top) and the new model composed of a multipole + a dipole (bottom). It can be seen that the divergence of the observed footpaths is not reproduced by the VIP4 model. (from *Grodent et al.*, 2008a) (right) Polar map of the surface magnetic field intensity for the VIP4 model (top) and one of the alternative models perturbed with an additional dipole (bottom). Both models assume the same magnetodisk model (from *Grodent et al.*, 2008a).

4.3 Location of the Io footprint spots: key observations for validating the interaction models

Most of the material presented in the following section has been published by B. Bonfond, D. Grodent, J.-C. Gérard, A. Radioti, P.A. Delamere, V. Dols and J.T. Clarke under the title: *The Io UV footprint: Location, inter-spot distances and tail vertical extent* in Journal of Geophysical Research - Space Science (*Bonfond et al.*, 2009).

4.3.1 Introduction

The root cause for the Io-Jupiter interaction is the motion of Io with respect to the plasma torus, which generates Alfvén waves propagating along the magnetic field lines that connect Io's neighborhood and Jupiter (see review in *Saur et al.*, 2004). The propagation of these waves has been historically described by two competing models. The first proposed model is called "the steady state unipolar inductor model"(*Goldreich and Lynden-Bell*, 1969) at a time where the existence of neither the Io atmosphere nor the plasma torus had been observationally established. The electric current flowing through Io's atmosphere propagates along field lines to the northern and southern ionospheres of Jupiter, where it closes via the locally horizontal Pedersen current, thus forming a current loop connecting the satellite to the planet. The basic assumption of the model is that an Alfvén wave created at Io would be fast enough to reach the ionosphere of Jupiter and bounce back to intercept Io, establishing this steady current loop. The discovery of the dense plasma torus encompassing the orbit of Io challenged the assumptions of the unipolar inductor model. The high plasma density would slow down tremendously the propagation velocity of the Alfvén wave originating from Io. If this wave retardation is large enough, then, by the time the wave is reflected from Jupiter's ionosphere back to the torus, Io would have had time to slip free from the magnetic flux tube which intercepted it at the time the wave was originally launched.

Consequently, the interaction in this picture is better described in terms of propagation of MHD Alfvén waves which form ideal Alfvén wings. This type of wave carries a current approximately field-aligned, which does not require a closure in Jupiter's ionosphere (*Neubauer*, 1980). Detection by the Galileo spacecraft of a quasi-stagnated flow in the wake of Io, within half an Io radius of the surface (*Frank*

et al., 1996), regenerated interest in the unipolar inductor model in the literature: because of the strongly retarded flow, the Alfvén wave launched at Io could have the time to bounce back from the ionosphere and return to Io, which is the scenario of the unipolar inductor. Several authors recently proposed a formalism where the Alfvén wing model and the unipolar inductor are the two extreme cases of the same interaction (*Crary and Bagenal*, 1997; *Pontius*, 2002; *Saur*, 2004].

In principle, careful observations of the location of the Io spot could determine whether the interaction is better described with either the unipolar or the Alfvén framework, or a potential mix of the two. The distance between the observed IFP auroral emission and the instantaneous projection of Io on the Jovian ionosphere along the field lines is called the "lead-angle". The unipolar inductor model predicts a large lead angle $\geq 12°$, depending on the conductivities of Io and Jupiter but not on the location of Io in the torus. The Alfvén wave model predicts a smaller lead angle $\leq 6°$, independent of the Jovian conductivity but strongly dependent on the local plasma properties through which the Alfvén wave is traveling. Consequently the Alfvén wing model is strongly dependent on Io's latitudinal location in the torus. In both cases, the IFP is expected to occur downstream (along the direction of planetary rotation) of the position of Io as mapped along undisturbed magnetic field lines.

The first estimates of the lead angle were based on IR images and on the O6 magnetic field model (*Connerney et al.*, 1993). They suggested that the lead angle was independent of Io's System III longitude and was as large as 15-20°. These results were in favor of the unipolar inductor. However, *Clarke et al.* (1996)(1998), *Prangé et al.* (1998) and more recently *Gérard et al.* (2006) showed lead angle measurements based on HST FUV observations and on O6 or on VIP4 magnetic field models (*Connerney et al.*, 1998) indicating that the lead angle could vary with Io's longitude and even attain negative values. This later result is particularly puzzling since no model predicts an upstream bending of field lines nor a perturbation which propagates against the rotation of ambient magnetospheric plasma. The occurrence of lag angles was attributed to the lack of accuracy of the magnetic field longitudinal mapping. The VIP4 magnetic field model and its later improvements by *Grodent et al.* (2008a) are built in such a way that the mapping of the Io orbit along the field lines is constrained to fall on the locus of the IFP as seen on IR or UV images (the IFP reference contour). This method brings substantial improvements compared to earlier models which relied only on in-situ magnetic field measurements in the

equatorial plane. However, the longitude along the reference contour is not constrained by the observations. If the magnetic field models were directly linking Io to its northern and southern footprints by construction, then measurements of the lead angle would be meaningless. Nevertheless, it is not clear whether the absence of such a constraint provides more significant information.

Another method to determine the lead angle is based on measurements of the inter-spot distances. If the Alfvénic perturbations remain small compared to the ambient field, then the lead angle is directly linked to these distances. The relationship between secondary spot positions and Io's centrifugal latitude (i.e. latitude with respect to the rotational equator) was first suggested to be caused by reflections of the Alfvén waves on the torus boundaries (*Gérard et al.*, 2006). In this case, the maximum lead angle is expected to correspond to half of the maximum inter-spot distance. However the recent finding of a faint spot appearing upstream of the main emissions puts this interpretation into question. An alternative explanation assumes that the upstream or downstream secondary spots are caused by electron beams originating from the opposite hemisphere (*Bonfond et al.*, 2008). According to this trans-hemispheric electron beams model, when Alfvén waves dissipate their energy in the form of electron parallel acceleration, most electrons are accelerated towards the planet, creating the main Io spot. Part of the electron population, however, is accelerated towards the opposite hemisphere in the form of electron beams. Since these electrons are essentially undisturbed by the torus plasma (unlike the Alfvén waves), they may precipitate upstream or downstream of the other hemisphere's main spot depending on the Io centrifugal latitude. Three spots are defined in this framework: the Main Alfvén Wing spot (MAW spot), the Trans-hemispheric Electron Beam spot (TEB spot) and the Reflected Alfvén Wing spot (RAW spot). Accordingly, the maximum inter-spot distance between the MAW spot and the TEB spot would provide a good estimate of the maximum lead angle. Nevertheless, other models considering a stronger interaction do not predict such obvious relationships between the inter-spot distance and the lead angle. It is not clear how a pure unipolar model could explain the multi-spot structure and the systematic variation of the inter-spot distances. However, *Jacobsen et al.* (2007) suggested that strong non-linearities could trigger wave interference patterns leading to the occurrence of multiple spots and depending on Io's location in the torus.

The large Hubble Space Telescope (HST) campaign dedicated to Jupiter's aurora in Spring 2007 brought a wealth of new data concerning the IFP. Here we describe

the careful determination of the footprint location. We define a new IFP reference contour, and measure the lead angles as well as of the inter-spot distances on an unprecedented longitude coverage.

4.3.2 New Io reference contours

IR and UV observations have shown that the IFP follows a fixed path in S3, called the IFP reference contour. In order to fully determine this contour in each hemisphere, we need images of the IFP spanning all Io S3 longitudes. In previous HST campaigns, the observing geometry was mainly constrained by the visibility of the main auroral emission, systematically leaving some configurations unexplored. The latest ACS observations now fill most of these gaps and provide the missing data points. *Grodent et al.* (2008a) used this more complete ACS dataset to build reference contours for Io, Europa and Ganymede in the northern hemisphere by manually selecting the location of the footprint spots and Io's tail on the images. Following *Grodent et al.* (2008a), we assume the manually selected spots to be located 700 km above the 1 bar level. These observations include configurations where the IFP lies very close to the planetary limb, leading to large inaccuracies. The problem is particularly pronounced in the 350-100° Io S3 sector, where the reference contour does not seem to form a closed curve according to the simple polar projection of the observed footprint location (see Figure 1 in *Grodent et al.* (2008a)). In order to increase the accuracy of the IFP localization in this critical sector, we take advantage of the fact that our observations were designed to acquire images in the same Io S3 longitude but for different local time configurations. The Io S3 longitude difference tolerance between the two observations is as low as 0.25°, which is less than one third of the S3 longitude range covered by Io in 100 s. This means that, for each pair of images, Io is almost in the same position with respect to the Jovian magnetic field, but the footprint is seen from different points of view (with respect to the Jupiter-Earth line of sight). Assuming that the IFP is located exactly at the same place on both images[3], we determine the longitude/latitude couple that minimizes the distances in pixels between the computed point and the manually selected pixel on both images. The new IFP location typically lies within 2-3 pixels of the originally selected position. For example, the uncertainty on the IFP location around 0° Io S3 longitude, which was as large as 5° based on single images,

[3]I.e. assuming that local time and temporal effects are negligeable.

is now reduced down to $\sim 2°$ in longitude and $\sim 1°$ in latitude. In the sectors where such image pairs exist, we only take these new points into account (pale grey triangles in Figure 4.3). In sectors where images pairs are missing, we consider spot locations (dark grey diamonds) or tail locations (black crosses) derived from unique images. We are now in position to construct a new reference contour with a more realistic closure in the northern 30-60° Io S3 longitude range (Figure 4.3 left and Table 4.1). The agreement between our reference contour and the footprint positions measured on high resolution images (from 25.7 km/pixel to 133.7 km/pixel) in the visible wavelength by Galileo (*Vasavada et al.*, 1999) is convincing. We note that, in the North, our reference contour mainly differs from the VIP4 Io contour in the region influenced by the magnetic anomaly between 100 and 180° longitude. Some significant differences also arise between 210° and 290°.

As far as the southern hemisphere is concerned, the Io S3 coverage gaps were even wider than in the North. Most of them are now filled, making it possible to draw an updated southern Io footpath reference (Figure 4.3 right and Table 4.1). The agreement between the VIP4 Io contour and our reference contour is better in the South. Our footpath only lies a few degrees equatorward from the VIP4 contour near 0° and near 90°. Finally, we note that the two contours have very similar lengths: ∼173000 km for the North and ∼167 000 km for the South.

4.3.3 Lead angle and inter-spot distances

Now that we have an accurate relationship between the orbital longitude of Io and the corresponding position of the main IFP spots, computing the lead angles is relatively straightforward provided we have an accurate magnetic field model. In addition to the VIP4 model, we also used the second multipole + dipole model from *Grodent et al.* (2008a) in the North for comparison. It should be noticed that, where the northern contour is very close to the pole, a small distance on the planet corresponds to a large interval when expressed in terms of longitude. Moreover, measuring the longitudinal shift directly on the planet does not enable us to meaningfully compare values from opposite hemispheres nor to verify theoretical predictions since these usually implicitly assume an axisymmetric magnetic field. Consequently, in order to avoid these geometrical effects due to the shape of the contours, we provide measurements of the *equatorial* lead angles. Thus, contrary to *Clarke et al.* (1998) and *Gérard et al.* (2006), we do not magnetically map the

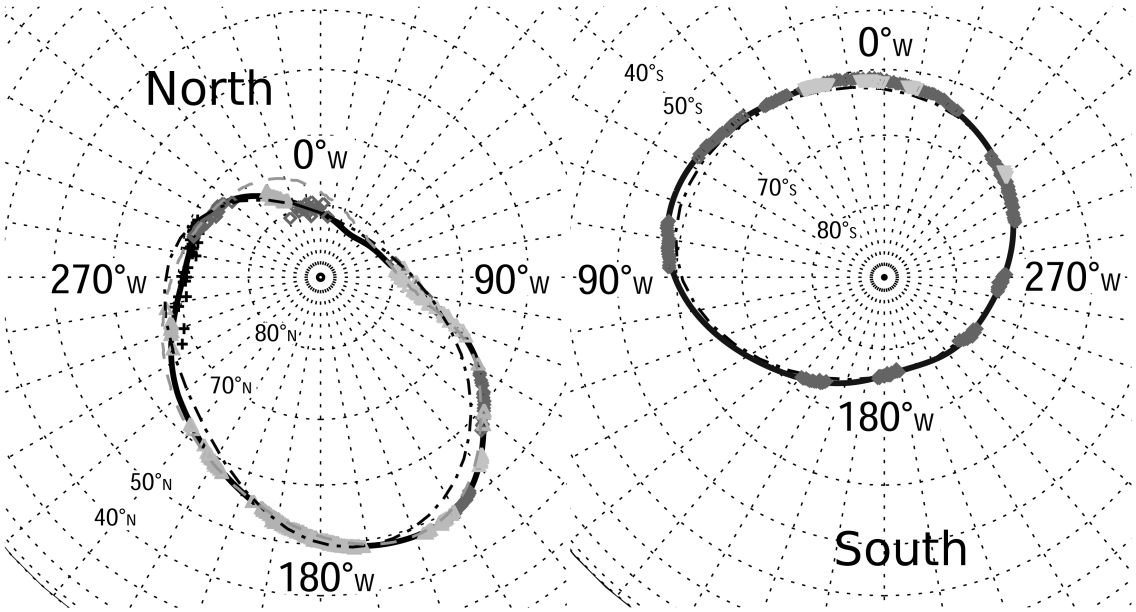

Figure 4.3: Planeto-centric polar projection of the Io reference contours for the northern and the southern hemispheres. The triangles represent IFP locations computed from coupling two images. The rhomboids represent IFP locations deduced from a unique image. The black crosses represent points selected in the IFP tail. The black dash-dotted line is the IFP contour from the VIP4 model, the dashed grey line is the IFP contour from the second model described in *Grodent et al.* (2008a) and the thick plain black line is the best fit to the data points.

Io S3 Longitude (°)	North IFP Longitude (°)	North IFP Latitude (°)	South IFP Longitude (°)	South IFP Latitude (°)
0	-32.0±2	76.9±1	5.1±1	-61.4±1
10	-22.6±5	78.5±1.5	14.1±1	-61.0±1
20	-2.1±7.5	81.0±2	23.2±1	-60.6±1
30	32.7	82.7	32.2±1.5	-60.1±1
40	70.7±3	81.4±2	40.9±1	-59.3±1
50	96.9±2	77.0±1.5	49.2±1	-58.5±1
60	110.1±1	69.3±1.5	56.9±1	-57.7±1
70	118.6±1.5	64.3±1	64.1	-57.3
80	126.3±1.5	60.9±1	71.0	-57.3
90	132.6±1	57.9±1	77.8±1	-57.7±1
100	137.7±1	55.0±1	84.5±1	-58.6±1
110	142.1	52.6	91.3	-60.0
120	145.8±0.5	50.8±1	98.3	-61.8
130	150.0±0.5	49.5±1	105.5	-63.8
140	154.5±0.5	48.8±1	113.2	-66.0
150	158.4±0.5	48.6±1	121.8	-68.1
160	162.7	48.7	131.6	-70.2
170	168.1±0.5	48.9±0.5	143.3±1.5	-72.1±1
180	173.5±0.5	49.5±0.5	156.8±1.5	-73.9±1
190	178.4±0.5	50.4±0.5	172.1±2.5	-75.6±1.5
200	183.2±1	51.7±0.5	188.6±2.5	-76.8±1.5
210	188.5±1	53.3±1	205.4	-76.8
220	194.3±1	55.0±1	221.7	-76.2
230	200.5±1	56.6±1	236.6±1.5	-75.6±1
240	207.5±1	58.5±1	250.1	-75.0
250	214.6±1	60.4±1	262.0±2	-74.2±1
260	220.8±2	61.6±1	272.8±2	-73.0±1
270	228.0±3	63.0±1	282.9	-71.7
280	238.8±1.5	65.1±0.5	292.6±2.5	-70.4±1
290	252.1±1.5	67.7±0.5	302.2±2	-69.0±1
300	265.4	69.8	311.7±1.5	-67.8±1
310	278.4	70.9	321.0±1.5	-66.5±1
320	290.6±5	71.6±1.5	330.0	-65.2
330	301.5±5	72.5±1.5	338.8±1.5	-64.0±1
340	311.6±5.5	73.9±1.5	347.5±1	-62.9±1
350	320.7	75.5	356.3±1	-62.0±1

Table 4.1: Planeto-centric coordinates of the Io northern and southern reference contours. Assuming a selection uncertainty of 3 pixels, the mean geometric uncertainty is provided only when it is constrained by data points.

location of Io to the ionosphere and then measure the longitudinal distance to the actual IFP. Instead, we link the IFP location to the nearest point on the model reference contour and we map this point back to the equatorial plane in order to measure the actual longitudinal shift with respect to Io. Figure 4.4a shows that the equatorial lead angle in the North is strongly model dependent. For example, the inexplicable negative lead angles in the 100° sector disappear when the magnetic mapping is done by the *Grodent et al.* (2008a) model. Figure 4.4b shows that the equatorial lead angle in the South has a more structured behavior, showing a smooth evolution as a function of Io's longitude. Nevertheless, the maximum and the minimum lead angles both appear when Io is in the center of the torus, i.e. close to 110° and 290° S3.

In Figure 4.5, we show the variations of the inter-spot distances for both hemispheres according to the trans-hemispheric electron beam model (see Chapter 3). In this plot, points are marked only when the secondary (and tertiary) spots are clearly observed on the image. The distances are shown in kilometers in order to avoid problems with the contour geometry and the use of magnetic field models. However, in order to provide a rough idea of the distances in terms of longitudinal shift, we can consider that 1° corresponds to ∼470 km (∼480 km in the North and ∼465 km in the South). In the North, the secondary spots are usually fainter than in the South. Thus these spots can only be distinguished from the main one when the inter-spot distance is large enough. However, between 0° and 100° in the southern hemisphere, the secondary spot becomes as bright as the main one and we can follow their merging on the images. The variations of the southern inter-spot distances look regular and correlated with the position of Io in the torus. Additionally, the inter-spot distances in the North and in the South appear to follow a symmetric behavior (see also Figure 3.4).

4.3.4 Discussion

The large amount of data collected during the HST/New Horizons campaign provided images of the Io footprint over a wide range of System III longitudes. *Grodent et al.* (2008a) carefully measured these footprint locations in order to build reference contours for the different satellite footprints in the northern hemisphere. However, the poor accuracy of the IFP locations around 0° S3 made the contour difficult to close in a reasonable way in the 0-60° range. We took advantage of IFP images

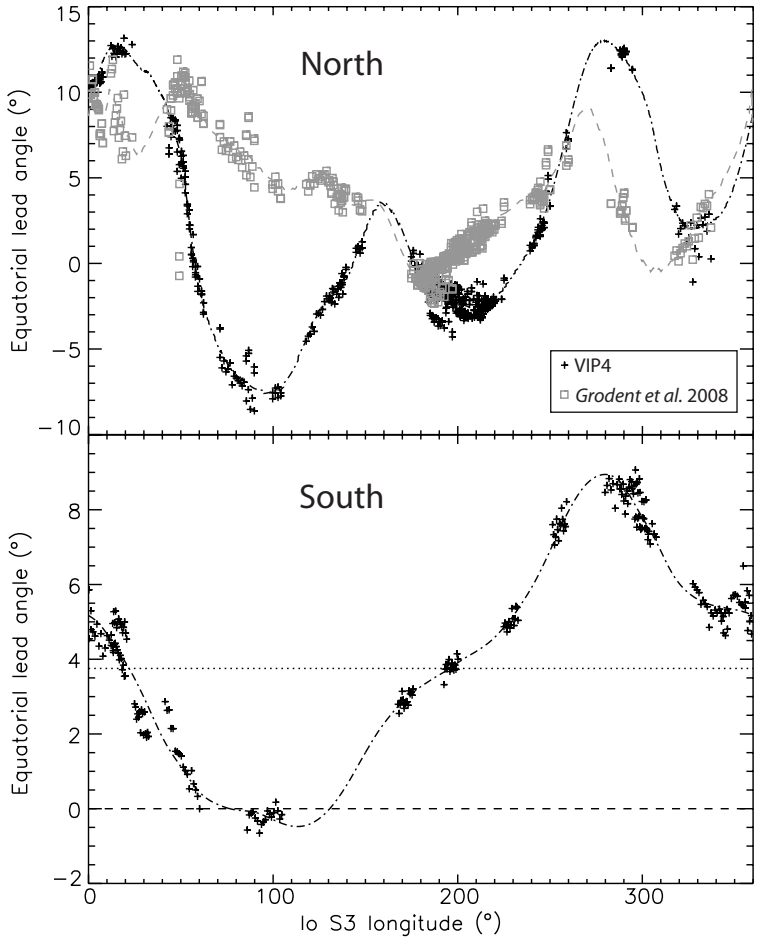

Figure 4.4: Equatorial lead angles for the northern and the southern footprints. The black crosses represent the data points as computed with the VIP4 model while the grey squares represent the equatorial lead angle using mapping from the second multipole+dipole model from *Grodent et al.* (2008a). The black dash-dotted and grey dashed curves are fifth order Fourier series fitting of the data points for the VIP4 and *Grodent et al.* (2008a) models respectively.

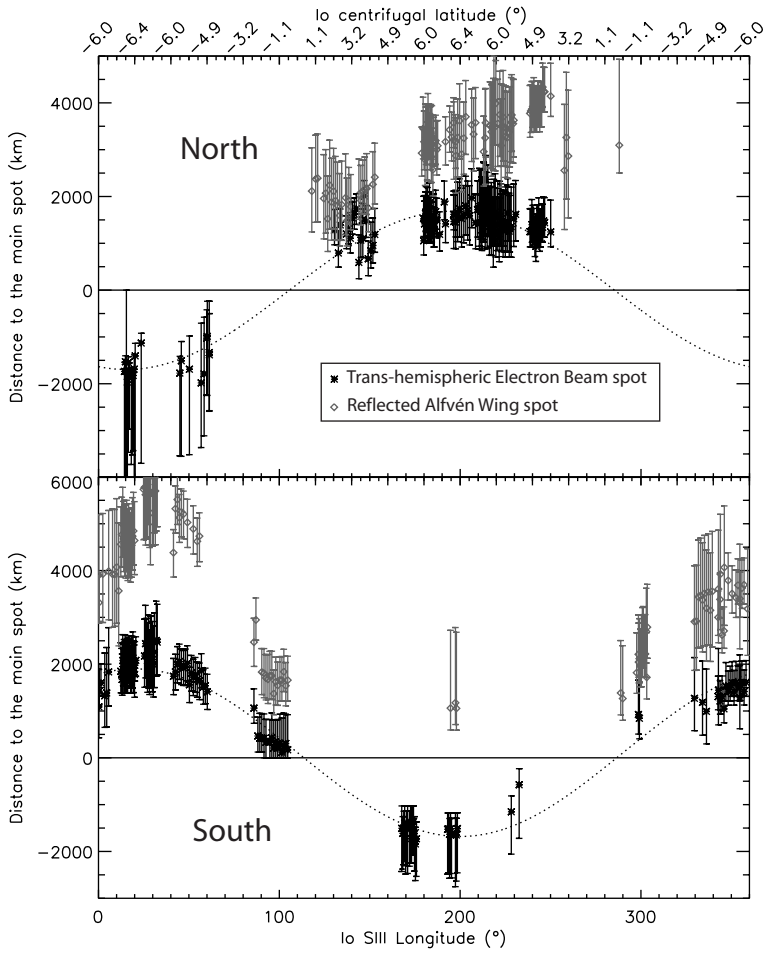

Figure 4.5: Inter-spot distances as a function of the Io S3 longitude of the northern (Top) and the southern hemispheres (Bottom). The error bars are built assuming a selection uncertainty of 1 pixel for the main spot and 2 pixels for the usually fainter secondary spot. The adopted theoretical framework to decide which is the main spot is the same as in *Bonfond et al.* (2008). The two curves correspond to the best fit of the points with a sinusoid function. The maxima lie around 1500-2000 km, which roughly corresponds to 3-4° into the equatorial plane.

with identical Io S3 latitudes but with different local time configurations to precisely locate the IFP for these critical longitudes. Finally, we constructed IFP reference contours for both hemispheres based on these IFP locations.

The new reference contours describing the IFP path were then used to compute the angle between the S3 location of Io and the projection of the IFP along the unperturbed magnetic field lines. Figure 4.4 shows that the lead angles vary with the S3 position of Io but are very model dependent. Additionally, in the northern hemisphere, the lead angles do not organize in a smooth trend, whatever the model. Even though the southern hemisphere curve shows some regularity, it implies that the lead angle when Io is in the dense torus center can vary from $\sim 0°$ to $\sim 9°$. We note that the lead angles vary with Io's longitude but do not follow the ideal Alfvén wing model expectations. In this interpretation framework, the maximum lead angle is supposed to occur when the Alfvén waves have to cross the entire torus, while the minimum value is expected when the Alfvén waves propagate through a relatively short path in the torus. It is thus surprising to find that the lead angle could reach both its minimum and maximum values when Io is exactly in the same position relative to the torus.

These results and the strong model dependence suggest that the current magnetic field models may not be accurate enough to provide trustworthy lead angle estimates. Possibly, future JUNO probe magnetic field observations will have the required precision for such measurements. Furthermore, the fact that inter-spot distances follow symmetric and regular curves when measured directly on the planet strengthens this conclusion. If the Alfvénic disturbance can be assumed to be linear, the inter-spot distances are related to the bending of the Alfvén wing. Then the secondary spot cannot be attributed to Alfvén wing reflections at the plasma torus boundaries because the distance would not be a minimum when Io is in the torus center. Only the trans-hemispheric electron beam scenario could explain the secondary spot behavior. In this case, the lead angle varies with Io's centrifugal latitude, and its maximum value corresponds to the maximum inter-spot distance and lies around 4°. However, Alfvén wing reflections could still account for the third spot as suggested by *Bonfond et al.* (2008). If non-linear wave interactions are significant, then the link between the lead angle and the inter-spot distance is less direct. Further simulations are required to test whether such models can better match the inter-spot distances reported here.

4.3.5 Conclusions

The lead-angle has been traditionally considered as a crucial parameter to test the far field interaction models. As long as the data were sparse, the measured lead angles have been claimed to favor the unipolar inductor model when the estimated value was large ($\sim 15-20°$) (*Connerney et al.*, 1993) or the ideal Alfvén wing model when it was small ($\sim 0-2°$) (*Vasavada et al.*, 1999). When the datasets began to fill out, the picture became more confused and the absence of clear trend was attributed to the lack of accuracy both on the measurements and on the model (*Clarke et al.*, 1998; *Gérard et al.*, 2006). Indeed, the fact that the modeled and observed reference contours do not match well demonstrates the limitations of a possible comparison between modeled and observed IFP positions (see Figure 4.2). But I claim that the problem is worse than that: we are asking magnetic field models, and VIP4 in particular, for information they cannot provide. It is not only a matter of accuracy but also a matter of construction. The VIP4 model and the *Grodent et al.* (2008a) models are built in such a way that the mapping of the Io orbit along magnetic field lines corresponds to an Io footprint reference contour. Even if the contour fit were infinitely accurate, the fact that a model field line passing through Io has its footprint on the Io contour does not guarantee that it will fall at the right place on this contour because the models are not longitudinally constrained. They would only be trustworthy if we could demonstrate that the x^{th} order multipole in use is the exact representation of the Jovian magnetic field.

This argument seems to be confirmed by our measurements of the equatorial lead angles based on the extended image database acquired in the Spring 2007. The variations of the equatorial lead angles as a function of the System III position of Io are found unexpected, erratic and strongly model dependent. This noting sharply contrasts with the smooth and regular evolution of the inter-spots distances and suggests that the current magnetic field models are not sufficiently accurate to provide information on the Alfvén wing's bending.

On the other hand, the inter-spot distances and the centrifugal latitude of Io are correlated, and the behavior of the curves in the northern and southern hemispheres is found symmetric. Whatever the hemishere, the minimum inter-spot distance between the main and the secondary spots is located in the torus center, which suggests that the secondary spot is not attributable to Alfvén wing reflections at the torus boundaries. Simulations of the MAW-TEB inter-spot distances based on density profiles from *Bagenal* (1994) and the VIP4 magnetic field model reproduce very

well the measured inter-spot distances, notably their maximum value (∼2000 km) and the maximum location (S. Jacobsen, private communication). This confirms that the trans-hemispheric electron beams interpretation is fully compatible with our measurements.

4.4 Epilogue

The satellites footprints positions tell us a lot about the Jovian magnetic field. They provide a unique way to get information on the surface magnetic field that was inaccessible from past fly-by and orbiting probes. Because of their direct connection to their related satellite, the Io, Europa and Ganymede footprints provide unique mapping information between the Jovian polar ionospheres and the magnetosphere. For this reason, the Io footprint, and then Europa's and Ganymede's footprints as well, have been used as constraints for improving magnetic field models.

However, the Io footprint location does not only provide information on the Jovian magnetic field, it also helps to understand the Io-Jupiter interaction. A fundamental result of our study is that we now have an accurate knowledge of the IFP location as a function of Io's longitude in the Jovian magnetic field. We can not only predict where the main spot is located, but we can also predict the relative position of the different spots. In addition, we showed that a parameter that was considered for years as the key parameter to validate the far field Io-Jupiter interaction models, the lead angle, is actually not reliable enough to meet this expectation. Hopefully, we demonstrated that the inter-spot distances are a much more useful quantity to discriminate between the models. We found that the trans-hemispheric electron beam model that we proposed in the previous chapter is fully compatible with the present qualitative measurements, contrary to many previous interpretations.

Additionally, the characterization of these position parameters is interesting by itself, but it is also a mandatory step for the next phase of our Io footprint exploration. For example, the new reference contours will be extremely precious to describe the evolution of the tail characteristics with the distance from the main spot. Moreover, the precise spots localization, both on the planet and respective to each other, will also prove to be extremely useful when we study the brightness of the different spots.

Chapter 5

The Io footprint tail emissions

5.1 Foreword

In the first steps of this work, we adressed basic but essential questions: "What does the Io footprint look like?" and "Where is the Io footprint?". We have seen that the systematic study of the footprint morphology and position lead us to very interesting conclusions. They forced us to discard some early oversimplified ideas and to propose a new interpretation of the footprint multiplicity.

So far, we mainly focused on the spots. Here we concentrate on the tail emission that appears downstream from the spots. The construction of an accurate Io reference oval proves to be extremely useful in the present study since it helps characterizing the tail emission as a function of the distance from the main spot. The Io footprint tail has been detected as early as the UV spots (*Prangé et al.*, 1996), but has not been studied as extensively as the spots. *Prangé et al.* (1998) called it the Io oval and claimed it could take place along a complete contour. However, subsequent images obtained with the much more accurate and sensitive STIS instrument did not show any complete oval, but instead a downstream tail extending downward to more then 100° (*Clarke et al.*, 2002). The term "Io oval" has also been used to designate the locus of all possible Io footprint locations in a reference frame fixed with System III (e.g. *Grodent et al.*, 2003a). As shown above, we now prefer to use "Io reference contour" (or simply "Io contour") to designate this footpath (*Grodent et al.*, 2008a; *Bonfond et al.*, 2009), since it does not form a closed pattern around the pole.

Clarke et al. (2002) claimed that this tail emission cannot be caused by an afterglow persisting after the cessation of particle precipitation, because the H and

H_2 excited upper states decay in a fraction of a second[1]. Hence, they concluded that the UV tail was continuously generated by precipitating charged particles.

The STIS instrument does not only take sharp UV images, it is also and above all a powerful spectrograph. FUV spectra can provide useful information on the amount of absorbing particles along the line of sight. On some STIS FUV spectra of the Jovian aurorae, the slit intercepted the Io footprint main spot or its tail (Figure 5.1). On these spectra, H_2 emissions below 1350 Åare attenuated by the methane while emissions above this threshold are not. The usual parameter to characterize this absorption is the UV color ratio, defined as:

$$CR = \frac{I_{(1550-1620)}}{I_{(1230-1300)}}$$

that is the ratio of the total emission in the wavelength range from 1550 to 1620 Åover the total emission in the wavelength range from 1230 to 1300 Å(*Gérard et al.*, 2002). *Gérard et al.* (2002) measured the color ratio as a function of the distance from the main spot and showed that it does not significantly vary (Figure 5.2). They thus concluded that the brightness decrease along the trail was essentially linked to a decrease of the energy flux rather than to a decrease of the incoming electron energy.

Moreover, with the use of appropriate models and hypotheses, the color ratio can also provide estimates of the precipitating electron energy. Among this set of hypotheses, the choice of a neutral atmosphere model is an important one. *Gérard et al.* (2002) used the North Equatorial Belt (NEB) model from *Gladstone et al.* (1996) adjusted to the gravity acceleration at a latitude of 60°. Another necessary assumption is the vertical distribution of methane in the atmosphere. This distribution is based on infrared spectral measurements in the auroral region obtained with the IRIS instrument on board Voyager 1(*Drossart et al.*, 1993). It also relies on a one-dimensional diffusion equation and on an eddy-diffusion coefficient at the homopause set to 1.4×10^6 cm^{2}s^{-1}. These atmospheric parameters being set, the energy deposition model described by *Grodent et al.* (2001) was used to compute the color ratio as a function of the electron energy, assuming a Maxwellian energy distribution. It should be stated that, contrary to the examples shown in *Grodent et al.* (2001), the thermal structure was not allowed to adjust to the thermal bal-

[1] At the exception of one metastable excited state, which have an expected lifetime of seconds, too short anyway to explain the tail.

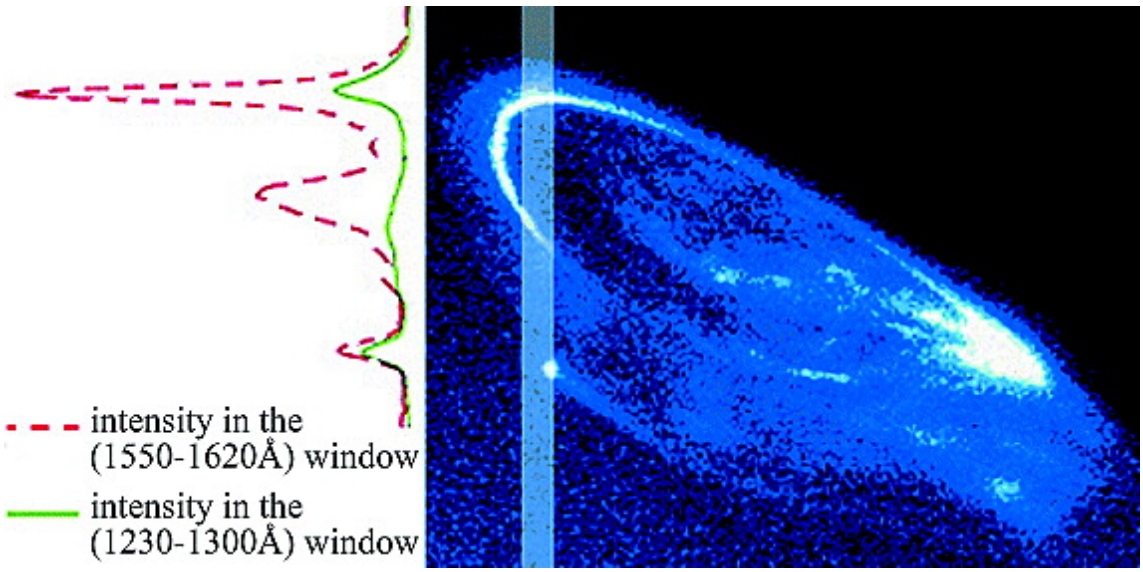

Figure 5.1: The image shows the location of the STIS spectral slit on an image obtained on 22 February 2000, 12 minutes before the spectrum acquisition. The two curves on the left are the intensities along the slit for the two spectral windows of the color ratio. The short wavelength window (in solid green line) is subject to methane absorption while the long wavelength one (in dashed red line) is not. (from *Gérard et al.* (2002))

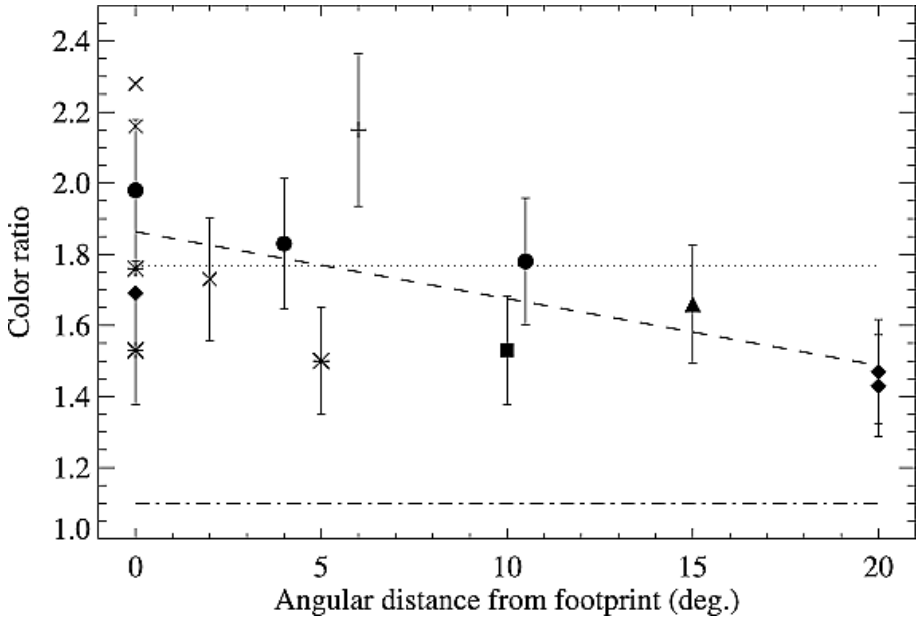

Figure 5.2: Variation of the color ratio observed along the Io trailing tail as a function of the angular distance from the footprint. Identical symbols are used for measurements obtained within one HST orbit. The closed symbols (circle, diamond, square, triangle) correspond to north data, the other symbols (*, +, X) to the south. The dashed line is the linear regression fitted to the north data and the dotted line is the mean color ratio. The dot-dashed horizontal line indicates the color ratio with no hydrocarbon absorption. (adapted from *Gérard et al.* (2002))

ance. In the frame of all these assumptions and models, the energies deduced from color ratio measurements range from 41 to 69 keV and thus a typical precipitating electrons energy in the Io footprint was estimated around 55 keV.

For the sake of completeness, it should be noted that the presence of a footprint tail is not restricted to the case of Io. *Grodent et al.* (2005a) detected a faint ($\sim$ 7 kR) tail extending downstream of the Europa spot over $\sim$ 5000 km. Interestingly, these authors noted that the tail was observed when Europa was between 65° and 115° System III longitude, i.e. when Europa is close to the plasma sheet. This could possibly correspond to a suggestion made by *Kivelson et al.* (1999) stating that a plasma plume would only be produced in the wake of Europa when it crosses the current sheet.

Back to Io, we will see in the next section that the longitudinal extent of the tail emission and its separation from the non-Io auroral emissions makes it possible to measure their characteristics with unprecedented accuracy. Most of the material

presented in the following section has been published by B. Bonfond, D. Grodent, J.-C. Gérard, A. Radioti, P.A. Delamere, V. Dols and J.T. Clarke under the title: *The Io UV footprint: Location, inter-spot distances and tail vertical extent* in Journal of Geophysical Research - Space Science (*Bonfond et al.*, 2009).

5.2 Introduction

There are currently few models addressing the tail electrodynamics and all of them assume steady state conditions. They also assume that the tail is the auroral signature of the horizontal divergence of the current crossing the Io plasma wake. This current is needed to reaccelerate the flux tubes, slowed through mass loading by Iogenic plasma, to almost full corotation. *Hill and Vasyliūnas* (2002) applied the same approach as the one proposed for the unipolar inductor model. The Jovian Pedersen conductivity limits the current in the loop connecting the plasma wake of Io and the Jovian ionosphere. Finite ionospheric conductivity thus impedes the return to corotation of the plasma behind Io. *Delamere et al.* (2003) computed the momentum transfer between the plasma in the torus and the plasma slowed by its interaction with Io's atmosphere. After this momentum transfer, they calculated a residual potential drop across the Io flux tube of ∼70 kV. They note that if the auroral electrons had to be accelerated by a static potential structure parallel to the field line to the ∼55 keV proposed by *Gérard et al.* (2002), then most of the ∼70 kV cross-flux tube potential drop available has to be used for this acceleration. They concluded that the corresponding horizontal electric field in Jupiter's ionosphere is thus small and that the Pedersen conductivity is not relevant. Contrary to Hill and Vasyliunas, they concluded that the plasma in the wake of Io is highly decoupled from the Jovian ionosphere. *Ergun et al.* (2009) used the Hill and Vasyliunas approach but added an equation describing the quasi-static potential drop along the magnetic field lines, using a current-voltage relation derived by *Knight* (1973). The Knight current-voltage relation is modified in the model of *Ergun et al.* (2009) to take into account the low plasma density at the foot of the flux tube that limits the parallel (field aligned) current. *Ergun et al.* (2009) computed self-consistently a precipitated electron energy flux of ∼1 mW/m^2 compatible with the UV observations, a tail extension comparable to the one deduced by Hill and Vasyliunas (see Section 5.4.2), and a precipitated electron energy of ∼1 keV , much smaller than the ∼55 keV estimate of *Gérard et al.* (2002).

Some images from the large HST database used for this work show the Io tail emission in such a configuration that its vertical profile can be directly measured. The position of the extracted profiles relative to the main spot was deduced using our new IFP reference contour. We present new measurements describing how the brightness, the peak altitude and the vertical distribution of the tail emission evolve with the distance from the main spot. We also use a Monte Carlo model of the energy degradation of the auroral electrons precipitating into a theoretical Jovian atmosphere in order to compute the UV emission rates from excited H_2 and H. By comparing the simulated emission rates and profiles with the observed ones we deduce the energy distribution of the precipitated electron flux. Consequently, the brightness profiles provide information on the precipitated electrons energies. This technique is therefore independent of the spectral color ratio method. Additionally, this deduced energy distribution gives insight into the physical process accelerating the electrons that we compare with the processes proposed in the models explaining the IFP tail, described earlier in this introduction.

5.3 Peak altitude and vertical profiles

On several ACS images from the 10862 observation campaign, we can clearly see the Io footprint, or at least its trailing tail, lying right above the limb (Figure 5.3). Consequently, we consider here a selection of images where the tail appears crossing the limb plane (Figure 5.4). These images originate from 10 different HST orbits. For this considered observation campaign, a typical orbit was made of 5 consecutive 100-second F125LP images followed by 9 100-second F115LP images and then another 5 100-second F125LP images. For each orbit, the 19 original images are assembled into 7 sets of three images acquired with the same filter (two images are thus used twice) in order to increase the signal to noise ratio while keeping the same integrated exposure time for each set. The first set is the sum of the first three F125LP images, the second is the sum of the 3rd, the 4th and the 5th F125LP images - the image number three is thus used twice. The next three sets sum groups of three images out of the 9 consecutive F115LP images. The last two sets are made of the remaining F125LP images and are respectively formed by the groups from the 15th to the 17th image and by the group from the 17th to the 19th image. Consequently, the 17th image is also used twice. The following data reduction steps are performed on the summed images (7 per orbit). We developed

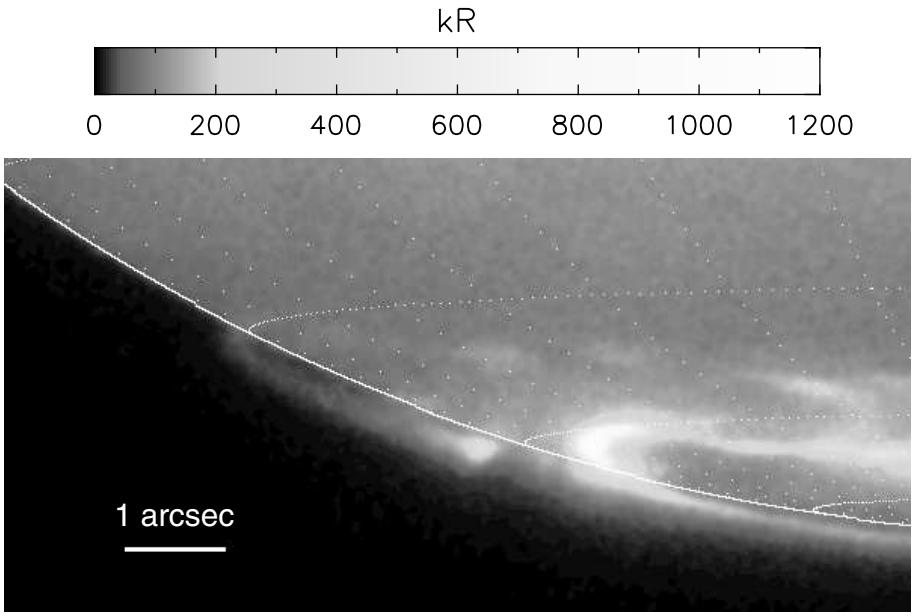

Figure 5.3: Example of Io footprint tail seen right above the limb plane in the southern hemisphere. The reference ellipsoid, where the 0 km altitude is set, has an equatorial radius of 71492 km and a polar radius of 66854 km. Parallel and meridian lines are drawn every 10°. (from *Bonfond et al.*, 2009)

a semi-automatic method to perform radial scans of the planetary limb every 0.1° in a manually selected sector. The routine measures the altitude of the emission peak as a function of the rotation angle, smooths out the resulting curve with a median filter and identifies the maximum altitude (Figure 5.6). If the precipitating particle mean energy is constant along the tail, then the emission peak appearing the furthest from the planetary edge lies in the limb plane. Additionally, the radial profile extracted at this location is assumed to reflect the actual vertical extent of the emission.

Non-auroral planetary disk emissions also contribute to the low altitude part of the observed profiles. Consequently, we built an empirical disk vertical profile extrapolated from profiles extracted at lower latitudes for each image. When we analyze the disk emission, we notice that on the sunlit side of the planet, for a given altitude, the intensity of the disk emission is not evolving significantly as a function of the rotation angle. Consequently, when the tail emission stands over the sunlit limb, the empirical disk profile is formed by the average of the profiles extracted a

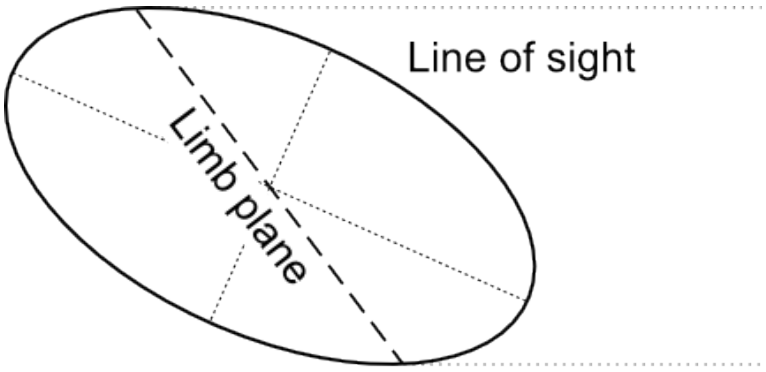

Figure 5.4: Illustration of the limb plane.

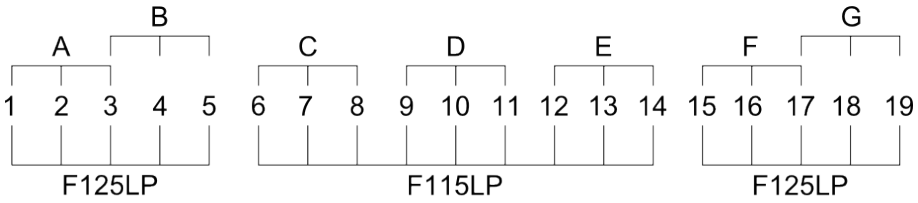

Figure 5.5: Schematic of the image regrouping used in this study. The purpose is to increase the signal-to-noise ratio by summing consecutive images acquired with the same filter while keeping the same total exposure time for each set. Images number 3 and 17 are thus used twice.

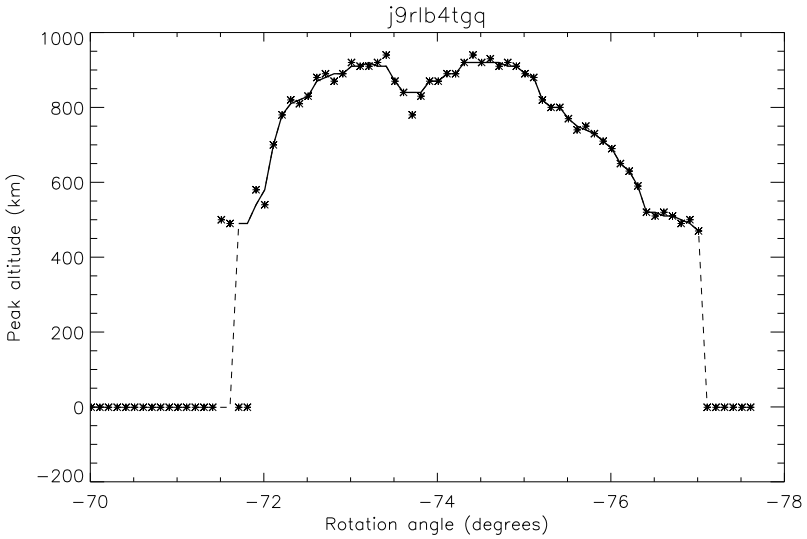

Figure 5.6: Example of the evolution of the Io tail peak altitude as a function of the rotation angle. We then applied a median filter (solid line) and identified the angles and the profile associated with the maximum altitude, which is around 900 km. In the example shown here, the gap in the middle of this profile is probably not significant.

few degrees equatorward from the auroral emissions. On the terminator side of the planet and for a given altitude, we note that the disk emission varies linearly with the rotation angle. Therefore in this case, for a given altitude level, the empirical disk intensity is interpolated from disk profile intensities measured a few tenths of degree equatorward from the tail. We remove this disk emission profile from the total profile in order to isolate the auroral emission. Then we fit the extracted vertical profiles with a Chapman profile of the form :

$$f(x) = C \exp\left(1 - \left(\frac{Z - Z_0}{H}\right) - \exp\left(-\frac{Z - Z_0}{H}\right)\right) \tag{5.1}$$

where C is a constant, Z is the altitude in km, Z_0 is the altitude of the peak in km and H is the scale height in km. The scale height of these emissions lies around 430 km $\pm$ 70 km and does not depend either on the filter nor on the distance from the main spot.

The mean altitude of the emission peak we derive from the profiles is 900 km $\pm$125km. Note that the standard deviation is fairly close to 120 km, which is the typical distance subtended by one pixel on Jupiter. This indicates that the variability due to measurement uncertainty provides an upper limit to the real, intrinsic fluctuations. Figure 5.7 shows the variation of the peak altitude as a function of the longitudinal distance from the Io footprint main spot according to the reference contour described above. The distances are expressed in kilometers along the reference contour to avoid complications owing to the contour geometry. From the length of the reference contours, 2000 km roughly corresponds to $\sim 4^\circ$ in the equatorial plane. Consequently, the furthest points on this plot are approximately 60° away from the main spot. The further the profile stands from the main spot, the higher is the altitude of the brightness peak. However, the correlation coefficient between the altitude and the distance is only 0.09 and is not significantly different from 0 for a confidence interval of 99%. This result justifies *a posteriori* our initial assumption of the constant altitude of the auroral curtain.

5.4 Estimate of the energy distribution

The emission peak altitude provides an estimate of the precipitating particle energy and it puts a strong constraint on the electron acceleration mechanism. Additionally, the emission profile reflects the shape of the energy spectrum. We selected a

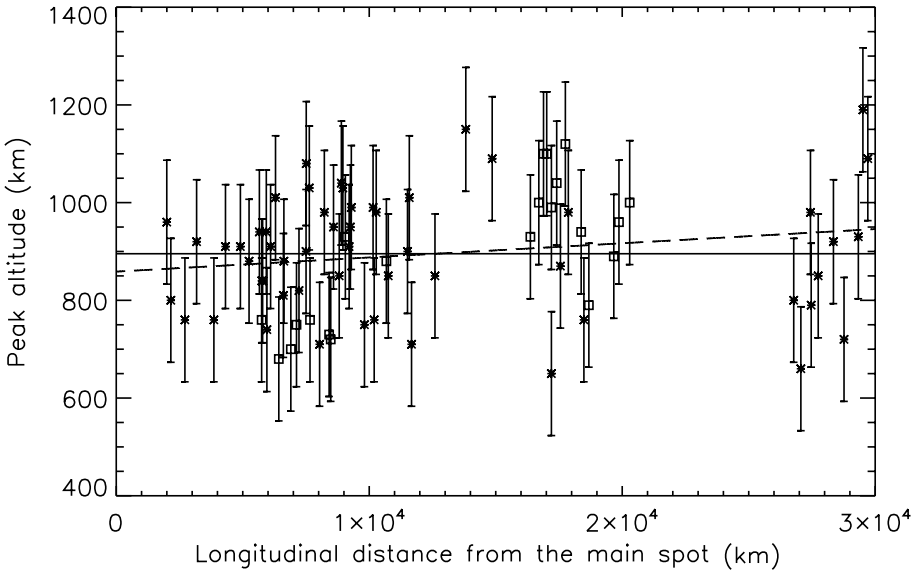

Figure 5.7: Altitude of the peak of the brightness profiles as a function of the distance of this profile from the IFP main spot location as described by our new reference contours. The stars and squares are for points in the northern or the southern hemisphere respectively. The mean altitude is 900km and the increase of the peak altitude is not statistically significant. This indicates that the precipitating electron energy is relatively constant with the distance to the main spot. (from *Bonfond et al.*, 2009)

sub-set of images coming from two consecutive HST orbits acquired on 24/02/2007 in the southern hemisphere to build a typical vertical profile of the tail. This set of 38 images has been chosen because the curtain is quasi-perpendicular to the observer and because auroral diffuse emissions do not contaminate the lower altitude part of the profile. We sum these 38 profiles to generate a typical observed profile with a signal to noise ratio as large as possible ($\frac{S}{N} \simeq 12$ in lieu of $\sim$2 for single images) and we compare it to different theoretical emission profiles (Figure 5.8). Spectral measurements showed that hydrocarbon absorption of the IFP FUV emissions was measurable but weak (*Gérard et al.*, 2002). However, we have very little observational information on the methane vertical distribution in the polar regions. Consequently, we consider that hydrocarbon absorption does not significantly affect the shape of the emission vertical profile.

The numerical model used to calculate electron transport in planetary atmospheres has been described in detail by *Shematovich et al.* (2008). The incident electrons lose their excess kinetic energy in elastic, inelastic and ionization collisions with the ambient atmospheric gas consisting of H_2, He, and H. If the collision produces ionization, a secondary electron is created and is randomly assigned an isotropically distributed pitch angle and an energy in accordance with the procedure given by *Garvey and Green* (1976), *Jackman et al.* (1977) and *Garvey et al.* (1977). The cross sections and scattering angles used to calculate the energy loss associated with elastic and inelastic collisions of electrons with H_2, He, and H were taken for H_2 from the AMDIS database (https://dbshino.nfs.ac.jp) and *Shyn and Sharp* (1981); for He and H from the NIST database (http://physics.nist.gov/PhysRefData/Ionization/) and *Jackman et al.* (1977), *Dalgarno et al.* (1999). Their transport is described by the kinetic Boltzmann equation. The Direct Simulation Monte Carlo (DSMC) method is used to solve atmospheric kinetic systems in the stochastic approximation (see *Shematovich et al.*, 2008 and references therein). The lower boundary is set at an altitude 0.25 μbar and the upper boundary is fixed at 6.5×10^{-11} μbar where the atmospheric gas flow is practically collisionless. The region of the atmosphere under study is divided into 49 vertical cells uniformly distributed on a logarithmic pressure scale. The evolution of the system of modeled particles due to collisional processes and particle transport is calculated from the initial to the steady state. The pressure-altitude relationship from *Grodent et al.* (2001) is adopted because it is the most realistic auroral atmosphere available. For a given initial mono-energetic beam, the model provides a vertical emission profile assuming an isotropic pitch

angle distribution at the top of the atmosphere.

If we consider a mono-energetic distribution, the curve that best fits the observations has a typical energy of 2 keV (Table 5.1). However, even after taking the point spread function (PSF) of the ACS camera into account, its vertical width is too small to reasonably reproduce the observations. Because of the curvature of the planet, an extended emission region leads to an apparent broadening of the emission profile. A simulation of the emission integration along the line of sight shows that the size of the emission region should be 20 times larger than the vertical scale height to generate significant effects. In our case, we determine that the curtain latitudinal width corresponds to the projected diameter of Io and lies between 100 and 200 km, i.e. only 0.25 to 0.5 times the observed scale height (∼400 km). Consequently, we may conclude that the width of the vertical emission profiles is due to a broad distribution in the energy of the precipitating electrons. We tested three different energy distributions in order to obtain information on the shape of the particle energy spectrum: a Maxwellian distribution

$$I = CE\exp(\frac{-E}{E_0}) \tag{5.2}$$

a power law distribution

$$I = CE^{-\gamma} \tag{5.3}$$

and a kappa distribution

$$I = CE(E + E_0\kappa)^{-1-\kappa} \tag{5.4}$$

where I is the differential intensity in $cm^{-2}s^{-1}sr^{-1}keV^{-1}$, E is the electron energy in keV, C is a constant, E_0 is the characteristic energy in keV, and γ and κ are the spectral indices of the power-law and the kappa distributions, respectively. For each distribution, we divide the energy range between 30 eV and 30 keV into 30 energy bins (uniformly distributed on a logarithmic energy scale) in which we compute the mean energy and the total energy flux[2]. We simulate an emission profile for each energy bin with the Monte Carlo model. Finally we weight the emission profiles with the channel total energy flux and we sum them to generate the emission profile corresponding to the adopted distribution and set of parameters. After smoothing

[2]In an energy range from E_1 to E_2, the total energy flux is calculated as:

$$E_t = \int_{E_1}^{E_2} EIdE$$

Distribution	Characteristic energy (E_0)	Spectral index (γ or κ)	Mean energy
Mono-energetic	2 keV (1.3 keV)	-	2 keV (1.3 keV)
Maxwellian	960 eV (540 eV)	-	1.9 keV (1.1 keV)
Kappa	70 eV (75 eV)	2.3 (2.4)	1.1 keV (0.8 keV)
Power-law	-	1.9 (1.8)	-

Table 5.1: Parameters of the best fit curves compared to the summed profile acquired $\sim$20° away from the main spot. The numbers between brackets are computed for a profile located approximately 40° away from the spot.

the profile with a boxcar function of the size of the PSF, we perform a least squares fit to compute the best parameter set for each energy distribution. The results are given in Table 5.1. Figure 5.9 presents the best fit energy spectra used to compute the corresponding emission profiles. Figure 5.8 shows the best simulated vertical profiles and compares them with the observations. One can note that only the kappa distribution generates a vertical profile compatible with the observations. The profiles that we used for the best fit lie approximately 20° away from the main spot. We also perform the same analysis with profiles taken approximately 40° away from the main spot (not shown here). Since the brightness is lower and only 19 images are used, the signal to noise ratio is lower but the results are very similar and are presented between brackets in Table 5.1.

5.4.1 Sensitivity tests

One of the main unknowns when we try to deduce the electron energy distribution based on a vertical profile is the pressure-altitude relationship for the atmosphere. We adopted here, as our basic model, an atmosphere model that takes heating due to particle precipitation in account (*Grodent et al.*, 2001). We also performed the same test for two other atmospheric models: the NEB model and an artificially hot atmosphere (designated as 2X hereafter) which is our basic atmosphere where all the altitudes were multiplied by a factor 1.5 and shifted by 80 km (see Figure 5.10).

Whatever the case, the mono-energetic and the Maxwellian distributions are

and the mean energy is computed as as the ratio of the energy flux over the particle flux:

$$E_m = \frac{\int_{E_1}^{E_2} EIdE}{\int_{E_1}^{E_2} IdE}$$

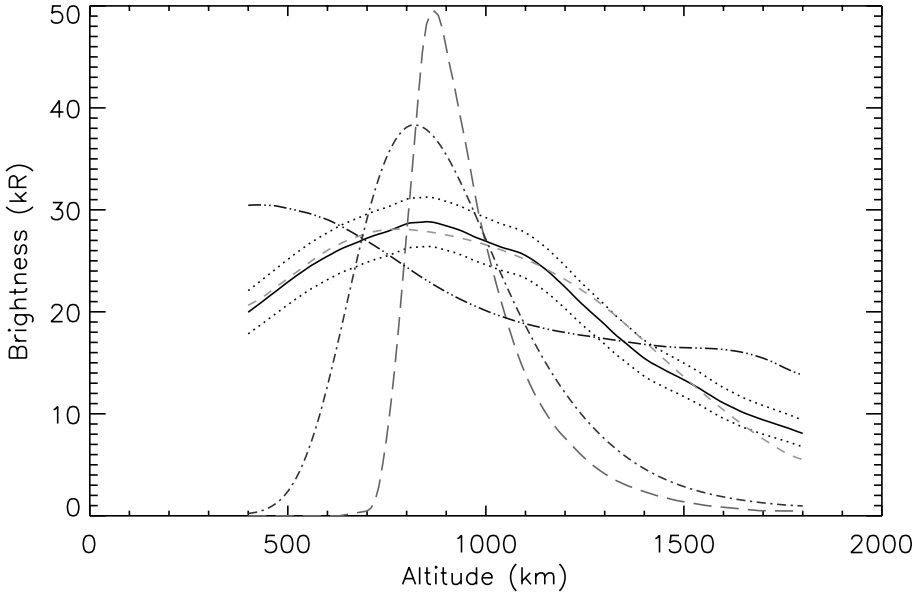

Figure 5.8: Observed and simulated vertical emission profiles. The observations and the estimated uncertainties are represented by the solid line surrounded by the dotted lines. The four other lines are the best fit vertical profiles based on the theoretical distributions described in the text. The long dashed line corresponds to the mono-energetic distribution, the small dashed line corresponds to the kappa distribution, the dash-dotted line corresponds to the Maxwellian distribution and the dash-dot-dot-dotted line corresponds to the power-law distribution. One can see that only the kappa distribution provides a reasonable fit of the observed curve. (from *Bonfond et al.*, 2009)

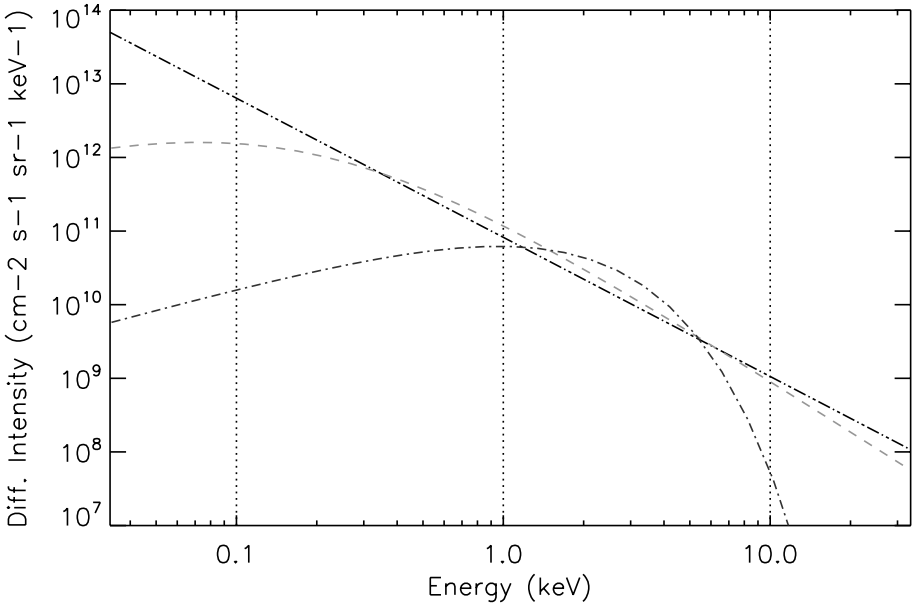

Figure 5.9: Energy spectra computed with the best fit parameters shown in table 5.1. The dashed line represents the kappa distribution, the dash-dotted line represents the Maxwellian distribution and the dash-dot-dot-dotted line represents the power-law distribution. In order to compute the differential intensities, the curtain is assumed to be 200 km wide. (from *Bonfond et al.*, 2009)

NEB Distribution	Characteristic energy (E_0)	Spectral index (γ or κ)	Mean energy
Mono-energetic	552 eV	-	552 eV
Maxwellian	283 eV	-	566 eV
Kappa	5 eV	2.12	177 eV

Table 5.2: Parameters of the best fit curves compared to the summed profile acquired $\sim$20° away from the main spot, considering the NEB atmosphere model.

2X Distribution	Characteristic energy (E_0)	Spectral index (γ or κ)	Mean energy
Mono-energetic	7.7 keV	-	7.7 keV
Maxwellian	2.7 keV	-	5.4 keV
Kappa	270 eV	2.35	3.6 keV

Table 5.3: Parameters of the best fit curves compared to the summed profile acquired $\sim$20° away from the main spot, considering the 2X atmosphere model.

always too narrowly peaked to reproduce the observation (Figures 5.11 and 5.12). In the case of the NEB atmosphere, even the kappa distribution cannot reproduce the observed curve. This can be easily explained by the fact that observations show significant emission at altitudes as high as 1500 km and above, while in the NEB model, the atmospheric pressure is already more than one order of magnitude lower than for the basic model. Thus, a very large amount of low energy electrons are required to reproduce the observations, but then the kappa distribution is no longer able to fit the remainder of the curve. Tables 5.2 and 5.3 show that the mean energies vary with a factor of 4 at maximum, if we exclude the kappa results for the NEB test.

Another source of uncertainty comes from the measured altitudes. Therefore, we also performed test fits after shifting the observed curve by $\pm$120 km. The mean energies are modified by a factor of two at most compared to the basic test. Additionally, the mono-energetic and the Maxwellian distributions are unable to reproduce the width of the observed profile, contrary to the kappa distribution. The computed distribution parameters for these two runs are collected in Tables 5.4 and 5.5.

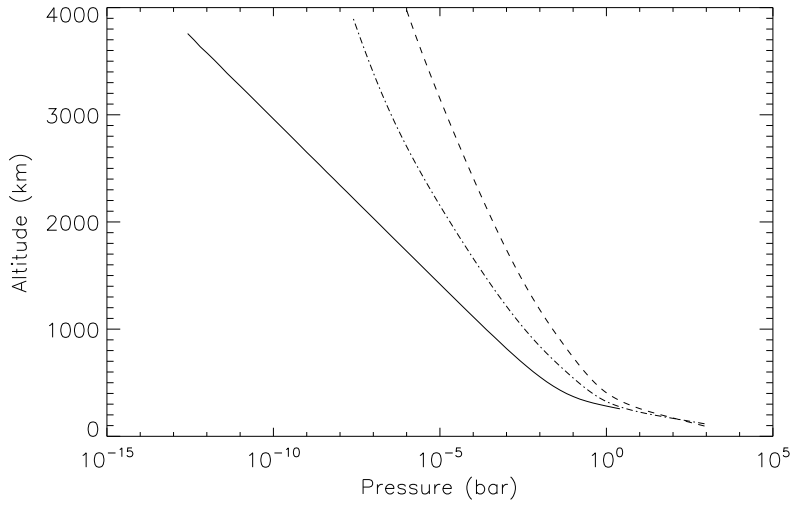

Figure 5.10: Altitude-pressure relationship for the NEB model in solid line, for the *Grodent et al.* (2001) model in dash-dotted line and for the artificially hot 2X model in dashed line.

+120 km Distribution	Characteristic energy (E_0)	Spectral index (γ or κ)	Mean energy
Mono-energetic	1.3 keV	-	1.3 keV
Maxwellian	650 eV	-	1.3 keV
Kappa	62.5 eV	2.4	750 eV

Table 5.4: Parameters of the best fit curves compared to the summed profile acquired $\sim$20° away from the main spot and shifted 120 km upward.

-120 km Distribution	Characteristic energy (E_0)	Spectral index (γ or κ)	Mean energy
Mono-energetic	3.3 keV	-	3.3 keV
Maxwellian	1.5 keV	-	3.0 keV
Kappa	57.5 eV	2.1	2.4 keV

Table 5.5: Parameters of the best fit curves compared to the summed profile acquired $\sim$20° away from the main spot and shifted 120 km downward.

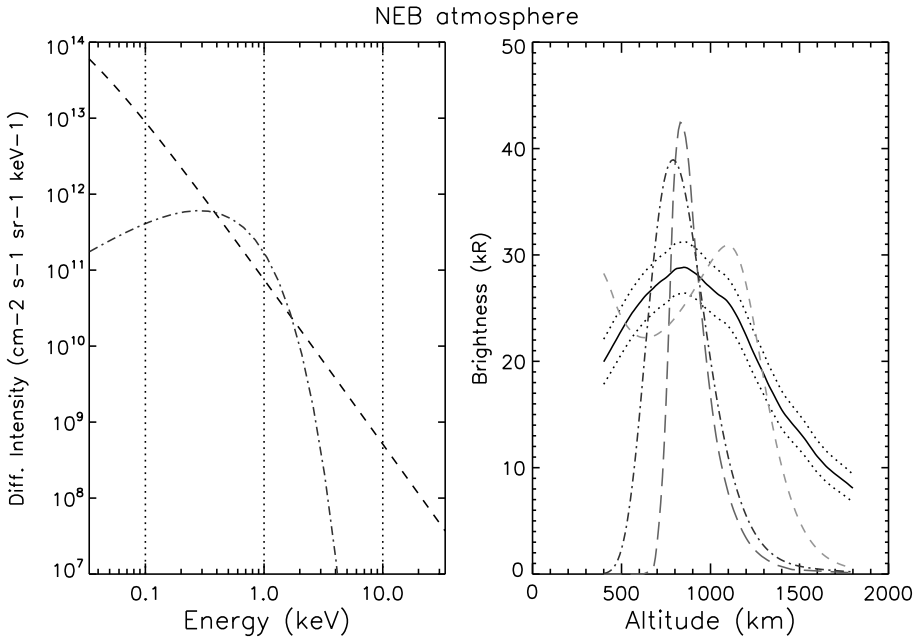

Figure 5.11: (left) Energy spectra computed with the best fit parameters shown in table 5.2. The small dashed line corresponds to the kappa distribution and the dash-dotted line corresponds to the Maxwellian distribution. (right) Observed and simulated vertical emission profiles for the NEB atmosphere. The observations and the estimated uncertainties are represented by the solid line surrounded by the dotted lines. The long dashed line corresponds to the mono-energetic distribution, the small dashed line corresponds to the kappa distribution and the dash-dotted line corresponds to the Maxwellian distribution.

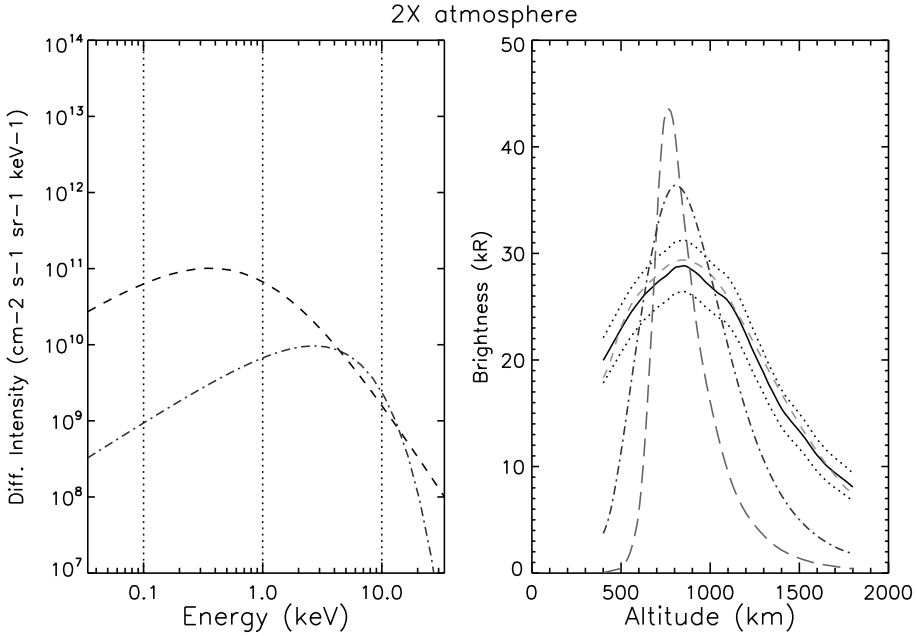

Figure 5.12: (left) Energy spectra computed with the best fit parameters shown in table 5.3. The small dashed line corresponds to the kappa distribution and the dash-dotted line corresponds to the Maxwellian distribution. (right) Observed and simulated vertical emission profiles for the 2X atmosphere. The observations and the estimated uncertainties are represented by the solid line surrounded by the dotted lines. The long dashed line corresponds to the mono-energetic distribution, the small dashed line corresponds to the kappa distribution and the dash-dotted line corresponds to the Maxwellian distribution.

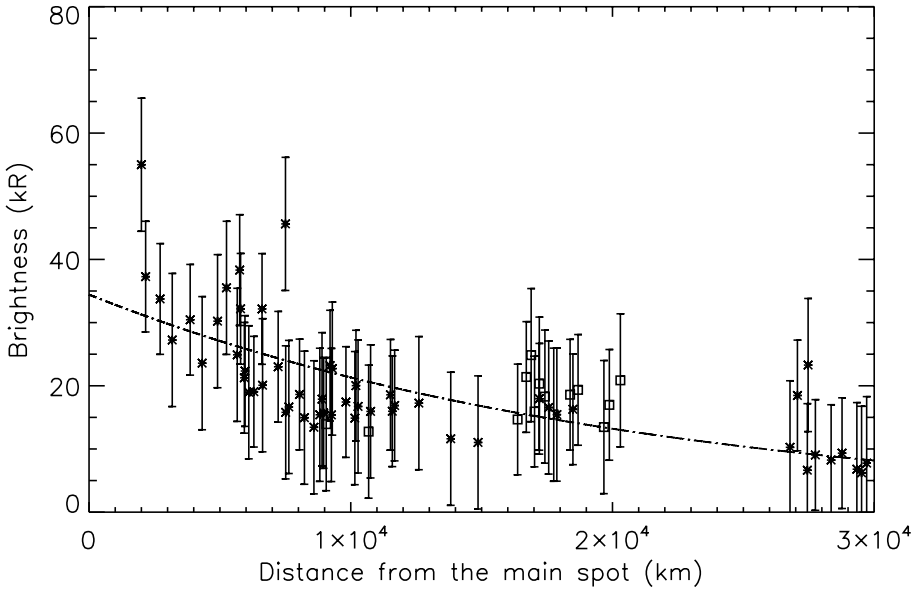

Figure 5.13: Maximum brightness as a function of the distance from the considered cuts to the IFP main spot location as described by our new reference contours. Note that this brightness is measured as seen from HST and does not correspond to the brightness an observer would see, when looking down vertically on the emission point. Northern hemisphere observations are represented by stars while southern hemisphere ones are represented by squares. The dash-dotted line is the least squares best fit with an exponential law. (from *Bonfond et al.*, 2009)

5.4.2 Tail brightness

The extracted vertical profiles also make it possible to measure the tail brightness as a function of the longitude angle between the profile and the main spot. Figure 5.13 shows the evolution of the maximum tail brightness with the distance from the spot. To compare these brightnesses, the tail is considered to be perpendicular to the line of sight. Consequently, the image brightness is corrected for the sine of the angle between the curtain direction and the line of sight. The least-squares fit of the brightness variation with an exponential law has an e-folding length of 21000 km and is shown on the same figure. This value is ∼4 times larger than the distance derived by *Hill and Vasyliūnas* (2002). However, their estimate is based on the first 15000 kilometers of the tail while our measurement includes points located twice as far. Considering that the latitudinal width of the tail is equal to Io's diameter as mapped along the field lines, we estimate the energy flux injected into the tail to be between 2 and 20 mW/m^2.

5.5 Discussion

The average altitude at the emission peak derived from vertical profiles is 900 km ± 125 km. This peak altitude is fairly constant with the distance from the main spot, which indicates that the mean energy of the precipitating electrons is relatively stable all along the tail. The decrease of the tail brightness shown in Figure 5.13 is most likely attributable to a drop in the particle flux, as suggested by color ratio measurements (*Gérard et al.*, 2002). However, the color ratio measurements only extend down to 20° downstream of the main spot while our data span the range from 4° to 60°. Figure 5.13 shows that the tail brightness appears to decrease faster close to Io than further downstream. This difference may be partly attributed to a contamination from emissions coming from secondary spots in the first few thousand kilometers. Nevertheless, it could also be consistent with models expecting the wake plasma velocity lag to decrease quickly before reaching an exponential regime. The injected energy fluxes inferred from the tail brightness lie between 2 and 20 mW/m^2 and are slightly higher than those predicted by *Ergun et al.* (2009). Assuming that the precipitating electron population is mono-energetic, the energy corresponding to 900 km is 2 keV if we consider the heated atmosphere from *Grodent et al.* (2001). On the other hand, *Gérard et al.* (2002) concluded that IFP electrons would have a typical energy of ∼55 keV under the assumption that the methane vertical profile and the pressure-altitude relationship at the North Equatorial Band (NEB) (*Gladstone et al.*, 1996) also apply to the polar regions. However, *Grodent et al.* (2001) showed that the thermal structure of the atmosphere is significantly modified by the auroral energy input. We note that our mean value is much lower than estimates inferred from color ratio measurements, but is closer to the energy that electrons would acquire in the 1 kV potential drop computed by *Ergun et al.* (2009). Nevertheless, the constant 430 km scale height of the vertical emission profiles indicates that the precipitating electron distributions can be neither mono-energetic nor Maxwellian. In the Earth's aurora, mono-energetic distributions are usually linked to inverted-V structures, where the electrons are accelerated by quasi-static potential drops. Maxwellian distributions are most often associated with isotropically heated populations. As expected, a power-law overestimates either the low energy part of the spectrum, if the spectral index is too high, or the high energy part in the opposite case, but it never produces a peaked curve resembling the observations. In the IFP tail case, the only distribution that reasonably reproduces the observations is a kappa

distribution with a relatively low characteristic energy. Such broad energy distributions could be related to electron acceleration by inertial Alfvén waves (*Ergun et al.*, 2006; *Swift*, 2007). The inertial Alfvén modes arise when one takes finite electron inertia into account in obtaining the dispersion relation and when the perpendicular wavelength of the Alfvén wave is on the order of the local electron skin depth (*Jones and Su*, 2008). Sensitivity tests performed either for the NEB atmosphere or for an empirical very hot atmosphere showed that the characteristic energies could change by a factor of four at most. However, vertical profiles produced by mono-energetic or Maxwellian distributions would never be as extended as observed, whatever the atmospheric model we use. Similarly, shifting the profile by 120 km up or down to simulate the 1-pixel pointing uncetainty could change the mean energies by a factor of two at most, but the conclusions on the best energy distribution would remain unchanged as well. Consequently, even if the predicted energy flux and the particle mean energy are reasonable, the assumption that electrons are accelerated by a localized static electric field as proposed by *Ergun et al.* (2009) does not seem to be in agreement with the vertical extent of the emission profile. Incidentally, we note that the κ spectral index we infer from our calculations is very similar to the $\kappa = 2.4$ value measured in the plasma torus by Ulysses (*Meyer-Vernet et al.*, 1995). However, an initial kappa population further accelerated through a static electric potential would lack low energy electrons, contradicting our observations.

Even if the definitive explanation is out of the scope of this paper, two possible reasons could be invoked to reconcile the high emission peak altitude and the weak but undeniable methane absorption in FUV spectra. First of all, energies derived from color ratio measurements assume a Maxwellian distribution of the precipitating electrons. We show here that a broader energy spectrum is needed to fit the observations. This implies that part of the impinging electrons can penetrate deep into the atmosphere, while another part will lose most of its energy in the upper atmosphere. Thus the observed absorption could result from the combination of strong absorption of the emissions caused by the more energetic particles and weak or no absorption of the high altitude emissions. The use of an auroral heated atmosphere as proposed by *Grodent et al.* (2001) could also help raise the methane homopause. Moreover, their 1D model only takes the diffusion of atmospheric particles into account, and does not consider 3D convective phenomena. Thus, the second possibility is that vertical winds triggered by auroral precipitation could also transport hydrocarbon molecules from the near homopause region to higher altitudes. The energy input

should be on the order of the total thermal energy in the atmospheric column to generate convection (*Smith*, 1998). At an altitude of 900 km, this thermal energy is equal to $\sim$ 125 J for a 1 m^2 cross section column. Consequently, assuming that tail precipitating energy flux is on the order of $10\,mW/m^2$, approximately 3.5 hours are required to provide this amount of energy. In a reference frame fixed to Jupiter, Io moves by $\sim 100°$ during this time interval. Strictly speaking, this would mean that convection is likely to take place above 900 km, but would be established in the downstream part of the tail only. However several points need to be taken into account that could mitigate this statement and lead to faster and deeper convection. First, we neglected the impact of the spots which are at least 10 times brighter than the tail. Secondly, we did not consider the fact that a point on the reference contour is heated repeatedly for 3.5 hours every Io rotation, i.e. approximately every 13h. Thirdly, we neglected Joule heating associated with Pedersen currents. And finally, it must be noted that the estimator provides the order of magnitude required to establish some convection, but does not replace a dynamic and self consistent 3D analysis of the impact of the IFP on Jupiter's upper atmosphere. Furthermore, a full 3D analysis would also take into account additional energy transport mechanisms such as conduction, horizontal advection and radiation, which may possibly mitigate or suppress the onset of convection. Further studies are needed to determine if and how convection takes place and whether it would originate deep enough to raise the hydrocarbon molecules.

5.6 Conclusions

Owing to its particular geometry and its isolation from any other auroral emissions on Jupiter, the tail vertical profiles provide a unique opportunity to verify that the observed emission profile is exactly in the limb plane. The observed peak altitude is surprisingly high ($\sim$900 km above the limb), which suggests that the involved electrons have a mean energy around 1-2 keV. As shown in the first section of this chapter, color ratio measurements showed that the tail is located approximately at the same altitude as the main spot and the precipitating electron energy was expected to be around 55 keV. Note that these estimates do not assume the same atmosphere model, but sensitivity tests performed with the NEB atmosphere indicate that such a difference in the energies cannot be attributed to the atmosphere model alone. The fact that hydrocarbon absorption was clearly observed was consid-

ered as the evidence that the emission takes place close to the methane homopause. Nevertheless, the estimate of the incoming electron energy rested on a set of hypotheses assumed to be reasonable but poorly constrained by measurements in the polar region. Consequently, the apparent disagreement between the occurrence of methane absorption and the observed tail altitude is an additional evidence that the structure of the atmosphere in the polar regions is still barely understood. The response of the atmosphere to the cyclic but highly localized energy input in the Io footprint would certainly deserve a detailed modelling, which is unfortunately out of the scope of this thesis.

The second surprise arising in this study is the width of the vertical profiles. The shape of the observed vertical emission profiles is too wide to be explained by a mono-energetic distribution of the precipitating electrons. Using the auroral heated atmosphere from *Grodent et al.* (2001), a best fit is obtained for a kappa distribution with a characteristic energy of $\sim$70 eV, a spectral index of 2.3 and a mean energy $\simeq$1 keV. Additionally, the peak altitude and the profile vertical width do not evolve significantly along the tail, while the brightness decreases with distance. Most of the previous interpretations of the tail emission, the most noticeable probably being the ones proposed by *Crary and Bagenal* (1997) and *Delamere et al.* (2003), assumed that the initial Alfvénic interaction would somehow evolve into a stationary process in the downstream direction. Hence, all the models specifically considering the tail generation mechanism assume a stationary regime (*Hill and Vasyliūnas*, 2002; *Delamere et al.*, 2003; *Ergun et al.*, 2009). In these stationary models, it seems natural (but not necessarily mandatory[3]) to attribute the electron acceleration to a static feature, i.e. a static electric field. The fact that our observations cannot be reproduced with mono-energetic or Maxwellian distributions puts this assumption into question. The broad energy spectrum suggests that inertial Alfvén waves accelerate the electrons that cause the tail aurora. One possible way to prove that inertial Alfvén waves are involved could rest on the presence of electron beams in the equatorial plane downstream of Io, showing that electrons are accelerated in both directions. Thus the same electron acceleration process could take place both for the spots and the tail.

After this detour on the spatial structure of the tail emission, the next chapter will come back to the spots and will examine the spatial structure of the spots. The understanding of the 3D extension of the Io footprint emissions is crucial for the

[3]Only the *Ergun et al.* (2009) model requires explicitly a static electric field

last step of the work: the study of the Io footprint brightness.

Chapter 6

Spots size

6.1 Foreword

In Chapter 3, I discussed the general morphology of the Io footprint, without considering the size of the different features in detail. We will now focus on this particular question and, once again, we will see that "simple" measurements of IFP characteristics on FUV images indeed provide us with precious information on the ongoing physics. The reader might be surprised that the essential but controversial problem of the IFP spots size appears so late in the present manuscript. This delay is totally deliberate. In Chapters 4 and 5, crucial Io footprint characteristics have been analyzed and new measurement techniques have been developed, which will prove to be indispensable to accurately establish the spatial extent of the IFP spots. The new IFP reference oval provides a great help in automating the measurement procedures, since we now know where to expect the spots to appear. Additionally, our systematic analysis of the relative positions of the spots showed that these features have to be interpreted individually. The study of the tail vertical extent led to the development of a new technique to systematize the analysis of emissions appearing above the limb. This method will now be extended to determine the spots altitude and vertical extent.

Therefore, the present chapter stands in the continuity of our previous investigations of the Io footprint characteristics. This present question is: How large is the Io footprint? This quantity is supposed to give us information on the size of the interaction region at Io. However, by looking for the answer to this obvious question, we will also find potentially surprising clues ... on the Jovian magnetic field.

6.2 Introduction

Various and potentially contradictory numbers can be found in the literature concerning the spatial extent of the Io footprint. *Connerney et al.* (1993) depicted the infrared IFP as a point source which could be 5° long at maximum. They suggested that the observed extension could be longer than the instantaneous charged particles precipitation area because the lifetime of H_3^+ lies between 10 and 1000 s. On one hand, studies based on the Faint Object Camera (FOC) onboard HST (*Prangé et al.*, 1996; *Prangé et al.*, 1998) describe the spot as being 400 (-200,+100) km long. Similarly, *Vasavada et al.* (1999), described the Io footprint as a 450 ± 100 km diameter circular patch, based on visible images acquired with the SSI instrument on board the Galileo probe. These results lead to the conclusion that the IFP size roughly corresponds to the projected size of Io in the Jovian ionosphere (see Figure 6.5 for more details). On the other hand, *Clarke et al.* (1996), using the second generation Wide Field and Planetary Camera 2 (WFPC2), measured the Io footprint spot to be as long as 1000 to 2000 km, much larger than Io's projected diameter. Later studies making use of the third generation Space Telescope Imaging Spectrograph (STIS) instrument showed that the Io spot can even be as long as 20° longitude (*Clarke et al.*, 2002). The authors explained the discrepancy with the FOC based measurements by the lack of sensitivity of this instrument, which would only be able to detect the brightest part of the emission. *Clarke et al.* (2002) found that the FUV emissions related to Io could sometimes appear as a pair of spots instead of a single one. These spots were found to be 12° apart at maximum and these authors noted that this length roughly corresponds to the mapping of the size of the stagnant plasma wake at Io (*Hinson et al.*, 1998). Consequently, they interpreted the brightest part of the Io footprint, no matter it is formed by one large spot or by multiple spots, as the signature of an interaction region consisting of Io and its plasma wake. On the contrary,*Gérard et al.* (2006) considered the different spots as distinct features and studied the spots multiplicity on a wider range of STIS images. By isolating the main spot, they measured its typical length to be on the order of 0.9° longitude. *Serio and Clarke* (2008) also measured the Io footprint size, but in a quite different way. They measured the footprint diameter as the FWHM width of the footprint perpendicular to the contour direction. They found that this quantity ranges from 500 to 2000 km and that it is not correlated with the Io centrifugal latitude (Figure 6.1). Finally, *Gladstone et al.* (2007) measured the main spot width

to be 400 km large. They also found that the the vertical extent of the main spot appears as long as 1000 km.

From the above review of the different numbers for the Io footprint size, it appears that the same name is sometimes used for different concepts. The Io footprint main spot is an emission volume which has a length (along the contour), a vertical extent and a width (perpendicular to the contour direction and horizontal). Depending on the orientation of the spot on the image, the measurable "size" of the footprint is usually a combined projection of these three parameters, with the exception of some particular cases. This situation was taken into account by *Prangé et al.* (1996), who clearly made the difference between the measured width and length. Since the exposure time may lead to strong corotational blurring, they rather relied on the width measurement, made possible by the particular location of the spot close to the limb. Then they verified that the measured length would be compatible with a 400 km spot blurred by the motion of the spot during the exposure. Nevertheless this noting does not necessarily invalidate issues related to the poor quality of FOC images. On the other hand, the footprint radii from *Serio and Clarke* (2008) appear to be a mix of projected width and vertical extension; a mix which is strongly dependent on the position of the spot on the image.

In order to determine the shape and size of the different spots, we made use of subsets of images showing the spots from different points of view. When the spots lie close to the central meridian line the footprint is generally seen from the side: a favorable configuration to estimate the lengths along the contour. On the other hand, some particular IFP curtain configurations observed when the spots are close to the limb show the IFP from above, allowing us to measure its width. Finally, we showed that it is possible to measure the vertical extent of the tail emissions since we can detect the point where the tail is right above the limb plane. Unfortunately, no image has been acquired in a configuration such that the spots are exactly above the limb, but there is a way to circumvent this issue.

6.3 The spots length

In the introductory section of this chapter, we have seen that the footprint length, whatever it means, has been expressed both in degrees of longitude and in kilometers. Which way is the more meaningful? How do we convert one unit into the other? Surprisingly, these questions do not have trivial answers. At first sight, units of

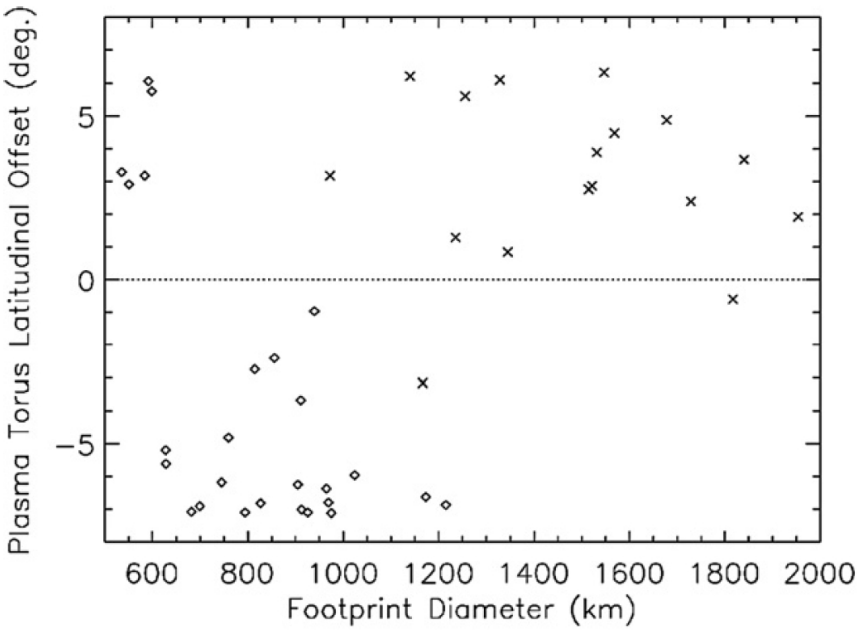

Figure 6.1: Plot of the footprint diameter as a function of the position of Io in the plasma torus. This quantity is measured as the FWHM of the emission perpendicularly to the contour direction. The diamonds correspond to the North and crosses to the South. (from *Serio and Clarke* (2008))

degrees seem far more convenient since they seem to allow an easy comparison with characteristic quantities in the Io orbital plane. However, this projection would only be accurate if the Jovian magnetic field was a perfect dipole aligned with the Jovian rotation axis. Actually, one degree of longitude measured at one point along the contour could correspond to a very different distance in kilometers than at another point, because of the off-centered configuration of the footpath, especially in the North. Additionally to this effect, the conversion from ionospheric longitudes to Io orbital plane longitudes is complicated by the convergence/divergence of the field lines[1] related to magnetic field anomalies. One definitive way to deal with the problem would be to map the distances along the magnetic field lines as we did on Figure 3.4. However, even if the results seem convincing at first sight, the accurate measurement of the footprint positions shed some doubts on the ability of the current magnetic field models to perform reliable mappings (Chapter 4).

Consequently, the question related to the link between degrees and kilometers remains, but the new Io reference oval can help us. Figure 6.2 shows the variation of the number of kilometers per degree measured in the Io orbital plane (solid line) as a function of the Io System III longitude based on our new reference contour. Therefore, for a given Io longitude the plot indicates the number of kilometers covered by the footprint when Io covers one degree along its orbit. The mean value is 481 km/° in the North and 463 km/° in the South. It is noteworthy that this quantity is fairly constant in the South but has two large peaks in the North, one at $\sim$50° and another one at $\sim$280°. These peaks mean that the spot moves quickly in these places, which can be explained by a divergence of field lines. The large increase around 50° of Io System III longitudes corresponds to IFP longitudes around 100°. Consequently, this IFP acceleration area clearly matches to the anomaly region described in *Grodent et al.* (2008a). Where does the second peak come from? A possible answer is that this peak corresponds to the so called "Dessler anomaly" (*Clarke et al.*, 2004). Indeed, the acceleration of the footprint along the contour suggests a divergence of the magnetic field lines in the contour direction. If this divergence (relative to the dipolar configuration) takes place in every direction, this could indicate that the magnetic field intensity is lower in this area, which could correspond to an "active sector" for radio emissions. We should however note that this argument is not a proof, since there is no one-to-one correspondence between a

[1] Two nearby field lines intercepting Io's orbit are always expected to converge when approaching the planet. By "diverging", I mean that they converge less than expected for a dipolar field.

divergence along a particular direction and the decrease of the field strength. In the southern hemisphere the VIP4 model predicts that the field intensity along the Io contour could vary by a factor of ∼2 without giving rise to any footprint acceleration, in accordance with the observations.

Nevertheless, our goal is to allow comparisons between distances measured in degrees and distances measured in kilometers. Therefore, we are interested in the number of kilometers per degree as measured on Jupiter. This quantity is represented by dashed lines on Figure 6.2. The mean values are 625 km/° in the North and 497 km/° in the South. However, we note that the conversion coefficient can vary by a factor of ∼5 in the North and ∼2 in the South. Consequently, there is no unique coefficient to convert degrees to kilometers. We will thus use both units to measure the MAW spot length before discussing which is the more convenient unit.

The first step consists in selecting images where the MAW spots are less than 30 degrees away from the central meridian line. We automatically extracted stripes along the IFP reference oval described in Chapter 4. Each stripe begins 5000 km upstream of the expected MAW spot position. Then, every 25 km in the downstream direction, we locate the corresponding pixel on the image and report its brightness. We repeat this operation for altitudes ranging from 0 to 2000 km. Once the stripes are formed, we add the brightnesses vertically in order to generate brightness profiles. The profiles are considerably more extended in the downstream direction because the tail emissions add to the downstream spots. Consequently, measurements of the profiles full width at half maximum (FWHM) cannot be used directly since they are usually contaminated with emissions unrelated to the MAW spot. Therefore, we chose to measure the upstream half width at half maximum (HWHM) in order to characterize the length of the main spot as if it were isolated from the other IFP emissions. The actual FWHM is then assumed to be twice as large as the measured HWHM. Figure 6.3 presents the main spot length FWHM expressed both in degrees and in kilometers. We note that the results in degrees are relatively constant for all longitudes and both hemispheres. The mean value is ∼900 km. Northern hemisphere measurements are only available between 110° and 230° System III longitudes. Based on Figure 6.2, we note that our value is in accordance with the 0.9° measured from *Gérard et al.* (2006). On the other hand, the mean FWHM expressed in degrees of longitude on the planet is twice longer in the South than in the North. Additionally, the southern hemisphere length varies with the Io longitude in an anti-correlated way compared to the number of kilometers per degree, as expected from previous

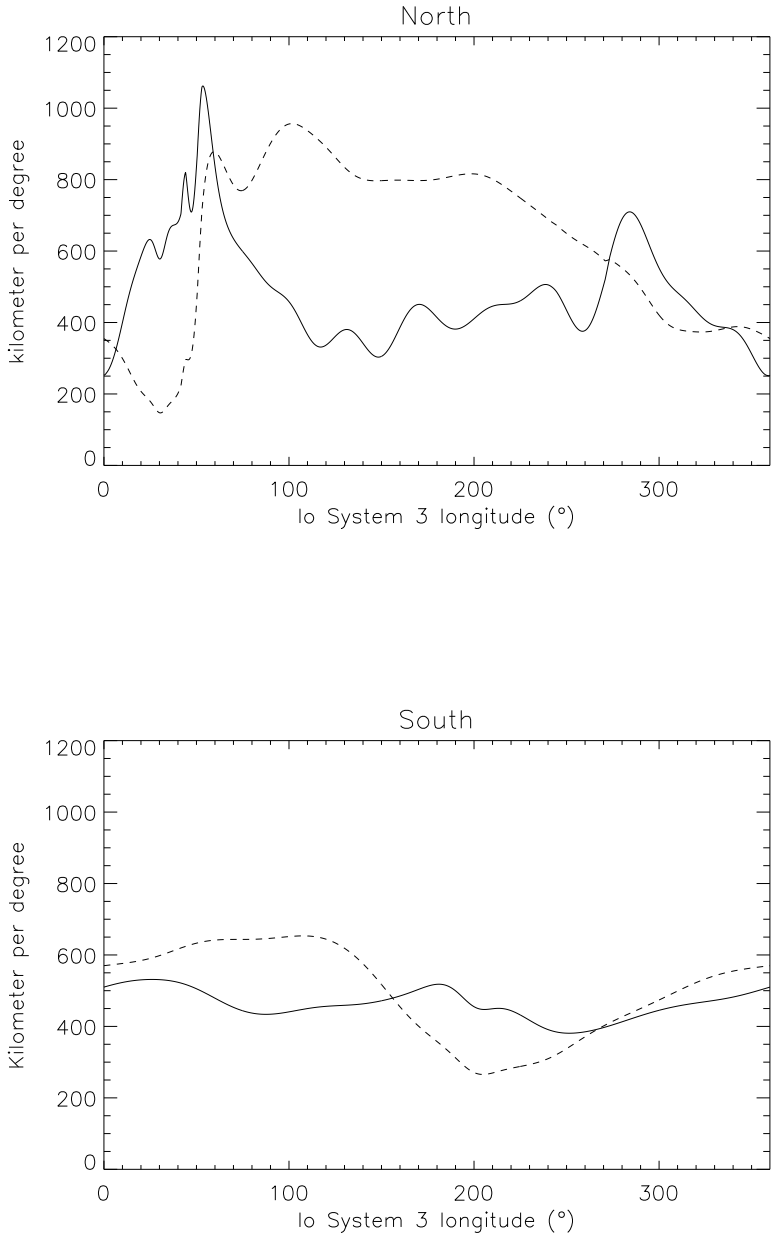

Figure 6.2: Evolution of the number of kilometers per longitude degree as a function of the System III longitude of Io for the northern and southern hemispheres. The solid line corresponds to longitudes measured along the orbit of Io while the dashed line corresponds to longitudes measured on the planet.

considerations.

The fact that both reference contours have roughly the same size and that the main spot length does not vary much (outside the anomaly regions) indicate that, compared to the dipole case often assumed in theoretical models, the observed contours are off-centered and distorted but the length measured in kilometers does not vary significantly. As a consequence, these distances should be preferentially used when comparing Io footprint characteristics.

In figure 6.3, three STIS southern hemisphere data points have considerably higher values than the other data points. These points are not outliers but correspond to exceptionally long footprints like the one shown in Figure 3.6 a. The plots clearly demonstrate that these cases are atypical and should be considered with caution when drawing conclusions on the spots length.

We have seen that the Io footprint typical length was around 900 km. This observationally derived value should be compared to two quantities: the length covered by the MAW spot on the image during a typical exposure time and the projected Io diameter along magnetic field lines. Figures 6.4 displays the length covered by the IFP in a reference frame fixed in local time for a typical 100 seconds exposure time. This quantity approximately varies in a similar way as the above mentioned number of kilometers per degree in the Io orbital plane. The main difference is that the distances are now computed in local time reference frame and not in a System III reference frame. This means that they combine not only the motion of the footprint along the contour, but also the apparent motion of the contour as seen from the Earth. The values plotted here should be projected relatively to the image viewing angle to provide the actual IFP motion on the image. However, this later step is not necessary for the issue we would like to discuss here. The displacement of the IFP during the exposure time generates a motion blur and we would like to know how this affects the measured footprint length. In the southern hemisphere, the covered distance ranges from $\sim$ 200 km to $\sim$ 350 km, while in the North, the distance varies from $\sim$50 km to $\sim$ 800 km. If we model the MAW spot brightness profile with a Gaussian function and if we convolve it with a step function as long as the original Gaussian FWHM, the resulting FWHM is only 20% longer. We will see in Chapter 7 that the footprint spots can experience brightness variations on the order of 50% of the intensity on timescales of one minute. In the worse case scenario, the spot brightness first decreases by a factor of 2 until the middle of the exposure time and then increases again up to the maximum. In this case, the length increases by

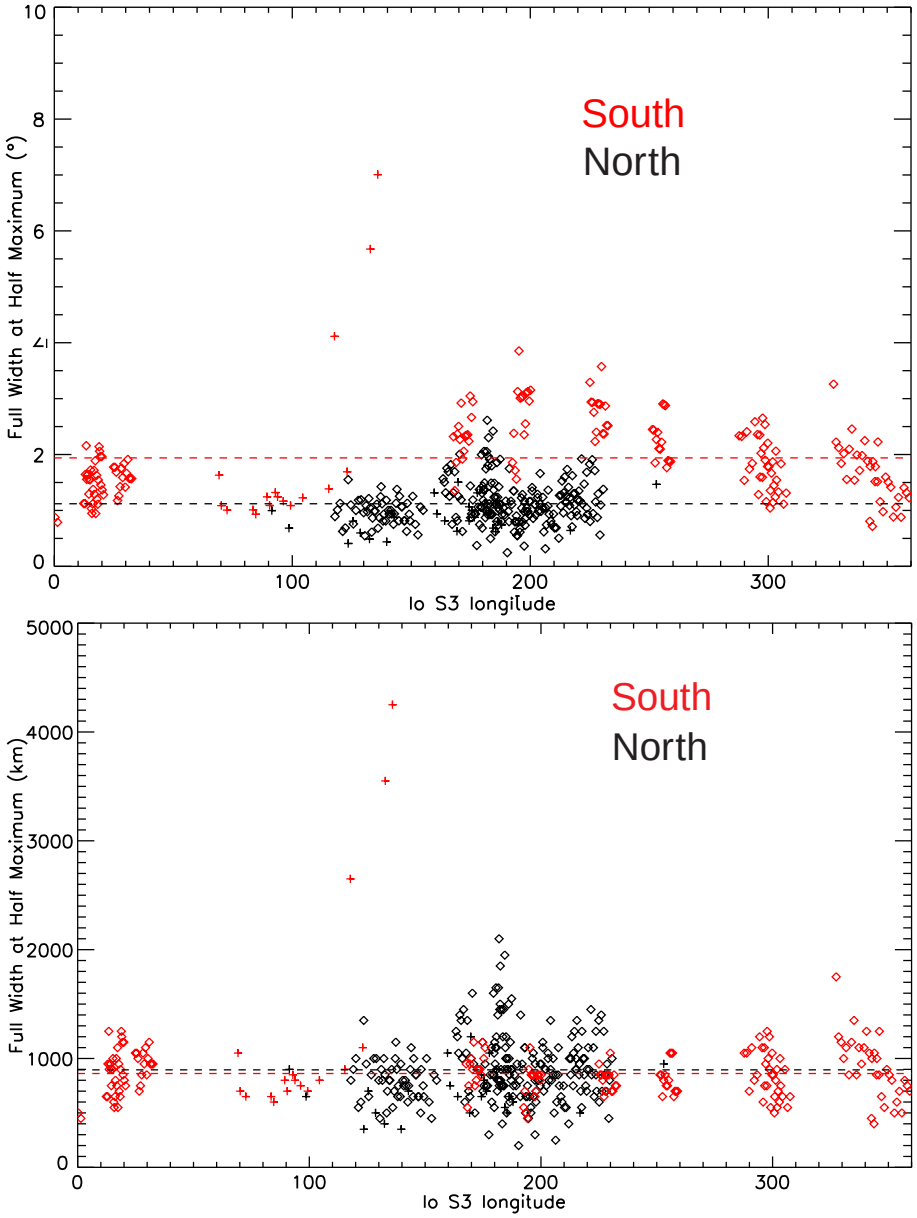

Figure 6.3: Length of the Io footprint main spot as a function of the Io System III longitude. The data points corresponding to STIS measurement are represented with crosses while ACS data are noted with diamonds. Black symbols are for measurements in the northern hemisphere while red symbols are measurements in the southern hemisphere. The Full Width at Half Maximum represented in the plots is actually computed as twice the Half Width at Half Maximum.

approximately 30%. Thus, even in the most critical cases, the length measured on 100s exposure images is only moderately affected by the motion blurring. However, in this study no measurements have been made in these critical areas of the northern hemisphere where the MAW spot length is difficult to observe. If the covered distance is one half of the initial Gaussian FWHM, the length increases by 7% at maximum. Consequently, we can consider that the measured length corresponds to the instantaneous length.

Figure 6.5 shows the size of the unperturbed Io flux tube footprint in the northern hemisphere according to the VIP4 magnetic field model. The IFT length varies from $\sim$ 200 km to $\sim$ 350 km. The FWHM of the STIS and ACS point spread functions are barely larger than two and one pixels respectively and, accordingly, the widening of the spot cannot be attributed to instrumental effects. As a result, the MAW spot length shown on Figure 6.3 appears to be three to four times more elongated than the expected flux tube length. This result does not necessarily mean that the interaction region at Io is three to four times as large as Io. The plasma interaction between Io and the Jovian magnetosphere implies a piling up of the field lines at Io. Therefore, it is expected that the real (i.e. perturbed) flux tube length is larger than the unperturbed one. However, the spot is not located at the foot of the Io flux tube but rather at the foot of the current carrying Alfvén wing. *Jacobsen et al.* (2007) showed that non-linear effects on the Alfvén waves propagation could considerably increase the length of the Alfvén wing (Figure 6.6). Additionally, *Jacobsen et al.* (submitted) showed that such non-linear effects are necessary to explain why the electron beams observed by Galileo are located so close to Io.

6.4 The spots vertical extent

In the previous chapter, we made use of images where the tail emissions were observed above the Jovian limb. Here we consider a subset of these images where the main spot can be seen above the limb. Contrary to the tail, we cannot be sure that the main spot is in the limb plane, or, more exactly, we are sure that the spot in not in the limb plane. Consequently, the apparent altitude is not the real altitude and we have to find another strategy to estimate the actual altitude of the main spot emission. Since we know the longitude and the latitude of the main spot thanks to the new reference contour, we can compute the expected MAW position on the image if its real peak altitude is the same as for the tail (i.e. $\sim$ 900 km). If the

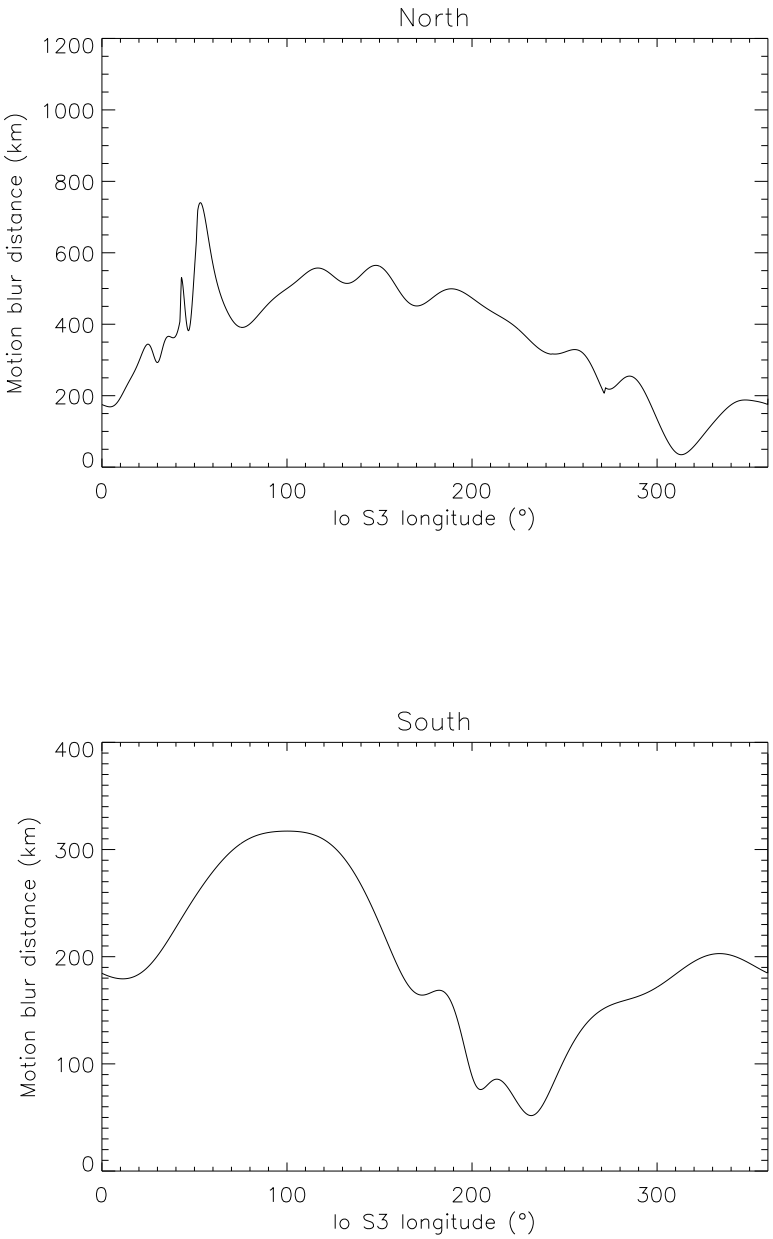

Figure 6.4: Plots of the motion blur distance for an exposure time of 100 seconds as a function of the Io System III longitude. The motion blur distance is the distance covered by the MAW spot in a reference frame fixed in local time. Contrary to Figure 6.2, this quantity includes both the motion of the footprint along the contour and the motion of the contour owing to the planetary rotation.

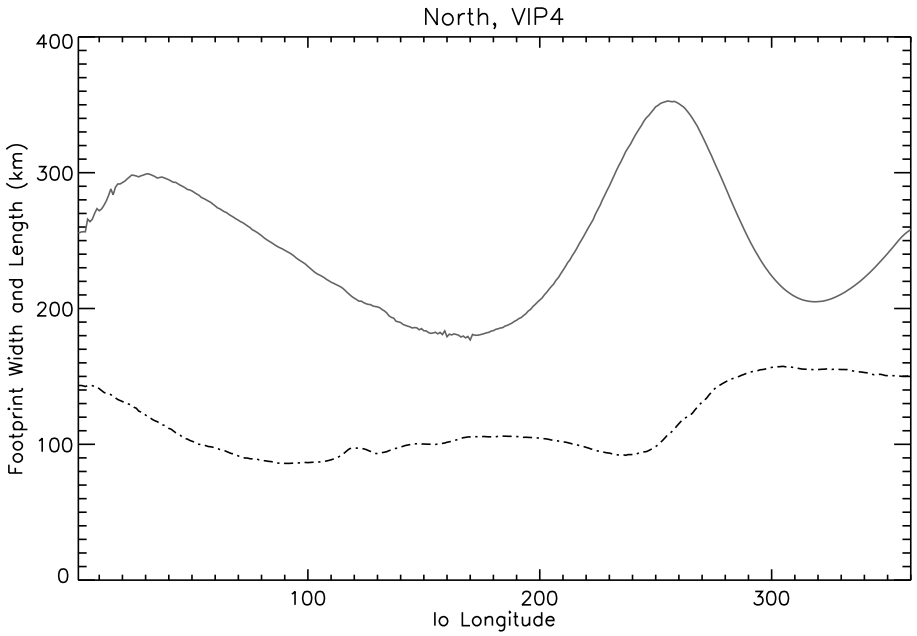

Figure 6.5: Projected size of Io along unperturbed magnetic field lines as modeled by VIP4 for the northern hemisphere. The solid line represents the Io diameter along the Io orbit projected in the northern Jovian ionosphere. This quantity thus stands for the length of the Io flux tube (IFT) footprint. The dashed line represents the diameter of Io along the Io-Jupiter line projected in the northern Jovian ionosphere. This quantity thus stands for the width of the Io flux tube (IFT) footprint.

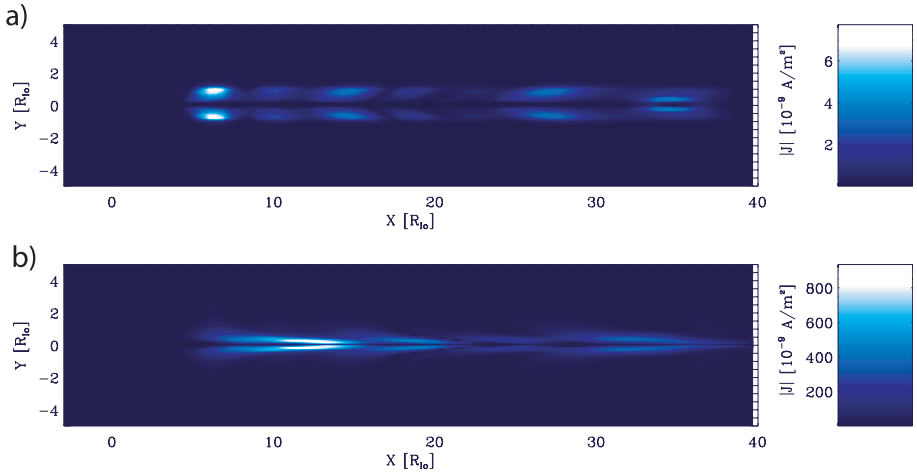

Figure 6.6: Projection of the absolute value of the current density in the northern Jovian ionosphere in the case of a quasi-linear interaction (a) and of a strongly non-linear interaction (b). The non-linear effects considerably stretch the Alfvén wing in the corotation direction, which could explain why the observed length of the MAW spot corresponds to three to four times the length of the unperturbed Io flux tube. (from *Jacobsen et al.* (2007))

observed peak altitude differs significantly from the simulation, this would indicate that the main spot is not at the assumed altitude.

During the 10862 observation program, the IFP MAW spot appears above the planetary limb for 14 orbits. Similarly to *Bonfond et al.* (2009), we gather image data as sets of 3 successive images and perform radial scans on the Io footprint area. This time, we are not looking for the highest peak altitude as a function of the scan angle, but we seek the maximum brightness. We compare the peak altitude of this particular profile with the simulated peak altitude (Figure 6.7). The mean difference between the modeled altitude and the observed one is 85 km with a standard deviation of 155 km. We can thus reasonably conclude that the the MAW spot peak altitude is similar to the tail peak altitude, which confirms results from color ratio measurements (see *Gérard et al.* (2002) and Chapter 5).

An important result from Chapter 5 is that the vertical scale height of the tail emission is so large that its width can be modeled only by assuming a kappa energy distribution for the incoming electrons. This result is not in agreement with expectations from electron acceleration by a static electric potential and favors mechanisms related to inertial Alfvén waves (*Swift*, 2007). Consequently, the shape of the emission vertical profile of the MAW spot is also expected to provide us with information

on the acceleration mechanism. Fits of a Chapman profile (Equation 5.1) on the observed curve indicates that the mean scale height is 366 km ± 53 km. These values are similar to those observed for the tail. Additionally, a Chapman profile with such a scale height has a FWHM of ∼850 km, which is consistent with the estimates from *Gladstone et al.* (2007). As a conclusion, the precipitating electrons generating the IFP main spot appear to have the same characteristics as for the tail, i.e. a kappa energy distribution with a mean energy $\sim 1 - 2$ keV.

On one single orbit, leading spot emissions can also be observed above the limb. The brightness and peak altitude profiles as a function of the rotation scan angle[2] are shown on Figure 6.7. While the observed and the modeled altitudes are fairly similar in the tail and for MAW spot, the observed altitude appears to be $\sim$ 200 km smaller. The fact that the TEB emissions peak at a lower altitude could also explain some misalignment between the TEB spot and the remainder of the tail. An example of such a misalignment can be seen on the top South stripe of Figure 1.10. This slight shift could be interpreted as a latitudinal shift or an altitude shift. Our new observations clearly favor the latter. These lower altitudes suggest that the TEB spot electrons mean energy is larger than for the MAW spot and the tail.

6.5 The spot width

The actual Io footprint width can be estimated only if two restricting conditions are fulfilled. First, the viewing angle should be such that the main spot is seen from the front or from above. Second, the exposure time should be short enough to avoid significant shift of the IFP position during the exposure. This latter constraint imposes the use of images derived from time-tag sequences.

Similarly to the method applied to estimate the spots length and vertical extent, the first step consists in identifying the images where the footprint is in such a configuration that the main spots and the beginning of the tail are seen from the front or from the top. Unfortunately, the number of suitable time-tag sequences is limited to two. In order to avoid the motion blur which affects the width without losing too much signal, the time-tag sequence list has been divided into 10-second exposure time images. These images were subsequently shifted in order to compensate for the

[2]Our method consist is taking radial cuts while rotating the planet on the images. 0° corresponds to the equator and -90° corresponds to the South pole, but the intermediate values are not strictly equivalent to latitudes because of the inclination of the planet.

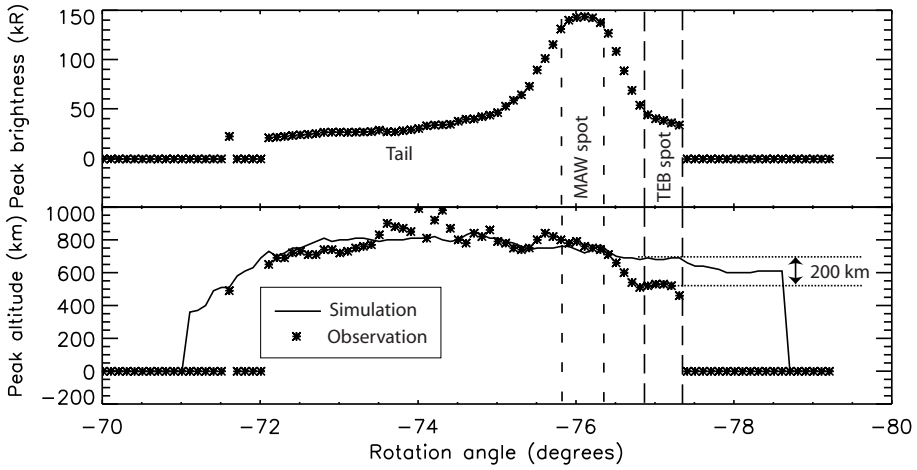

Figure 6.7: Example of tails and spot profiles above the limb as a function of the rotation scan angle (stars). The expected apparent altitude of an Io contour located at 900 km is represented in solid line. The MAW spot corresponds to the peak in the brightness profile. All along the tail as well as in the MAW spot region, the observed and the predicted apparent peak altitudes match fairly well. In this example, a faint TEB emission also appears upstream of the MAW. Its apparent altitude is 200 km lower than expected.

IFP motion.

Figure 6.8 shows an example of images generated from the same sequence with and without the motion compensation. It is noticeable that the motion seems to increase the IFP width, which directly indicates that the instantaneous IFP curtain width is significantly smaller than the motion blur extent. The width is measured by extracting a brightness profile perpendicular to the contour. However, the width of this profile is very dependent on the orientation of the footprint on the image, and thus does not represent the actual curtain width. Actually, even in our very restrictive case selection, the footprint is never observed exactly from the front or exactly along magnetic field lines and thus we have to model the real image geometry to take these orientation effects into account. To demonstrate the existence of these effects and evaluate their impact, we made use of the 3D IFP emission model we will use in the next chapter in order to simulate the apparent IFP width with different actual input width. The model will be described extensively later, but for now, it suffices to note that it consists in simulating the FUV optically thin emissions for an IFP formed of three independent spots and an extended tail. The length and the vertical extent of these different features is set according to the measurements

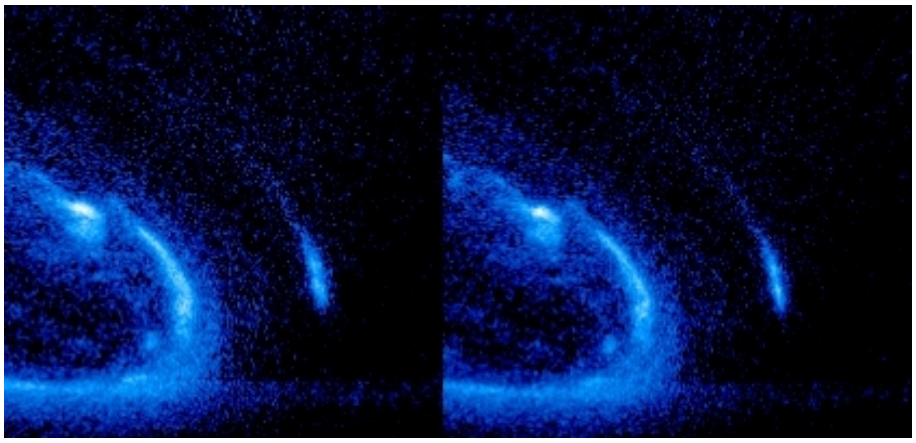

Figure 6.8: Example of Io footprint as seen from above without (left) and with motion compensation (right).

described above. We generate images of the IFP in agreement with the actual IFP geometry but varying the width. Among the unavoidable hypotheses we have to take on the IFP geometry (see section 7.4 for more details), we postulate that all the IFP features, i.e. the three spots under consideration and the tail, have the same width. Then we compare these modeled apparent widths with the measured one (Figure 6.9).

In both cases, the observed profile is as thin or even slightly thinner than the thinnest model profile. We note that, because of the finite pixel size and PSF size, at some point, reducing the input width has a minor impact on the model output. As long as the simulated FWHM input remains less than ∼170-190 km, the modeled width remains fairly similar to the measured ones. Major differences only arise when this threshold is overtaken. As a result, only an upper limit can be estimated for the IFP width and its value is around 200 km.

The expected projection of Io's width along VIP4 magnetic field lines lies between 100 and 160 km (Figure 6.5). Contrary to the spots length, no interaction model predicts a significant increase of the IFP width compared to the projected Io width (Figure 6.6). Our measurements only provide a maximum value for the width, but they show that the diameter of the interaction region as seen from the front cannot be wider than twice the size of Io. These values are in accordance with the idea that the IFP width is similar to the projected diameter of Io.

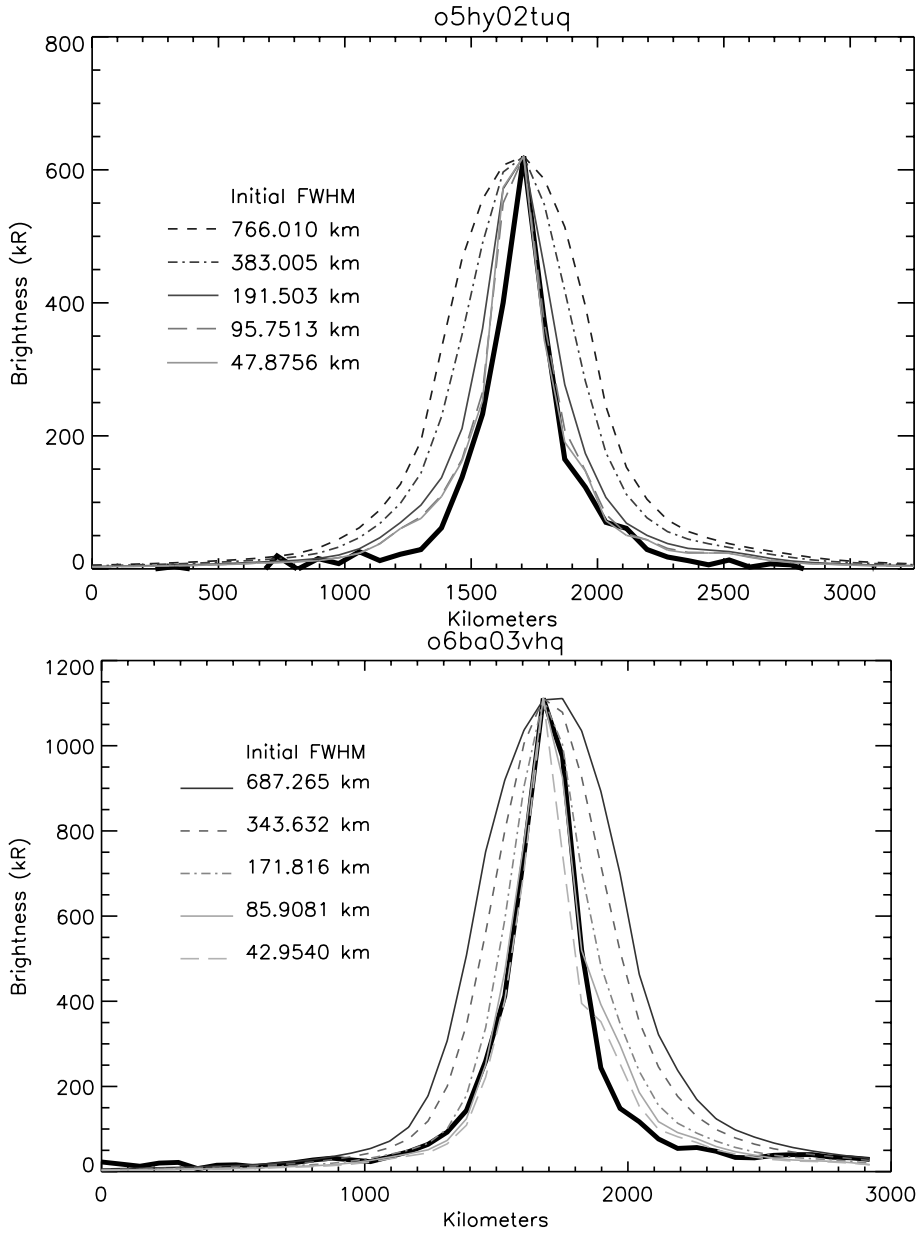

Figure 6.9: Comparison of measured Io footprint width profile with simulated output profiles computed with different input widths. Both cases are from the northern hemisphere. The Io System III longitude is 209° in the first case and 145° in the second one.

6.6 Conclusions

The size of the Io footprint is an important issue for understanding the Io-Jupiter interaction. Based on the apparent restricted size of the Io footprint on some images, some authors suggested that the interaction should be limited to Io itself. On the other hand, its apparent extended length as seen on other images led other authors to reach the opposite conclusion: i.e. the interaction region should be as large as the stagnating wake observed downstream of Io. We took advantage of the increased number of images benefiting from both high resolution and high sensitivity to sort out these contradictory results.

First of all, we argue that the 3D structure of the Io footprint has often been misunderstood. Following *Gérard et al.* (2006) as well as conclusions from the previous chapters, the different spots are distinct features that must be considered separately. Secondly, each feature has a length along the contour, a vertical extent and a width. Therefore, each image is a 2D projection of a three dimensional emission region. With the help of the observations catalog and our knowledge of the IFP spots location, we carefully selected subsets of images where the spots were respectively seen from the side, above the limb or from above.

The length of the main spot is on the order of 900 km FWHM. We showed that this value is not a consequence of the motion of the spot during the exposure nor caused by the instrumental PSF. This length is significantly larger than the size of Io but also significantly smaller than the size of the stagnating plasma wake when projected along unperturbed magnetic field lines. However, the field lines are indeed perturbed by the presence of Io and the subsequent broadening of the main spot length along the contour was expected from simulations, even if the core of the interaction remains relatively close to the satellite.

The IFP width measurement is by far the most delicate measurement. Our measurements only provide a maximum value ($\sim$ 200 km) but this number is also consistent with an interaction region restricted to the immediate Io neighborhood.

As far as the MAW spot vertical extent is concerned, no obvious difference is observed compared to the tail emissions. The peak altitude lies around 900 km and the scale height is approximately 350-400 km. As a result, the mean precipitating electron energy is on the order of 1-2 keV. Additionally, the broadness of the impinging electrons energy distribution suggests that inertial Alfvén waves are the root cause for the electrons acceleration. This conclusion is nevertheless less surprising for the

MAW spot than for the tail since no steady state was expected to be established for the spots. The TEB spot peak altitude appears to lie at 700 km, implying a larger mean electron energy than for the MAW spot.

As far as previous studies are concerned, we may conclude that the large spot sizes observed by *Clarke et al.* (2002) are untypical and 0.9-degree long MAW spots as measured by *Gérard et al.* (2006) correspond much more likely to the actual typical length. The small length of the IFP, as estimated from visible instruments (*Vasavada et al.*, 1999; *Gladstone et al.*, 2007) and from the FOC camera (*Prangé et al.*, 1996; *Prangé et al.*, 1998), is most probably a consequence of their limited sensitivity. Moreover, our observations confirm our initial expectation concerning the IFP diameter as measured by *Serio and Clarke* (2008): the quantity that they have measured is not the actual width of the IFP but the projection of its vertical extent, which is strongly dependent on the viewing angle.

Finally, our analysis of the motion of the MAW spot on the northern hemisphere shows the presence of two sectors where the spot is significantly accelerating along the contour. If these regions are associated with magnetic anomalies, the largest one is related to the large anomaly identified by *Grodent et al.* (2008a) while the smallest one could be related to the so-called "Dessler anomaly".

Chapter 7

Brightness variations

7.1 Foreword

The Io footprint is made of distinct spots (at least three) followed by a downstream tail. In the previous chapters, we analyzed their position, their relative motion, their altitude, their respective sizes, etc.. All these quantities define the spatial characteristic of the phenomenon and were based either on the localization of the features or on the measurement of their extent. It is now time to focus on the second type of information contained in an image: the brightness.

The present chapter is divided into two parts. In the first part, we will mainly focus on short-timescale relative variations of this brightness. Indeed, the Io footprint fluctuates with several different timescales, and each of them is typical of one or several processes. Analyzing these characteristic periods can thus help us in identifying the different ongoing processes.

Moreover, we are also interested into the absolute values of the emitted brightness and power. This information is essential to understand the energies at play both in the whole interaction and in its different parts. Nevertheless, we will see that converting the number of counts accumulated in the detector pixels to a meaningful information is not as easy as it might seem at first sight. First, it is necessary to correctly identify which feature is measured. For example, does the measured power encompass all the spots or just isolate one? On which basis is the mean brightness computed? Second, the observing geometry has to be well understood. Hence, the brightness of a three dimensional optically thin emission region strongly depends both on the observer's position and on the size of the source region, since the light will not accumulate in the same way along the line of sight. As a consequence, new

measurement methods had to be developed based on the accurate estimate of the position and the size of the different footprint features, which is the reason why this chapter comes at the end. All the issues related to the observation geometry which need to be addressed are now discussed in detail.

7.2 Short timescale brightness variations

7.2.1 Publication: *The ultraviolet Io footprint short timescale dynamics*

B. Bonfond, J.-C. Gérard, D. Grodent

Laboratoire de Physique Atmosphérique et Planétaire Université de Liège, Belgium

J. Saur

Institut für Geophysik und Meteorologie Universität zu Köln, Germany

This article was originally published in the March 2007 issue of Geophysical Research Letters (*Bonfond et al.*, 2007).

7.2.1.1 Abstract

The electromagnetic interaction between Io and Jupiter's magnetic field leads to single or multiple ultraviolet spots near the feet of the Io flux tube. Variations of spot numbers and brightness and of inter-spot distances have been observed to be linked to Io's position in its plasma torus. We have studied the evolution of the Io UV footprints with a time resolution of a few tens of seconds using the Space Telescope Imaging Spectrograph (STIS) in time-tag mode. We present evidence of systematic strong brightness variations of the main spots (up to 50%) with a typical growth time of 1 minute. Additionally, unanticipated simultaneous fluctuations of both primary and secondary spots have also been found in the southern hemisphere. Our findings suggest that the footprint brightness is not only actively controlled by the plasma directly interacting with Io but also by the poorly constrained electron acceleration region between Io and Jupiter.

7.2.1.2 Introduction

The presence of ultraviolet (UV) footprints shifted up to 15° downstream from the estimated location of the extremities of the field lines passing through Io (*Clarke et al.*, 1998) is a spectacular signature of the interaction between a satellite and its planet. These features provide an outstanding possibility to remotely sense Io's interaction with Jupiter's magnetosphere. Io's interaction is created by the motion of Io relative to the Io plasma torus (see reviews in *Saur et al.*, 2004 and *Thomas et al.*, 2004), which perturbs the plasma and the magnetic field around Io, and which is also the root cause for the Io footprints (IFP). The first model for Io's interaction, the unipolar-inductor model, was developed before the plasma torus was discovered. In this description, a steady state current loop is formed which connects Io with Jupiter's ionosphere along its magnetospheric field. (e.g. *Goldreich and Lynden-Bell*, 1969). Although Alfvén waves have been considered early for Io's interaction (*Goldreich and Lynden-Bell*, 1969; *Goertz and Deift*, 1973), their importance was firmly established only after the discovery of the dense Io plasma torus by Voyager (*Neubauer*, 1980; *Goertz*, 1980). In this framework, Alfvén waves propagate the perturbations caused by Io towards Jupiter and form an Alfvén wing system, which is inclined with respect to Jupiter's magnetic field in the downstream direction. Later models (e.g. *Wright and Schwartz*, 1989) predict substantial reflections of the Alfvén waves at the torus boundaries. Furthermore, models considering the electron finite inertia (*Crary*, 1997) imply the generation of electron beams towards Jupiter. Analysis of Galileo observations (*Chust et al.*, 2005) suggests that the low frequency Alfvén waves should be reflected while high frequency, small scale waves are able to cross the torus boundaries. Io's interaction also generates a wake of slow plasma behind Io. The eventual acceleration of the wake particles through momentum transfer from the Jovian ionosphere drives an electric current along the field lines (*Hill and Vasyliūnas*, 2002; *Delamere et al.*, 2003) that causes the trailing tail observed downstream of the footprints on ultraviolet and infrared images (e.g. *Clarke et al.*, 2002; *Connerney and Satoh*, 2000). Observations of the IFP demonstrate that Io's interaction leads to acceleration and precipitation of ∼50 keV electrons in the Jovian ionosphere (*Gérard et al.*, 2002). The collision of these particles withH_2 molecules and H atoms causes optical emissions at both UV and IR wavelengths. The primary spot is frequently followed downstream by one or several secondary spots (*Clarke et al.*, 2002; *Connerney and Satoh*, 2000). Their location and the inter-spot distances appear to be consistent with Alfvén wave reflections

inside the torus (*Gérard et al.*, 2006). The interaction between the plasma torus and Io's ionosphere also gives rise to auroral emissions at Io. Auroral emission is observed within Io's atmosphere on the sub-Jovian and the anti-Jovian sides of Io (*Roesler et al.*, 1999; *Oliversen et al.*, 2001). The authors show that the intensity of this emission includes temporal variability on time scales of ca. 15 min. The present study focuses on the footprint UV emissions and their fluctuations. An increase of the footprint brightness has been found when Io is near the center of the torus, where the plasma is denser (*Gérard et al.*, 2006). This result suggests that the IFP long timescale brightness variations are controlled by the strength of the Io-plasma torus interaction. In situ measurements (*Frank and Paterson*, 2000a) and Io auroral observations (*Roesler et al.*, 1999; *Oliversen et al.*, 2001) have shown that the interaction between Io and the plasma torus contains a fastly varying component, but no counterpart has been observed so far for the footprint. Here we present evidence that the IFP is also a highly dynamic process on timescales around one minute.

7.2.1.3 Data processing

Most of the previous work on the Io UV footprints used time integrated images provided by the successive cameras (e.g. FOC, WFPC2, STIS and ACS) on board the Hubble Space Telescope (HST). During the five Jovian auroral observation programs conducted with the HST/STIS camera throughout its lifetime (from 1997 to 2004), 43 imaging observations (31 in the northern hemisphere and 12 in the southern one) were obtained in time-tag mode. In this observation mode, the positions and the arrival time of the incoming photons are registered. This specific capability of the Multi-Anode Microchannel Array (MAMA) photon counting technology has a time resolution of 125 µs. Each pixel of the 1024×1024 pixel detector subtends a 0.024 arcsec angle and the point spread function covers approximately a 3×3 pixels square. All the observations considered in this study were made with the SrF2 filter (central wavelength: 148 nm, FWHM: 28 nm) which rejects most of the Ly-α emission, largely contaminated by the geocoronal dayglow emissions. The duration of the time-tag sequences varied from 120 to 300 seconds. Most include one or two event stream interruptions due to buffer overflows. The collections of photon detection events are used to reconstruct images which may be integrated over any chosen exposure time by selecting the events in the required time range. In order to achieve an adequate balance between time-resolution and signal-to-noise

ratio, we build 10-second exposure images from the time-tag datasets. The resulting sequences of images were then processed as standard STIS images, that is, dark count, flat field and geometric corrections have been performed. All time-tag observations considered here focus on the auroral morphology, but not specifically on Io footprints. Therefore, the Io footprint is not always visible nor in a favorable position. As a result, only 12 sequences in the north and 5 in the south turned out to be suitable. The Io longitudes coverage (System III) corresponding to the northern footprint observations ranges from 123° to 201° while the southern one spans 84° to 99°. In order to compensate for the footprint motion during the exposure, the sub-images were shifted according to the deviation deduced from the VIP4 magnetic field model (*Connerney et al.*, 1998). This technique allows one to stack the footprint sub-images from the same sequence in the same reference frame. We then subtracted the Jovian background emissions in order to isolate the intrinsic IFP emissions. The footprint emission brightness as a function of longitude was obtained by extracting a 21-pixel wide stripe containing the main spots and the beginning of the tail. The brightnesses were integrated over the 21 pixels in order to obtain a linear profile. Figure 7.1 presents an example of a linear profile and its characteristic behavior during a time-tag sequence. Using the correction deduced from the VIP4 model, all the profiles can be plotted in the same reference frame with the x-axis for the longitudes and the y-axis for time to visualize the temporal evolution of the footprints. Figure 7.2 shows examples of the typical behavior of aligned and color-coded profiles both for the northern and the southern hemispheres. That way, successive profiles can be summed in order to integrate the brightness over a longer time period, and therefore to increase the signal-to-noise ratio. In Figure 7.2, a temporal smoothing of the profiles has been performed since all the lines represent profiles with a 20-second integration time, even if the time step between two lines is 10 seconds. The vertical alignment of the brightness peaks of the profiles in this figure confirms that the VIP4 accuracy is sufficient for lining-up the profiles.

7.2.1.4 Observations

Brightness fluctuations In the northern footprint brightness profiles (e.g. Figure 7.1), the main spot can always be clearly distinguished from the secondary ones and from the trailing tail. The second spot is usually fainter and can hardly be identified in short exposures (∼10s) but it is revealed by increasing the integration time. Significant brightness variations of the main spot are systematically observed

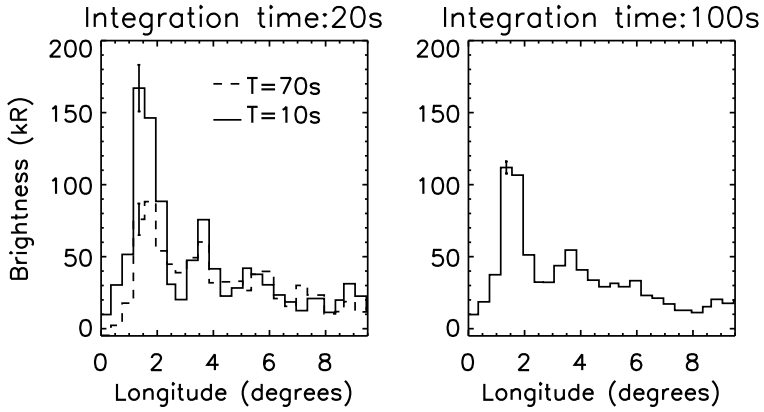

Figure 7.1: (Left) Profiles of the northern footprint integrated over 20 seconds. The first exposure starts 10 seconds after the beginning of the time-tag sequence while the second one starts 60 seconds later. This typical time-tag sequence shows significant brightness variations of the main footprint. (Right) Profile of the same northern footprint integrated over 100 seconds. The weak secondary footprint barely identifiable on 20-second exposures is now clearly distinguished. The sequence was observed the 26 February 2000 at 01:57:41 UT.

in all northern hemisphere datasets, ranging from 17% to 50%. Figure 7.3 demonstrates that these fluctuations are far above the noise level and independent from background fluctuations. Moreover, a characteristic growth time of ∼60 seconds can be determined from the light curves (Figure 7.4a). No System III influence of the short timescale brightness variability has been identified, although the limited number of sequences does not permit any definitive conclusion. In the southern hemisphere, when a secondary spot is present, it is generally as bright or brighter than the primary spot, so that both spots can be clearly identified in the profiles. In all southern sequences, the brightness variations are on the same order of magnitude as in the north. The variations range from 25% to 36% for the primary spot and from 20% to 32% for the secondary spot.

Simultaneous fluctuations In the southern hemisphere, the correlation between the brightness of the first two spots is striking (see for example Figure 7.4b and 7.4c). In the present dataset, the secondary spot is separated from the first one in four out of five cases. In three cases out of four, the correlation coefficients for the temporal evolution of the intensities of the primary and the secondary spot calculated for the sequences preceding the data interruptions is as high as 0.9, largely above the significance threshold (∼0.7 at 99%). In the fourth case, no correlation is observed.

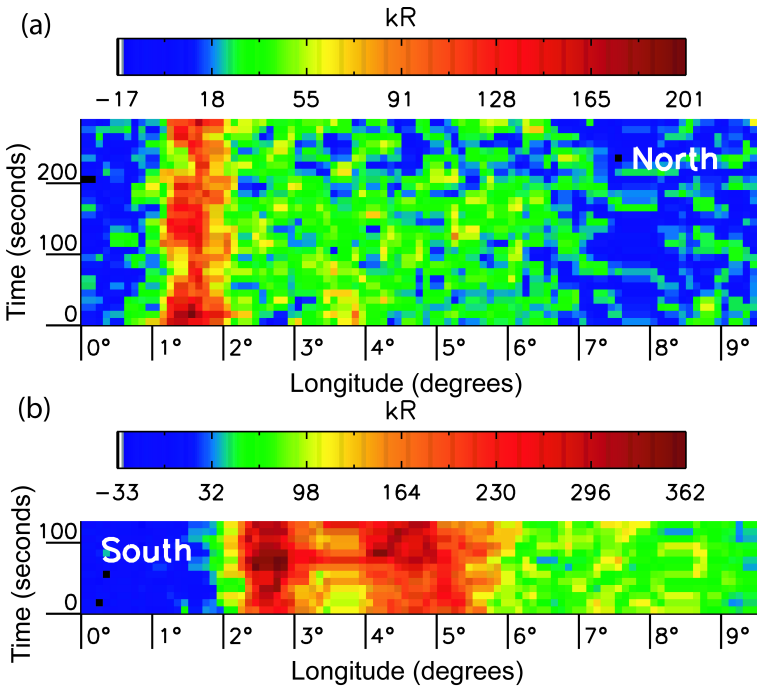

Figure 7.2: (a) Evolution of the profiles of the same northern footprint as in Figure 7.1. The horizontal axis represents the longitude (one mark is equivalent to 1°) and the vertical axis represents the time (one mark corresponds to 100 seconds). Each line is a color-coded profile with a 20 seconds exposure time. (b) Evolution of the profiles of the southern footprint sequence observed the 8 August 1999 at 12:56:47 UT. Both main and secondary footprints brightnesses increase simultaneously.

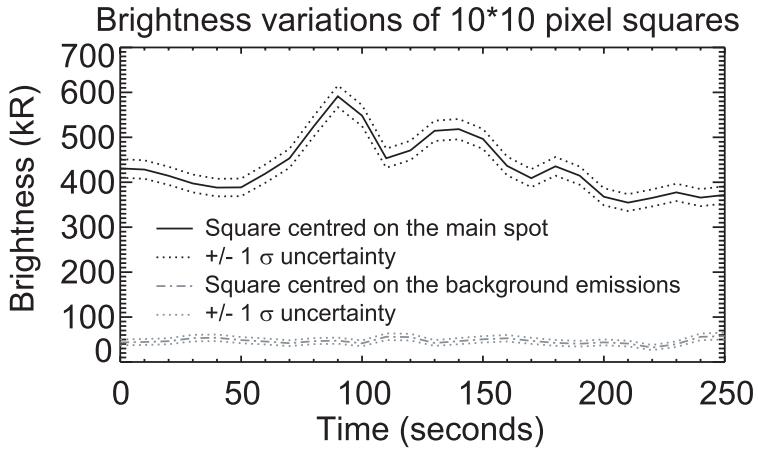

Figure 7.3: Light curves of 10×10-pixel squares centered respectively on the main spot and on the background Jovian emissions close to the footprint. The IFP brightness fluctuations are clearly statistically significant and independent from background variations. This northern footprint sequence was observed the 16 December 2000 at 11:25:51 UT.

These three cases occurred when Io was located in the same range of longitudes (i.e. between 84° and 99°). In this sector, Io is southward from the centrifugal equator of the torus (i.e. centrifugal latitudes between –1.2° and –2.9°), but still in its central region. Figures 4b and 4c show two examples of light curves of both primary and secondary southern spots. These plots suggest that in the first case, the variations of the second spot lag by ∼10 seconds the variations of the first one, while in the other case the secondary spot maximum precedes the primary one. Nevertheless, considering the brightness inaccuracies and the 10 seconds time step of the samples, this slight shift of the light curves is possibly not significant.

7.2.1.5 Discussion

We found significant footprint brightness variations for all observed sequences (i.e. both North and South), even though they were acquired at different times between 1999 and 2003. This provides strong evidence that the Io controlled auroral emissions are not in a steady state but highly dynamic. This variability may be attributed to intrinsic inhomogeneities of the interacting media (i.e. Io's ionosphere, the plasma torus, the Jovian ionosphere, etc.) or to non-linearities occurring during the propagation of the perturbation (i.e. wave breaking, phase mixing, etc.). *Roesler et al.* (1999) have observed fluctuations of the auroral emissions on Io with a timescale

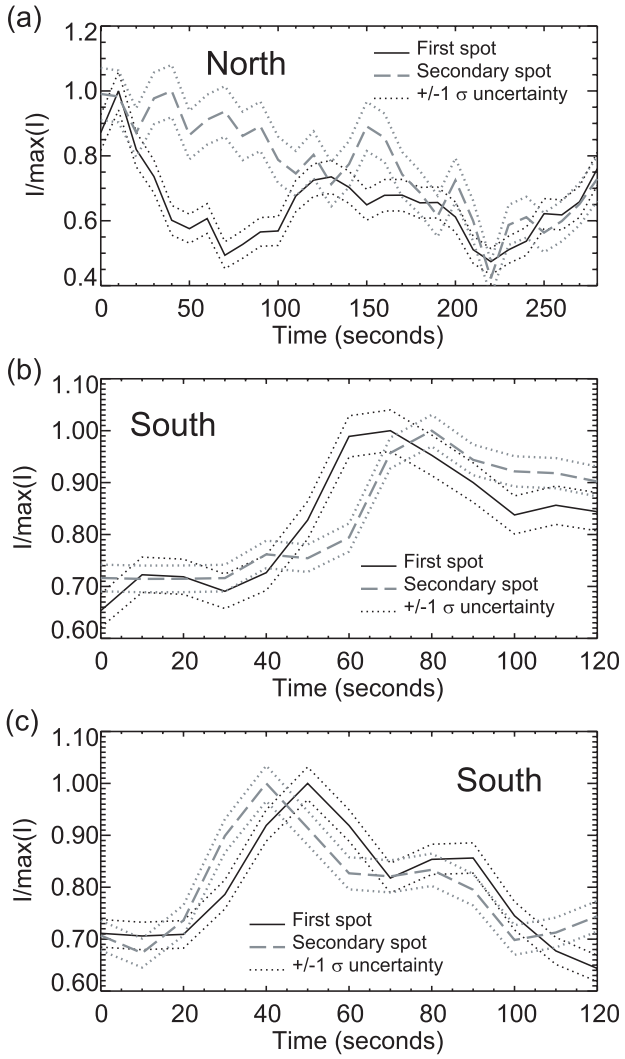

Figure 7.4: (a) Temporal evolution of the relative brightness of the first and the secondary spots in the profiles showed in Figure 1. The fluctuations of the first spot have a typical growth time of ~1 minute. Variations of the faint secondary spot are also present, but are not correlated to those of the main spot. (b) Temporal evolution of the relative brightness of the first and the secondary spots of a southern footprint. The sequence was observed the 8 August 1999 at 12:56:47 UT. On these light curves, the significant variations of both spots are clearly correlated. (c) Second example of time evolution of the relative brightness of the first and the secondary spots of a southern footprint observed the 12 August 2000 at 09:15:18 UT.

of 15 minutes and ascribed them to large-scale local variations in the plasma torus, while *Oliversen et al.* (2001) more precisely attributed them to electron energy flux variations in the torus. These fluctuations are one order of magnitude longer than those observed in our time-tag data. However, given the weakness of the auroral emissions on Io, the short timescale variations described here would remain indistinguishable in the auroral data for Io. Io related decametric radio emissions also show a short timescale component (S-bursts) occurring between Jupiter's surface and 0.4 Jovian radius (e.g. *Ergun et al.*, 2006). However, the time scales (from 0.25 second to 0.025 second) as well as the electron energies involved ($\sim$4 keV with 1 keV potential jumps) (*Hess et al.*, 2007) can hardly be linked to the timescales ($\sim$1 min) and the energies ($\sim$50 keV) discussed here. The simultaneous variations of the southern spots are even more intriguing. Indeed, if the brightness variations are due to a temporally varying strength of the interaction generated at Io, a delay between the primary and the secondary brightness peaks is expected. In the Alfvén wing theory, the very occurrence of the secondary spot is due to this delay, as the consequence of the longer path of the reflected perturbation. If one considers reflections inside the torus and given the Alfvén speed in the dense torus, the delay would be on the order of 13 minutes (*Crary and Bagenal*, 1997). If reflections occur between the Jovian ionosphere and the outer edge of the torus, the associated delay would remain between 30 and 90 seconds. Moreover, the calculated inter-spot distance would lie between 0.14° and 0.7° and would be independent of Io's position in the torus, in contrast with the observations. As a consequence, even if localized fluctuations of the initial Io-plasma torus interaction may partly explain the footprint brightness variability, they provide no explanation for the simultaneous fluctuations of the southern spots. This result might imply that the acceleration mechanism leading to the electron precipitation also experiences short timescale variations. At Earth, flickering auroras are very localized spots whose brightness is probably modulated by plasma wave induced processes also occurring in the acceleration region (e.g. *Sakanoi et al.*, 2005). Pulsating auroras are another type of fastly-varying auroral phenomenon at Earth. They appear to involve oscillations between auroral precipitation and generation of whistler waves in the equatorial plane (e.g. *Nemzek et al.*, 1995).

7.2.1.6 Conclusions

This study has unveiled a previously unexplored aspect of the Io footprint auroral emissions: their short timescale (∼1 minute) dynamics. Additionally, quasi-simultaneous and highly correlated variations of primary and secondary footprint brightness suggest that the modulation is not only driven by the Io-plasma torus interaction as suggested by the long timescale brightness variations, but also by the acceleration process occurring between the torus and Jupiter. Since the acceleration mechanism is still poorly understood because of the lack of observational constraints, the amplitude of the brightness variations as well as their characteristic lengths provide essential characteristics for building future quantitative models.

7.3 Epilogue

During the 10862 large HST observation program, several orbits have been specifically dedicated to the Io footprint. The exposure time of these images has been reduced to 30 seconds, with an image acquired every ∼70 seconds. This sampling rate does not allow one to track the brightness variations with as much accuract as for time-tag sequences, even though brightness variations of similar scale have been found (Figure 7.5).

Subsequent observations confirmed the significance of the study of the short timescale variations of the footprint brightness. First, *Grodent et al.* (2009) found similar brightness variations for the Ganymede footprint. Based on seven STIS time-tag sequences, these authors showed that the GFP power experiences quasi-periodic variations (Figure 7.6 a and b) or more chaotic behaviors (7.6 c), but with similar timescales. They proposed two possible mechanisms for these variations. These variations could be related to bursty reconnection events which are expected to occur on timescales of several tens of seconds. As a matter of fact, MHD simulation by *Jia et al.* (2009b) indicate that Ganymede's magnetopause could oscillate with such timescales, which appears to be consistent with in-situ Galileo magnetic field observations. On the other hand, quasi-periods of 100 seconds could also be a typical timescale for the generation of double layers in the Jovian ionosphere when subject to strong electric currents. Indeed, the second type of Io related observations with similar timescale has been reported by *Hess et al.* (2009), based on the analysis of S-burst radio emissions revealing vertically drifting acceleration structures with a re-

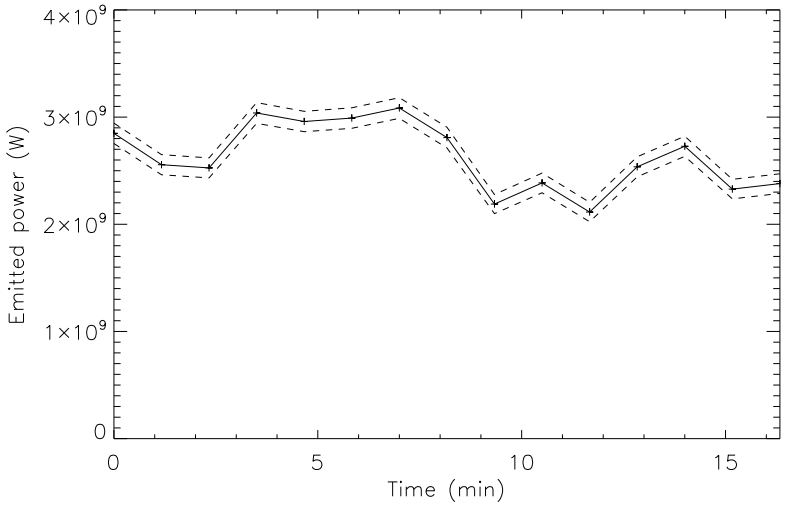

Figure 7.5: Variations of the MAW spot emitted power in the southern hemisphere in the Io System III longitude range between 12° and 20°. The variations are on the order of 37% of the mean power.

appearance quasi-period of 200 seconds. These variable acceleration structures are probably not the main cause for the electron acceleration but can possibly provide additional energy and trigger the fast brightness fluctuations. The interpretation of the 100 second timescale as a typical timescale of the Jovian ionosphere offers the advantage to explain both the Io and Ganymede footprint variations with a single mechanism.

7.4 System III related brightness variations

7.4.1 Introduction

7.4.1.1 Possible scenarios for System III related brightness variations

While the short timescale variability of the IFP spots was relatively unexpected, a correlation of the brightness with the System III location, i.e. a variability on timescales of several hours (one Io revolution in System III lasts for ∼13 hours), is less surprising. Several scenarii relating both quantities can be viewed. *Serio and Clarke* (2008) considered three of them:

1. Collisional interaction at Io: if the strength of the interaction at Io controls the intensity of the Alfvén waves and if intermediate processes do not cause further modulation of the brightness, the evolution of the brightness should be the same in both hemispheres and peak when Io is near the dense torus center.

2. Poynting flux loss: this scenario puts the emphasis on the possible Poynting flux loss when the Alfvén waves travel into the plasma torus. When Io is in the northern part of the torus, the waves traveling towards the north pole can fastly escape the torus while waves going towards the south have to cross the entire torus and weaken and vice-versa when Io is in the southern part of the torus. As a consequence, the northern main spot would be the brightest at 200° System III longitude and the weakest around 20°. The southern footprint would exactly follow the opposite behavior.

3. Pitch-angle diffusion aurora: if the incoming electrons have a given pitch angle distribution, the maximum brightness will occur when the loss cone is maximum, i.e. when the magnetic field strength is minimum in the Jovian ionosphere.

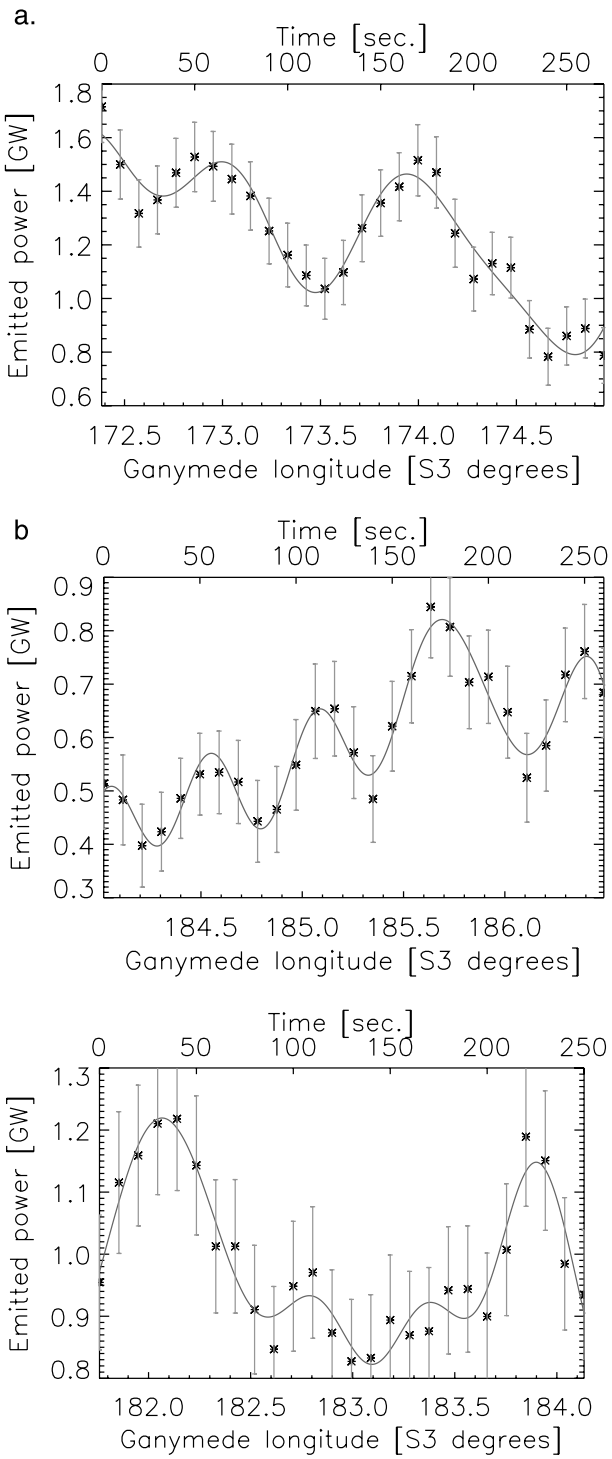

Figure 7.6: Short timescale variations of the Ganymede footprint brightness. In panels a) and b), quasi-periodic variations of the emitted power can be seen while variations shown in panel c) are irregular, but the growth time remains similar (from *Grodent et al.*, 2009).

A fourth scenario was foreseen by *Connerney et al.* (1993) with consequences similar to the third scenario. If the Jovian ionospheric Pedersen conductivity is the main parameter controlling the current intensity and if the precipitation flux is correlated with this current, the maximum brightness should be found when the conductivity is maximum. Since the Pedersen conductivity is approximately inversely proportional to magnetic field strength, the brightest spots should be seen when the surface magnetic field intensity is minimum. A fifth reason to anticipate an increase of the MAW spot maximum brightness is the motion of the TEB spot relative to it. When Io is near the torus center, the two spots merge together and the resulting spot should be as bright as the sum of their individual brightness. It is noteworthy that this scenario has broadly similar consequences as the first one. It should also be noted that these scenarii do not necessarily exclude each other and thus a combination of these effects could also be expected.

We showed in the previous chapters that the different spots have different origins and their response to the various relevant parameters could also change from one spot to another. The MAW spot is expected to be the consequence of the direct electron acceleration at the foot of the direct Alfvén wing. On the other hand and according to our interpretation, the TEB spot is caused by the anti-planet-ward acceleration of trans-hemispheric electron beams. Since it is caused by electrons accelerated in one hemisphere and precipitated into the other, the TEB spot brightness could be more sensitive to the asymmetry between the northern and southern magnetic field strength than the other two. Another possible reason that would justify a different behavior for the different spots could be that the RAW spot is the most sensitive to the Poynting flux loss because of the larger path length.

7.4.1.2 Previous studies

The Io footprint brightness in the FUV domain ranges between 25 and 700 kR (see Table 1.1). In the present section, we will only recall the studies that specifically studied the variations of the brightness as a function of the Io longitude. *Connerney et al.* (1993) suggested that the apparent lack of detection of the infrared northern IFP in the 90°-240° System III longitude range could be related to the expected high surface magnetic field strength in this region. Later observations acquired in the FUV domain with the WFPC2 camera infirmed this absence of detection, since several occurrences of northern footprints were seen in this longitude range (*Clarke et al.*, 1998). However, despite the noticeable scatter of the data points, they did not

find any trend between the IFP brightness and Io's longitude, most probably because of the large error bars related to the WFPC2 low sensitivity. The first conclusive relationship between the brightness and the Io location was reported by *Gérard et al.* (2006), based on STIS observations acquired between December 2000 and February 2003. They showed that the maximum IFP brightness increases when Io's centrifugal latitude decreases (Figure 1.11). They also applied a correction assuming a plane parallel atmosphere to take the limb brightening effect into account. The authors attributed the increase of the IFP brightness as Io settles into the dense torus center to the expected enhancement of the Io-magnetosphere interaction. Finally, *Serio and Clarke* (2008) studied the evolution of the footprint brightness on STIS images acquired from August 1999 to January 2001. They tested the variation of the brightness against the three scenarii mentioned above and concluded, like *Gérard et al.* (2006), that the strength of the interaction is the main driver for the mean IFP brightness.

7.4.2 How to estimate the brightness?

Most studies discussing the intensity of the auroral features express the brightness in Rayleighs or in kilo-Rayleighs. However, the Rayleigh (R) is a very peculiar unit that should be handled with care. This radiance unit "measures the absolute angular surface brightness of spatially extended light emitting sources" (*Baker*, 1974). 1kR represents 10^9 photons $m^{-2}s^{-1}$ within 4π steradians. This unit was initially used for airglow emissions on Earth. It is also very convenient to use in the case of auroral emission because its measurement summarizes the light emission in the air column. Consequently, it can be related to the precipitated energy flux through the use of appropriate energy degradation models (*Gérard and Singh*, 1982).

An important issue when providing brightnesses in Rayleigh is the spectrum of emission source and the instrumental throughput effects. The number of counts/s measured on different images acquired with different filters varies with the throughput of these filters. Nevertheless, we would like to be able to compare images acquired with a filter rejecting the Lyman-α with images including these emissions. The idea is to multiply a synthetic H_2 and H FUV auroral spectrum attenuated below $\sim$130 nm by a factor of 0.4[1] with the suitable instrumental throughput to compute the ratio between the number of originally emitted photons and the number of

[1]This level of methane absorption corresponds to a color ratio of 2.5.

	brightness	power
CLEAR	667.56	$\frac{d^2}{7.5161\times10^9}$
F25SRF2	1975.5	$\frac{d^2}{2.5397\times10^9}$
F115LP	328.06	$\frac{d^2}{1.0024\times10^{10}}$
F125LP	468.21	$\frac{d^2}{7.0234\times10^9}$

Table 7.1: Conversion coefficients from counts per second to kilo-Rayleighs and Giga-Watts. d represents the Earth-Jupiter distance in km. For the two ACS filters, i.e. the F115LP filter and the F125LP filter, these coefficients should be applied after the 1.63 coefficient correction described in Section 2.5.2.

actually received photons (*Grodent et al.*, 2003a). Assuming all auroral emissions have approximately the same FUV spectrum, we can then convert count rates into emitted radiance (see Table 7.1). It should be nevertheless noted that a corollary to this process is that the conversion coefficients from counts per second to kilo-Rayleigh are only appropriate for H_2 and H auroral emissions. Studies focusing on the reflected sunlight for example should consider another conversion coefficient based on its specific spectrum. In conclusion, when we provide numbers in kilo-Rayleighs, we should always specify the emitting source under consideration.

Another key issue is the limb brightening. When analyzing HST images of giant planet aurorae, emissions appearing close to the limb always look brighter than those appearing closer to the planetary center. This limb brightening is caused by the geometrical accumulation of optically thin emissions along the line of sight. Since this effect can increase the observed brightness by a factor of 10 (*Grodent et al.*, 1997), previous works made use of different strategies to circumvent this issue. In order to compare images with different observation geometries *Clarke et al.* (1998) applied the plane parallel correction[2] to convert the apparent brightness to the brightness that would be expected if the IFP was located on the central meridian at 67° latitude. *Gérard et al.* (2006) divided the observed brightness by the cosine of the zenith angle, implicitly assuming an extended plane parallel emitting layer as well. Contrary to *Clarke et al.* (1998), they provided a corrected value for an observer looking at nadir. Alternatively, *Serio and Clarke* (2008) do not provide a description of their correction method, but the fact that their correction

[2]The plane parallel correction assumes that the atmosphere can be modeled as a flat emitting layer. If α is the zenithal angle, i.e. the angle between the observer and the normal to the plane, than the correction coefficient to convert the observed brightness into the brightness that an observer looking at the nadir would see is simply $1/\cos(\alpha)$.

only depends on the distance to the limb suggests that it relies on the assumption of an extended emitting shell. Indeed, we managed to reproduce fairly well their optical depth correction factor by means of a spherical shell with an exponential vertical profile (Figure 7.7). In this figure, the vertical dash-dotted line represents the minimum distance to the limb under which *Serio and Clarke* (2008) consider their correction to become unreliable. We note that above this value, differences with the plane parallel correction are barely noticeable. Finally, their corrected value assumes a footprint located on the central meridian at 67° latitude like in *Clarke et al.* (1998).

The two above methods assume that the horizontal extent of the IFP is large. As detailed in Chapter 6, this assumption is not justified since images of the IFP when observed from the side demonstrate that the IFP is a thin curtain not broader than 200 km. Figure 7.8 shows simulated images of the hypothetical footprints made of a single spot (900×200 FWHM) followed by an extended tail (e-folding distance: 20000 km). Their spatial extent is exactly the same on every image, but the contour along with they are set is (from left to right) the equator, the 50th parallel and the 80th parallel respectively. We note that the maximum brightness decreases as the spot approaches the limb, which is the opposite behavior than expected from limb brightening from an extended area. Nevertheless, tail emissions on the right-hand image shows that some limb brightening actually takes place and increases the apparent brightness in some places. In conclusion, no simple correction can be applied to deduce the vertical brightness from the apparent one. All the complexity of the observing geometry has to be accounted for to retrieve information on the precipitated energy fluxes. As a result, we propose a new method to estimate the vertical brightness of the IFP spots and tail. It consists in comparing the emissions observed with the HST STIS and ACS instruments with realistic simulations of the emission regions.

7.4.3 Emission model

The purpose of our emission model is to reproduce as accurately as possible the shape and brightness of the different constituents of the Io footprint in order to compare model images to the actual planetary disk subtracted images. For each HST image, four model images are computed. One for each of the three spots and one for tail. Each sub-image is built such that the maximum brightness as seen from

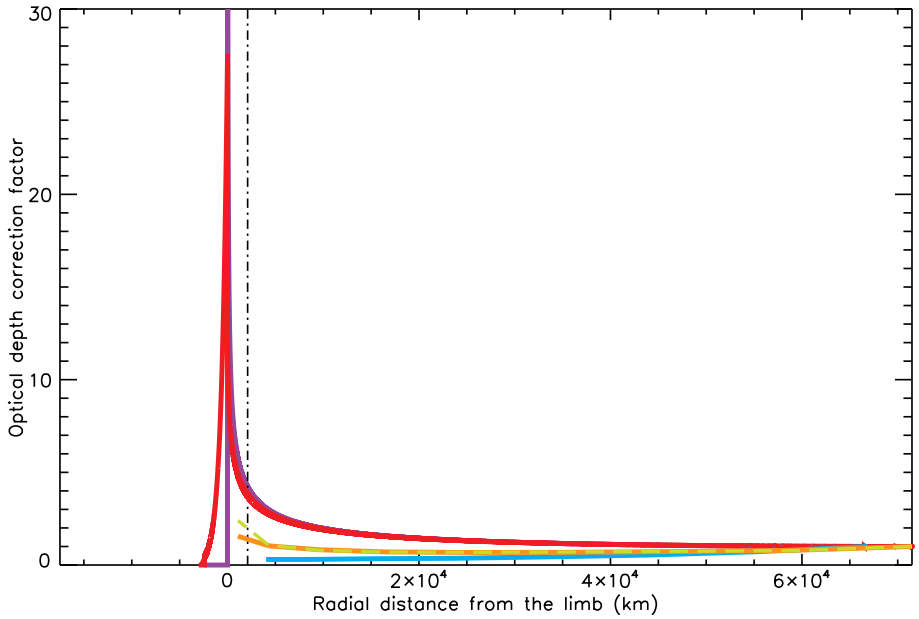

Figure 7.7: Evolution of the optical depth correction factor as a function of the radial distance from the limb. The purple line stands for the $1/\cos(\alpha)$ correction (with α being the zenith angle). The red line represents the spherical shell correction assuming an exponential vertical profile (scale height: 600 km). The cyan line stands for the correction assuming a realistic IFP curtain moving along the central meridian line as on Figure 7.8. The orange and the dashed green lines represent the correction assuming the same realistic curtain moving along the equator either toward dawn or toward dusk.

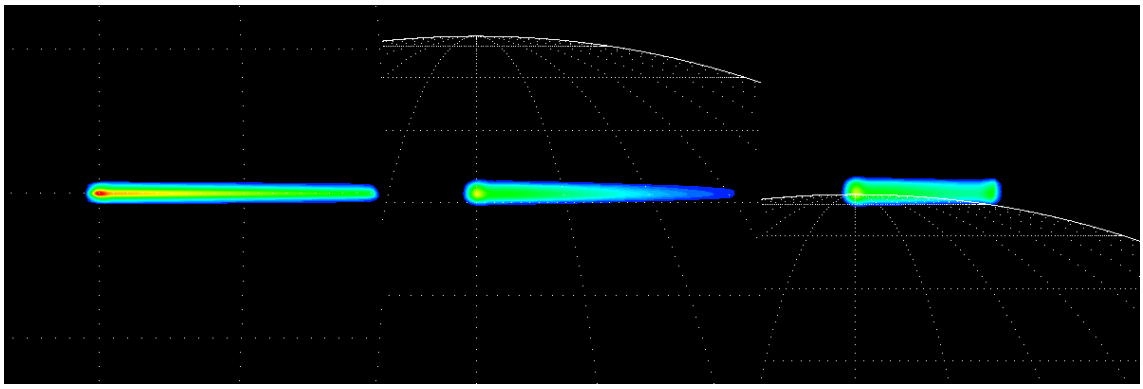

Figure 7.8: Evolution of the apparent brightness as a function of the latitude of the IFP (0°, 50° and 80°, respectively). The footprint is modeled as a single spot and an extended tail with a constant length. Because the IFP is a thin curtain with a large vertical extent, its apparent maximum brightness decreases when the spot approaches the limb along the central meridian. On the right side image, it is noticeable that the limb brightening effect induces an apparent brightness enhancement in the tail.

the nadir is 1 kR. Then we compute the best set of multiplicative coefficients (in the sense of the least squares) for the linear combination of the sub-images to reproduce the actual one.

All four sub-structures are aligned along the IFP reference contours described in Chapter 4. The relative position of the spots varies as a function of the System III longitude of Io as described in the same chapter. For spot "x", the vertically integrated brightness varies along and perpendicularly to the contour following a Gaussian law:

$$I_x(i,j) = e^{\left(-\frac{(i-lon_x)^2}{2\sigma^2_{lon_x}} - \frac{(j)^2}{2\sigma^2_{lat_x}}\right)}$$

where i is the distance along the contour, j is the distance perpendicular to the contour, lon_x is the position of the spot maximum along the contour as defined by the reference contour, σ_{lon_x} characterizes[3] the spot width along the contour, σ_{lat_x} characterizes the spot width perpendicularly to the contour.

As far as the tail is concerned, the perpendicular brightness profile is described by a Gaussian as well, but the evolution of the brightness along the contour is

[3]The relationship between the σ parameter of a Gaussian and its full width at half maximum ($FWHM$) is:

$$FWHM = 2.3548 * \sigma$$

	$FWHM_{lon}$ or e-folding distance	$FWHW_{lat}$	vertical scale height	peak altitude
MAW spot	900 km	200 km	400 km	900 km
TEB spot	900 km	200 km	200 km	700 km
RAW spot	900 km	200 km	400 km	900 km
Tail	20000 km	200 km	400 km	900 km

Table 7.2: Size parameters for the simulated spots and tail.

described by a function which starts as a polynomial law and then evolves as a decreasing exponential law. The form might look complex, but has been chosen because it allows to easily tune all the relevant parameters such as the position of the maximum and the e-folding distance:

$$I_{trail}(i,j) = a_t(i-d_{lon})^{n_t} e^{\left(-b_t*(i-d_{lon})-\frac{(j)^2}{2\sigma^2_{lat_t}}\right)}$$

with

$$a_t = \left(\frac{1}{lon_t}\right)^{n_t} e^{n_t}$$

$$b_t = \frac{n_t}{lon_t}$$

$$n_t = \frac{e^1}{\left(\frac{H}{lon_t}\right) - \ln\left(\frac{H}{lon_t}\right) - 1}$$

and where H is the e-folding distance, lon_t is the position of the tail maximum along the contour which is set to $lon_{MAW} + \sigma_{MAW}$ and d_{lon} is the tail starting position along the contour, which is set to $lon_{MAW} - \sigma_{MAW}$.

The brightness in the above equations corresponds to the vertically integrated brightness, which is the relevant parameter to derive the incoming particle flux. However, to compute the model images corresponding to an oblique observation, the vertical emission rate profile has to be specified and is described with a Chapman profile (see Equation 5.1). The parallel and perpendicular sizes of the different sub-structure as well as their altitude maximum and their vertical scale height are gathered in Table 7.2.

At this step of the process, we have defined the longitude, the latitude, the altitude and emission rates of the emission points corresponding to the different spots and the tail. The spatial coordinates are converted into x-y-z coordinates linked to

the HST image, x and y corresponding the image abscissae and ordinates and z corresponding to the depth. For each x-y couple, the emissions rates are summed along the z direction to produce the pixel brightness. One image is produced for each sub-structure and this image is subsequently convolved with the point spread function (PSF) corresponding to the relevant instrument and filter.

Because of the finite accuracy of the reference contour, the fine tuning of the simulated images position is computed by adjusting the barycenter of the MAW spot to the one of the disk emissions-free original image (see Chapter 2 for a description of the background planetary disk removal). The final step is a least squares fit of the relative brightnesses of the different IFP features to the original image. The fitting coefficients provide the maximum vertical brightness for each sub-structure in kR.

The two major limitations of this measurement method are 1) the impossibility to disentangle the MAW and the TEB spot when the Io centrifugal latitude is close to zero and 2) the description of the initial part of the tail. When the absolute value of the Io centrifugal latitude is below 2.5°, the TEB spot is no longer taken into account and the modeled MAW spot alone simulates the combination of the two spots. It is thus important to keep this fact in mind when interpreting the MAW brightness in these sectors. As far as the beginning of the tail is concerned, we chose a reasonable empirical formulation of the brightness along the contour because current models focus either on the initial phase of the interaction, leading to the spots, or on the tail when it is well established, but not specifically on the transition phase (Phase 2 in the *Delamere et al.* (2003) formulation).

7.4.4 Results and discussion

The method described above is not easy to implement and only preliminary results are available and presented here.

One of the main reasons to use brightness units instead of power units is the direct connection between the brightness as measured vertically from the emission point and the precipitating power. However, in the case of HST observation of the Jovian polar regions, the zenith angle is far from 0°. If the emission region is an extended area, the observed brightness can be easily converted into the vertical brightness by means of the parallel plane or the spherical shell approximations. Unfortunately, our measurements of the IFP size and shape demonstrated that the Io footprint is a thin curtain made of different spots and a tail and cannot be considered as an extended

area. Figure 7.7 showed that values computed with any correction method based on the extended area assumption are much smaller than the observed brightness, while a zenith observer would actually measure larger values than HST. Figure 7.9 shows the maximum brightness of the MAW spot as a function of the System III longitude of Io without any correction. The global trend seems to follow the previous conclusions from *Gérard et al.* (2006) and *Serio and Clarke* (2008). The maximum brightness is observed around 110°, and a possible second peak appears around 290° for the northern IFP, which corresponds to the region where Io is near the torus center. The main difference lies in the number of data points and in the brightness values, which are not reduced by any limb brightness correction.

Our new measurement method adresses a totally different point of view and tries to answer the question: What is the maximum vertical brightness that should be injected into the different spots and in the tail to reproduce the observations? The results for the MAW spot are shown in Figure 7.10.

First, we note that the plotted values are much larger than for earlier estimates (see Table 1.1). The first reason stems from the fact that the maximum brightness as observed from above is higher than seen from the side since the vertical scale height is assumed to be $\sim$ 400 km while the width is only $\sim$ 200 km wide. The second reason is related to the point spread function (PSF). In the above chapter related to the position and the size of the different features, we argued that the PSF has little effect because its FWHM is between one and two pixels. As far as the maximum brightness is concerned, the impact of the PSF cannot be neglected any more because a significant part of the energy is spread into the PSF wings.

Assuming that 10 kR seen looking at the nadir corresponds to an incoming electron energy flux of 1 mW/m^2, we find that the incoming flux for the MAW spot ranges between 100 and 500 mW/m^2. Consequently, the presence of such values raises once again the issue of the atmospheric response to such an sudden and concentrated energy supply.

Second, as for the non-corrected brightness, the behavior of the southern MAW spot vertical brightness shows two noticeable peaks around 110° and 290°. These sectors correspond to Io centrifugal latitudes around 0°, i.e. when Io is near the torus center. This result favors two possible scenarii: the one related to the strength of the interaction at Io and the one involving the merging of the spots.

Third, we note a huge brightness difference between the northern and the southern MAW spots in the longitude range between 150° and 200°. In this sector, Io is

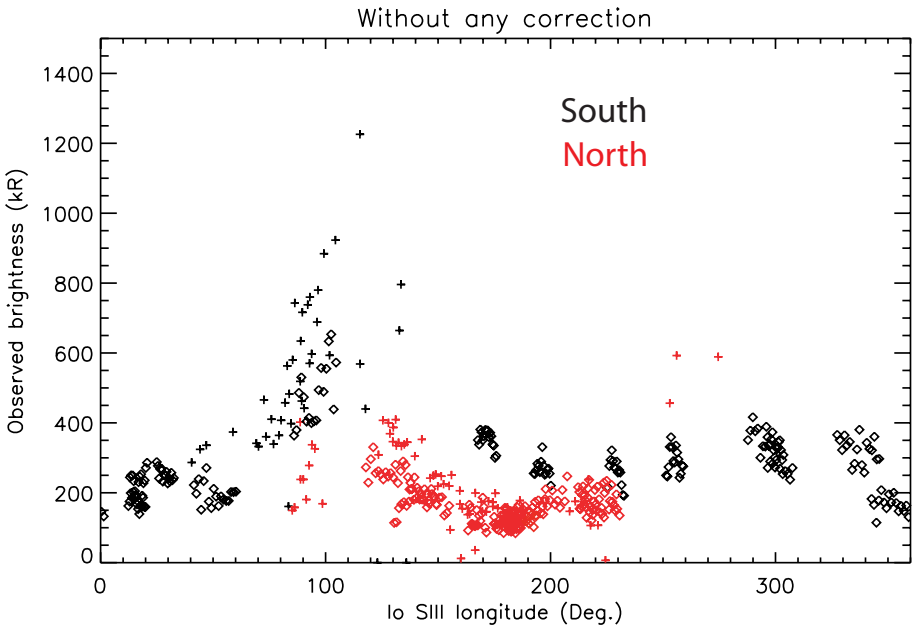

Figure 7.9: Evolution of the maximum observed brightness as a function of the Io longitude. Black symbols are for the southern hemisphere while red symbols are for the northern hemisphere. The "plus" symbols represent STIS observations while the "diamond" symbols represent ACS observations. No limb brightening correction was applied to the plotted values.

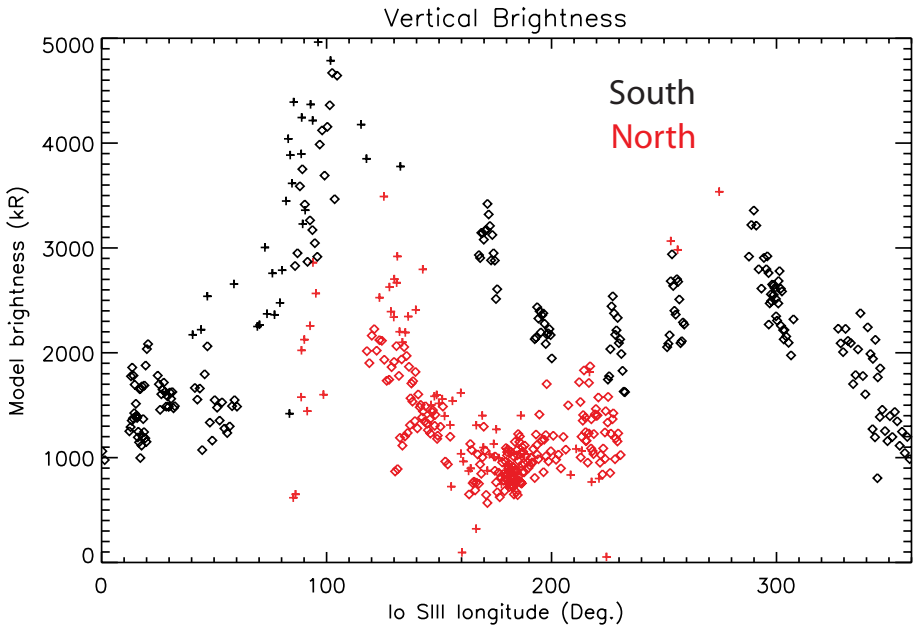

Figure 7.10: Evolution of the modeled maximum vertical brightness as a function of the Io longitude. Black symbols are for the southern hemisphere while red symbols are for the northern hemisphere. The "plus" symbols represent STIS observations while the "diamond" symbols represent ACS observations.

progressively moving from the torus center to the northern torus boundary. Figure 7.11 shows the emitted power as measured during two consecutive HST orbits. The telescope was pointing to the south pole during the first half of the orbit and then it is directed to the north. The northern spots are so faint that the MAW spot is fainter than the TEB spot in the south. The second orbit begins with North IFP observations and then the field of view shifts toward the South. This case is very interesting to test the different scenarii mentioned above because no long term variation of the torus density can be invoked to explain the observed differences. The different spots are well separated, so that their mixing cannot explain the spots brightness variations in this sector. On the other hand, if the strength of the interaction were the only driver for the spots brightness, then both hemispheres would have shown the same spots brightness. The Poynting flux loss hypothesis could not explain this difference either: since Io has positive centrifugal latitudes in this sector, the southward Alfvén wing crosses a longer distance in the torus than the northward wing. Consequently, the southern MAW spot should be weaker than the northern one, contrary to observations. The only remaining scenario that justifies

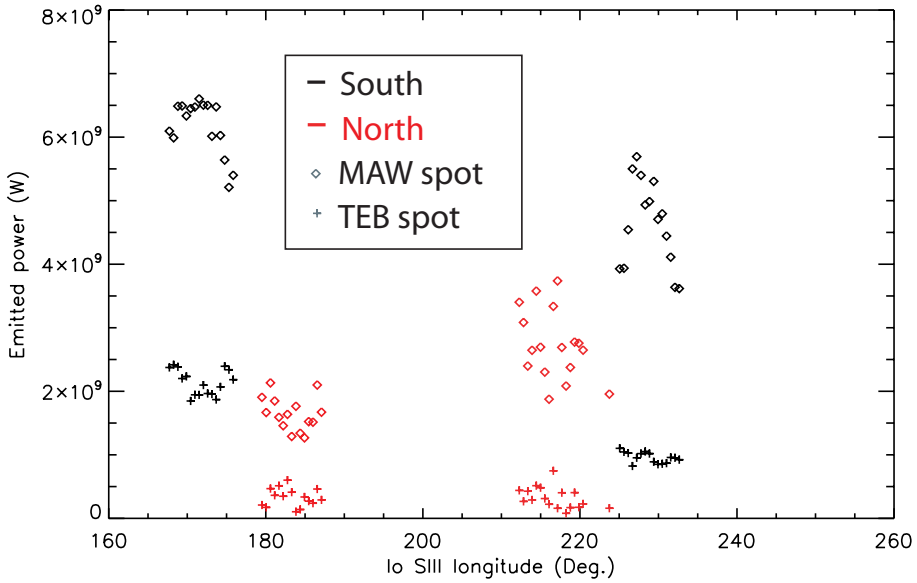

Figure 7.11: Evolution of the MAW spot ("diamond" symbols) and the TEB spot ("plus" symbols) emitted power during two consecutive orbits. The black symbols represent observations in the southern hemisphere and the red symbols represent observations in the northern hemisphere. The spot emissions are weaker in the North than in the South, which could be attributed to the difference of surface magnetic field strength.

the asymmetry between the hemispheres is the surface magnetic field. Indeed, the VIP4 magnetic field model predicts a weaker field strength in the south than in the north, facilitating electron precipitation. The influence of the surface magnetic field strength could also explain why the peak at 110° in the South is higher than at 290°. Similarly, it would also explain why the southern MAW spot is weaker around 10° than around 200°.

We have seen in the previous chapters that the different spots should be understood as individual features and we suggested that they might be caused by different mechanisms. It is thus necessary to analyze their behavior independently. Figure 7.12 shows the evolution of the MAW spot power and the TEB spot power for a southern IFP. In this range of longitudes, Io is coming from its southern most position and approaches the torus center. On the images, we can clearly see the spots progressively approaching each other. This case approximately corresponds to the case studied by *Serio and Clarke* (2008). They observed that the overall mean brightness increases whith time and they attributed this behavior to the enhancement of the interaction at Io. However, when we analyze the spots separately, only

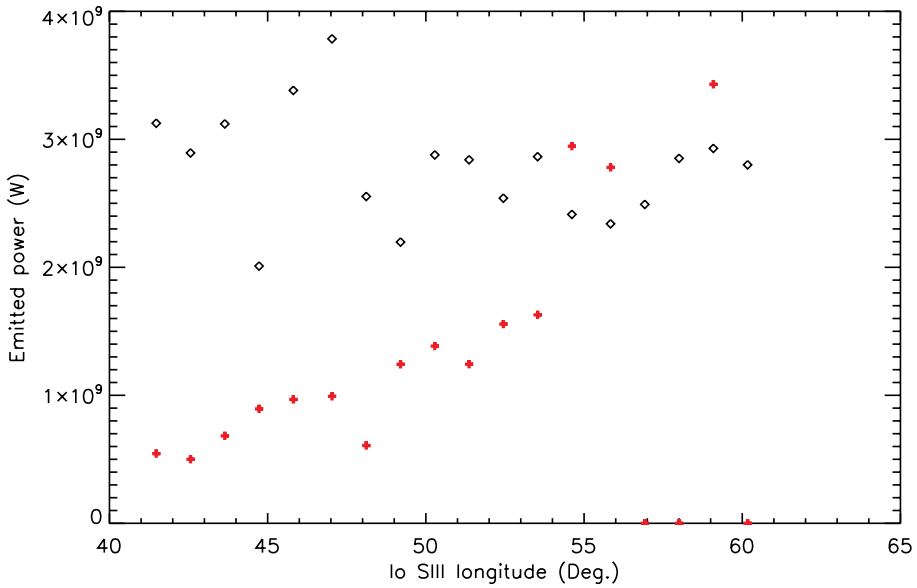

Figure 7.12: Evolution of the MAW spot (black "diamond" symbols) and the TEB spot (red "plus" symbols) emitted power during a single orbit in the southern hemisphere. As the TEB spot approaches the MAW spot, the power of the TEB spot increases while the power of the MAW spot remains roughly constant.

the TEB spot emitted power increases while the MAW spot power remains approximately constant. This observation thus challenges the previous interpretation of the brightness variations since, if the interaction at Io was driving the emitted power for both spots, both should be enhanced at the same time.

At this stage of our study, we must nevertheless be careful when interpreting the measurements. When Io's longitude is 60°, Io is not yet close to the torus center and the MAW spot brightness could still rise later because of the increasing interaction strength. The fact that the spots do not evolve in a correlated way on timescales on tens of minutes just confirms the idea that they originate from different processes. This finding does not necessarily contradict our previous finding of simultaneous fast variations of the same spots since the timescales are different.

7.5 Conclusions

The measurement of the Io footprint brightness requires a good understanding of the observing geometry. We use the spatial information gathered during the course of this work, such as the spots positions and the inter-spot distances as well as the

respective size and altitude of the different features, to develop a new method of analysis. This method consists in assessing how many times simulated spot images with well-known vertical brightness are necessary to best fit the original HST image. When possible, we try to distinguish the different spots. However, in sectors where the TEB and the MAW merge, i.e. when Io is close to the torus center, they cannot be disentangled. This could partly explain the apparent brightness enhancements of the MAW spot in these locations. Another scenario remains possible since the strength of the Io-magnetosphere increases in the dense torus center, which is also expected to lead to a brighter spot as well. When the spots are well separated, the MAW and the TEB spots can behave differently, one remaining constant while the other brightens with time. This finding seems to confirm one of the main results of this work: the different spots should be considered independently because they have different origins.

Another important result is the finding of an asymmetry of the northern brightness compared to the southern brightness. Added to the fact that the southern brightness at 110° is larger than at 290° while Io is at the same location in the torus, this information indicates that the surface magnetic field strength also plays a major role in the control of the spots brightness.

Moreover, the vertical brightness that we derive implies precipitating electron energy flux between 100 and 500 mW/m^2 for the MAW spot while previous estimates were lying closer to 30 mW/m^2.

Finally, we highlighted for the first time brightness variations on timescales of one minute. These variations reach up to 50% of the brightness with a typical growth time of 100 seconds. In some cases, the MAW and the TEB spot experience simultaneous variations over such short timescales, which suggests that the driving mechanism for the fast variations is located close to Jupiter. Brightness variations over similar timescales have later been found for the Ganymede footprint and in radio S-burst measurements. The latter also indicates that they could be related to an additional electron acceleration region located close to the planet. The idea that two acceleration mechanisms simultaneously contribute to the electron precipitation could also explain why correlated variations of the spots are seen on short timescales while a differentiated behavior is observed on longer timescales. The main electron acceleration mechanism would be related to the inertial Alfvén waves and would have a maximum efficiency around 1 R_j away from the planet (*Jones and Su*, 2008). Since the acceleration takes place relatively far from the planet, the surface magnetic field

strength could have an influence on the precipitated flux. Then, a second mechanism related to vertically migrating acceleration structures would appear at altitudes around $0.1R_j$. This interpretation would however require further observations and simulations to be fully confirmed.

Chapter 8

Conclusions

8.1 Discussion

The Io footprint is a particularly spectacular signature of the Io-Jupiter electromagnetic interaction. In the present work, we demonstrated that a careful analysis of its characteristics can modify our comprehension of the ongoing physical processes. In the framework of this thesis we methodically analyzed the high resolution images acquired by the Hubble Space Telescope in the far UV domain. The very first step consisted in creating a complete and standardized database. Additionally to the image processing, we developed new techniques to retrieve accurate pointing information directly from the images them selves. At the same time as the data were gathered and processed, we generated an exhaustive catalog compiling technical, telemetry and ephemeris parameters. The database and the related catalog have been used extensively in many other studies based on the FUV images of the Jovian aurora.

Numerous models have been proposed to explain various aspects of the auroral footprint of Io. By rigorous measurements of the different footprint characteristics, we can validate or discard these theoretical ideas and thus improve our understanding of the phenomenon. However, in some cases, no existing model is able to explain the new observations. For example, the overall evolution of the IFP spots multiplicity in general and of the inter-spot distance in particular, did not match the expectations of the traditional models. We discovered that a faint spot was systematically seen upstream of the main spot in one hemisphere when only downstream spots were seen in the opposite hemisphere. Moreover, the minimum distance between the first two spots is observed when Io is in the torus center. These observations contra-

dicted all previous models and we thus proposed a new interpretation of the spots multiplicity. This contribution can be considered as the main result of this work. The Io footprint is formed of at least three individual spots and an extended trailing tail in each hemisphere. According to this new framework, one spot, generally the brightest one, is located at the foot of the direct Alfvén wing and we named it the Main Alfvén Wing (MAW) spot. Another spot is related to electrons accelerated away from the planet in one hemisphere, crossing the equatorial plane in the form of electron beams and precipitating in the opposite hemisphere. This spot is called the trans-hemispheric electron beam (TEB) spot. Finally the third spot is located at the foot of the reflected Alfvén wing (RAW) on the torus boundary and is called the RAW spot.

This new interpretation offers the advantage to explain many different observations whithin a common framework. The electro-magnetic interaction between Io and the incoming torus plasma generates Alfvén waves propagating towards Jupiter in the form of Alfvén wings. Part of these waves is reflected by the plasma density gradient while the remainder escapes the torus. Between the torus border and Jupiter, inertial effects become more and more important, resulting in the acceleration of electrons both toward and away from the planet. As a consequence, some electrons are directly propelled into the Jovian ionosphere at the foot of the Alfvén wing, creating the MAW spot. The electrons accelerated in the opposite direction then form an electron beam and cross the Io orbit plane, as observed in situ by Galileo instruments. Part of the electrons from the beam then precipitate into the opposite hemisphere, generating the TEB spot. When the reflected Alfvén wing reaches the opposite torus boundary, part of the waves can finally escape from the torus and generate the RAW spot. This interpretation explains both quanlitatively and quantitatively the evolution of the inter-spot distances as a function of the position of Io in the plasma torus.

However, analysis of the Io footprint does not only provide information on the Io-Jupiter interaction. The detailed study of the Io footprint position brings useful constraints to improve the magnetic field models of Jupiter, since it provides us with information on the surface magnetic field which is inaccessible to magnetometric instruments on board flying-by or orbiting spacecraft. For example, the large divergence of the Io, Europa and Ganymede footpaths around 100° System III longitude in the northern hemisphere is an evidence for a large magnetic field anomaly in this sector. The analysis of the speed of the MAW spot revealed that this anomaly

might be accompanied by a fainter anomaly around 290° System longitude. Finally, we demonstrated that the current magnetic field models are not accurate enough to allow us to estimate the shift between the actual MAW spot position and the location of the foot of the unperturbed field lines passing through Io (i.e. the lead angle). This parameter was supposed to decide which far field interaction model, between the unipolar inductor and the ideal Alfvén wing models, was the best one. However, it appears that the inter-spot distance is a much more reliable tool which showed that none of these models is suitable, as stated above.

The increased amount of available data also allowed us to resolve some apparent contradictions in the literature concerning the the size of the Io MAW spot. Some authors suggested that the footprint had approximately the projected size of Io along unperturbed field lines. Others claimed that the footprint size was much larger and reflected the size of an extended interaction region at Io which includes the wake of stagnating plasma. Recognizing that the Io footprint is a three-dimensional structure made of several distinct features, we carefully selected the favorable observing geometries to derive the length ($\sim$ 900 km), the width ($<$ 200 km) and vertical extent (scale height:$\sim$ 400 km, peak altitude: $\sim$ 900 km) of the MAW spot. The measured length is three to four times larger than the length of an unperturbed Io flux tube, in accordance with simulations taking the non-linear effects in the Alfvén waves propagation into account (*Jacobsen et al.*, 2007). The width roughly corresponds to the projected width of Io, which also agrees with model expectations. The large scale height of the MAW emissions implies a broad distribution of the impinging electrons, which strengthens the hypothesis of electron acceleration mainly driven by inertial Alfvén waves. The peak altitude is nevertheless surprisingly high since spectral observations showed some methane absorption while the methane homopause was expected to lie around 250 km. Similar peak altitudes and scale heights have been found for the tail. We modeled the vertical emission profile based on several theoretical electron energy distributions and the best fit was achieved with a kappa distribution with $\kappa = 2.4$ and a mean energy of $\sim$ 1 keV. This result is even more puzzling since a recent model postulated that a quasi-static electric field is the cause for the tail emission (*Ergun et al.*, 2009), which would have led to a much more peaked electron distribution. This result suggests that the electron acceleration in the tail also originates from Alfvén waves. Finally, the altitude of the TEB spot appears to be 200 km lower than the MAW spot of the tail.

As far as the brightness of the IFP is concerned, we studied two different timescales

for which significant variations can be found. The shortest timescale is on the order of one minute and systematically observed fluctuations are on the order of 30% of the mean brightness but can reach up to 50%. Correlated variations of the MAW and the TEB spots suggested that the mechanism leading to these rapid fluctuations should be located close to the Jovian surface. On timescales of tens of minutes to hours, the different spots nevertheless appear to behave independently, confirming the hypothesis of a different origin for these spots. Additionally, even if the brightness peaks when Io is near the torus center, strong asymmetries are observed between the hemispheres. The global behavior favors the idea that the interaction strength at Io and/or the mixing of the spots are the main drivers for the MAW spot brightness, but the asymmetries suggest that the surface magnetic field strength also plays a significant role.

8.2 Future work and perspectives

So far, the new measurement method for the spots brightness and emitted power only provided preliminary results and additional ones are expected in the near future. When its reliability will be fully assessed, even for faint emissions, it will be interesting to study in detail the evolution of the brightness for all the spots, which could help confirming the scenario of the trans-hemispheric electron beams.

Indeed, our new interpretation of the secondary spot as being related to trans-hemispheric electron beams solves many problems related to the understanding of the Io-Jupiter electro-magnetic interaction. For example, this interpretation simultaneously explains the evolution of the inter-spot distances in the ionosphere and the observation of electron beams at Io. However, this model requires further improvements to be completely validated. First of all, this interpretation postulates that electrons are accelerated in both directions in the acceleration region. If bi-directional electron acceleration is known to be possible in the presence of inertial Alfvén waves, it should nevertheless be demonstrated 1) that a sufficient amount of energy can escape the torus in the form of Alfvén waves and 2) that the inertial Alfvén waves are accelerating the electrons with an adequate efficiency in both directions. Galileo in situ measurements of radio emissions suggested that filamentation of the Alfvén waves should take place in the plasma torus(*Chust et al.*, 2005). *Hess et al.* (in preparation)*Hess et al.* (in preparationa) claim that this filamentation is indeed necessary for the energy to leave the torus in the form of Alfvén waves but

that it also considerably increases the efficiency of the electron acceleration at high latitude.

Another theoretical issue is the location of the observed electron beams. These beams have not only been observed downstream from Io but also above the polar caps. The unipolar inductor scenario could explain why the beams are falling back on Io, but it is unable to explain the occurrence of secondary spots. On the other hand, the ideal Alfvén wing model would locate the beams much downstream from the places where they were observed. *Jacobsen et al.* (submitted) show that simulations realistically computing the non-linear effects on the Alfvén waves propagation can reproduce convincingly both the location of the electron beams at Io and the inter-spot distances in the Jovian ionosphere.

Other issues deserve further attention. One of the most intriguing finding of this thesis consists in the short timescale variations and the correlated brightness variations of the MAW and the TEB spots in the southern hemisphere. One important question on these rapid variations concerns their periodicities. Are they related to bursty events or are they repetitive? If they are quasi-periodic, is this period varying and what could drive these variations? The simultaneous evolution of adjacent spots suggests that the mechanism driving this short timescale variability is located relatively close to the planetary surface. However, the number of observed cases is extremely limited and more observations are required to confirm this observation and to precise the conditions needed for these simultaneous variations. For example, we would like to know if the distance between the spots should remain below a given threshold. Thanks to the recent restoration of the STIS instrument, new time-tag sequences of the southern Io footprint have been acquired in late August-early September 2009 with the above questions in mind, but the data have not been processed yet.

Another interesting topic is the link between the Io footprint and the Io related decametric radio emissions. Our new Io reference contour and the measured inter-spot distances are of considerable help in this domain since it pinpoints the exact spots location when radio emissions are observed (*Hess et al.*, in preparationb). Additionally, the magnetic field anomalies that we highlighted in this work and the subsequent magnetic field model improvements could also be useful to better understand location of the active regions as well as the shape of the radio arcs on the dynamic spectra.

Moreover, footprint observations in the infrared domain, and particularly spec-

tra, could provide a wealth of precious information on the state of the atmosphere. We found that both the hydrocarbon profile and the pressure-altitude relationship in the polar regions in general and at the Io footprint are not similar to the ones measured near the equator. Information on the temperature and on the hydrocarbon profile could be retrieved from these spectra. Simulations of the atmospheric response to the sudden and massive input of energy related to the Io footprint could also be necessary to fully understand the observations. Finally, no systematic analysis of the Io footprint has been made on IR auroral images. Future studies could verify that the overall morphology is evolving similarly to the FUV morphology, and, possibly more interestingly, that the relative spot brightness is also varying in the same way.

8.3 Final words

The present work is currently the most detailed study of the Io UV footprint. The measurements reported here and their interpretation helped to clarify some controversial issues, dissipated some misunderstandings and significantly modified our view of the Io-Jupiter interaction in general and of the Io footprint in particular. One of the most striking results, if confirmed, is the identification of auroral emissions caused by electrons originating from the opposite hemisphere. Similar emissions are expected to occur on Earth as well (e.g. *Carlson et al.*, 1998), but they are much more complex to demonstrate since we cannot track the electron beams from one hemisphere to the other. Moreover, electron beams are also observed in the Kronian magnetosphere (*Saur et al.*, 2006; *Mitchell et al.*, 2009) as well as in other places in the Jovian magnetosphere (*Mauk and Saur*, 2007), suggesting that anti-planetward electron acceleration is a universal process. However, contrary to all these examples, the geometry of the field lines is known with a much better accuracy at Io, which allows us to relate more easily auroral and equatorial observations. Consequently, the Io-Jupiter case is not only the paradigm of systems consisting in a conducting celestial body orbiting a strongly magnetised one. It also appears to be a natural laboratory to study some physical processes related to Alvén waves, such as their reflection on density gradients, their filamentation and the electron acceleration that is related to them.

Appendix A

Altitude of Saturn's aurora

A.1 Forewords

Most of the techniques developed to study the Io footprint on HST images can and have been extended to other studies based on the same type of images. We noted in Chapter 2 that the scripts used to generate the Jupiter HST imaging and spectral database and catalog have been adapted to build similar Saturn HST imaging database and catalog. The analysis of Saturn images demonstrates that radial cuts inflection points can be used to reliably and automatically compute the planetary center position on the HST images. Similarly, the methods developed to study the Io footprint tail vertical profiles can also be applied to Saturn's auroral emissions. The present appendix presents a peper in which we used the limb-scanning technique developed for the Io tail emissions to study the altitude of Saturn's aurora. The main difference is that, in the present case, we cannot be sure that the emission region is exactly in the limb plane. Actually, the measured peak altitude represents the minimum value for the real peak altitude for geometrical reasons: if the emission region is not located exactly in the limb plane, its apparent altitude is smaller than its real altitude (see Figure A.1). If the UV light hydrocarbon absorption were strong, the opposite effect, i.e. an over-estimation of the actual peak altitude, would take place. No short wavelength light could escape from the atmosphere from below the hydrocarbon homopause, setting an apparent peak altitude threshold. However, this latter effect is very unlikely to affect our images since UV spectra usually show little or no FUV absorption signature (see the discussion in the next section).

The estimate of the peak auroral altitude, together with measurements of the emission region pressure and temperature, led us to modify the equatorial atmo-

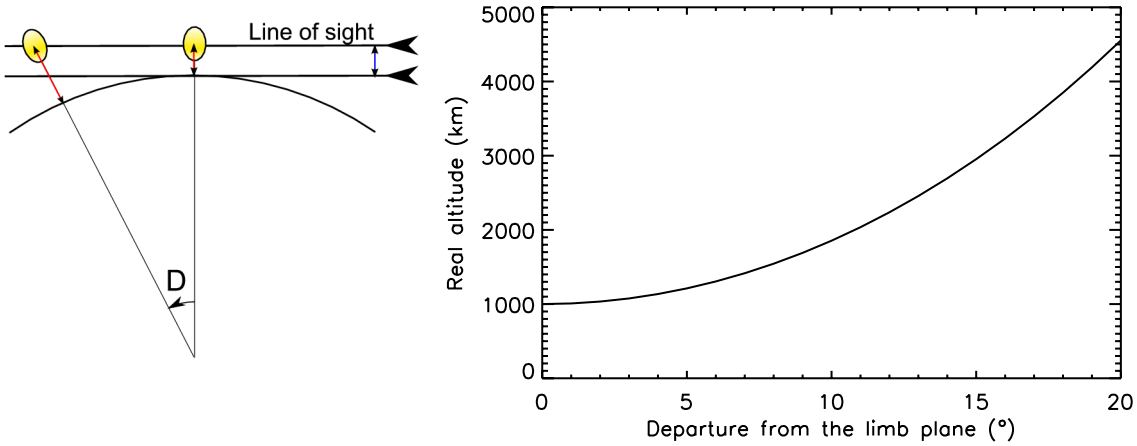

Figure A.1: (right) Evolution of the real emission altitude as a function of the angular distance (D) from the limb plane. The observed emission altitude is set at 1000 km.

spheric model in order to meet the observational constraints in the polar regions. Additional details on the way this model is built are given in Section A.3. Finally, in the last section of this appendix, I describe how the routines that I developed to derive the precipitating electron energy distribution in the Io footprint tail were applied to characterize the energy distribution leading to the Kronian main auroral emissions.

A.2 Publication: Altitude of Saturn's aurora and its implications for the characteristic energy of precipitated electrons

J.-C. Gérard, B. Bonfond, J. Gustin, D. Grodent

Laboratoire de Physique Atmosphérique et Planétaire, Université de Liège, Liege, Belgium

J. T. Clarke

Center for Space Physics, Boston University, Boston, Massachusetts, USA

D. Bisikalo, V. Shematovich

Insitute of Astronomy, Moscow, Russia

Published in the January 2009 issues of Geophysical Research Letters (*Gérard et al.*, 2009).

A.2.1 Abstract

Images of Saturn's aurora at the limb have been collected with the Advanced Camera for Surveys on board the Hubble Space Telescope. They show that the peak of Saturn's nightside emission is generally located 900– 1300 km above the 1-bar level. On the other hand, methane and H_2 columns overlying the aurora have been determined from the analysis of FUV and EUV spectra, respectively. Using a low-latitude model, these columns place the emission layer at or above 610 km. One possibility to solve this apparent discrepancy between imaging and spectral observations is to assume that the thermospheric temperature in the auroral region sharply increases at a higher pressure level than in the low-latitude regions. Using an electron transport code, we estimate the characteristic energy of the precipitated electrons derived from these observations to be in the range 1–5 keV using a low latitude model and 5–30 keV in case of the modified model.

A.2.2 Introduction

Images collected with the Hubble Space Telescope (HST) have shown that Saturn's auroral morphology is characterized by a dynamic aurora ring located between 70° and 80° which responds to the solar wind dynamic pressure (*Gérard et al.* (2004); *Clarke et al.* (2005); *Grodent et al.* (2005a)). The energy of the primary auroral electrons exciting the H2 emissions in Saturn's ultraviolet aurora has so far only been determined indirectly using two distinct spectral methods. The first approach makes use of the FUV color ratio, taking advantage of the strong wavelength dependence of the methane absorption cross section between 130 and 145 nm. When the emission layer is located below the homopause, the altitude where the molecular and eddy diffusion coefficients are equal, wavelengths <145 nm are partly absorbed by the overlying hydrocarbon column. Ultraviolet spectra of Saturn's aurora at ∼3 nm resolution were first obtained with the UVS instrument during the Voyager 1 and 2 flybys of the planet (*Broadfoot et al.* (1981); *Sandel et al.* (1982)). *Broadfoot et al. (1981)* noted that limb scans with the UVS slit locate the auroral emission approximately 800 km above the limb. *Sandel et al.* (1982) found that, unlike the Jovian aurora, most spectra of Saturn's aurora did not indicate the presence of absorption by hydrocarbons. A particularly bright spectrum was best fitted with a CH_4 column of 8×10^{15} cm^{-2}, suggesting an electron energy of ∼10 keV. Six auroral spectra obtained with the Space Telescope Imaging Spectrograph (STIS) were analyzed by *Gérard et al.* (2004) who found indications of a weak absorption by methane. Using *Moses et al. (2000)* low latitude atmosphere model and an electron energy – H_2 column relationship, they derived a primary electron energy of 12 ± 3 keV. Recently, *Gustin et al.* (2009) analyzed a Cassini-UVIS FUV spectrum moderately absorbed by a vertical CH_4 column of 1.2×10^{16} cm^{-2}, corresponding to electron energies near ∼10 keV. Other UVIS spectra were found to be unabsorbed by methane (J. Gustin, private communication, 2008), suggesting that the maximum electron energy is ∼15 keV, which corresponds to an altitude of ∼620 km in the low-latitude atmospheric model by *Moses et al. (2000)*. A second approach is based on the presence of self-absorption of H_2 lines below 120 nm. Transitions connecting to the ground state $v'' = 0$ and 1 vibrational level may be self-absorbed by the overlying H_2 gas, leading to a weakening of EUV specific lines and an increase of intensities at longer wavelengths (*Gustin et al.* (2004a)). *Sandel et al.* (1982) found that one UVS spectrum was best fitted using a spectral model with an overlying H_2 column of 1×10^{20} cm^{-2}. *Gustin et al.* (2009) used a detailed spectral model

to make a thorough analysis of spectra at ∼0.2 resolution collected with the Far Ultraviolet Spectroscopic Explorer (FUSE) satellite. An excellent fit to the line intensity distribution found a rotational temperature of ∼400 K, in agreement with the 420 ± 50 K obtained by *Melin et al.* (2007) from ground based H_3^+ IR spectra. A foreground vertical H_2 abundance of 3×10^{19} cm^{-2} derived from the FUSE spectra corresponds to a pressure level of ∼0.1 µbar, independently of any atmospheric model, and to an altitude of ∼660 km in the *Moses et al.* (2000) model.

A.2.3 Observations and Data Analysis

The HST FUV images used for this study were taken during the HST-Cassini campaign (GO 10862 program) between January 13, 2007 and February 16, 2008 when the subsolar latitude ranged from 14.2° S to 8.3° S. They were obtained with the photon-counting Multi-Anode Micro-channel Array (MAMA) of the High Resolution Camera Solar Blind Channel (SBC) on the Advanced Camera for Surveys (ACS). The point spread function is <2 pixels FWHM. Images were taken both with the F125LP filter (sensitive to the H_2 Lyman and Werner bands but excluding the H Lyman–α line) and with the F115LP filter (which includes Lyman–α). In this program, a typical orbit sequence consists of five 100-s exposures taken with the F125LP filter (Ly-α rejected), followed by nine 100-s exposures with the F115LP filter (Ly-α included) and finally another five 100-s exposures with the F125LP filter. The field of view of 35×31 arcsec^2 is wider than Saturn's apparent equatorial diameter of 10 arcsec, and thus also includes part of the ring system of the planet.

After dark current subtraction and flat-field and geometric corrections, the final image plate scale is 0.0301 arcsec/pixel in each direction. The first step in the analysis consists in the accurate determination of the planetary center. Since the HST pointing accuracy is limited by the onboard guide star catalogue that may include a 1-arcsec (∼30 pixels) uncertainty, the planetary central pixel must be determined using the image itself. Given the Earth-Saturn distance for the time of the observation and the plate scale, our automatic method fits elliptic ribbons to the Kronian A, B and C rings. The center of these ellipses provides an estimate of Saturn's center position in the field of view of ACS with an accuracy of ∼1 pixel. The plate scale is then directly converted into an altitude scale so that the location of the 1-bar level may be determined. To improve the signal to noise ratio, images have been co-added by sets of 5 consecutive images obtained with the same filter.

Radial cuts of the planetary disk at different angles are then generated and are rebinned to increase the signal to noise ratio.

Figure A.9 shows an example of an ACS exposure obtained on January 21, 2007 at 0322 UT with the F115LP filter clearly showing a brightness gap between the limb and the auroral emission. The altitude of the 1-bar level calculated from the camera plate scale is indicated by the white contour. It is seen that this contour agrees within one pixel with the position of the observed sunlit limb, corresponding to the 1-bar altitude level. Figure A.9 also shows the observed light curve along a radial cut through the auroral region. The location of the calculated 1-bar level altitude is shown by the vertical dashed line. The brightness decreases rapidly above the limb but increases again beyond 650 km. The light curve shows a peak near 1150 km, corresponding to the auroral emission layer observed on the image of the planetary disk.

A.2.4 Altitude of the Auroral Emission Peak

To analyze the dataset, an automatic algorithm performs radial scans from the planet's center with 0.1° steps to cover the entire southern auroral region. For each step, the algorithm determines the maximum in the light curve between 0 and 2000 km. A median filtering over 20 profiles (i.e. ∼2°) is then performed and the code identifies the longest sequence of points above 500 km. This sequence retains only the points where the light curve gap is observed under the auroral emission. We then compute the maximum peak altitude in this point sequence with the median filter. This method provides the actual altitude of the emission layer assuming that the aurora is located in the plane of the observed planetary limb and provides a lower limit otherwise. Our statistical study is based on 836 individual images leading to 176 light curves. We find that the average emission peak is 1111 ± 347 km for exposures taken with the F115LP filter, 1181 ± 251 km with the F125LP filter, leading to an average value of 1145 ± 305 km when all images are considered. The 70 km difference between the two filters is not significant, considering the value of the standard deviations.

We now examine the implications of this altitude determination and how they fit with the other constraints based on analysis of FUV and EUV spectra. To summarize, the FUSE spectra indicate that the auroral emission originates from a level of ∼0.1 µbar in a region where the temperature is ∼400 K, a value incompatible

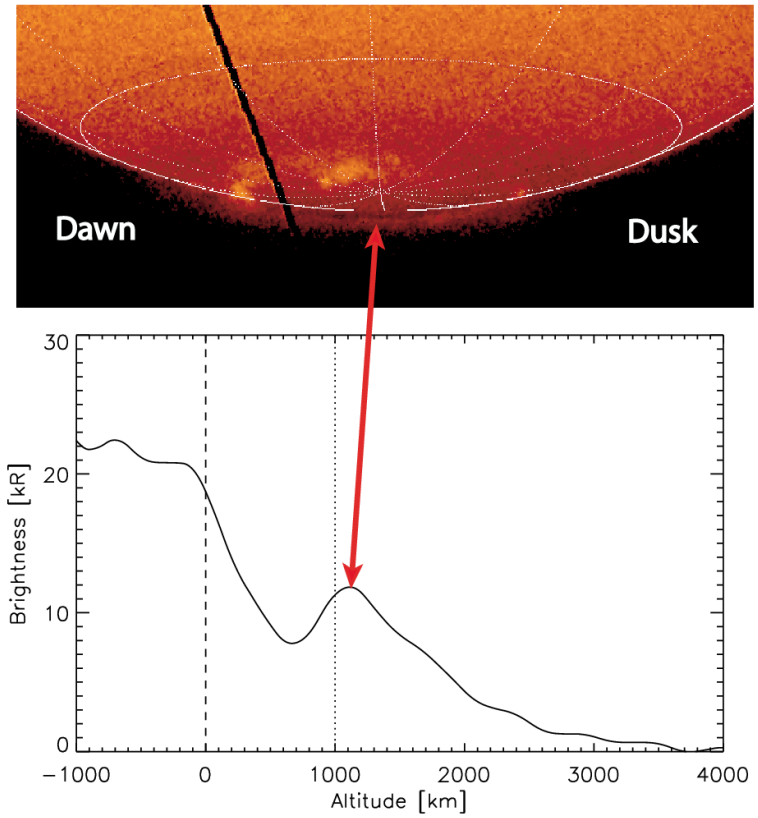

Figure A.2: (top) Zoom on an image of Saturn's south polar region obtained with the ACS camera. Auroral emission is clearly observed beyond the nightside limb. The white contours indicate the calculated location of the 1-bar level; parallels and meridians are shown 30° apart. The dark oblique stripe is the shadow of the detector repelling wire of the ACS camera. The dashed and the dotted lines indicate the 0 and 1000 km respectively. (bottom) Cut through the auroral region showing an emission peak near 1150 km.

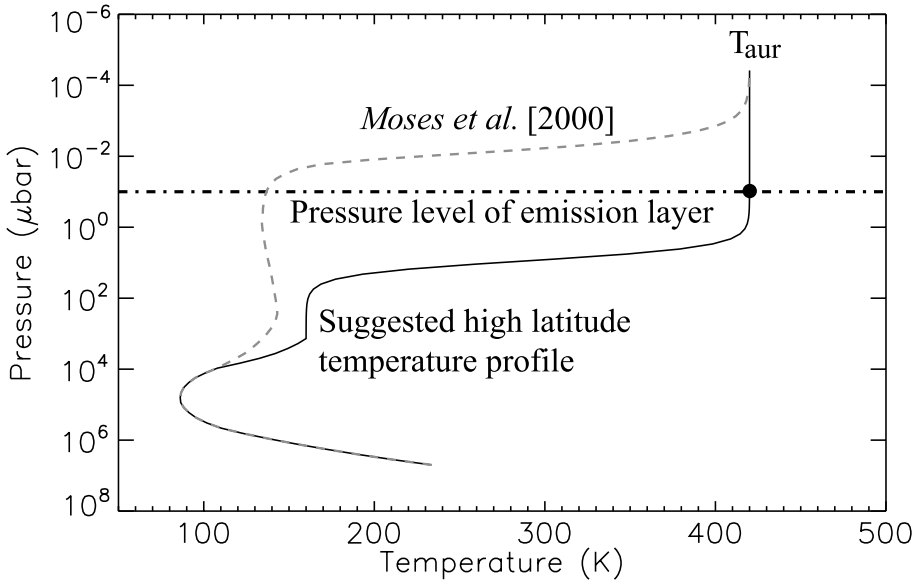

Figure A.3: Pressure-temperature relationship in the *Moses et al.* (2000) model transposed to polar latitudes (dashed line) and in an alternative possible high-latitude model (solid line). The horizontal line indicates the 0.1 μbar level and the full circle indicates the temperature at this pressure level.

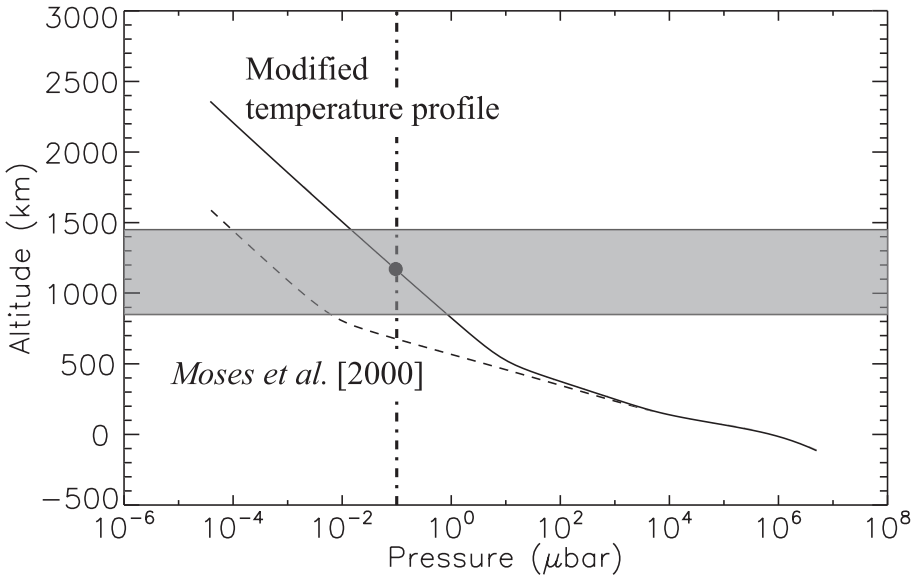

Figure A.4: Altitude-pressure relationship in the *Moses et al.* (2000) model adapted to polar latitudes (dashed line) and in the modified model (solid line). The vertical line indicates the 0.1 μbar level deduced from spectral constraints and the grey zone shows the range of peak altitudes derived from the present study. The full circle indicates the region meeting the pressure and altitude observational constraints.

with 135 K at 0.1 µbar provided by the low-latitude model of *Moses et al.* (2000). Figure A.3 compares observational results with the pressure-temperature relationship in the low-latitude model by *Moses et al.* (2000) adapted to auroral latitudes by adjusting the value of the gravity. The 0.1-µbar pressure determined from the FUSE spectra is indicated by a horizontal line and the auroral temperature of 400 K derived from the H_3^+ and the H_2 spectra is indicated by a closed circle. Another disagreement between auroral observations and the Moses et al. model is clearly apparent in Figure A.4 showing the altitude-pressure relationship. The vertical lines at 0.1 µbar show the emission level based on the FUSE spectra and the horizontal bars define the range of variability of the auroral emission peak centered on 1150 km. The circle locates the central point meeting both constraints. It is situated at a pressure level approximately two orders of magnitude larger than the *Moses et al.* (2000) model at 1150 km. Inversely, in the Moses et al. model, the 0.1 µbar pressure is at an altitude of ∼600 km, 550 km below our auroral limb observations. We thus conclude that the low latitude model cannot match the observational evidence derived from a recent set of auroral spectral observations. In particular, Figure A.3 shows that the strong evidence (from both IR and FUV spectra) of an auroral tem-

perature of ∼400 K is met at pressures less than 2×10^{-2} µbar. To reconcile both datasets, we speculate that the thermal structure of the auroral upper atmosphere of Saturn is modified by the presence of auroral particle and Joule heating whose effect is to deposit energy and heat up the region located below the 10^{-2} µbar level. This heating does not appreciably increase the local exospheric temperature since meridional transport efficiently redistributes heat from the polar to the equatorial regions. The role of transport was demonstrated by *Smith et al.* (2005) using a three-dimensional atmospheric circulation model. As an example, Figure A.3 presents an alternative model meeting the observational constraints listed before. We arbitrarily modified the temperature between 10^3 and 10^{-4} µbar in such a manner as to reach a value of ∼400 K at the 0.1 µbar level. The functional dependence used by *Yelle et al.* (1996) for Jupiter's thermosphere is adopted with a mesospheric temperature $T_0 = 160$ K, an α parameter = 0.03, and an exospheric temperature $T_\infty = 420$ K reached at $z_m = 650$ km. Between 1 and 10 mbars, the temperature profile is a linear combination between *Moses et al.* (2000) values and the expression given by *Yelle et al.* (1996). From this modified pressure-temperature relationship, the new pressure-altitude curve is derived assuming hydrostatic equilibrium and shown in Figure 3. Incidentally, we note that the faster increase of temperature above the 1-bar level probably implies a lowering of the altitude of the homopause compared to the low latitude value. In this case, the full circle corresponding to a pressure of 0.1 µbar and an altitude of 1150 km falls near the center of the rectangle defined by the observational constraints from the FUSE spectra and the HST limb images, while meeting the 400 K determination from the EUV and infrared auroral spectra.

We now examine what may be inferred from the altitude of the emission layer about the characteristic energy of the auroral electrons. For this purpose, a series of simulations has been made with an electron transport code to calculate the vertical distribution of the H_2 FUV volume emission rate. These calculations are based on a direct simulation Monte Carlo method solving the Boltzmann equation described by *Shematovich et al.* (1994) for the Earth's thermosphere. It was subsequently applied by *Bisikalo et al.* (1996) to an H_2-dominated upper atmosphere by replacing cross sections by those appropriate to proton and electron collisions with H_2 and H. Figure A.5 illustrates the altitude distribution of the total H_2 Lyman and Werner band emission calculated for a series of monoenergetic electron beams ranging from ∼750 eV to 30 keV with an isotropic pitch angle distribution. The dashed line curves have been obtained using the *Moses et al.* (2000) model adapted to gravity in the

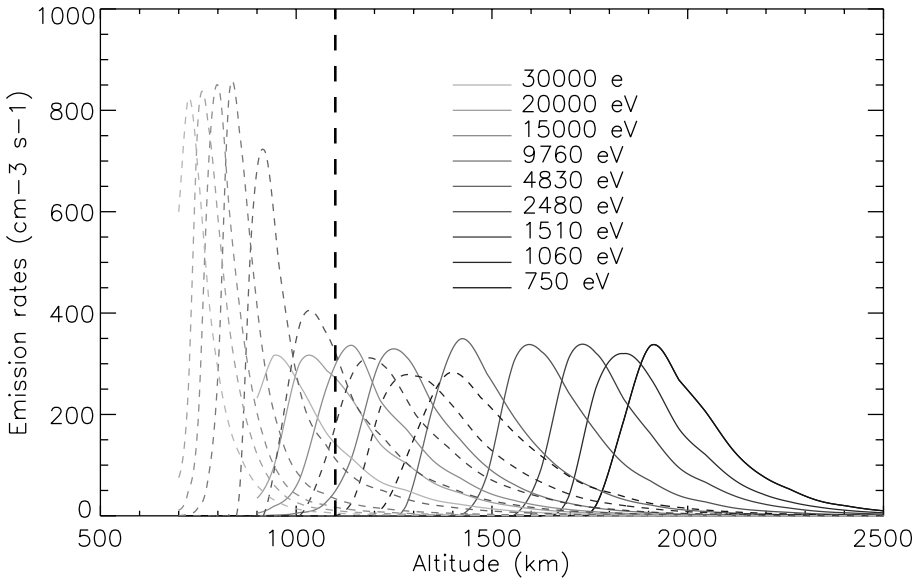

Figure A.5: Volume emission rate of H_2 FUV emissions calculated with a Monte Carlo electron transport code for various primary electron energies. Dotted lines, the low latitude model by *Moses et al.* (2000) is used; solid lines, same using the modified temperature profile model shown in Figure A.3.

polar regions. To generate an emission peak at 1100 km, simulations show that electron energies need to be about 2 keV. This value is close to the that obtained in recent models (*Cowley et al.* (2008), and references therein) as the minimum field-aligned voltage required to produce the current density compatible with Cassini observations.

The simulations also show that electrons about 20 keV are required to generate an emission peak at 0.1 µbar, independently of the temperature profile. The consequence is that in order to produce auroral emission at 1100 km, the pressure levels must be located at a higher altitude than in the low-latitude model. For comparison, calculations performed with the modified model are illustrated in Figure 4 by the solid lines. As expected, all curves for a given energy are now located at a higher altitude. In particular, electrons with energies of about 20 keV produce an emission peak at 1100 km, the auroral altitude determined in this study.

We also note that this result depends somewhat on the adopted pitch angle distribution. For example, if the precipitation is field-aligned, the pressure reached by 20 keV electrons would be less than doubled, changing from 0.06 to 0.1 µbar. In other words, the energy required for field aligned electrons to reach a given pressure

level would be approximately divided by 2, corresponding to an energy of ∼10 keV.

A.2.5 Conclusions

Analysis of over 800 images of Saturn's FUV aurora above the nightside limb indicate that the maximum H_2 emission is observed at an altitude of about 1100 km. A set of independent spectral observations indicate that i) the temperature prevailing in the region of emission is close to 400 K, ii) the auroral electron energy is occasionally high enough to produce a weak absorption by methane, iii) the H_2 column overlying the emission layer corresponds to a pressure level of about 0.1 µbar. Electrons of 15–20 keV deposit their energy at this pressure level, independently of the detailed thermal structure. We find that the set of different observations can only be reconciled if the thermal structure of the high-latitude thermosphere is different from the low-latitude reference model available so far.We estimate the characteristic energy of the precipitating electrons giving a luminosity peak near 1100 km to be in the range 1–5 keV using a low latitude model and 5–30 keV in case of the modified model.

The occasional presence of hydrocarbon absorption in the FUV spectra may result from sporadic hardening of the energy spectrum of the precipitated electrons. The results of our numerical simulations in Figure A.5 indicate that >10 keV electrons may produce emission near the homopause region located at ∼800 km in the low-latitude model. However, ∼100 keV electrons would be needed in our modified profile, in which the homopause altitude is close to 500 km, in order to generate a significant absorption in the FUV. Further study of the circumstances when hydrocarbon absorption is observed should help to clarify this issue.

A.3 Additional details on the modified Kronian polar atmospheric model

In the above section, we highlighted the danger to extrapolate atmospheric models constrained by equatorial measurements to the polar regions. We already discussed this issue on Section 5.5 when we tried to reconcile direct altitude measurement and color ratio measurements for the IFP tail. On Saturn, we proposed a modified model for the polar region atmospheric vertical profiles on Saturn. Here I provide more details on how this modified atmosphere is built and some underlying consequences.

The modified model is basically an empirical modification of the equatorial atmosphere model from *Moses et al.* (2000) (hereafter called Moses model) designed to meet three observational constrains: the pressure (∼0.1µbar), the temperature (∼ 400 K) and the altitude (∼1100 km) of the auroral emissions. The pressure-temperature profile we adopted is divided into three parts:

- for pressures bellow $10^3\mu$bar, the temperature is described by the following formula (from *Yelle et al.* (1996)):

$$T(a) = T_0 + \frac{T_\infty - T_0}{1 + e^{-\alpha(a-a_m)}}$$

  where a is the altitude of the considered point[1] (in km), T_0 is the mesospheric temperature (in K), T_∞ is the exospheric temperature (in K), α is linked to the maximum temperature gradient [2] and a_m is the maximum gradient altitude (in km). The adopted values are: $T_0 = 160$K, $T_\infty = 420$K, $\alpha = 0.04$ and $a_m = 550$ km.

- for pressures above $10^4\mu$bar, the pressure temperature relationship is identical to the one from the Moses model,

- between $10^3\mu$bar and $10^4\mu$bar, the temperature profile is a linear combination transition between the 2 above profiles.

Starting from our new pressure-temperature relationship, we computed the altitude profile as a function of the pressure, based on the hydrostatic equilibrium formula:

$$z_1 = z_0 - (p_1 - p_0)\frac{kT_1}{M_1 g_1}$$

where k is the Boltzmann constant[3] and z_x is the altitude (in m), p_x is the pressure (in Pa), T_x is the temperature (in K), M_x is the mean molecular mass (in kg) and g_x is the gravity acceleration (in m/s) at level x. Note that the gravity acceleration is evaluated for each step assuming a latitude of 80°. The mean molecular mass is also re-evaluated for each step based on the pressure-composition profiles from the Moses model. It can be seen in Figure A.4 that this new profile meets the

[1] At this stage, the altitude-pressure relationship is still the one from the Moses model. We will only adapt this relationship later in the process.

[2] $\alpha = \frac{4}{T_\infty - T_0}\frac{dT}{dz}|_{z=z_m}$ where z_m is the altitude of maximum temperature gradient.

[3] $k = 1.3807 \times 10^{-23}$J/s.

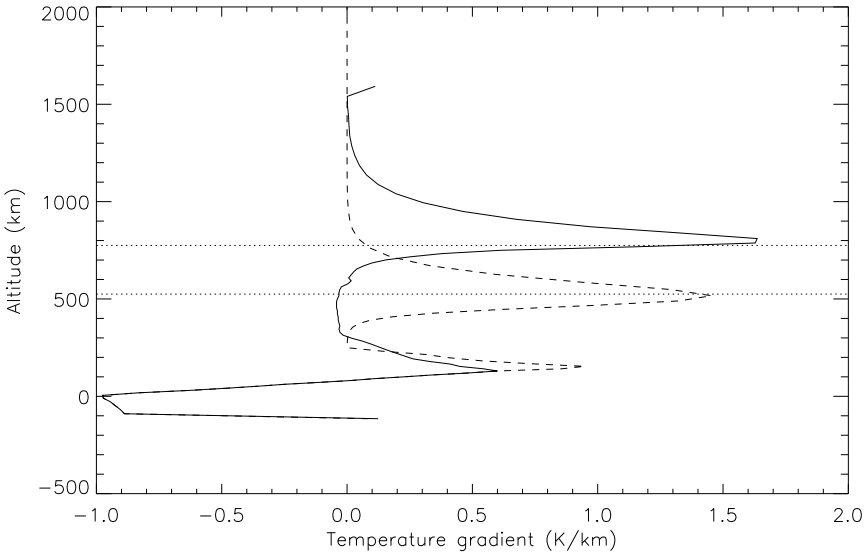

Figure A.6: Plot of the vertical temperature gradient. The solid line corresponds to the Moses model and the dashed line represents the modified profile.

observational constraints while the Moses profile, even adapted for the gravity a 80° latitude does not.

Figure A.6 shows that the new temperature-pressure relationship keeps approximately the same maximum temperature gradient value, but this maximum is shifted from 800 km to 500 km.

The density profile is then computed from the perfect gas law:

$$n = \frac{p}{kT}$$

where n is the density, p is the pressure, k is the Boltzmann constant and T is the temperature. Figure A.7 shows the original Moses density profile (i.e. for a 30° latitude) in dotted line, the Moses profile adapted for the gravity at 80° latitude in solid line and the new modified profile in dashed line.

The modifications we propose to make the polar atmosphere model compatible with measurements is purely ad-hoc and empirical. However, the fact that the temperature raises deeper than in the equatorial regions has physical causes. Usually,

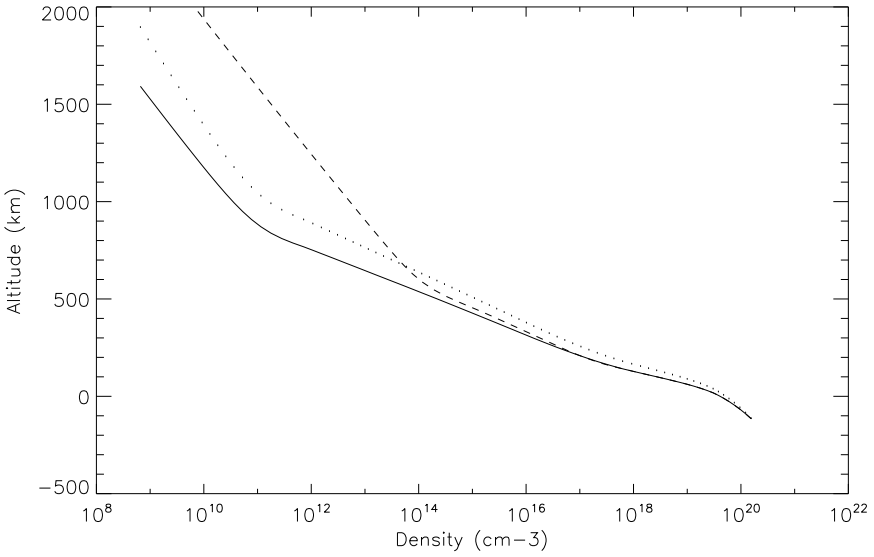

Figure A.7: Density profiles. The solid line represents the profile from the equatorial Moses model adapted for 80° latitude. The dotted line line represents the original Moses profile at 30° latitude. The dashed line represents the output of the new modified model.

the region where the temperature abruptly increases in giant planet atmospheres corresponds to the hydrocarbon homopause. Indeed these molecules generally act as a cooler for the atmosphere, radiating the excess energy to space in the form of IR emissions. The hydrocarbon content of the atmosphere sharply decreases when turbulent diffusion is not sufficient to homogenize the atmospheric constituents. The dominant hydrocarbon molecule in the giant planets atmospheres is methane (CH_4). The methane homopause is defined as the point where the molecular and eddy diffusion coefficients for methane are equal. The changes we propose for the temperature profile, and therefore, to the density profile also affect the molecular diffusion coefficient. This coefficient can be computed with the following formula (*Gladstone*, 1982):

$$D(z) = 2.3 \times 10^{17} \frac{T(z)^{0.765}}{n(z)} \sqrt{\frac{16.04}{m} \frac{m + 2.016}{18.059}}$$

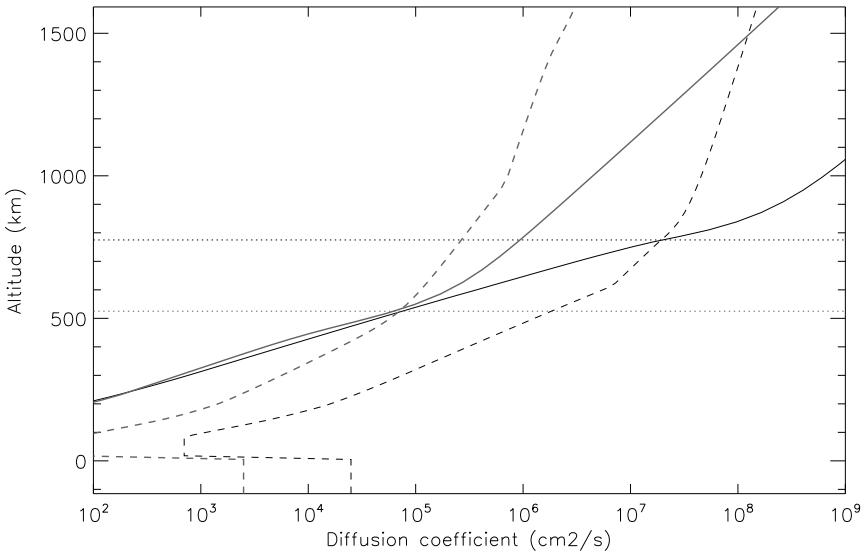

Figure A.8: Profiles of the diffusion coefficients as a function of the altitude. The black lines correspond to the Moses model while the red lines correspond to the modified atmosphere. The molecular diffusion coefficients are show on solid lines and the eddy diffusion coefficients are shown in dashed lines.

where m is the CH_4 molecular mass ($m_{CH_4} = 16$),$D(z)$ is the molecular diffusion coefficient in cm^2s^{-1}, $T(z)$ is the temperature in K and $n(z)$ is the total density in cm^{-3}. Figure A.8 shows the molecular diffusion coefficients both from the Moses model and the modified model. The eddy diffusion coefficient is much more complex and poorly constrained. We chose here to keep the relationship between eddy diffusion coefficient and the pressure from the Moses model. We determine that we need to divide the eddy diffusion coefficient by a factor of 15 to get an homopause altitude corresponding to the new temperature gradient altitude.

A.4 Estimate of the particle energy distribution

Since we are able to extract vertical profiles of Saturn's auroral emissions, it is also possible to remove an empirical background disk intensity profile in order to obtain

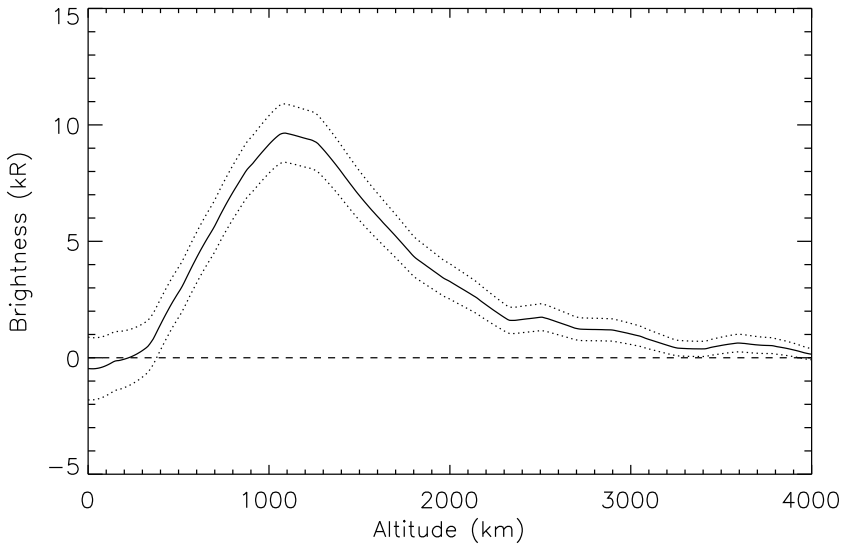

Figure A.9: Example of radial profile through the Kronian aurora. An empirical background disk profile has been removed.

a vertical profile only containing the auroral contribution (Figure A.9). On the case of Saturn, the disk profile is simply a radial profile extracted outside of the auroral region. We note that by removing the disk background, the mean peak altitude decreased down to 1050 km (which remains within the uncertainty bars of the previous estimate). Moreover, if we try to fit a Chapman profile (see Equation 5.1) to the observed curve, as we did for the Io tail, the emission scale height is 550 ± 115 km.

We can now try to find the theoretical electron energy distribution that matches the observed profile, as we did for tail profiles on Jupiter. Assuming a mono-energetic, a Maxwellian or a Kappa distribution, we seek for the set of parameters that best fits the observed profile (Figure A.10). The corresponding differential intensities are shown in Figure A.11. The mean energies deduced from the best fits range from $\sim$10 keV for the Kappa distribution to $\sim$20 keV for the mono-energetic one, the mean energy for the Maxwellian distribution being around $\sim$12 keV. Similarly to the Io tail profiles, the Kronian profile width can neither be reproduced satisfactorily with a mono-energetic distribution nor by a Maxwellian distribution. However, even the Kappa distribution seems unable to reproduce the high altitude part of the profile. Consequently, the energy spectrum of these three theoretical

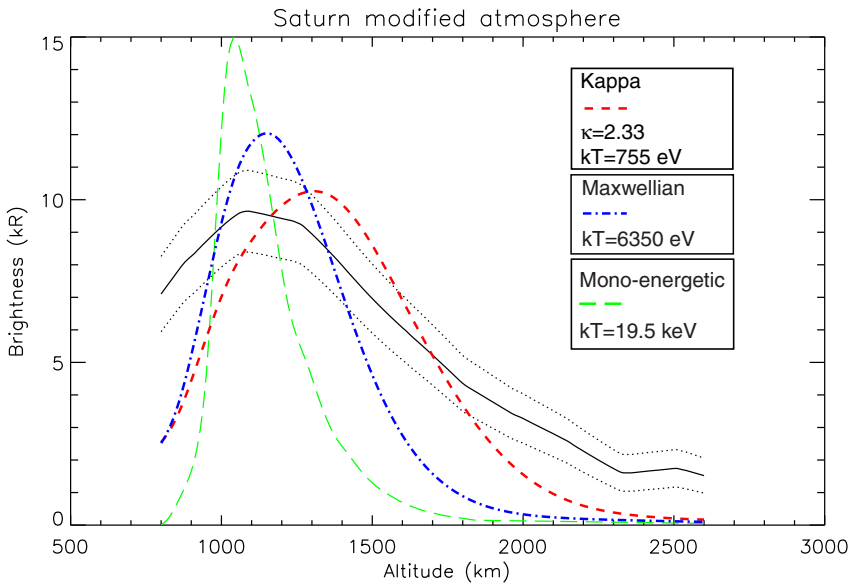

Figure A.10: Observed and simulated vertical emission profiles. The observations and the estimated uncertainties are represented by the solid line surrounded by the dotted lines. The three other lines are the best fit vertical profiles based the theoretical distributions. The green long dashed line corresponds to the mono-energetic distribution, the red small dashed line to the kappa distribution and the blue the dash-dotted line to the Maxwellian distribution. None of these theoretical profiles provides a reasonable fit of the observed curve because they underestimate the high altitude emissions.

distributions is too narrow and a soft energy component appears to be missing.

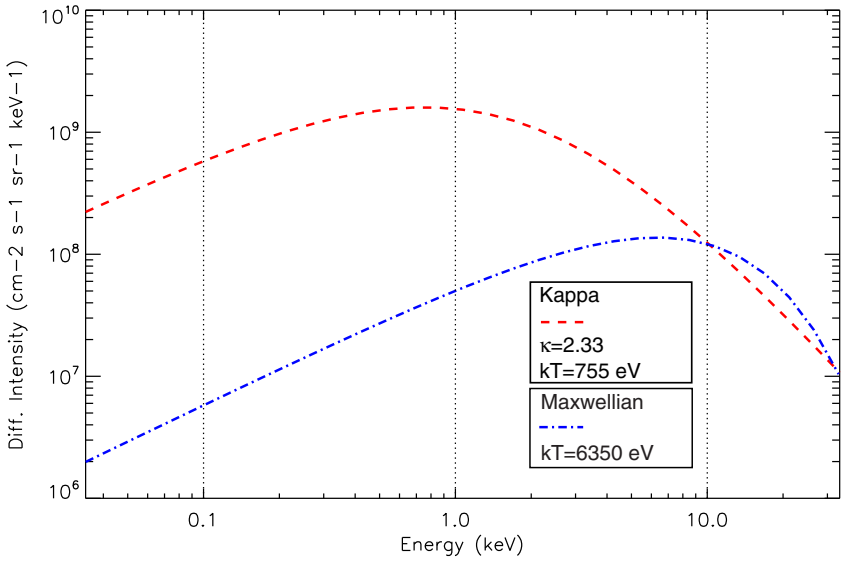

Figure A.11: Energy spectra computed with the best fit parameters for a kappa distribution (red dashed line), and a Maxwelllian distribution (blue dash-dotted line). Note that these intensities are computed assuming an auroral curtain width of 1000 km. This implies that if the real width of the curtain is 500 km, these values should be multiplied by a factor of 2.

Bibliography

Alexeev, I. I., and E. S. Belenkaya (2005), Modeling of the Jovian Magnetosphere, *Annales Geophysicae*, *23*, 809–826.

Bagenal, F. (1994), Empirical model of the Io plasma torus: Voyager measurements, *J. Geophys. Res.*, *99*, 11,043–11,062, doi:10.1029/93JA02908.

Baker, D. J. (1974), Rayleigh, the unit for light radiance., *Applied Optics*, *13*, 2160–2163.

Bhardwaj, A., and M. Michael (2002), Io-Jupiter system: a unique case of moon-planet interaction, in *Earth-like Planets and Moons*, *ESA Special Publication*, vol. 514, edited by B. H. Foing and B. Battrick, pp. 115–121.

Bigg, E. K. (1964), Influence of the Satellite Io on Jupiter's Decametric Emission, *Nature*, *203*, 1008–+.

Bisikalo, D. V., V. I. Shematovich, J.-C. Gérard, G. R. Gladstone, and J. H. Waite (1996), The distribution of hot hydrogen atoms produced by electron and proton precipitation in the Jovian aurora, *J. Geophys. Res.*, *101*, 21,157–21,168, doi: 10.1029/96JE01952.

Boffi, F. R., M. Sirianni, R. A. Lucas, N. R. Walborn, and C. R. Proffitt (2008), Delivery of a new ACS SBC throughput curve for Synphot, *Technical Instrument Report ACS 2008-002*, STSCI, tIR ACS 2008-002.

Bonfond, B., J.-C. Gérard, D. Grodent, and J. Saur (2007), Ultraviolet Io footprint short timescale dynamics, *Geophys. Res. Lett.*, *34*, 6201–+, doi: 10.1029/2006GL028765.

Bonfond, B., D. Grodent, J.-C. Gérard, A. Radioti, J. Saur, and S. Jacobsen (2008), UV Io footprint leading spot: A key feature for understanding the UV Io footprint multiplicity?, *Geophys. Res. Lett.*, *35*, 5107–+, doi:10.1029/2007GL032418.

Bonfond, B., D. Grodent, J.-C. Gérard, A. Radioti, V. Dols, P. A. Delamere, and J. T. Clarke (2009), The Io UV footprint: Location, inter-spot distances and tail vertical extent, *J. Geophys. Res.*, *114*, 7224–+, doi:10.1029/2009JA014312.

Broadfoot, A. L., B. R. Sandel, D. E. Shemansky, J. B. Holberg, G. R. Smith, D. F. Strobel, J. C. McConnell, S. Kumar, D. M. Hunten, S. K. Atreya, T. M. Donahue, H. W. Moos, J. L. Bertaux, J. E. Blamont, R. B. Pomphrey, and S. Linick (1981), Extreme ultraviolet observations from Voyager 1 encounter with Saturn, *Science*, *212*, 206–211, doi:10.1126/science.212.4491.206.

Carlson, C. W., J. P. McFadden, R. E. Ergun, M. Temerin, W. Peria, F. S. Mozer, D. M. Klumpar, E. G. Shelley, W. K. Peterson, E. Moebius, R. Elphic, R. Strangeway, C. Cattell, and R. Pfaff (1998), FAST observations in the downward auroral current region: Energetic upgoing electron beams, parallel potential drops, and ion heating, *Geophys. Res. Lett.*, *25*, 2017–2020, doi:10.1029/98GL00851.

Chust, T., A. Roux, W. S. Kurth, D. A. Gurnett, M. G. Kivelson, and K. K. Khurana (2005), Are Io's Alfvén wings filamented? Galileo observations, *Planet. Space Sci.*, *53*, 395–412, doi:10.1016/j.pss.2004.09.021.

Clarke, J. T., G. E. Ballester, J. Trauger, R. Evans, J. E. P. Connerney, K. Stapelfeldt, D. Crisp, P. D. Feldman, C. J. Burrows, S. Casertano, J. S. Gallagher, III, R. E. Griffiths, J. J. Hester, J. G. Hoessel, J. A. Holtzman, J. E. Krist, V. Meadows, J. R. Mould, P. A. Scowen, A. M. Watson, and J. A. Westphal (1996), Far-Ultraviolet Imaging of Jupiter's Aurora and the lo "Footprint", *Science*, *274*, 404–409.

Clarke, J. T., G. E. Ballester, J. Trauger, J. Ajello, W. Pryor, K. Tobiska, J. E. P. Connerney, G. R. Gladstone, J. H. Waite, L. Ben Jaffel, and J.-C. Gérard (1998), Hubble Space Telescope imaging of Jupiter's UV aurora during the Galileo orbiter mission, *J. Geophys. Res.*, *103*, 20,217–20,236.

Clarke, J. T., J. Ajello, G. Ballester, L. Ben Jaffel, J. Connerney, J.-C. Gérard, G. R. Gladstone, D. Grodent, W. Pryor, J. Trauger, and J. H. Waite (2002), Ultraviolet

emissions from the magnetic footprints of Io, Ganymede and Europa on Jupiter, *Nature*, *415*, 997–1000.

Clarke, J. T., D. Grodent, S. W. H. Cowley, E. J. Bunce, P. Zarka, J. E. P. Connerney, and T. Satoh (2004), *Jupiter's aurora*, pp. 639–670, Jupiter. The Planet, Satellites and Magnetosphere.

Clarke, J. T., J.-C. Gérard, D. Grodent, S. Wannawichian, J. Gustin, J. Connerney, F. Crary, M. Dougherty, W. Kurth, S. W. H. Cowley, E. J. Bunce, T. Hill, and J. Kim (2005), Morphological differences between Saturn's ultraviolet aurorae and those of Earth and Jupiter, *Nature*, *433*, 717–719, doi:10.1038/nature03331.

Connerney, J. E. P. (1981), The magnetic field of Jupiter - A generalized inverse approach, *J. Geophys. Res.*, *86*, 7679–7693, doi:10.1029/JA086iA09p07679.

Connerney, J. E. P., and T. Satoh (2000), The H_3^+ ion: a remote diagnostic of the jovian magneto sphere, in *Astronomy, physics and chemistry of H+3*, pp. 2471–+.

Connerney, J. E. P., R. Baron, T. Satoh, and T. Owen (1993), Images of Excited H_3^+ at the Foot of the Io Flux Tube in Jupiter's Atmosphere, *Science*, *262*, 1035–1038.

Connerney, J. E. P., M. H. Acuña, and N. F. Ness (1996), Octupole model of Jupiter's magnetic field from Ulysses observations, *J. Geophys. Res.*, *101*, 27,453–27,458, doi:10.1029/96JA02869.

Connerney, J. E. P., M. H. Acuña, N. F. Ness, and T. Satoh (1998), New models of Jupiter's magnetic field constrained by the Io flux tube footprint, *J. Geophys. Res.*, *103*, 11,929–11,940, doi:10.1029/97JA03726.

Cowley, S. W. H., E. J. Bunce, T. S. Stallard, and S. Miller (2003), Jupiter's polar ionospheric flows: Theoretical interpretation, *Geophys. Res. Lett.*, *30*(5), 050,000–1, doi:10.1029/2002GL016030.

Cowley, S. W. H., C. S. Arridge, E. J. Bunce, J. T. Clarke, A. J. Coates, M. K. Dougherty, J.-C. Gérard, D. Grodent, J. D. Nichols, and D. L. Talboys (2008), Auroral current systems in Saturn's magnetosphere: comparison of theoretical models with Cassini and HST observations, *Annales Geophysicae*, *26*, 2613–2630.

Crary, F. J. (1997), On the generation of an electron beam by Io, *J. Geophys. Res.*, *102*, 37–50, doi:10.1029/96JA02409.

Crary, F. J., and F. Bagenal (1997), Coupling the plasma interaction at Io to Jupiter, *Geophys. Res. Lett.*, *24*, 2135–+.

Dalgarno, A., M. Yan, and W. Liu (1999), Electron Energy Deposition in a Gas Mixture of Atomic and Molecular Hydrogen and Helium, *The Astrophysical Journal Supplement Series*, *125*, 237–256, doi:10.1086/313267.

Das, A., and W.-H. Ip (2000), Field aligned current and particle acceleration in the near-Io plasma torus, *Planet. Space Sci.*, *48*, 127–131, doi:10.1016/S0032-0633(99)00086-0.

Delamere, P. A., F. Bagenal, R. Ergun, and Y.-J. Su (2003), Momentum transfer between the Io plasma wake and Jupiter's ionosphere, *J. Geophys. Res.*, *108*, 11–1, doi:10.1029/2002JA009530.

Dols, V. (2001), The interaction of io and the jovian magnetic field: Io's alfvén wings and particle acceleration, Master's thesis, University of Alaska Fairbanks.

Dols, V., J. C. Gérard, J. T. Clarke, J. Gustin, and D. Grodent (2000), Diagnostics of the Jovian Aurora Deduced from Ultraviolet Spectroscopy: Model and HST/GHRS Observations, *Icarus*, *147*, 251–266, doi:10.1006/icar.2000.6415.

Dols, V., P. A. Delamere, and F. Bagenal (2008), A multispecies chemistry model of Io's local interaction with the Plasma Torus, *J. Geophys. Res.*, *113*, 9208–+, doi:10.1029/2007JA012805.

Drossart, P., B. Bezard, S. K. Atreya, J. Bishop, J. H. Waite, Jr., and D. Boice (1993), Thermal profiles in the auroral regions of Jupiter, *J. Geophys. Res.*, *98*, 18,803–+, doi:10.1029/93JE01801.

Ergun, R. E., Y.-J. Su, L. Andersson, F. Bagenal, P. A. Delemere, R. L. Lysak, and R. J. Strangeway (2006), S bursts and the Jupiter ionospheric Alfvén resonator, *J. Geophys. Res.*, *111*, 6212–+, doi:10.1029/2005JA011253.

Ergun, R. E., L. Ray, P. A. Delamere, F. Bagenal, V. Dols, and Y.-J. Su (2009), Generation of parallel electric fields in the Jupiter-Io torus wake region, *J. Geophys. Res.*, *114*, 5201–+, doi:10.1029/2008JA013968.

Frank, L. A., and W. R. Paterson (1999), Intense electron beams observed at Io with the Galileo spacecraft, *J. Geophys. Res.*, *104*, 28,657–+.

Frank, L. A., and W. R. Paterson (2000a), Observations of plasmas in the Io torus with the Galileo spacecraft, *J. Geophys. Res.*, *105*, 16,017–16,034, doi: 10.1029/1999JA000250.

Frank, L. A., and W. R. Paterson (2000b), Return to Io by the Galileo spacecraft: Plasma observations, *J. Geophys. Res.*, *105*, 25,363–25,378, doi: 10.1029/1999JA000460.

Frank, L. A., and W. R. Paterson (2002), Plasmas observed with the Galileo spacecraft during its flyby over Io's northern polar region, *J. Geophys. Res.*, *107*, 1220–+, doi:10.1029/2002JA009240.

Frank, L. A., W. R. Paterson, K. L. Ackerson, V. M. Vasyliunas, F. V. Coroniti, and S. J. Bolton (1996), Plasma Observations at lo with the Galileo Spacecraft, *Science*, *274*, 394–395.

Garvey, R. H., and A. E. S. Green (1976), Energy-apportionment techniques based upon detailed atomic cross sections, *Physical Review A (General Physics)*, *14*, 946–953, doi:10.1103/PhysRevA.14.946.

Garvey, R. H., H. S. Porter, and A. E. S. Green (1977), An analytic degradation spectrum for H2, *Journal of Applied Physics*, *48*, 190–193, doi:10.1063/1.323308.

Geissler, P. E., W. H. Smyth, A. S. McEwen, W. Ip, M. J. S. Belton, T. V. Johnson, A. P. Ingersoll, K. Rages, W. Hubbard, and A. J. Dessler (2001), Morphology and time variability of Io's visible aurora, *J. Geophys. Res.*, *106*, 26,137–26,146, doi:10.1029/2000JA002511.

Gérard, J.-C., and V. Singh (1982), A model of energy deposition of energetic electrons and EUV emission in the Jovian and Saturnian atmospheres and implications, *J. Geophys. Res.*, *87*, 4525–4532, doi:10.1029/JA087iA06p04525.

Gérard, J.-C., J. Gustin, D. Grodent, P. Delamere, and J. T. Clarke (2002), Excitation of the FUV Io tail on Jupiter: Characterization of the electron precipitation, *J. Geophys. Res.*, *107*, 30–1, doi:10.1029/2002JA009410.

Gérard, J.-C., D. Grodent, J. Gustin, A. Saglam, J. T. Clarke, and J. T. Trauger (2004), Characteristics of Saturn's FUV aurora observed with the Space Telescope Imaging Spectrograph, *J. Geophys. Res.*, *109*, 9207–+, doi: 10.1029/2004JA010513.

Gérard, J.-C., A. Saglam, D. Grodent, and J. T. Clarke (2006), Morphology of the ultraviolet Io footprint emission and its control by Io's location, *J. Geophys. Res.*, *111*, 4202–+, doi:10.1029/2005JA011327.

Gérard, J.-C., B. Bonfond, J. Gustin, D. Grodent, J. T. Clarke, D. Bisikalo, and V. Shematovich (2009), Altitude of Saturn's aurora and its implications for the characteristic energy of precipitated electrons, *Geophys. Res. Lett.*, *36*, 2202–+, doi:10.1029/2008GL036554.

Gladstone, G. (1982), Radiative transfer and photochemistry in the Upper atmosphere of Jupiter, Ph.D. thesis, California institute of Technology, Pasadena.

Gladstone, G. R., M. Allen, and Y. L. Yung (1996), Hydrocarbon Photochemistry in the Upper Atmosphere of Jupiter, *Icarus*, *119*, 1–52, doi:10.1006/icar.1996.0001.

Gladstone, G. R., S. A. Stern, D. C. Slater, M. Versteeg, M. W. Davis, K. D. Retherford, L. A. Young, A. J. Steffl, H. Throop, J. W. Parker, H. A. Weaver, A. F. Cheng, G. S. Orton, J. T. Clarke, and J. D. Nichols (2007), Jupiter's Nightside Airglow and Aurora, *Science*, *318*, 229–, doi:10.1126/science.1147613.

Goertz, C. K. (1980), Io's interaction with the plasma torus, *J. Geophys. Res.*, *85*, 2949–2956, doi:10.1029/JA085iA06p02949.

Goertz, C. K., and P. A. Deift (1973), Io's interaction with the magnetosphere, *Planet. Space Sci.*, *21*, 1399–1415, doi:10.1016/0032-0633(73)90232-8.

Goldreich, P., and D. Lynden-Bell (1969), Io, a jovian unipolar inductor, *Astrophys. Journal*, *156*, 59–78.

Grodent, D., G. R. Gladstone, J. C. Gerard, V. Dols, and J. H. Waite (1997), Simulation of the Morphology of the Jovian UV North Aurora Observed with the Hubble Space Telescope, *Icarus*, *128*, 306–321, doi:10.1006/icar.1997.5740.

Grodent, D., J. Waite, and J.-C. Gérard (2001), A self-consistent model of the Jovian auroral thermal structure, *J. Geophys. Res.*, *106*, 12,933–12,952, doi: 10.1029/2000JA900129.

Grodent, D., J. T. Clarke, J. Kim, J. H. Waite, and S. W. H. Cowley (2003a), Jupiter's main auroral oval observed with HST-STIS, *J. Geophys. Res.*, *108*, 2–1, doi:10.1029/2003JA009921.

Grodent, D., J. T. Clarke, J. H. Waite, S. W. H. Cowley, J.-C. Gérard, and J. Kim (2003b), Jupiter's polar auroral emissions, *J. Geophys. Res.*, *108*, 1366–+, doi: 10.1029/2003JA010017.

Grodent, D., J.-C. Gérard, J. T. Clarke, G. R. Gladstone, and J. H. Waite (2004), A possible auroral signature of a magnetotail reconnection process on Jupiter, *J. Geophys. Res.*, *109*, 5201–+, doi:10.1029/2003JA010341.

Grodent, D., J.-C. Gérard, S. W. H. Cowley, E. J. Bunce, and J. T. Clarke (2005a), Variable morphology of Saturn's southern ultraviolet aurora, *J. Geophys. Res.*, *110*, 7215–+, doi:10.1029/2004JA010983.

Grodent, D., J.-C. Gérard, A. Saglam, J. Gustin, J. T. Clarke, and J. E. Connerney (2005b), Location and Morphology of Io's FUV Footprint Emissions on Jupiter, in *Magnetospheres of the Outer Planets 2005*.

Grodent, D., B. Bonfond, J.-C. Gérard, A. Radioti, J. Gustin, J. T. Clarke, J. Nichols, and J. E. P. Connerney (2008a), Auroral evidence of a localized magnetic anomaly in Jupiter's northern hemisphere, *J. Geophys. Res.*, *113*, 9201–+, doi:10.1029/2008JA013185.

Grodent, D., J.-C. Gérard, A. Radioti, B. Bonfond, and A. Saglam (2008b), Jupiter's changing auroral location, *J. Geophys. Res.*, *113*, 1206–+, doi: 10.1029/2007JA012601.

Grodent, D., B. Bonfond, A. Radioti, J.-C. Gérard, X. Jia, J. D. Nichols, and J. T. Clarke (2009), Auroral footprint of Ganymede, *J. Geophys. Res.*, *114*, 7212–+, doi:10.1029/2009JA014289.

Gustin, J., P. D. Feldman, J.-C. Gérard, D. Grodent, A. Vidal-Madjar, L. Ben Jaffel, J.-M. Desert, H. W. Moos, D. J. Sahnow, H. A. Weaver, B. C. Wolven, J. M. Ajello, J. H. Waite, E. Roueff, and H. Abgrall (2004a), Jovian auroral spectroscopy with FUSE: analysis of self-absorption and implications for electron precipitation, *Icarus*, *171*, 336–355, doi:10.1016/j.icarus.2004.06.005.

Gustin, J., J.-C. Gérard, D. Grodent, S. W. H. Cowley, J. T. Clarke, and A. Grard (2004b), Energy-flux relationship in the FUV Jovian aurora deduced from HST-STIS spectral observations, *J. Geophys. Res.*, *109*, 10,205–+, doi: 10.1029/2003JA010365.

Gustin, J., J.-C. Gérard, W. Pryor, P. D. Feldman, D. Grodent, and G. Holsclaw (2009), Characteristics of Saturn's polar atmosphere and auroral electrons derived from HST/STIS, FUSE and Cassini/UVIS spectra, *Icarus*, *200*, 176–187, doi: 10.1016/j.icarus.2008.11.013.

Hess, S., P. Zarka, and F. Mottez (2007), Io Jupiter interaction, millisecond bursts and field-aligned potentials, *Planet. Space Sci.*, *55*, 89–99, doi: 10.1016/j.pss.2006.05.016.

Hess, S., P. Zarka, F. Mottez, and V. B. Ryabov (2009), Electric potential jumps in the Io-Jupiter flux tube, *Planetary and Space Science*, *57*, 23–33, doi: 10.1016/j.pss.2008.10.006.

Hess, S., P. Delamere, V. Dols, B. Bonfond, and D. Swift (in preparationa), Power transmission and particle acceleration along the io flux tube.

Hess, S., A. Petin, P. Zarka, B. Bonfond, and B. Cecconi (in preparationb), Lead angles and emitting electron velocities of the southern io-controlled radio arcs.

Hill, T. W., and V. M. Vasyliūnas (2002), Jovian auroral signature of Io's corotational wake, *J. Geophys. Res.*, *107*, 27–1, doi:10.1029/2002JA009514.

Hinson, D. P., A. J. Kliore, F. M. Flasar, J. D. Twicken, P. J. Schinder, and R. G. Herrera (1998), Galileo radio occultation measurements of Io's ionosphere and plasma wake, *J. Geophys. Res.*, *103*, 29,343–29,358, doi:10.1029/98JA02659.

Ingersoll, A. P., A. R. Vasavada, B. Little, C. D. Anger, S. J. Bolton, C. Alexander, K. P. Klaasen, and W. K. Tobiska (1998), Imaging Jupiter's Aurora at Visible Wavelengths, *Icarus*, *135*, 251–264, doi:10.1006/icar.1998.5971.

Jackman, C. H., R. H. Garvey, and A. E. S. Green (1977), Electron impact on atmospheric gases. I - Updated cross sections, *J. Geophys. Res.*, *82*, 5081–5090, doi:10.1029/JA082i032p05081.

Jacobsen, S., F. M. Neubauer, J. Saur, and N. Schilling (2007), Io's nonlinear MHD-wave field in the heterogeneous Jovian magnetosphere, *Geophys. Res. Lett.*, *34*, 10,202–+, doi:10.1029/2006GL029187.

Jacobsen, S., J. Saur, F. M. Neubauer, B. Bonfond, J. C. Gérard, and D. Grodent (submitted), The location and spatial shape of electron beams in io's wake.

Jia, X., M. G. Kivelson, K. K. Khurana, and R. J. Walker (2009a), Magnetic Fields of the Satellites of Jupiter and Saturn, *Space Science Reviews*, pp. 25–+, doi: 10.1007/s11214-009-9507-8.

Jia, X., R. J. Walker, K. M. G., K. K. Khurana, and J. A. Linker (2009b), Properties of ganymede's magnetosphere inferred from improved three-dimensional mhd simulations, *J. Geophys. Res.*, *114*, A09,209, doi:10.1029/2009JA014375.

Jones, S. T., and Y.-J. Su (2008), Role of dispersive Alfvén waves in generating parallel electric fields along the Io-Jupiter fluxtube, *J. Geophys. Res.*, *113*, 12,205–+, doi:10.1029/2008JA013512.

Khurana, K. K. (1997), Euler potential models of Jupiter's magnetospheric field, *J. Geophys. Res.*, *102*, 11,295–11,306, doi:10.1029/97JA00563.

Khurana, K. K., M. G. Kivelson, V. M. Vasyliunas, N. Krupp, J. Woch, A. Lagg, B. H. Mauk, and W. S. Kurth (2004), *The configuration of Jupiter's magnetosphere*, pp. 593–616, Cambridge University Press.

Kivelson, M. G., K. K. Khurana, D. J. Stevenson, L. Bennett, S. Joy, C. T. Russell, R. J. Walker, C. Zimmer, and C. Polanskey (1999), Europa and Callisto: Induced or intrinsic fields in a periodically varying plasma environment, *J. Geophys. Res.*, *104*, 4609–4626, doi:10.1029/1998JA900095.

Kivelson, M. G., F. Bagenal, W. S. Kurth, F. M. Neubauer, C. Paranicas, and J. Saur (2004), *Magnetospheric interactions with satellites*, pp. 513–536, Jupiter. The Planet, Satellites and Magnetosphere.

Knight, S. (1973), Parallel electric fields, *Planet. Space Sci.*, *21*, 741–750, doi: 10.1016/0032-0633(73)90093-7.

Kopp, A., G. T. Birk, and A. Otto (1998), On the formation of Io-related Jovian discrete auroral phenomena, *Advances in Space Research*, *21*, 1469–1473.

Krupp, N., V. M. Vasyliunas, J. Woch, A. Lagg, K. K. Khurana, M. G. Kivelson, B. H. Mauk, E. C. Roelof, D. J. Williams, S. M. Krimigis, W. S. Kurth, L. A. Frank, and W. R. Paterson (2004), *Jupiter. The Planet, Satellites and Magnetosphere*, chap. Dynamics of the Jovian magnetosphere, pp. 617–638, Cambridge University Press.

Lainey, V., J.-E. Arlot, Ö. Karatekin, and T. van Hoolst (2009), Strong tidal dissipation in Io and Jupiter from astrometric observations, *Nature*, *459*, 957–959, doi:10.1038/nature08108.

Landsman, W. (1998), Characteristic of the fuv-mama dark rate, *Tech. rep.*, Raytheon ITSS.

Maiz-Apellaniz, J., and L. Ubeda (2004), A new geometric-distortion solution for the stis nuv-mama, *Tech. rep.*, STSCI, iSR 2004-01.

Mauk, B. H., and J. Saur (2007), Equatorial electron beams and auroral structuring at Jupiter, *J. Geophys. Res.*, *112*, 10,221–+, doi:10.1029/2007JA012370.

Mauk, B. H., D. J. Williams, and A. Eviatar (2001), Understanding Io's space environment interaction: Recent energetic electron measurements from Galileo, *J. Geophys. Res.*, *106*, 26,195–26,208, doi:10.1029/2000JA002508.

Mauk, B. H., J. T. Clarke, D. Grodent, J. H. Waite, C. P. Paranicas, and D. J. Williams (2002), Transient aurora on Jupiter from injections of magnetospheric electrons, *Nature*, *415*, 1003–1005.

McComas, D. J., and F. Bagenal (2007), Jupiter: A fundamentally different magnetospheric interaction with the solar wind, *Geophys. Res. Lett.*, *34*, 20,106–+, doi:10.1029/2007GL031078.

Melin, H., S. Miller, T. Stallard, L. M. Trafton, and T. R. Geballe (2007), Variability in the H_3^+ emission of Saturn: Consequences for ionisation rates and temperature, *Icarus*, *186*, 234–241, doi:10.1016/j.icarus.2006.08.014.

Meyer-Vernet, N., M. Moncuquet, and S. Hoang (1995), Temperature inversion in the Io plasma torus., *Icarus*, *116*, 202–213, doi:10.1006/icar.1995.1121.

Miller, J. (2009), Analysis quantifies effects of tides in Jupiter and Io, *Physics Today*, *62*(7), 11–12.

Mitchell, D. G., W. S. Kurth, G. B. Hospodarsky, N. Krupp, J. Saur, B. H. Mauk, J. F. Carbary, S. M. Krimigis, M. K. Dougherty, and D. C. Hamilton (2009), Ion conics and electron beams associated with auroral processes on Saturn, *J. Geophys. Res.*, *114*, 2212–+, doi:10.1029/2008JA013621.

Moncuquet, M. (1997), Équilibre et confinement du tore de plasma d'io dans la magnétosphère de jupiter : observations d'ulysse et modélisation, Ph.D. thesis, Université Paris VII - Denis Diderot.

Moses, J. I., B. Bézard, E. Lellouch, G. R. Gladstone, H. Feuchtgruber, and M. Allen (2000), Photochemistry of Saturn's Atmosphere. I. Hydrocarbon Chemistry and Comparisons with ISO Observations, *Icarus*, *143*, 244–298, doi: 10.1006/icar.1999.6270.

Nemzek, R. J., R. Nakamura, D. N. Baker, R. D. Belian, D. J. McComas, M. F. Thomsen, and T. Yamamoto (1995), The relationship between pulsating auroras observed from the ground and energetic electrons and plasma density measured at geosynchronous orbit, *J. Geophys. Res.*, *100*, 23,935–23,944, doi: 10.1029/95JA01756.

Neubauer, F. M. (1980), Nonlinear standing Alfven wave current system at Io - Theory, *J. Geophys. Res.*, *85*, 1171–1178.

Oliversen, R. J., F. Scherb, W. H. Smyth, M. E. Freed, R. C. J. Woodward, M. L. Marconi, K. D. Retherford, O. L. Lupie, and J. P. Morgenthaler (2001), Sunlit Io atmospheric [O I] 6300 Å emission and the plasma torus, *J. Geophys. Res.*, *106*, 26,183–26,194, doi:10.1029/2000JA002507.

Pagano, I., A. F. Lanza, G. Leto, S. Messina, P. Barge, and A. Baglin (2009), CoRoT-2a Magnetic Activity: Hints for Possible Star-Planet Interaction, *Earth Moon and Planets*, *105*, 373–378, doi:10.1007/s11038-009-9301-3.

Pavlovsky et al., C. (2006), *Advanced Camera for Surveys Instrument Handbook for Cycle 16*, STScI, version 7.1 ed., http://www.stsci.edu/hst/acs.

Piddington, J. H., and J. F. Drake (1968), Electrodynamic Effects of Jupiter's Satellite Io, *Nature*, *217*, 935–+.

Pontius, D. H. (2002), The Io current wing, *J. Geophys. Res.*, *107*, 1165–+, doi: 10.1029/2001JA000331.

Prangé, R., D. Rego, D. Southwood, P. Zarka, S. Miller, and W. Ip (1996), Rapid energy dissipation and variability of the Io-Jupiter electrodynamic circuit, *Nature*, *379*, 323–325, doi:10.1038/379323a0.

Prangé, R., D. Rego, L. Pallier, J. Connerney, P. Zarka, and J. Queinnec (1998), Detailed study of FUV Jovian auroral features with the post-COSTAR HST faint object camera, *J. Geophys. Res.*, *103*, 20,195–20,216, doi:10.1029/98JE01128.

Queinnec, J., and P. Zarka (1998), Io-controlled decameter arcs and Io-Jupiter interaction, *J. Geophys. Res.*, *103*, 26,649–26,666, doi:10.1029/98JA02435.

Quijano et al., C. (2007), *STIS Instrument Handbook*, STScI, version 8.0 ed., http://www.stsci.edu/hst/stis/.

Radioti, A., J.-C. Gérard, D. Grodent, B. Bonfond, N. Krupp, and J. Woch (2008a), Discontinuity in Jupiter's main auroral oval, *J. Geophys. Res.*, *113*, 1215–+, doi:10.1029/2007JA012610.

Radioti, A., D. Grodent, J.-C. Gérard, B. Bonfond, and J. T. Clarke (2008b), Auroral polar dawn spots: Signatures of internally driven reconnection processes at Jupiter's magnetotail, *Geophys. Res. Lett.*, *35*, 3104–+, doi:10.1029/2007GL032460.

Radioti, A., D. Grodent, J.-C. Gérard, E. Roussos, C. Paranicas, B. Bonfond, D. G. Mitchell, N. Krupp, S. Krimigis, and J. T. Clarke (2009a), Transient auroral features at Saturn: Signatures of energetic particle injections in the magnetosphere, *J. Geophys. Res.*, *114*, 3210–+, doi:10.1029/2008JA013632.

Radioti, A., A. T. Tomás, D. Grodent, J.-C. Gérard, J. Gustin, B. Bonford, N. Krupp, J. Woch, and J. D. Menietti (2009b), Equatorward diffuse auroral emissions at Jupiter: Simultaneous HST and Galileo observations, *Geophys. Res. Lett.*, *36*, 7101–+, doi:10.1029/2009GL037857.

Retherford, K. D., H. W. Moos, D. F. Strobel, B. C. Wolven, and F. L. Roesler (2000), Io's equatorial spots: Morphology of neutral UV emissions, *J. Geophys. Res.*, *105*, 27,157–27,166, doi:10.1029/2000JA002500.

Retherford, K. D., H. W. Moos, and D. F. Strobel (2003), Io's auroral limb glow: Hubble Space Telescope FUV observations, *J. Geophys. Res.*, *108*, 1333–+, doi:10.1029/2002JA009710.

Retherford, K. D., J. R. Spencer, S. A. Stern, J. Saur, D. F. Strobel, A. J. Steffl, G. R. Gladstone, H. A. Weaver, A. F. Cheng, J. W. Parker, D. C. Slater, M. H.

Versteeg, M. W. Davis, F. Bagenal, H. B. Throop, R. M. C. Lopes, D. C. Reuter, A. Lunsford, S. J. Conard, L. A. Young, and J. M. Moore (2007), Io's Atmospheric Response to Eclipse: UV Aurorae Observations, *Science*, *318*, 237–, doi: 10.1126/science.1147594.

Roesler, F. L., H. W. Moos, R. J. Oliversen, R. C. Woodward, Jr., K. D. Retherford, F. Scherb, M. A. McGrath, W. H. Smyth, P. D. Feldman, and D. F. Strobel (1999), Far-Ultraviolet Imaging Spectroscopy of Io's Atmosphere with HST/STIS, *Science*, *283*, 353–+.

Russell, C. T., Z. J. Yu, K. K. Khurana, and M. G. Kivelson (2001), Magnetic field changes in the inner magnetosphere of Jupiter, *Advances in Space Research*, *28*, 897–902, doi:10.1016/S0273-1177(01)00513-0.

Saglam, A. (2004), Determination et analyse de la morphologie de l'aurore polaire de saturne à l'aide d'observations hst-stis, Master's thesis, Université de Liège.

Sakanoi, K., H. Fukunishi, and Y. Kasahara (2005), A possible generation mechanism of temporal and spatial structures of flickering aurora, *J. Geophys. Res.*, *110*, 3206–+, doi:10.1029/2004JA010549.

Sandel, B. R., D. E. Shemansky, A. L. Broadfoot, J. B. Holberg, G. R. Smith, J. C. McConnell, D. F. Strobel, S. K. Atreya, T. M. Donahue, H. W. Moos, D. M. Hunten, R. B. Pomphrey, and S. Linick (1982), Extreme ultraviolet observations from the Voyager 2 encounter with Saturn, *Science*, *215*, 548–553, doi: 10.1126/science.215.4532.548.

Saur, J. (2004), A model of Io's local electric field for a combined Alfvénic and unipolar inductor far-field coupling, *J. Geophys. Res.*, *109*, 1210–+, doi: 10.1029/2002JA009354.

Saur, J., F. M. Neubauer, D. F. Strobel, and M. E. Summers (1999), Three-dimensional plasma simulation of Io's interaction with the Io plasma torus: Asymmetric plasma flow, *J. Geophys. Res.*, *104*, 25,105–25,126, doi: 10.1029/1999JA900304.

Saur, J., F. M. Neubauer, D. F. Strobel, and M. E. Summers (2000), Io's ultraviolet aurora: Remote sensing of Io's interaction, *Geophys. Res. Lett.*, *27*, 2893–2896, doi:10.1029/2000GL003824.

Saur, J., F. M. Neubauer, D. F. Strobel, and M. E. Summers (2002), Interpretation of Galileo's Io plasma and field observations: I0, I24, and I27 flybys and close polar passes, *J. Geophys. Res.*, *107*, 1422–+, doi:10.1029/2001JA005067.

Saur, J., D. F. Strobel, F. M. Neubauer, and M. E. Summers (2003), The ion mass loading rate at Io, *Icarus*, *163*, 456–468, doi:10.1016/S0019-1035(03)00085-X.

Saur, J., F. M. Neubauer, J. E. P. Connerney, P. Zarka, and M. G. Kivelson (2004), *Jupiter. The Planet, Satellites and Magnetosphere*, chap. Plasma interaction of Io with its plasma torus, pp. 537–560, Cambridge University Press.

Saur, J., B. H. Mauk, D. G. Mitchell, N. Krupp, K. K. Khurana, S. Livi, S. M. Krimigis, P. T. Newell, D. J. Williams, P. C. Brandt, A. Lagg, E. Roussos, and M. K. Dougherty (2006), Anti-planetward auroral electron beams at Saturn, *Nature*, *439*, 699–702, doi:10.1038/nature04401.

Serio, A. W., and J. T. Clarke (2008), The variation of Io's auroral footprint brightness with the location of Io in the plasma torus, *Icarus*, *197*, 368–374, doi:10.1016/j.icarus.2008.03.026.

Shematovich, V. I., D. V. Bisikalo, and J. C. Gérard (1994), A kinetic model of the formation of the hot oxygen geocorona. 1: Quiet geomagnetic conditions, *J. Geophys. Res.*, *99*, 23,217–+, doi:10.1029/94JA01769.

Shematovich, V. I., D. V. Bisikalo, J.-C. Gérard, C. Cox, S. W. Bougher, and F. Leblanc (2008), Monte Carlo model of electron transport for the calculation of Mars dayglow emissions, *J. Geophys. Res.*, *113*, 2011–+, doi:10.1029/2007JE002938.

Shkolnik, E., G. A. H. Walker, and D. A. Bohlender (2003), Evidence for Planet-induced Chromospheric Activity on HD 179949, *The Astrophysical Journal*, *597*, 1092–1096, doi:10.1086/378583.

Shkolnik, E., G. A. H. Walker, D. A. Bohlender, P.-G. Gu, and M. Kürster (2005), Hot Jupiters and Hot Spots: The Short- and Long-Term Chromospheric Activity on Stars with Giant Planets, *The Astrophysical Journal*, *622*, 1075–1090, doi:10.1086/428037.

Shyn, T. W., and W. E. Sharp (1981), Angular distributions of electrons elastically scattered from H_2, *Physical Review A (General Physics)*, *24*, 1734–1740, doi: 10.1103/PhysRevA.24.1734.

Smith, C. G. A., A. D. Aylward, S. Miller, and I. C. F. Müller-Wodarg (2005), Polar heating in Saturn's thermosphere, *Annales Geophysicae*, *23*, 2465–2477.

Smith, R. (1998), Vertical winds: a tutorial, *Journal of Atmospheric and Solar-Terrestrial Physics*, *60*(14), 1425 – 1434, doi:DOI: 10.1016/S1364-6826(98)00058-3.

Smyth, W. H., and M. L. Marconi (1998), An explanation for the east-west asymmetry of the Io plasma torus, *J. Geophys. Res.*, *103*, 9091–9100, doi: 10.1029/97JA03597.

Swift, D. W. (2007), Simulation of auroral electron acceleration by inertial Alfvén waves, *J. Geophys. Res.*, *112*, 12,207–+, doi:10.1029/2007JA012423.

Thomas, N., F. Bagenal, T. W. Hill, and J. K. Wilson (2004), *Jupiter. The Planet, Satellites and Magnetosphere*, chap. The Io neutral clouds and plasma torus, pp. 561–591, Cambridge University Press.

Vasavada, A. R., A. H. Bouchez, A. P. Ingersoll, B. Little, C. D. Anger, and The Galileo SSI Team (1999), Jupiter's visible aurora and Io footprint, *J. Geophys. Res.*, *104*, 27,133–+.

Vasyliunas, V. M. (1983), *Physics of the Jovian magnetosphere*, chap. Plasma distribution and flow, pp. 395–453, Cambridge University Press.

Vincent, M. B., J. T. Clarke, G. E. Ballester, W. M. Harris, R. A. West, J. T. Trauger, R. W. Evans, K. R. Stapelfeldt, D. Crisp, C. J. Burrows, J. S. Gallagher, R. E. Griffiths, J. Jeff Hester, J. G. Hoessel, J. A. Holtzman, J. R. Mould, P. A. Scowen, A. M. Watson, and J. A. Westphal (2000), Mapping Jupiter's Latitudinal Bands and Great Red Spot Using HST/WFPC2 Far-Ultraviolet Imaging, *Icarus*, *143*, 189–204, doi:10.1006/icar.1999.6232.

Walker, G. A. H., B. Croll, J. M. Matthews, R. Kuschnig, D. Huber, W. W. Weiss, E. Shkolnik, S. M. Rucinski, D. B. Guenther, A. F. J. Moffat, and D. Sasselov

(2008), MOST detects variability on τ Bootis A possibly induced by its planetary companion, *Astronomy and Astrophysics*, *482*, 691–697, doi:10.1051/0004-6361:20078952.

Walsh, J. R., P. Goodfrooij, and E. Malumuth (2001), Stis geometric distortion - smov3a tests for ccd, nuv-mama and fuv-mama, *Tech. rep.*, STSCI, iSR 2001-02.

Weiss, J. W. (2004), *Jupiter. The Planet, Satellites and Magnetosphere*, chap. Appendix 2: Planetary Parameters, pp. 699–706, Cambridge University Press.

Williams, D. J., and R. M. Thorne (2003), Energetic particles over Io's polar caps, *J. Geophys. Res.*, *108*, 7–1, doi:10.1029/2003JA009980.

Williams, D. J., B. H. Mauk, R. E. McEntire, E. C. Roelof, T. P. Armstrong, B. Wilken, J. G. Roederer, S. M. Krimigis, T. A. Fritz, and L. J. Lanzerotti (1996), Electron Beams and Ion Composition Measured at Io and in Its Torus, *Science*, *274*, 401–403.

Williams, D. J., R. M. Thorne, and B. Mauk (1999), Energetic electron beams and trapped electrons at Io, *J. Geophys. Res.*, *104*, 14,739–14,754, doi: 10.1029/1999JA900115.

Wolven, B. C., H. W. Moos, K. D. Retherford, P. D. Feldman, D. F. Strobel, W. H. Smyth, and F. L. Roesler (2001), Emission profiles of neutral oxygen and sulfur in Io's exospheric corona, *J. Geophys. Res.*, *106*, 26,155–26,182, doi: 10.1029/2000JA002506.

Wright, A. N. (1987), The interaction of Io's Alfven waves with the Jovian magnetosphere, *J. Geophys. Res.*, *92*, 9963–9970.

Wright, A. N., and S. J. Schwartz (1989), The transmission of Alfven waves through the Io plasma torus, *J. Geophys. Res.*, *94*, 3749–3754.

Wu, C. S. (1985), Kinetic cyclotron and synchrotron maser instabilities - Radio emission processes by direct amplification of radiation, *Space Science Reviews*, *41*, 215–298.

Yelle, R. V., L. A. Young, R. J. Vervack, R. Young, L. Pfister, and B. R. Sandel (1996), Structure of Jupiter's upper atmosphere: Predictions for Galileo, *J. Geophys. Res.*, *101*, 2149–2162, doi:10.1029/95JE03384.